U.S. DEPARTMENT OF ENERGY

FutureGen 2.0 Monitoring Systems Design Basis and Technology Selection: Geohydrologic, Geochemical, and Geophysical Considerations

VR Vermeul
JE Amonette
CE Strickland
JE Szecsody
MD Williams
A Bonneville
TA Johnson
TC Johnson
M Oostrom
SL Porse
FA Spane
CF Spencer
JN Thomle

November 2014

Pacific Northwest NATIONAL LABORATORY

Proudly Operated by Battelle Since 1965

DISCLAIMER

This report was prepared as an account of work sponsored by an agency of the United States Government. Neither the United States Government nor any agency thereof, nor Battelle Memorial Institute, nor any of their employees, makes **any warranty, express or implied, or assumes any legal liability or responsibility for the accuracy, completeness, or usefulness of any information, apparatus, product, or process disclosed, or represents that its use would not infringe privately owned rights**. Reference herein to any specific commercial product, process, or service by trade name, trademark, manufacturer, or otherwise does not necessarily constitute or imply its endorsement, recommendation, or favoring by the United States Government or any agency thereof, or Battelle Memorial Institute. The views and opinions of authors expressed herein do not necessarily state or reflect those of the United States Government or any agency thereof.

PACIFIC NORTHWEST NATIONAL LABORATORY
operated by
BATTELLE
for the
UNITED STATES DEPARTMENT OF ENERGY
under Contract DE-AC05-76RL01830

Printed in the United States of America

Available to DOE and DOE contractors from the
Office of Scientific and Technical Information,
P.O. Box 62, Oak Ridge, TN 37831-0062;
ph: (865) 576-8401
fax: (865) 576-5728
email: reports@adonis.osti.gov

Available to the public from the National Technical Information Service
5301 Shawnee Rd., Alexandria, VA 22312
ph: (800) 553-NTIS (6847)
email: orders@ntis.gov <http://www.ntis.gov/about/form.aspx>
Online ordering: http://www.ntis.gov

This document was printed on recycled paper.
(8/2010)

PNWD-4435

FutureGen 2.0 Monitoring Systems Design Basis and Technology Selection: Geohydrologic, Geochemical, and Geophysical Considerations

VR Vermeul
JE Amonette
CE Strickland
JE Szecsody
MD Williams
A Bonneville
TA Johnson
TC Johnson
M Oostrom
SL Porse
FA Spane
CF Spencer
JN Thomle

November 2014

Prepared for
the U.S. Department of Energy
under Contract DE-AC05-76RL01830

Pacific Northwest National Laboratory
Richland, Washington 99352

Summary

Advances in carbon capture and storage (CCS) technology show promise for addressing carbon dioxide (CO_2) emissions and global climate change concerns related to coal-fueled energy production. The FutureGen 2.0 project is intended to demonstrate 1) the technical feasibility of oxy-combustion technology as an approach for implementing carbon capture at new and existing coal-fueled energy facilities, and 2) utility-scale integration of CO_2 transport and permanent storage in a deep geologic formation. Development of the FutureGen 2.0 CO_2 storage site is part of a larger project to design, build, and operate a commercial-scale CCS system capable of capturing, treating, and storing the CO_2 off-gas from a 168-MW(e) gross capacity oxy-combustion coal-fueled power plant located in Meredosia, Illinois—a first-of-its-kind, near-zero emissions coal-fueled power plant with CCS. In cooperation with the U.S. Department of Energy, the FutureGen 2.0 project partners will repower a previously retired oil-fired power plant with oxy-combustion technology to capture approximately 1.1 million metric tons of CO_2 each year—more than 90 percent of the plant's carbon emissions. Emissions such as sulfur oxides, nitrogen oxides, and mercury will be reduced to near-zero levels. Safe and proven pipeline technology will be used to transport the CO_2 to the storage site and inject it deep into the subsurface through a network of deep-injection wells for long-term storage through geologic sequestration.

An evaluation that considered pertinent hydrologic, geochemical, and geophysical processes was performed during development of the testing and monitoring program for the FutureGen 2.0 project. This evaluation informed the technology screening process and, in conjunction with project- and regulation-driven monitoring objectives, was the basis for monitoring technology selection. A summary of the overall monitoring approach adopted by the FutureGen 2.0 project, and a detailed description of the testing and monitoring activities that the FutureGen Industrial Alliance, Inc. will undertake at the FutureGen 2.0 storage site near Jacksonville, Illinois, are documented in a project-maintained testing and monitoring plan. All testing and monitoring activities will be performed in accordance with Title 40 of the Code of Federal Regulations (CFR) Sections 146.89, 146.90, and 146.91 (40 CFR §146.89, 146.90, and 146.91) to verify that the storage site is operating as permitted and is not endangering any underground sources of drinking water (USDWs). Results from the evaluation of geohydrologic, geochemical, and geophysical monitoring considerations are described in this report and are summarized below.

Laboratory Studies of Biogeochemical Processes

Laboratory experiments showed that low viscosity supercritical carbon dioxide ($scCO_2$) displacement of the brine in Mount Simon Sandstone and Eau Claire Formation cores occurs slowly by advection, as scCO2 travels predominantly in larger pores, leaving a significant amount of brine in smaller pores. As the $scCO_2$ displaces the brine in larger pores and carbonate partitions into the brine, the resulting acidification (to pHs of 3 to 4) causes short-term dissolution of minerals, desorption of ions, and movement of iron oxide particles. Major aqueous geochemical and biological changes observed over 1.2 years from core/brine/$scCO_2$ interaction studies include 1) significant increase in Mg^{2+}, K^{+}, and SO_4^{2-} concentrations (10s to 100s of mmol/L), 2) dissolution of the hematite coating on the quartz grains, 3) significant precipitation of NaCl and KCl, and 4) some anaerobic microbial growth. Electron microprobe analysis demonstrated formation of NaCl and KCl precipitates, but the amount of precipitate formed was too small to significantly change permeability. Anaerobic microbial growth associated with $scCO_2$

injection was also too small to influence permeability. Overall, injection of $scCO_2$ into the brine-filled Mount Simon Sandstone cores resulted in small geochemical and biological changes over the time scales evaluated.

Geohydrologic Monitoring Considerations

A modeling study was conducted to determine whether pressure measurements from reservoir monitoring wells can be used to infer the spatial extent of $scCO_2$ during evolution of the CO_2 plume. This monitoring concept relies on the fact that pressures measured in the injection wells and reservoir monitoring wells will tend to decrease (or increase less over time) as the lower viscosity $scCO_2$ plume grows and increases the relative permeability of the injection zone formation materials throughout the region where $scCO_2$ is present. The resulting change in hydraulic conductivity may result in appreciable changes in hydraulic response during the periodic injection stoppage/restart operations associated with power plant maintenance outages. Preliminary simulation results show that while the peak pressures generated during each annual cycle were still increasing over the 10-year simulation period, the increases were becoming smaller as the simulation progressed and the amplitude of pressure cycles were also reduced. These results indicate that collection and analysis of geohydrologic monitoring data have the potential to provide corroborative evidence for the spatial extent, symmetry, and evolution of the $scCO_2$ plume. The utility of this approach will continue to be evaluated during the construction and initial operational phases of the project.

Geochemical Monitoring Considerations

Based on an evaluation of aqueous- and gas-phase monitoring considerations, the geochemical monitoring program will initially rely on intrinsic and CO_2-related aqueous geochemical signals as the primary geochemical indicators of leakage response. Selection of the initial list of parameters was based on their relevance for detecting the presence of fugitive brine and CO_2. The relative benefit (and cost) of each analytical measurement will be evaluated throughout the construction and initial injection testing phase of the project to identify the analytes best suited to meeting project monitoring objectives under site-specific conditions. If some analytical measurements are shown to be of limited use and/or are cost-prohibitive relative to regulatory required parameters, they will be removed from the analyte list and not carried forward through the operational phases of the project. This selection process will consider the uniqueness and signature strength of each potential analyte and whether their characteristics provide for a high-value leak-detection capability. The introduction of co-injected tracers was also considered. Although this preliminary evaluation of co-injected tracers has initially screened them from consideration, this decision may be revisited during the construction and initial operational phases of the project. If future assessment indicates that intrinsic and/or CO_2-related geochemical signatures are unlikely to provide an acceptable degree of sensitivity to leakage through the primary confining zone, then addition of co-injected tracers may be implemented. With respect to gas-phase monitoring, soil-gas composition (both geochemical and isotopic) and metabolic mass balance monitoring will be conducted to establish baseline conditions. In the event that deep early-leak−detection monitoring indicates that a significant loss of containment has occurred, the need for establishing a long-term soil-gas monitoring program will be reevaluated.

Geophysical Monitoring Considerations

Geophysical monitoring methods are sensitive to subsurface changes that result from injection of CO_2 and will be used for 1) tracking the spatial extent of the free-phase CO_2 plume, 2) monitoring advancement of the pressure front, 3) identifying or mapping areas where induced seismicity occurs, and 4) identifying and mapping regions of increased risk for brine or CO_2 leakage from the reservoir. Site-specific suitability and cost-effectiveness were evaluated for a number of geophysical monitoring methods: passive seismic monitoring, reflection seismic imaging, integrated surface deformation, time-lapse gravity, pulsed-neutron capture logging, cross-borehole seismic, electrical resistivity tomography, magnetotellurics, and controlled-source electromagnetics. The results of this evaluation indicate that CO_2 injection monitoring using reflection seismic methods would be challenging at the FutureGen 2.0 site. Electrical methods also exhibited low sensitivity to the expected CO_2 saturation changes and would be affected by metallic infrastructure at the field site. Passive seismic, integrated surface deformation, time-lapse gravity, and pulsed-neutron capture monitoring were selected for implementation as part of the FutureGen 2.0 storage site monitoring program.

Assessment of Early-Leak-Detection Capabilities

The monitoring program will include direct monitoring of the reservoir and early-leak-detection monitoring directly above the primary confining zone. A preliminary modeling study was conducted to evaluate scenarios of hypothetical leakage into the first permeable unit above the primary confining zone (Ironton Sandstone) and to assess early-leak−detection capabilities. This modeling evaluation considers both pressure response and geochemical signals in the overlying Ironton Sandstone resulting from theoretical, volumetric-rate−based leakage scenarios. The scenarios include leakage of 1 percent of the total injected CO_2 mass, but spread out over different time periods (20, 100, and 500 years) with each case yielding a different mass flux (i.e., smaller mass fluxes for longer duration leakage cases). A brine leakage scenario using a volumetric leakage rate comparable to the 20-year 1 percent CO_2 case was also considered. A comparison of results from this preliminary evaluation demonstrates that distinctions in leak-detection sensitivity can be made between the various leak-detection signals for the leakage scenarios and monitoring locations investigated (distances of 80, 455, and 955 ft from the leak). Overall, both $scCO_2$ and brine simulations show that pressure is likely to be the earliest indicator of leakage, as demonstrated by the rapid pressure responses seen for all leakage scenarios evaluated. Given the accuracy and resolution of the sensors that will be used to monitor pressure at the FutureGen 2.0 storage site (2 and 0.05 psi, respectively), it is expected that a pressure response would be detected within a week for all of the 20- and 100-year leakage scenarios at all of the monitoring locations evaluated. For the 500-year leakage scenario, higher resolution equipment may be necessary for pressure detection. Comparisons of the arrival times of aqueous CO_2 (for $scCO_2$ simulations) and tracer (for brine simulations) show that geochemical signals are much more localized and take much longer to develop than the pressure responses. In addition, because of the buoyancy effect associated with $scCO_2$ injection, early-leak−detection monitoring for these leakage scenarios is best achieved through monitoring of the upper portion of the monitoring interval, near the interface with the overlying lower permeability materials, where the CO_2 plume shows the largest lateral migration.

Acknowledgments

The FutureGen 2.0 project is supported by a $1 billion commitment in U.S. federal funding from the American Recovery and Reinvestment Act. The program is implemented under Cooperative Agreement DE-FE0001882 between the U.S. Department of Energy and the FutureGen Industrial Alliance, Inc. (Alliance), a non-profit membership organization created to benefit the public interest and the interests of science through research, development, and demonstration of near-zero emissions coal technology. Members of the Alliance include some of the largest coal producers, coal users, and coal equipment suppliers in the world. For more information about the FutureGen 2.0 project, please visit www.futuregenalliance.org.

Acronyms and Abbreviations

1D	one-dimensional
2D	two-dimensional
3C	three-component
3D	three-dimensional
4D	four-dimensional
A	ampere(s)
ACZ	above confining zone
Alliance	FutureGen Industrial Alliance, Inc.
AMS	accelerator mass spectrometry
AoR	Area of Review
AR	artificial reflector
AVA	amplitude versus angle
bgs	below ground surface
CCS	carbon capture and storage
CSEM	controlled-source electromagnetics
CFR	Code of Federal Regulations
cm	centimeter(s)
cm^2	square centimeter(s)
CMG	Computer Modeling Group
C/O	carbon/ oxygen (ratio)
CO_2	carbon dioxide
CRDS	cavity ringdown spectroscopy
DC	direct current
DGPS	differential global positioning system
DIC	dissolved inorganic carbon
DInSAR	differential interferometric synthetic aperture radar
DLAS	diode laser adsorption spectrometry
DOE	U.S. Department of Energy
EC	electrical conductivity
EPA	U.S. Environmental Protection Agency
ERT	electrical resistivity tomography

FR	Federal Register
ft	foot(feet)
µGal	microGal(s)
GC-ECD	gas chromatography with an electron-capture detector
GC-MS	gas chromatography-mass spectrometry
GC-TCD	gas chromatography with thermal conductivity detector
GHG	greenhouse gas
g/L	gram(s) per liter
g/m^3	gram(s) per cubic meter
g/cm^3	gram(s) per cubic centimeter
g/ml	gram(s) per milliliter
GPS	global positioning system
GWP	global warming potential
HEPA	high-efficiency particulate air
Hz	hertz
ICP	inductively coupled plasma
InSAR	interferometric synthetic aperture radar
ISGS	Illinois State Geological Survey
km	kilometer(s)
L	liter(s)
LSC	liquid scintillation counting
LOS	line-of-sight
µm	micron(s)
m	meter(s)
MCNP	Monte Carlo N-Particle
MeV	million electron volts
m/s^2	meter(s) per square second
mi	mile(s)
mL	milliliter(s)
mm	millimeter(s)
mmol/L	millimole(s)/liter

MMT	million metric tons
MPa	megapascal(s)
MT	magnetotellurics
MVA	monitoring, validation, and accounting
MVA-ULT	MVA upper layer transport
Myr	million years
OGS	optogalvanic spectroscopy
OVSP	offset vertical seismic profile
PDCB	perfluorodimethylcyclobutane
PDCH	perfluoro-1,2-dimethylcyclohexane
PEEK	polyetheretherketone
PFBA	pentafluorobenzoic acid
PFT	perfluorinated tracer
pmol	picomole
PNC	pulsed-neutron capture
ppb	parts per billion
ppbv	parts per billion by volume
ppm	parts per million
ppmv	parts per million by volume
ppt	parts per thousand
psi	pounds per square inch
PTCH	perfluorotrimethyl-cyclohexane
P/T/SpC	pressure, temperature, and specific conductance
RAT	reservoir access tube
RTK	real-time kinematic
SAR	synthetic aperture radar
SCAR	saturated-absorption cavity ringdown spectroscopy
$scCO_2$	supercritical carbon dioxide
SLR	single-level in-reservoir (monitoring well)
SLR2	SLR well 2 (reconfigured FG1 stratigraphic well)
S/m	Siemens per meter
SNR	signal-to-noise ratio
SS	stainless steel
STOMP	Subsurface Transport Over Multiple Phases

UIC	Underground Injection Control
USDW	underground sources of drinking water
V	volt(s)
VSP	vertical seismic profile (or profiling)
WAVSP	walk-away vertical seismic profile
ZOVSP	zero-offset vertical seismic profile

Contents

Figures

Tables

1.0 Introduction

The advancement of carbon capture and storage (CCS) technology shows promise for addressing carbon dioxide (CO_2) emissions and global climate change concerns associated with coal-fueled energy production. The objectives of the FutureGen 2.0 project are to demonstrate the technical feasibility of oxy-combustion technology as an approach for implementing carbon capture at new and existing coal-fueled energy facilities, and demonstrate the utility-scale integration of CO_2 transport and permanent storage in a deep geologic formation. Implementation of the FutureGen 2.0 project supports these objectives by establishing the feasibility of producing electricity from coal with at least 90 percent CO_2 capture during steady-state operation and near-zero emissions of air pollutants.

Development of the FutureGen 2.0 CO_2 storage site near Jacksonville, Illinois (hereafter referred to as the FutureGen 2.0 storage site), is part of a larger project to design, build, and operate a commercial-scale CCS system capable of capturing, treating, and storing the CO_2 off-gas from a 168-MW(e) gross capacity oxy-combustion coal-fueled power plant located in Meredosia, in Morgan County, Illinois. The FutureGen 2.0 project will design and build a first-of-its-kind, near-zero emissions coal-fueled power plant with CCS. In cooperation with the U.S. Department of Energy (DOE), the FutureGen 2.0 project partners—the FutureGen Industrial Alliance, Inc. (Alliance)—will repower a previously retired oil-fired power plant with oxy-combustion technology to capture approximately 1.1 million metric tons (MMT) of CO_2 each year, which is more than 90 percent of the plant's carbon emissions. Other emissions, such as sulfur oxides, nitrogen oxides, and mercury, will be reduced to near-zero levels. Using safe and proven pipeline technology, the CO_2 will be transported approximately 28 mi to the storage site near Jacksonville, Illinois, and injected into a deep saline reservoir (~ 4,000 ft below ground surface [bgs]) through a network of horizontal injection wells, where it will be stored long-term through geologic sequestration.

Researchers at the Pacific Northwest National Laboratory (PNNL) conducted an evaluation of geohydrologic, geochemical, and geophysical processes during development of the testing and monitoring program for the FutureGen 2.0 project. The evaluation (documented herein) informed the technology screening process and, in conjunction with project- and regulation-driven monitoring objectives, was the basis for monitoring technology selection.

Section 2.0 of this report contains a description of the project's monitoring approach and a summary of the FutureGen 2.0 storage site monitoring program. Section 3.0 discusses laboratory-scale studies of biogeochemical processes that were performed using site-specific core materials. Sections 4.0, 5.0, and 6.0 provide a detailed discussion of geohydrologic, geochemical, and geophysical monitoring considerations, respectively. Section 7.0 documents an assessment of early leak-detection capabilities and a summary of results and conclusions is presented in Section 8.0. References are provided in Section 9.0.

2.0 Monitoring Approach

This section provides a summary of the overall monitoring approach adopted by the FutureGen 2.0 project, and the testing and monitoring activities that the Alliance will undertake at its FutureGen 2.0 storage site. A more detailed description of the monitoring program is available in a project-maintained testing and monitoring plan (Vermeul et al. 2014), which is a working project document that will be routinely evaluated and updated (as required) throughout the life of the project. All testing and monitoring activities will be performed in accordance with Title 40 of the Code of Federal Regulations (CFR) Sections 146.89, 146.90, and 146.91 (40 CFR §146.89, 146.90, and 146.91) to verify that the storage site is operating as permitted and is not endangering any underground sources of drinking water (USDWs).

The primary objective of the monitoring program is to implement a suite of monitoring technologies that are both technically sound and cost-effective and provide an effective means of 1) monitoring the evolution of the CO_2 plume and pressure front, 2) evaluating CO_2 mass balance, and 3) detecting any unforeseen loss in CO_2 containment. The monitoring program will include injection well testing and monitoring activities, groundwater quality monitoring immediately above the primary confining zone and in the lowermost USDW aquifer, and injection-zone monitoring that will consist of 1) direct pressure monitoring, 2) direct geochemical monitoring, and 3) indirect (i.e., geophysical) monitoring of the CO_2 plume and pressure-front evolution. The monitoring infrastructure will include a network of deep monitoring wells and a surface-based network of combined passive seismic/surface deformation monitoring stations. The CO_2 injection stream will be continuously monitored as part of the instrumentation and control systems for the FutureGen 2.0 project; injection stream monitoring will also include periodic collection and analysis of grab samples to track CO_2 composition. A summary of the planned monitoring technologies and measurement frequency is provided in Table 2.1.

Both direct and indirect measurements will be used collaboratively with numerical models of the injection process to verify that CO_2 is effectively sequestered within the targeted deep geologic formation and that the stored CO_2 mass is accounted for. Prior to injection of CO_2, background levels of any anticipated hydrogeologic, geochemical, and geophysical parameters will be measured to establish a baseline against which subsequent measurements will be compared.

The monitoring approach is based in part on early-detection monitoring wells that target regions of increased leakage potential (e.g., areas of highest pressure buildup containing wells that penetrate the caprock). Leak-detection monitoring can be divided into two distinct modes. The first is “detection” mode, which focuses on detecting a leak at the earliest possible opportunity. Because of its larger areal extent of detectability, this mode will most likely be informed by changes in fluid pressure, although localized changes in aqueous geochemistry might also be detected. If a leak is detected, this would trigger a secondary “assessment” mode of monitoring wherein the focus would be on quantifying the rate and extent of the leak. This mode would continue to be informed by pressure data, but characterization of changes in aqueous geochemistry within the early leak-detection monitoring interval would likely play an increased role in the assessment. In the assessment mode, monitoring costs may increase if additional analytes and/or more frequent sample collection are required to adequately characterize the leak. While CCS projects must plan for both modes of leak-detection monitoring, the expectation is that the assessment mode will never be required.

Table 2.1. Monitoring frequencies by method and project phase.

		DOE Active Phase			Commercial Phase	
Monitoring Category	Monitoring Method	Baseline 3 yr	Injection (startup) ~3 yr	Injection ~2 yr	Injection ~15 yr	Post-Injection 50 yr
CO_2 Injection Stream Sampling and Analysis	Grab sampling and analysis	3 events, during commissioning	Quarterly	Quarterly	Quarterly	NA
CO_2 Injection Stream Monitoring	Continuous monitoring of injection process (injection rate, pressure, and temperature; annulus pressure and volume)	NA	Continuous	Continuous	Continuous	NA
Corrosion Monitoring	Corrosion coupon monitoring of injection well materials	NA	Quarterly	Quarterly	Quarterly	NA
Mechanical Integrity Testing (ACZ/USDW wells excluded)	PNC and temperature logging (frequency shown for injection wells)	Once after well completion	Annual	Annual	Annual	Annual until wells plugged
	Cement-evaluation and casing inspection logs	Once after well completion	During well workovers	During well workovers	During well workovers	NA
	Annular pressure monitoring	NA	Continuous	Continuous	Continuous	NA
Pressure Fall-Off Testing	Injection well pressure fall-off testing	NA	Every 5 yr	Every 5 yr	Every 5 yr	NA
Groundwater Quality Monitoring	Fluid sampling and analysis in ACZ and USDW monitoring wells	3 events	Quarterly	Semi-Annual	Annual	Every 5 yr
	Electronic P/T/SpC probes installed in ACZ and USDW wells	1 yr min	Continuous	Continuous	Continuous	Continuous
Direct CO_2 Plume and Pressure-Front Monitoring	Fluid sample collection and analysis in SLR monitoring wells	3 events	Quarterly	Semi-Annual	Annual	Every 5 yr
	Electronic P/T/SpC probes installed in SLR wells	1 yr min	Continuous	Continuous	Continuous	Continuous
Indirect CO_2 Plume and Pressure-Front Monitoring	Passive seismic monitoring	1 yr min	Continuous	Continuous	Continuous	Continuous
	Integrated deformation monitoring	1 yr min	Continuous	Continuous	Continuous	Continuous
	Time-lapse gravity	3 events	Annual	Annual	Annual	NA
	PNC logging of RAT wells	3 events	Quarterly	Quarterly	Annual	Annual

ACZ = above confining zone; NA = not applicable; PNC = pulsed-neutron capture; P/T/Spc = pressure, temperature, and specific conductance; RAT = reservoir access tube; SLR = single-level in-reservoir; USDW = underground source of drinking water.

A comprehensive suite of geochemical and isotopic analyses will be performed on fluid samples collected from the reservoir and overlying monitoring intervals. These analytical results will be used to characterize baseline geochemistry and provide a metric for comparison during operational phases of the project. A primary design consideration for "detection" monitoring is minimizing lifecycle cost without sacrificing the ability to detect a leak. As a result, only select parameters measured during the baseline monitoring period will be routinely measured during operational phases of the project. Indicator parameters will be used to the extent possible to inform the monitoring program. Once baseline conditions and early CO_2 arrival responses have been established, observed relationships between analytical measurements and indicator parameters will be used to guide less frequent aqueous sample collection in later years.

If a significant CO_2 and/or brine leakage response is detected, a modeling evaluation will be used to assess the magnitude of containment loss and make bounding predictions regarding the potential for CO_2 migration above the confining zone, including any resulting impacts on shallower intervals, and ultimately, the potential for adverse impacts on USDW aquifers or other ecological receptors. Observed and simulated arrival responses at the early-leak−detection wells and shallower monitoring locations will be compared throughout the life of the project and results will be used to calibrate and verify the model, and improve its predictive capability for assessing the long-term environmental impacts of any fugitive CO_2. If pressure and/or geochemical responses in deep early-leak−detection monitoring wells indicate that primary confining zone leakage has occurred, a comprehensive near-surface-monitoring program will be evaluated (in consultation with the Underground Injection Control [UIC] Program Director) and, if warranted, activated to fully assess environmental impacts relative to previously established baseline conditions.

The monitoring network will address prediction uncertainty by adopting an "adaptive" or "observational" monitoring approach (i.e., the monitoring approach will be adjusted as needed based on observed monitoring and updated modeling results). This monitoring approach will continually evaluate monitoring results and make adjustments to the monitoring program as needed, including the option to install additional wells in outyears to verify CO_2 plume and pressure-front evolution and/or evaluate leakage potential. To meet permit requirements for pressure-front monitoring, at least one additional injection-zone monitoring well will be installed within 5 years of the start of injection. The well will be installed outside the lateral extent of the CO_2 plume but within the lateral extent of the defined pressure-front Area of Review (AoR). The final placement of this well will be informed by any observed asymmetry in pressure-front development, and the distance beyond the CO_2 plume boundary will be selected to provide information that will be useful for both leak detection and model calibration. It is estimated that the well will be located within 5 mi of the predicted CO_2 plume extent.

2.1 Monitoring Network Summary

The monitoring network design is based on the Alliance's current conceptual understanding of the site and predictive simulations of injected CO_2 fate and transport. The model used in the design analysis was parameterized based on site-specific characterization data collected from the initial stratigraphic borehole and reflection seismic surveys conducted at the FutureGen 2.0 storage site (Alliance 2012). The network design also considered other available regional data, including the effects of structural dip, regional groundwater flow conditions, and the potential for heterogeneities or horizontal/vertical anisotropy within the injection zone and overburden materials (Alliance 2013). The monitoring network

will be in place and completely functional prior to any CO_2 injection (and associated pressure buildup) to establish the baseline conditions with which to compare and evaluate future injection/post-injection conditions. CO_2 injection will only proceed once baseline levels have been established for all implemented monitoring methods. Active wells (i.e., wells not yet decommissioned) will continue to be monitored for the duration of the project to characterize subsurface pressure and CO_2 migration and guide operational and regulatory decision-making.

2.1.1 Monitoring Well Network

The monitoring well network, which includes both injection-zone monitoring wells and monitoring wells installed above the primary confining zone, is designed to detect unforeseen leakage from the reservoir as soon after the first occurrence as possible. Two aquifers above the primary confining zone will be monitored for any unforeseen leakage of CO_2 and/or brine out of the injection zone. These include the aquifer immediately above the confining zone (Ironton Sandstone) and the St. Peter Sandstone, which is separated from the Ironton by several carbonate and sandstone formations and is considered to be the lowermost USDW at the site. In addition to directly monitoring for CO_2, wells will be monitored for changes in geochemical and isotopic signatures that provide indication of CO_2 and/or brine leakage. Direct monitoring of the lowermost USDW aquifer is required by the U.S. Environmental Protection Agency's (EPA's) UIC Program for CO_2 geologic sequestration (75 FR 77230) and is a primary objective of this monitoring program. Wells will also be instrumented to detect changes in the stress regime (via pressure in all wells and microseismicity in selected wells) to avoid over-pressurization within the injection or confining zones that could compromise sequestration performance.

The monitoring well network consists of two wells monitoring changes within the injection zone (Elmhurst/Mount Simon Sandstones), two wells within the first permeable interval immediately above the primary confining zone (Ironton Sandstone), one well within the lowermost USDW (St. Peter Sandstone), and three reservoir access tubes (RATs), which will be used to monitor CO_2 saturation in the reservoir and caprock. Well locations are shown in Figure 2.1 and a hydrogeologic cross section illustrating the relative position and depth interval of the various wells is shown in Figure 2.2.

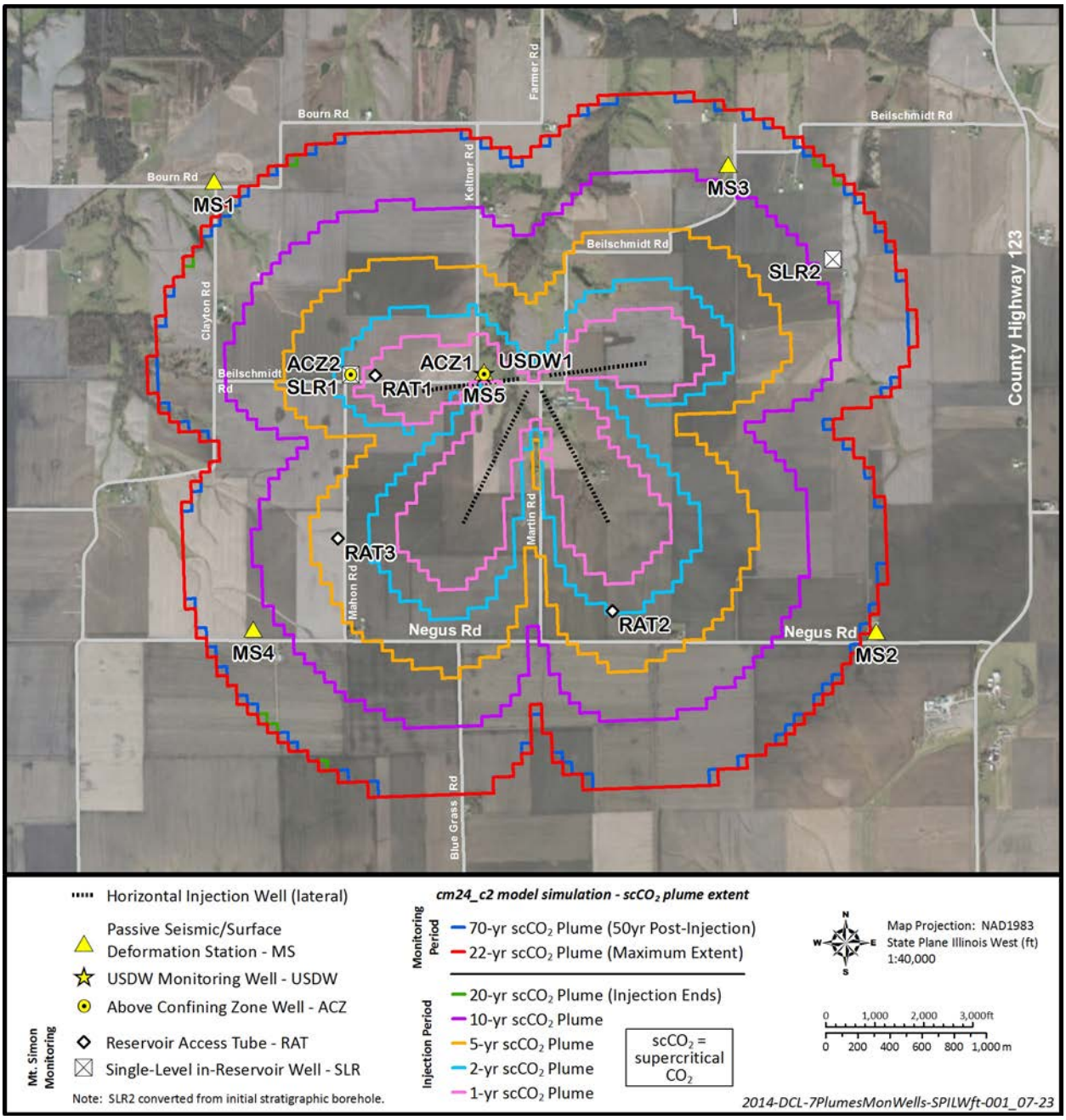

Figure 2.1. Nominal well network layout for the injection and monitoring wells and modeled $scCO_2$ plume. The monitoring well locations are approximate and subject to landowner approval.

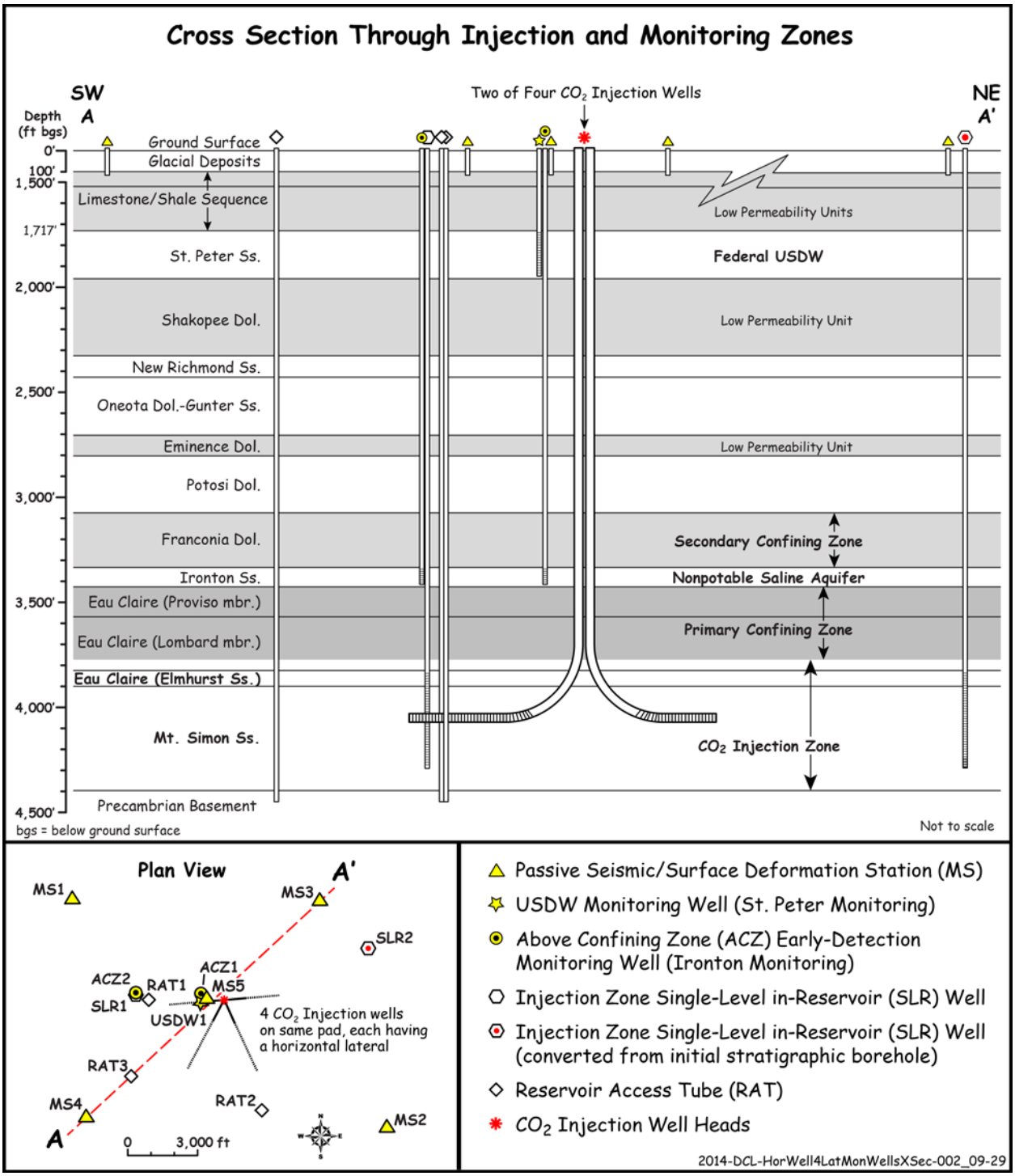

Figure 2.2. Cross-sectional view of the injection and monitoring well network.

Two single-level, in-reservoir (SLR) wells will monitor the injection zone beyond the east and west ends of the horizontal CO_2-injection laterals. One of the SLR monitoring wells, SLR2, is a reconfiguration of the initial stratigraphic borehole, which was drilled to characterize the site in 2011; this well is located approximately 1.25 mi east-northeast of the injection site. The other in-reservoir monitoring well, SLR1, is located approximately 0.75 mi west of the injection site. These wells will be

used to continuously and directly monitor changes in fluid pressure, temperature, and specific conductance (P/T/SpC), and will be routinely sampled to monitor changes in aqueous chemistry during the pre-injection, injection, and post-injection monitoring periods. Measurements at these locations will be compared with numerical model predictions and used to calibrate the model as necessary.

The above confining zone (ACZ) "early-detection" monitoring wells are completed in the Ironton Sandstone and will be continuously monitored for changes in P/T/SpC and seismicity, and will be routinely sampled to characterize any changes in aqueous chemistry. The ACZ monitoring wells are located immediately above the primary confining zone and are central to the overall monitoring strategy because they allow for identifying any unforeseen leakage from the reservoir as early as possible. Leakage to the ACZ monitoring interval would most likely be identified based on pressure response, but it could also result in changes in aqueous chemistry. One of the ACZ wells is located approximately 1,000 ft west of the injection site, within the region of highest pressure buildup. The other ACZ well is located approximately 0.75 mi west of the injection site within 50 ft of SLR1 and 500 ft of RAT1. Both of these ACZ well locations represent areas of increased potential for leakage (i.e., areas of increased pressure where wells penetrate the primary confining zone). If ACZ monitoring results provide any indication of leakage, a modeling evaluation will be performed to assess the magnitude of leakage and make bounding predictions regarding the potential for CO_2 migration and expected impacts on shallower intervals, and ultimately, the potential for adverse impacts on USDW aquifers or other ecological receptors.

The monitoring network also includes one well located in the lowest USDW (St Peter Sandstone). This well will be instrumented to continuously monitor P/T/SpC, and will be routinely sampled to characterize any changes in aqueous chemistry. This USDW well is co-located with the ACZ well located closest to the injection well site (ACZ1).

In addition to the five planned monitoring wells, there will be three RAT installations used to track the evolution of the CO_2 plume (see Figure 2.1). The RATs are non-perforated, cemented casings used to monitor CO_2 arrival and quantify saturation levels via downhole PNC (pulsed-neutron capture) geophysical logging across the reservoir and confining zone. PNC logging is a proven method for quantifying CO_2 saturation around the borehole. These three monitoring installations are located at increasing distances from the injection site to provide measures of CO_2 saturation at the predicted 1-, 2- and 3- to 4-year arrival times, and CO_2 arrival information for three of the four predicted lobes of the CO_2 plume. These near-field CO_2 saturation measurements will allow for calibration of the numerical model early in the injection phase of the project and verify whether the CO_2 plume is developing as predicted. The RAT installations will continue to be monitored for the duration of the project to assess the potential for vertical migration of CO_2 into the caprock material.

2.1.2 Geophysical Monitoring Network

Geophysical monitoring methods are sensitive to subsurface conditions that can change as a result of changes in fluid saturation or pressure associated with CO_2 injection. Geophysical monitoring methods considered for the FutureGen 2.0 storage site included electrical resistivity tomography, passive seismic monitoring, two- and three-dimensional (2D and 3D) surface seismic surveys, vertical seismic profiling, cross-well seismic imaging, time-lapse gravity, magnetotelluric soundings and controlled-source electromagnetics, integrated deformation monitoring, and PNC logging. This comprehensive suite of

technologies was evaluated with respect to site-specific conditions and subjected to a screening process; then suitable methodologies were selected for deployment as part of the monitoring program. This selection process, which is documented in Section 6.0, considered the level of sensitivity, spatial resolution, the costs to install and operate, and potential interference with other monitoring activities. Technologies that were selected for implementation included passive seismic monitoring, time-lapse gravity, integrated deformation monitoring, and PNC logging.

Integrated deformation monitoring and passive seismic monitoring are two indirect monitoring techniques that will be used to detect and characterize development of the pressure front resulting from injection of CO_2. The objective of deformation monitoring is to provide a means of detecting any asymmetry in the CO_2 plume development and help guide the adaptive monitoring strategy. The objective of the passive seismic monitoring network is to accurately determine the locations, magnitudes, and focal mechanisms of injection-induced seismic events with the primary goals of

- addressing public and stakeholder concerns related to induced seismicity,
- estimating the spatial extent of the pressure front from the distribution of seismic events, and
- supporting assessments of caprock integrity and the potential for containment loss.

Another indirect monitoring technique—PNC logging—will be the primary means of tracking the advancement and evolution of the CO_2 plume, as discussed Section 2.1.1. Time-lapse gravity will provide additional low-cost measurements that will supplement the PNC logs and support the assessment of plume evolution.

2.1.3 Near-Surface Environmental Monitoring Network

At the direction of the UIC Program Director, no surface or near-surface monitoring methodologies have been included as a requirement of the Class VI Underground Injection Control permit. Even though near-surface monitoring is not required at the FutureGen 2.0 storage site, the Alliance has initiated several approaches, including surficial groundwater monitoring, surface-water monitoring, soil-gas monitoring, atmospheric monitoring, and an evaluation of spatiotemporal mapping of vegetation and surface conditions through remote sensing. Initially, only the collection of baseline data sets is planned, with the exception of atmospheric monitoring, which may continue throughout the life of the project. The need for additional near-surface monitoring approaches will be continually evaluated throughout the construction and operational phases of the project, and selected monitoring technologies may be reinstituted if conditions warrant. Based on the current conceptual understanding of the subsurface environment, early and appreciable impacts on near-surface environments are not expected, so extensive networks of surficial aquifer, surface-water, soil-gas, and atmospheric monitoring stations are not warranted at this time. Any implemented surface monitoring networks would be optimized to provide good areal coverage while also focusing on areas of higher leak potential. As discussed in the monitoring approach outlined above, if deep early-detection monitoring locations indicate that primary confining zone leakage has occurred, a comprehensive near-surface monitoring program will be evaluated (in consultation with the UIC Program Director), and if warranted, it will be activated to fully assess environmental impacts relative to previously established baseline conditions.

3.0 Laboratory Studies of Biogeochemical Processes

This chapter describes the evaluation of changes in water quality, formation permeability, and associated biogeochemical processes resulting from $scCO_2$ injection into a saline reservoir, because these processes could lead to decreased permeability (from precipitation or substantial microbial growth), increased permeability (from mineral dissolution), and changes in the mobility of major components (such as precipitation of carbonate mass) and trace metals.

3.1 Characterization of Mount Simon Core Mineralogy, Pore Structure, and Fluids

The mineralogy of the Upper Mount Simon cores, permeability of the Upper Mount Simon Sandstone and Eau Claire Formation, and brine and $scCO_2$ fluids used in geochemical experiments are described in the following sections.

3.1.1 Mineralogy of the Upper Mount Simon Cores Used in Geochemical Experiments

The upper portion of the brine-filled Mount Simon Sandstone will be the primary injection zone so advection will dominate over this interval and will result in spatially and temporally variable brine and $scCO_2$ distributions (see Section 3.1.3). The Elmhurst Sandstone of the Eau Claire Formation, which overlies the upper Mount Simon Sandstone, will receive $scCO_2$ primarily as a result of buoyancy-driven flow (i.e., upward migration) of the $scCO_2$. An extensive description of the geology of the upper Mount Simon Sandstone is found elsewhere (Alliance 2012, 2013); this section provides additional detailed characterization of the sandstone and fluids used in geochemical experiments. The large-scale (i.e., 10s to 100s of meters) marine depositional environment of the Mount Simon Formation resulted in interbedded sandstone, shale, and limestone as the shoreline transgressed or regressed, because coarser grained particles are deposited near shore. In cores collected from the FutureGen 2.0 storage site at 3,949 ft bgs, fine-scale (sub-mm) variability is observed with coarser (~0.3 mm) and finer (~0.13 mm) grain sizes, and iron oxide deposits (Figure 3.1). The ferric iron oxides may be secondary deposits, hence not part of the original depositional environment.

Thin sections of the upper Mount Simon Sandstone were taken for electron microprobe analysis of specific elements. Photographs of the sandstone at 10x and 40x magnification show the fine-scale structure (Figure 3.2).

X-ray diffraction analysis of the bulk sandstone shows 96.2% quartz, 1.8% mica, 1.2% mullite [$Al_6Si_2O_{13}$), and 0.76% hematite (Fe_2O_3). Mullite is an aluminosilicate mineral of post-clay genesis (forms at >1,100°C from kaolinite). The lower detection limit of X-ray diffraction of 0.5% to 1% limits identification of trace mineral phases precipitated between silica grains. However, electron microprobe analysis (below) was used to identify element distributions and mineral phases at a ~2- to 3-µm scale.

Thin-section analysis shows coarser 0.3-mm and finer 0.13-mm quartz grain layers with iron oxides between the two layers, and widespread abundance of orthoclase in coarser layers (Figure 3.2). An electron backscatter image of a core thin section using an electron microprobe (Figure 3.3a) clearly shows

zones of low electron density (black) with greater pore space, zones of moderate electron density (grey – silica sand grains), and smaller horizontal zones of high electron density (white – iron oxides, as described below). This image indicates the coarser sand grains (average size 0.3 mm) have the greatest porosity, and zones of finer sand grains (average size 0.13 mm) have a greater mass of interstitial precipitates such as iron oxides or other minerals in the pore space.

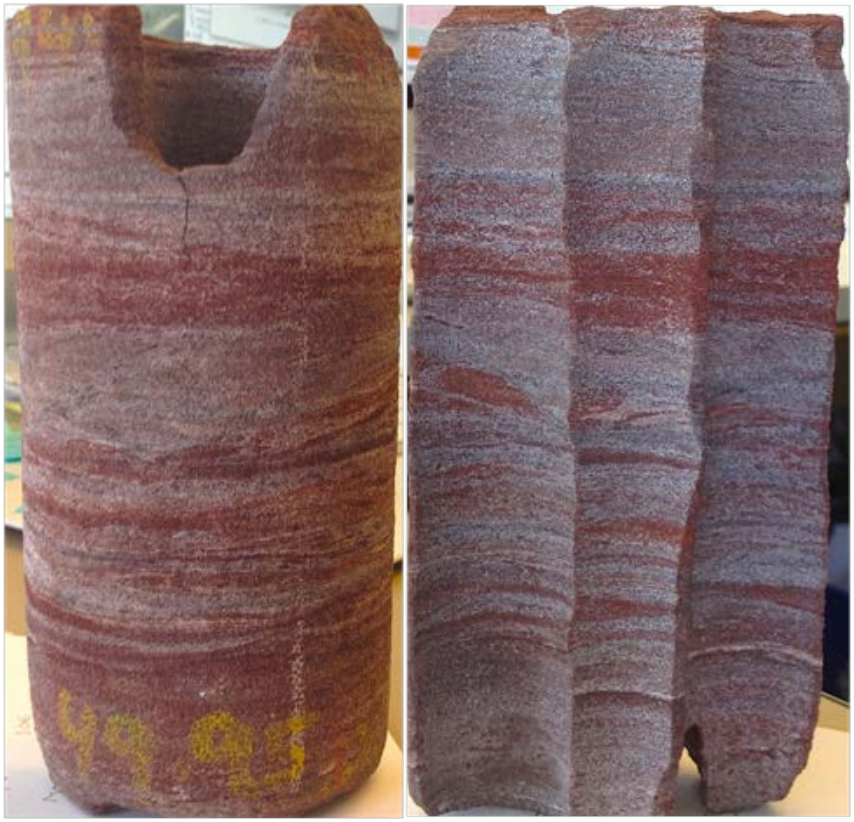

Figure 3.1. Upper Mount Simon core from 3,949-ft depth with fine-scale variability in sand size and red (ferric) iron oxides.

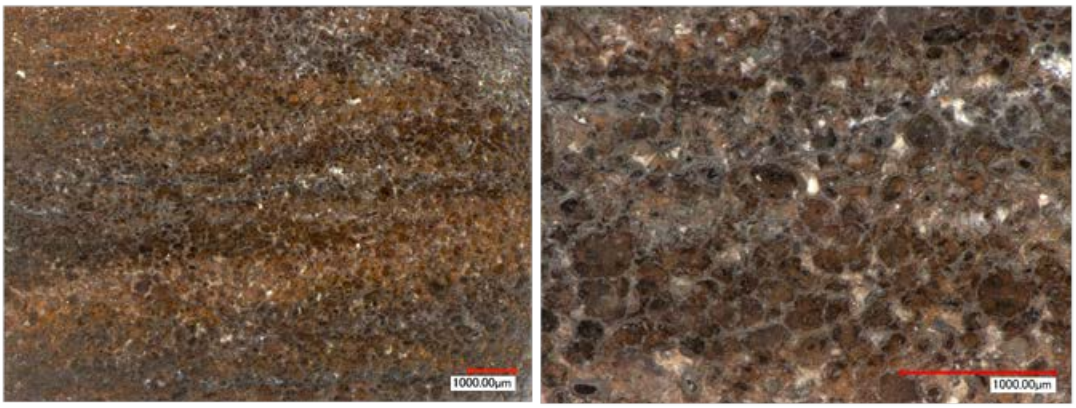

Figure 3.2. Thin section of the upper Mount Simon Sandstone (3,949-ft depth) at ~10x and 40x magnification.

Elemental analysis of the upper Mount Simon core at the 3,949-ft depth at a resolution of 2- to 3-µm clearly shows the high concentration of silica (Figure 3.3b) and likely the mullite aluminosilicate in the coarser grains. As suggested by the yellow-brown stains in the thin-section micrographs (Figure 3.2), the highest Fe concentrations are in the finer grains (Figure 3.3h). In addition to silica and mullite, the bulk X-ray diffraction data indicated the presence of 1.8% mica, but could not distinguish among the three major micaceous minerals, muscovite ($KAl_2(AlSi_3O_{10})(OH)_2$), biotite ($K(Mg,Fe)_3(AlSi_3O_{10}(OH)_2$), and phlogopite ($KMg_3(AlSi_3O_{10})(OH)_2$). The electron microprobe results, however, show that the spatial distribution of K is similar to that of Al (Figure 3.3d and c) and not that of Fe or Mg (Fig. 3.3 h and i), consistent with the presence of muscovite. Fe and Mg, thus, are likely present in non-micaceous minerals. The Na distribution was mainly in large pores and not co-located with Cl, so likely not NaCl.

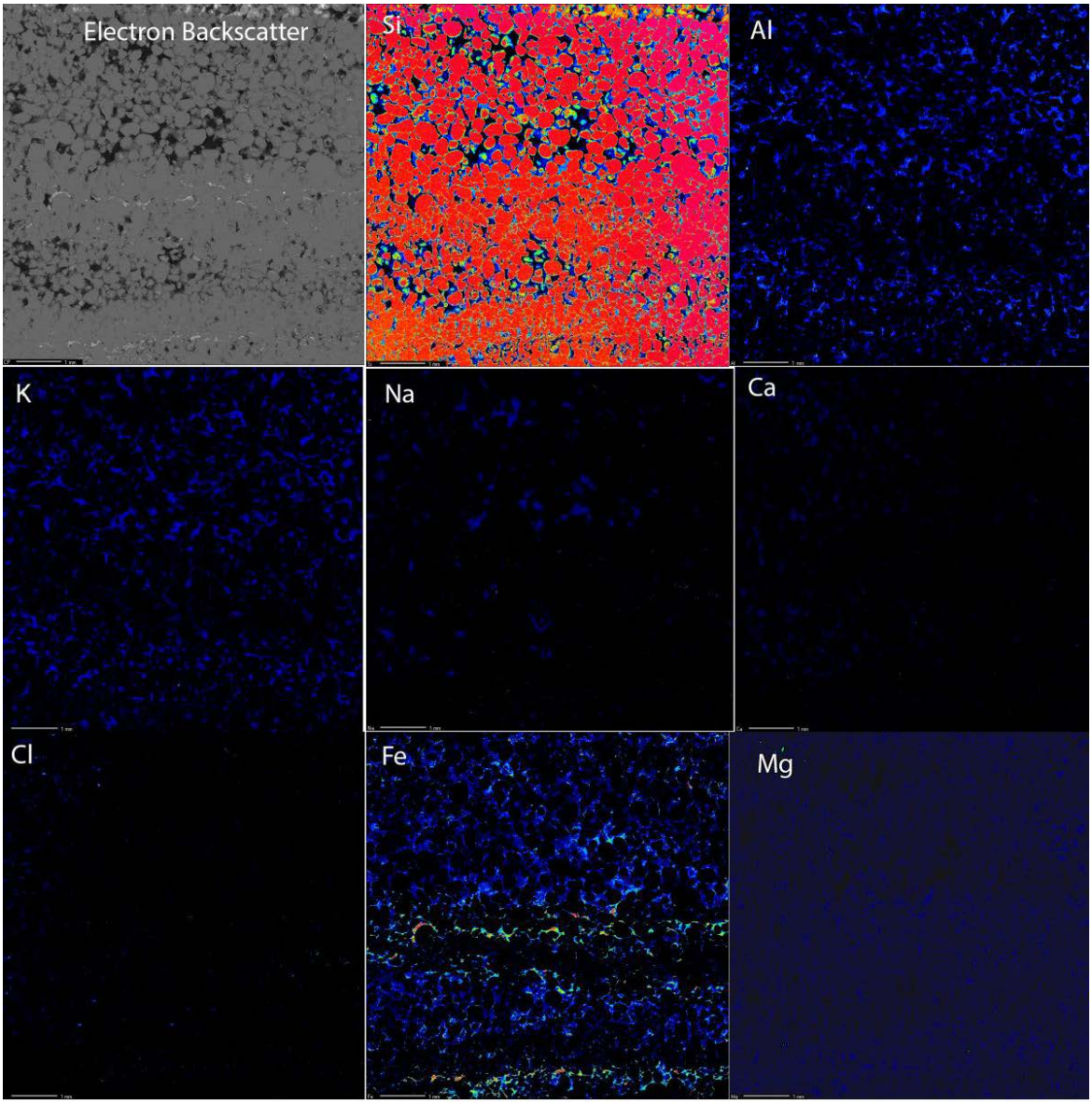

Figure 3.3. Electron microbe analysis of Mount Simon thin section showing a) an electron backscatter image, b) Si c) Al, d) K, e) Na, f) Ca, g) Cl, h) Fe, and i) Mg by elemental detection.

Additional microprobe analysis was conducted to further identify surface-phase precipitates in this untreated sandstone for comparison to sandstone subjected to 1.2 years of brine/scCO_2 treatment (see Section 3.3.4). Electron backscatter images at low to moderate magnification showed silica particles were subangular with extensive surface precipitates (lighter spots on grain surfaces are indicative of a higher molecular weight element which results in higher electron backscatter). Trace mineral phases identified included calcite (Figure 3.4c, d), sylvite (KCl) and iron oxides (Figure 3.4e, f), and barium carbonate (Figure 3.4g, h).

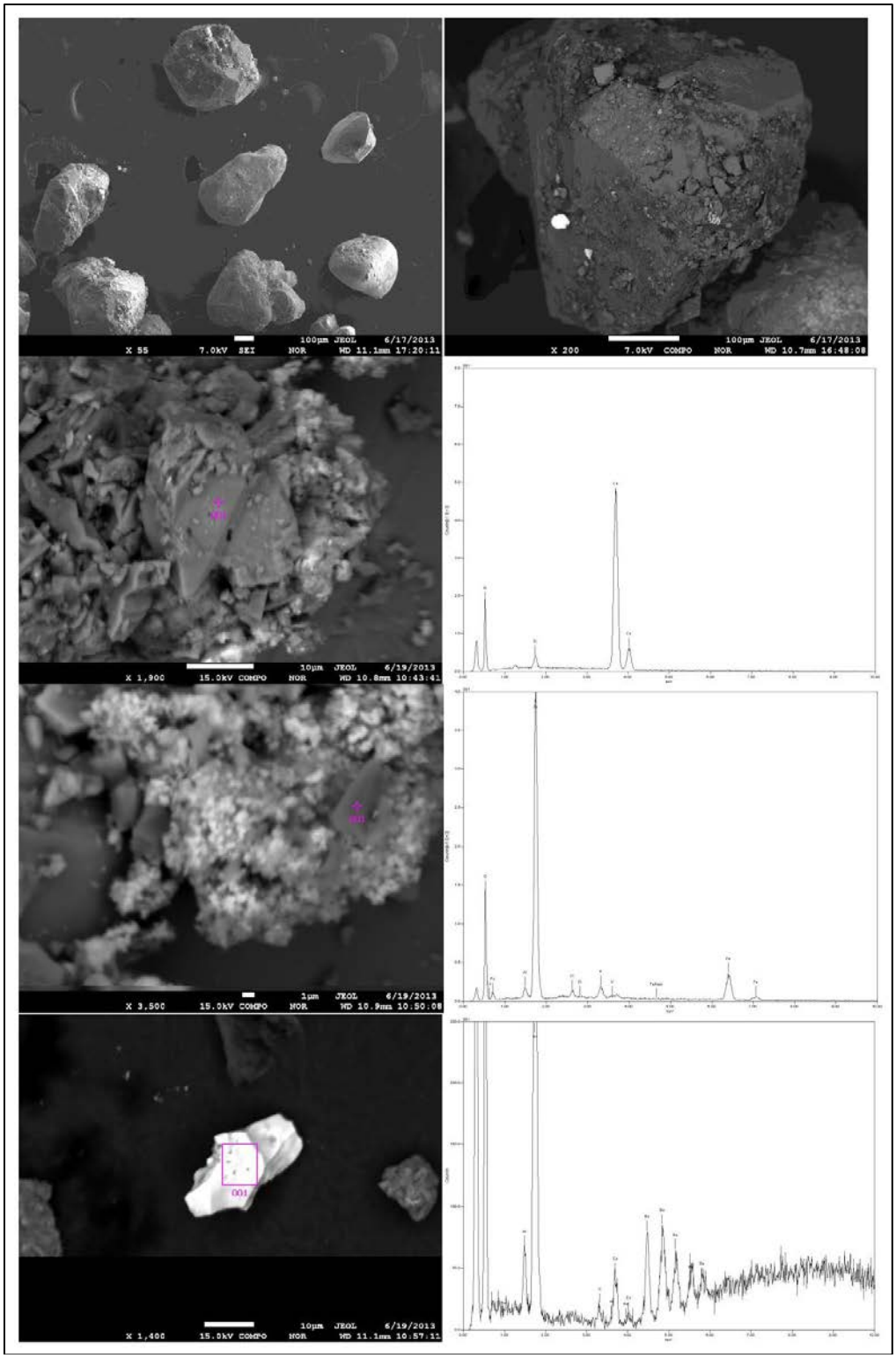

Figure 3.4. Electron microbe analysis of Mount Simon thin section showing a) and b) electron backscatter images, c) higher magnification electron backscatter image of calcite, with elemental analysis shown in (d), e) electron backscatter image of a mixture of sylvite (KCl) and iron oxide coatings on silica with analysis in (f), and g) electron backscatter image of a barium-calcium carbonate coating on a silica grain with elemental analysis in (h).

3.1.2 Permeability of the Upper Mount Simon Sandstone and Eau Claire Formation

Geochemical experiments were initially conducted with crushed drill cuttings collected from specific depths, then additional experiments were conducted using intact cores of 1-in. diameter by 3- to 6-in. length subsampled from the 4- to 5-in. diameter by 6-in. long cores; all cores and cuttings were obtained from the initial stratigraphic borehole. The porosity of cores was measured by weight difference between oven-dried cores and water-saturated cores, accounting for the density of the brine. Water-saturated constant flow hydraulic conductivity measurements based on pressure difference were conducted at four or five flow rates for each core. Some of the 1-in.-diameter core subsamples were drilled horizontally through the 4-in.-diameter vertical cores to compare vertical and horizontal hydraulic conductivity.

The mean porosity of all cores was 0.186 ± 0.0492, with an upper Mount Simon mean of 0.2009, lower Mount Simon mean of 0.1804, and Eau Claire mean of 0.1170 (Table 3.1). The average dry bulk density of the upper Mount Simon was 2.344 g/cm^3, lower Mount Simon was 2.288 g/cm^3, and Eau Claire was 2.487 g/cm^3. The measured brine density (see Section 3.1.3 for composition) was 1.0456 g/cm^3. The mean hydraulic conductivity of all cores was 1.13± 1.67 x 10^{-5} cm/sec, with an upper Mount Simon average of 1.24 x 10^{-5} cm/sec, lower Mount Simon average of 7.07 x 10^{-6} cm/sec, and Eau Claire average of 1.06 x 10^{-5} cm/sec. The anisotropy ratio of horizontal to vertical hydraulic conductivity was 0.224, 7.67, and 0.890 for three pairs of cores where both horizontal and vertical core subsamples were available.

Table 3.1. Core porosity and permeability measured in 1-in.-diameter subcores used in geochemical experiments.

#	Formation	depth (ft)	core orientation	dry bulk density (g/cm^3)	porosity	H_2O mean K_{sat} (cm/sec)	H_2O std dev K_{sat} (cm/sec)
B1	upper Mt Simon	3946.5	vertical	2.391	0.1715	6.39E-05	1.61E-05
B2	upper Mt Simon	3949.7	vertical	2.393	0.2453	7.25E-06	2.62E-07
B3	upper Mt Simon	3949.7	vertical	2.390	0.1873		
B4	upper Mt Simon	3946.5	vertical	2.390	0.2520	1.36E-05	3.54E-06
B5	upper Mt Simon	3949.7	vertical	2.389	0.1382	1.39E-06	6.52E-08
B6	upper Mt Simon	3949.7	vertical	2.306	0.1562	1.23E-06	1.55E-07
B7	upper Mt Simon	3931.7	horizontal	2.585	0.1722	9.14E-07	1.40E-07
B8	upper Mt Simon	3931.7	vertical	2.230	0.2148	4.07E-06	1.13E-07
B9	upper Mt Simon	3931.7	vertical	2.198	0.2008	1.59E-05	3.27E-06
B10	upper Mt Simon	3931.7	vertical	2.172	0.2709	3.51E-06	1.57E-07
B11	lower Mt Simon	4405.0	vertical	2.288	0.1521	1.63E-06	5.77E-07
B12	lower Mt Simon	4405.0	horizontal	2.288	0.2087	1.25E-05	1.82E-06
B13	Eau Claire SS	3884.2	vertical	2.545	0.1002	1.12E-05	6.13E-07
B14	Eau Claire SS	3884.2	horizontal	2.429	0.1338	9.96E-06	1.37E-07
B17	upper Mt Simon	3929.1	vertical		0.0982		

3.1.3 Brine and $scCO_2$ Fluids Used in Geochemical Experiments

The water in the upper Mount Simon Sandstone formation is a brine with a density greater than sea water (1.0456 g/cm^3). The brine concentration increases with depth in the differing formations. An analyzed water composition of the upper Mount Simon Sandstone (O'Connor and Rush 2005) shows mainly a NaCl water (Table 3.2). The high aqueous iron concentration (18.6 mg/L) is ferrous iron (much higher than ferric iron solubility at this pH of 7.6), which indicates reducing conditions. A synthetic brine composed of several major ions was used in some geochemical and microbial experiments (Table 3.3). Trace metals present in minor concentrations in fly ash (and to some extent potentially in the $scCO_2$ injection solution [Meij and Winkel 2004; Rizeq et al. 1994]) include Mn, Mg, Co, Ni, B, Mo, P, Zn, Se, Fe, NH_4, Ca, Cr, As, Pb, V, Hg, Al, Ti, K, and S. Some of these elements are already present as major ions in solution or would be present in low concentrations as a result of desorption or dissolution of the sandstone, but for some experiments additional trace metals were added (Table 3.4). The major gas (and water vapor) components in the $scCO_2$ injection stream include $scCO_2$, oxygen, N_2, argon, NOx, SOx, and water vapor (Table 3.5). In some experiments, just $scCO_2$ was used. A special gas mixture was made that included these components to investigate the influence of these minor components on geochemical or microbial reactions. For example, although the aquifer is initially reducing, the introduction of oxygen gas could lead to precipitation of redox sensitive metals when oxidized (ferrous iron, arsenite, Mn^{2+}). Movement of particulate and precipitated iron is described in Section 3.3.4. Anaerobic microbial activity may be stimulated with the addition of trace metals, N, and S sources (in addition to the $scCO_2$). With the introduction of oxygen, aerobic microbial activity (by different microbes and/or facultative microbes) may also be stimulated, as described in Section 3.5.

Table 3.2. Upper Mount Simon major ions (O'Connor and Rush 2005).

ion	conc. (mg/L)
Ca^{2+}	2670
Fe_{total}	18.6
Mg^{2+}	1280
K^+	141
silica	10.8
Na^+	23400
Cl-	49600
CO_2 (aq)	70
CO_3^{2-}	50
F^-	83.3

Table 3.3. Synthetic brine with only major ions used for some experiments.

compound	conc. (mg/L)
NaCl	59440
$CaCl_2 \bullet 2H_2O$	9884
$MgCl_2 \bullet 7H_2O$	10820
KCl	269
NaF	185
$FeCl_2$	54.3
Na_2CO_3	166
$SiO_2 \bullet 2H_2O$	37

Table 3.4. Synthetic brine trace metals added for some experiments.

compound	conc. (mol/L)
$MnCl_2$	3.97E-08
$CoCl_2$	3.85E-08
$NiCl_2$	1.16E-07
H_3BO_3	2.43E-06
Na_2MoO_4	2.43E-08
NaH_2PO_4	2.08E-06
$ZnCl_2$	1.83E-07
Na_2SeO_3	2.89E-07
NH_4Cl	5.60E-03
$NaHAsO_4$	1.00E-06
$NaCrO_4$	4.35E-07
$PbCO_3$	1.87E-08
$V^{III}Cl_3$	1.00E-06
$HgCl_2$	1.84E-08

Table 3.5. Major components in proposed $scCO_2$ injection stream.

gas component	%
CO_2	0.97
inerts (N_2,Ar)	0.02
NO_x (NO, NO_2)	0.0012
SO_x (SO_2)	0.0012
O_2	0.00002
water vapor	0.00002

3.2 Displacement of Reservoir Fluids by $scCO_2$

As $scCO_2$ is injected into the Mount Simon aquifer, reservoir fluids (i.e., high-ionic−strength brine) will be displaced. In general, varying mixtures of brine/$scCO_2$ result and the fraction of $scCO_2$ increases

over time. Geochemical reactions that may occur when these brine/CO_2 mixtures contact reservoir solids are described in the following sections.

3.2.1 Density and Viscosity of $scCO_2$ at Different Pressures and Temperatures

The displacement of the brine (density ~1.05 g/cm^3, viscosity 1.0 cP at 20°C, with 5% NaCl 1.05 cP) by the much lower viscosity $scCO_2$ (density 0.6 to 0.9 g/cm^3, viscosity 0.06 to 0.1 cP, see Figure 3.5) was measured experimentally in one-dimensional (1D) columns. The purpose of these displacement experiments was to determine what the residual water saturation would be after $scCO_2$ injection. Because Mount Simon cores were not available (experiments conducted prior to May 2012 core acquisition), columns were packed with cuttings from the upper Mount Simon injection zone (3,900- to 4,200-ft depth). Experiments were conducted to measure the weight of dry, packed column (porous media and column weight) and weight of the water-saturated column, then mixed water/CO_2 at differing amounts of $scCO_2$injection. The total void volume in the column was considered a pore volume, and residual water saturation is reported relative to the number of pore volumes of $scCO_2$ injected.

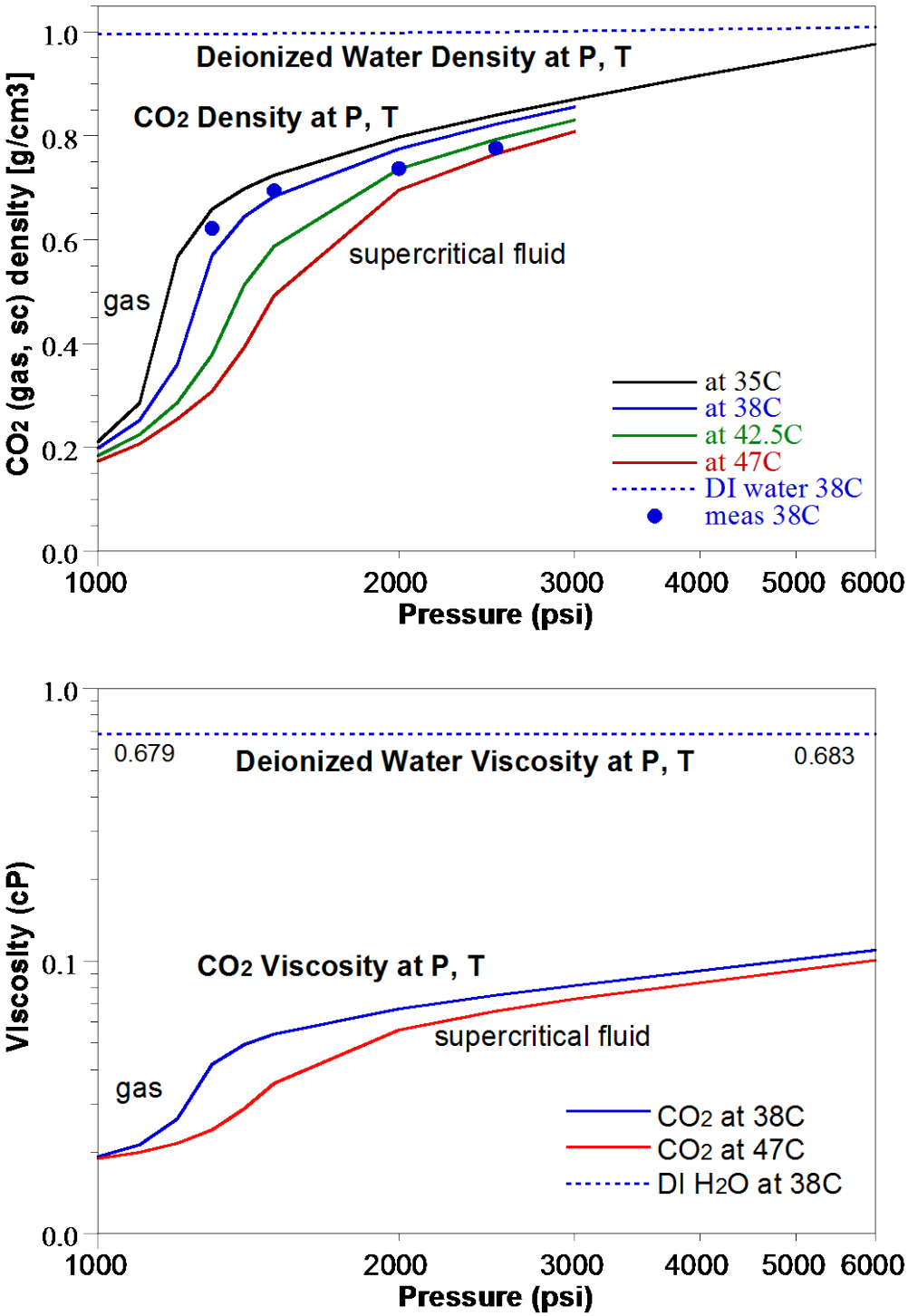

Figure 3.5. Calculated density (a) and viscosity (b) for CO_2 and water at relevant temperatures and pressures.

Because water has a high affinity for most mineral phases, it is predicted that injected CO_2 with a ~10x lower viscosity would displace water in larger pores, but there would be some residual water saturation in smaller pores. In addition, because of the relatively large water/CO_2 viscosity ratio, the low

viscosity CO_2 being injected is an unstable front and will advance into the brine by "fingers" rather than by a uniform front advance. A number of experimental and/or simulation studies of $scCO_2$ displacement of water in porous media (Pruess et al. 2003; Juanes et al. 2006; Ahmadlouydarab et al. 2012; Pruess and Garcia 2002; Bennion 2008; Suekane et al. 2004) describe 1) residual water saturation, 2) heterogeneous flow (i.e., CO_2-rich channels), 3) redistribution of water by the buoyancy of water, and 4) redistribution of water once flow stops results in discontinuous CO_2 zones. Smaller pores tended to contain water, with an occasional flow of a CO_2 bubble (Suekane et al. 2004). Residual water saturations were generally not reported, but 28% was reported for a system composed 70-µm glass beads (~14-µm average pore diameter).

3.2.2 Displacement of Brine by $scCO_2$ Injection

Column experiments were conducted in which residual water saturation was measured over a range of $scCO_2$ injection volumes ranging from zero pore volumes (i.e., initial condition of 100% brine-saturated porous media) to 100 pore volumes of $scCO_2$ injection, which showed a fairly high residual brine saturation of ~45% after 100 pore volumes. This residual saturation was reached relatively quickly, with 50% of the pores being brine saturated by 10 pore volumes of injection (Figure 3.6). These calculated brine (and CO_2) saturations depend on constant pressure and temperature and an accurate CO_2 density (Figure 3.5). Values are similar to those reported in literature (Perrin et al. 2008 data shown in Figure 3.6).

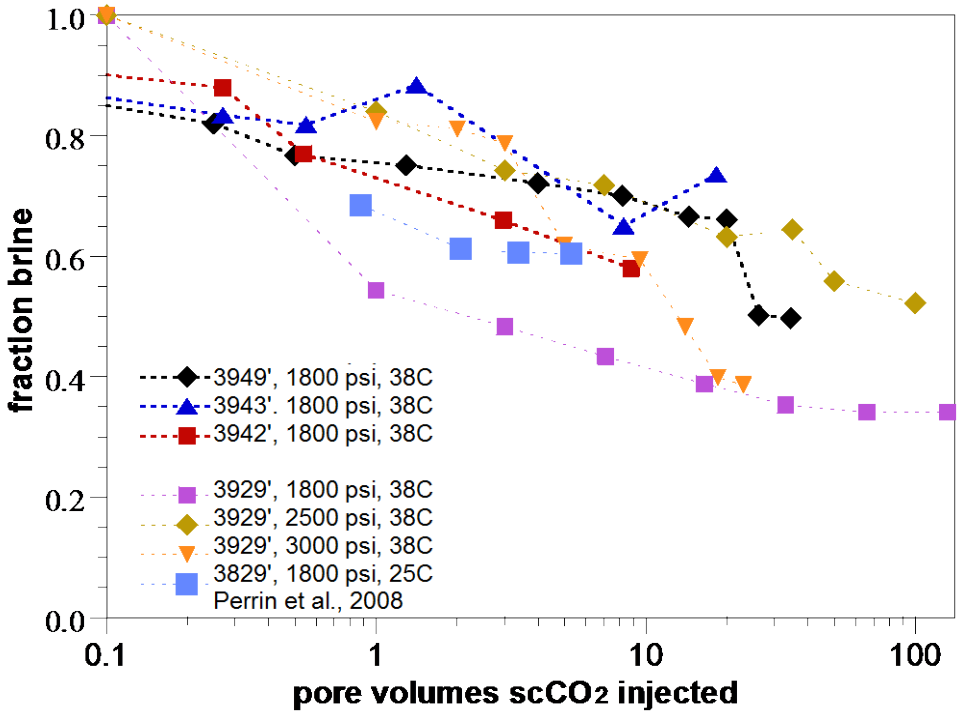

Figure 3.6. Experimental data of residual water saturation of $scCO_2$ injection into brine-saturated Mount Simon cores as a function of pore volumes injected.

Residual water saturation experiments were conducted at 1,500, 2,200, and 3,000 psi (at 42°C), which are all in the $scCO_2$ region, but CO_2 density changes significantly at these different pressures (Figure

3.5a). There was no observable trend in residual water saturation in response to the different pressures (Figure 3.6).

The hypothesis of high water saturation and fingering during $scCO_2$ injection is consistent with others, as shown in Figure 3.6 (Perrin et al. 2008 data), with brine saturation of 60% after 5.5 pore volumes of $scCO_2$ injection. These experiments were subjected to high-resolution magnetic resonance imaging scans, which shows the spatial variability of the brine and $scCO_2$ in the core (Figure 3.7). The $scCO_2$ is apparently traveling along sandstone bedding planes, which are at a 30 degree angle to the core.

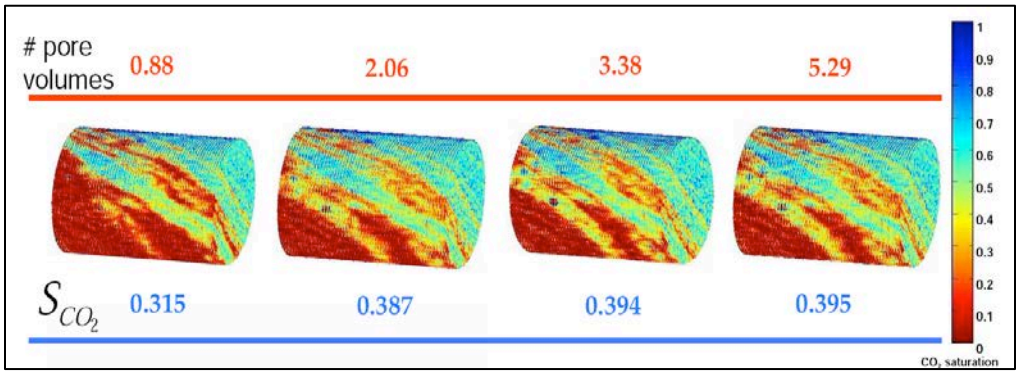

Figure 3.7. Displacement of brine (red) by $scCO_2$ injection (blue) in the Brea sandstone core (Perrin et al. 2008).

3.2.3 Influence of Buoyancy and Buoyancy Time Scale for scCO2 Injection into a Brine-Filled System

Because the $scCO_2$ has a density of ~0.7 g/cm^3 (1,800 psi, 38^{o}C) and FutureGen 2.0 storage site brine densities are on the order of 1.05 g/cm^3, the $scCO_2$ will tend to migrate upward over time. This buoyancy effect occurs rapidly in bulk solution (i.e., in the absence of porous media), as shown below through simulations and experimental data, but occurs over longer time scales in porous media depending on formation permeability. The $scCO_2$ migration from advection (i.e., injection) or buoyancy is also highly influenced by the large viscosity difference between the $scCO_2$ (0.07 cP at 1,800 psi, 38^{o}C) compared with the brine (0.68 cP,Figure 3.5).

A simulation of $scCO_2$ injection into brine in a 2D system containing no sediment (Figure 3.8) shows the upward migration of $scCO_2$ due to its lower density. This migration occurs along "fingers" rather than along a uniform injection front.

The buoyancy effect has also been demonstrated experimentally in this study. When $scCO_2$ was injected into the bottom of an empty column (i.e., flow upward), the $scCO_2$ immediately flowed to the column outlet and out of the column (Figure 3.9, black diamonds). So even after 2 pore volumes of $scCO_2$ injection, the brine saturation was still 0.98 to 1.0, because the buoyancy-driven $scCO_2$ flowed through the brine and left it in the column. For a column filled with an upper Mount Simon Sandstone (average grain size 0.3 mm, so average pore size 0.05 mm) and flow upward, after 20 pore volumes of $scCO_2$ are injected (upward, red squares in Figure 3.9), some brine is displaced, but the brine saturation is still 65%. With the same column but with injection of the $scCO_2$ downward in the column (i.e., so there would be no influence of buoyancy), the change in brine saturation is the same (blue triangles, Figure

3.10) as it is with upward flow. These two experiments show that on the time scale of these experiments (<2 h), there is no influence of buoyancy on $scCO_2$ transport through the fine sandstone, even though field-scale simulations predict significant effects of buoyancy over 10s to 100s of years. The major process controlling $scCO_2$ transport through brine-filled sandstone is the viscosity difference producing fingering (illustrated in Figure 3.8), which results in a very slow displacement of the in situ brine by the very low viscosity $scCO_2$ (shown in Figure 3.6 and Figure 3.10). The relevance of this process (also observed by others: Pruess et al. 2003; Juanes et al. 2006; Ahmadlouydarab et al. 2012; Pruess and Garcia 2002; and Suekane et al. 2004) at field scale is that the $scCO_2$ injected plume will be significantly larger than if the $scCO_2$ was fully displacing the in situ brine.

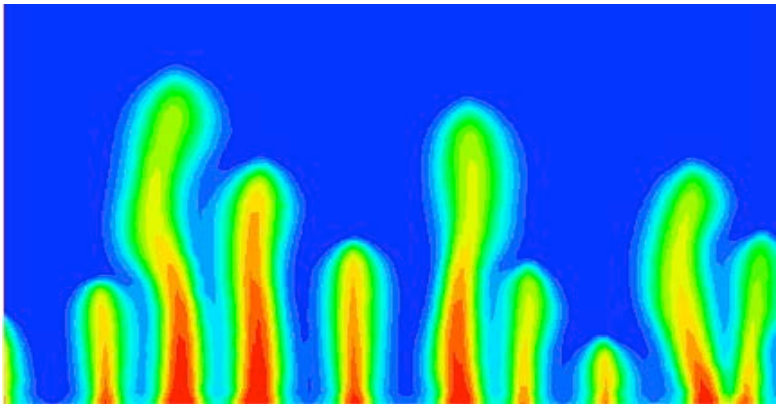

Figure 3.8. Simulation of injection of $scCO_2$ (red) into brine (blue) without sediment present, showing the buoyancy of the $scCO_2$ along unstable (fingering) injection front (Los Alamos National Laboratory, unpublished).

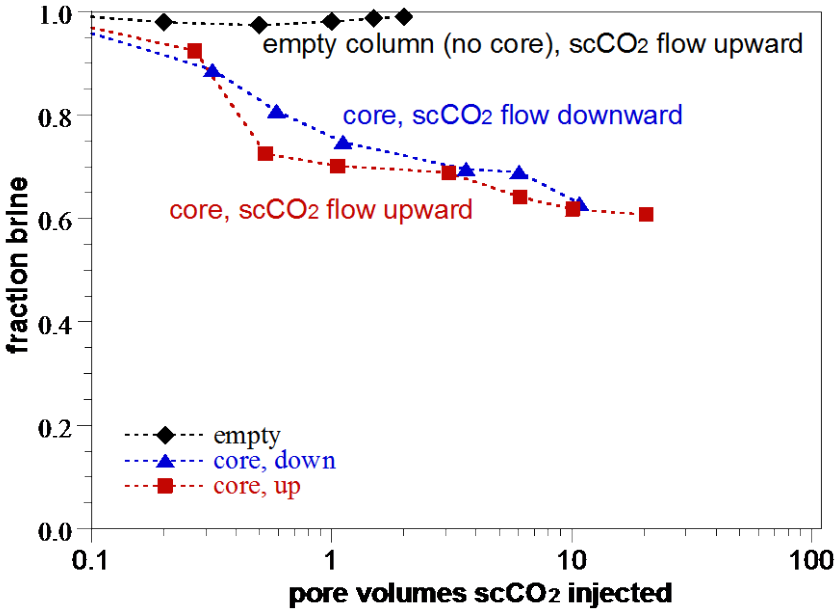

Figure 3.9. Buoyancy time scale of $scCO_2$ injection into empty column (black) or upper Mount Simon Sandstone cores (blue, red).

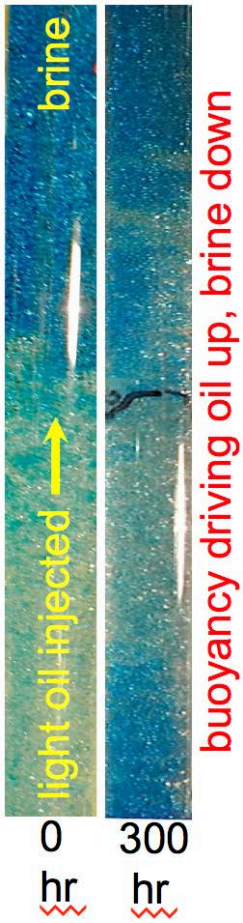

Figure 3.10. Buoyancy time-scale experiment with brine (with blue dye) and a light oil (density 0.72 g/cm^3) in porous media (glass beads, average 2.2-mm particle size). Brine is initially 50% displaced with oil injection into the bottom half of the system and by 300 hours the oil has migrated upward to some extent.

The slow buoyancy is further demonstrated in a column filled with coarse glass beads (2.2-mm size, so average pore size 0.36 mm) with the injection of oil (density similar to that of the $scCO_2$, Figure 3.10) at the bottom of a column filled with brine. After 300 hours, there is some movement of the unstable front due to buoyancy.

3.2.4 Displacement of $scCO_2$ by Brine Injection

Although the field-scale $scCO_2$ injection process is mainly supported by experiments of $scCO_2$ injection into brine-filled cores, over longer time scales (10s to 100s of years) as $scCO_2$ migrates upward due to buoyancy, and in some cases laterally due to advection, brine will displace $scCO_2$-occupied pores in the lower portion of the injection zone. Some experiments were conducted to characterize the residual $scCO_2$ saturation during brine injection. In this case, the injection solution applied at the bottom of the column (brine) is of higher density (30% greater than the $scCO_2$ occupying the pore space) and has a 10x higher viscosity than the $scCO_2$ initially in the Mount Simon Sandstone core. In addition, the brine has an affinity for the mineral surfaces (i.e., 0^o wetting angle), whereas $scCO_2$, which, as an organic liquid, has little

affinity for the mineral surfaces (i.e., >90° wetting angle). Therefore, it is hypothesized that long-term experiments (injection over years or longer, as would occur at field scale) would result in $scCO_2$-filled pores being fully saturated with the injected brine. As shown in the previous section, over the hours to days time frame of these fluid displacement laboratory experiments, buoyancy has little influence in fine-grained cores. However, it is still hypothesized that brine should displace nearly all of the $scCO_2$ after a few pore volumes of injection.

Surprisingly, brine injection into $scCO_2$-filled sandstone left considerable $scCO_2$-filled pores, even after 20 pore volumes (Figure 3.9). After 1 pore volume of brine injection, the brine saturation in three experiments averaged 40%; after 10 pore volumes of brine injection, brine saturation ranged from 48% to 68%; and after 20 pore volumes of brine injection, brine saturation ranged from 58% to 78%. Therefore, there is considerable heterogeneity in the upper Mount Simon Sandstone, even at a small (cm) scale, which leads to non-uniform displacement of fluids, regardless of whether the fluid properties of the injectate are favorable for displacement of the initial fluid.

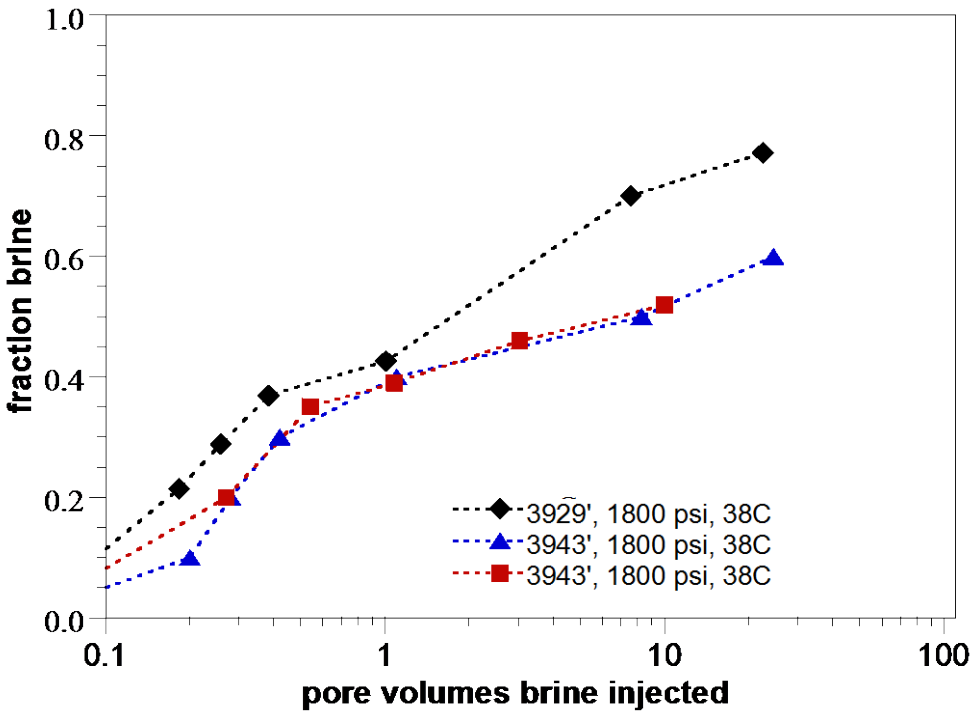

Figure 3.11. Brine injection into $scCO_2$-filled pores and resulting fraction of brine.

3.3 Major Aqueous Ion Changes Caused by $scCO_2$ Injection

Injection of $scCO_2$ causes major changes in the ionic composition of the aqueous phase driven by several related, dynamic geochemical processes. These processes include carbonate partitioning from $scCO_2$ and the associated acidification, mineral dissolution and precipitation, and trace-metal mobilization. Dissolution and precipitation are dynamic processes that operate both in the near-term and

the long-term. Laboratory experiments and modeling to characterize these processes and the changes they drive are described in the following sections.

3.3.1 Carbonate Partitioning from $scCO_2$ into Aqueous Solution and pH

Under aquifer conditions of 38°C and ~1,800 psi, a considerably larger amount of CO_2 gas is soluble in aqueous solution, which results in a decrease in pH. Acidic conditions can lead to desorption of cations and dissolution of some sediment minerals such as quartz and clays. Simulation of the theoretical pH of an aqueous solution that would result from incorporation of carbonate under different pressures (Figure 3.12) shows in this case that the initial NaCl-laden brine at pH 7 decreased to pH 2.9 at 1,800 psi. This simulation assumes essentially no buffering capacity of the solution (other than aqueous carbonate species) and no buffering from mineral dissolution/precipitation. In a real system with a very high sediment/water ratio (i.e., porosity is 15% for the upper Mount Simon Sandstone), there would be considerable buffering capacity due to mineral dissolution and precipitation. Therefore, although there would be a general trend of acidification, it would not be to the extent shown in Figure 3.12.

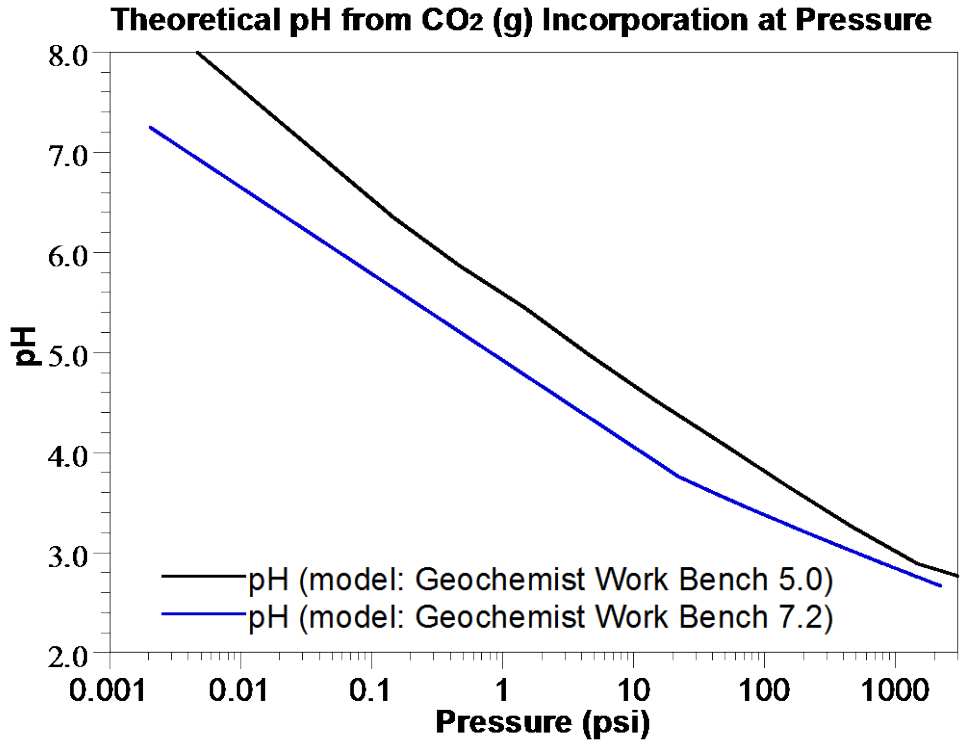

Figure 3.12. Simulation of resulting aqueous pH of aqueous solution in contact with CO_2 at different pressures. No mineral phases are present in the simulation.

Although the upper Mount Simon Formation (injection zone) is not a designated USDW aquifer, possible water-quality concerns include 1) precipitation of iron or carbonates in sufficient quantities to decrease permeability, 2) sufficient dissolution of mineral phases to increase permeability, and 3) increases in solubility of a toxic metal as a result of pH or Eh changes. The increased risk due to toxic metals solubility is not a significant concern in the Mount Simon reservoir itself, rather only if CO_2 and/or brine were released from the injection zone and resulted in impacts on overlying aquifers.

Measurements of pH, solution electrical conductivity, and major cation/anion changes over time were conducted in batch experiments in which different water/CO_2 ratios were used (i.e., 97% CO_2 approximating near-injection well conditions to 10% CO_2 approximating conditions on the leading edge of the scCO_2 plume). The pH measurements (Figure 3.13a) showed some acidification, from a value of 7.5 (brine) to as low as pH 4.8 for the experiment containing 97% CO_2. There was a general trend of greater acidification for systems that contained a greater fraction of CO_2, which is consistent with theoretical predictions (Figure 3.12). It should be noted that although these measured pH values demonstrate a trend, they are not accurate in the specific sense, because when experimental systems (at 1,500 to 3,000 psi with high CO_2 aqueous solubility) are depressurized for pH measurement and sample collection, some CO_2 is outgassed. Accurate pH values could be measured using a high-pressure pH electrode. Acidification generally reached equilibrium by ~100 hours, with some cases showing a pH increase by 1,000 hours (which may indicate precipitation was occurring). By 10,000 hours, the pH had leveled off or neutralized somewhat, likely as a result of precipitation reactions.

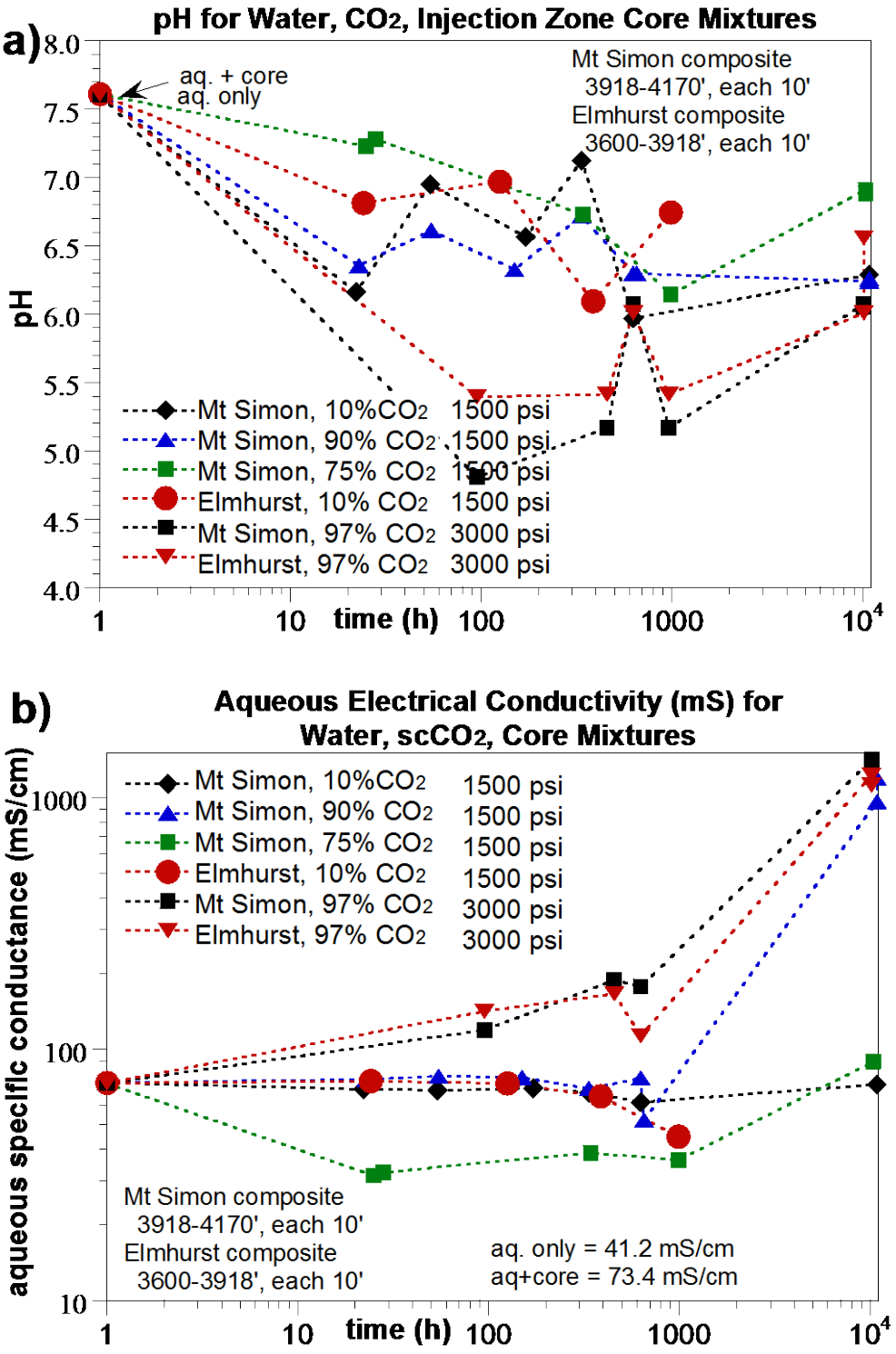

Figure 3.13. Experimental measurement of pH (top) and aqueous solution electrical conductivity (bottom) for porous media-water-CO_2 systems.

Electrical conductivity measurements were also made on the aqueous solutions over time in experiments with different sediment/water/CO_2 contents (Figure 3.13b). Addition of CO_2 (a hydrophobic

solution) should increase dissolved carbonate, which would result in an increase in solution electrical conductivity. As in measurements of pH, outgassing of CO_2 lowers the solution electrical conductivity and the values reported indicate trends rather than absolute results. Most experimental systems showed little change in aqueous electrical conductivity (Figure 3.13b) for the first few hundred hours, with some decrease in conductivity by 1,000 hours. A decrease in solution conductivity may indicate precipitation is occurring.

In contrast, the two experiments conducted with 97% CO_2 and 3% water (at 3,000 psi) showed a large increase (3x) in solution conductivity. These two experiments also showed the greatest acidification (Figure 3.13a), which would be expected to increase mineral dissolution. In this case, the electrical conductivity increase occurred over hundreds to thousands of hours. By 10,000 hours, the electrical conductivity had increased about 20x. The average electrical conductivity increase for the change in pressure (Figure 3.14) shows a 20x increase from atmospheric conditions to 1,800 psi, mainly due to increased concentrations of carbonate ions (at the short time scale of these pressure studies, few mineral dissolution reactions are occurring).

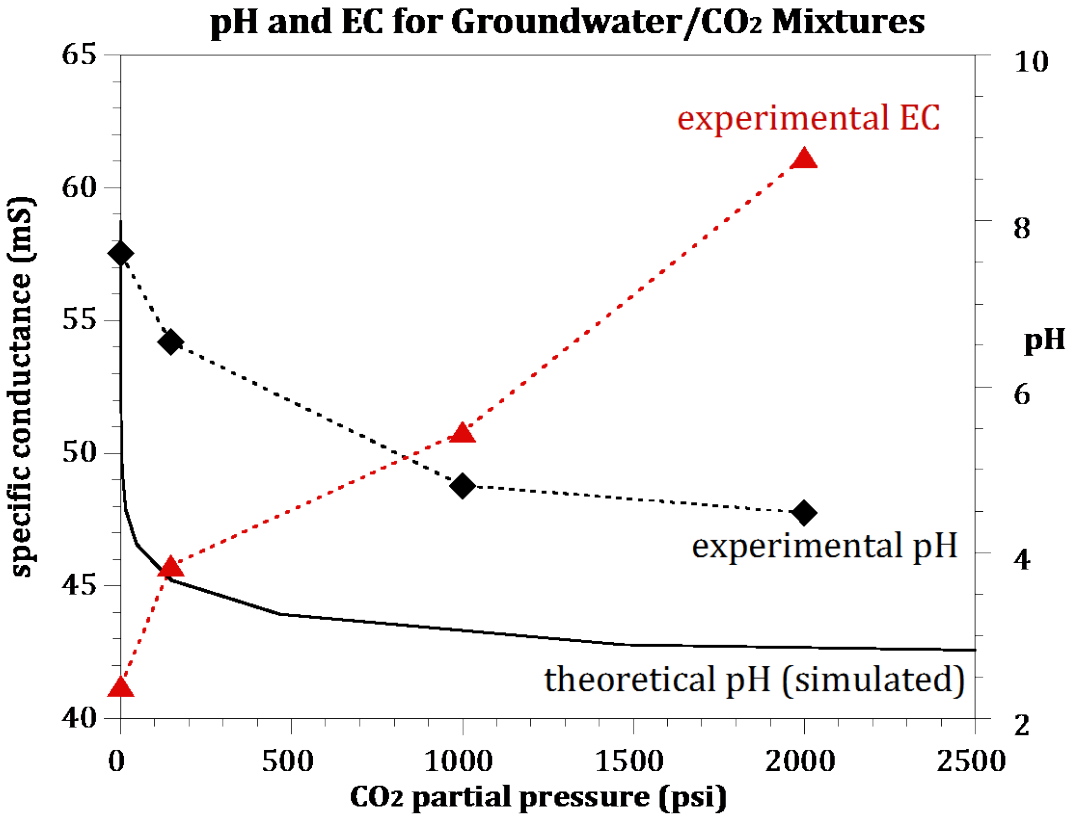

Figure 3.14. Simulation of resulting aqueous pH and measured pH as a function of pressure. Measured electrical conductivity is also shown.

3.3.2 Short-Term Cation and Anion Changes Resulting from Mineral Dissolution

With the introduction of $scCO_2$ into the saline reservoir at ~1,800 psi, there will be a significant increase in the total carbonate ion concentration in aqueous solution (described in the previous section)

due to the change in pressure, temperature, and also specific ions present in the brine. Changes in major cations/anions are indicative of mineral dissolution or precipitation (i.e., "salting out") of ions initially present in the brine, and can affect CO_2 injectivity if permeability is influenced. Changes in trace-metal concentrations are typically too small for the volume of precipitates to have any influence on permeability, but are of interest as an increase in the aqueous concentration of a toxic trace metal in the Mount Simon saline reservoir could affect an overlying USDW aquifer in the unlikely event of a leak. Results reported below are only aqueous ion changes. Electron microprobe analysis of the surface phases is described in the following section to identify possible mineral phases that are dissolving (i.e., mineral surfaces will be pitted) or precipitating (i.e., additional surface precipitates observed in reacted core materials). Geochemical equilibrium modeling would help identify possible precipitate phases that would occur based on observed ion concentrations.

The difference in total carbonate ion concentration at standard atmospheric conditions is influenced by multiple factors including: 1) calcite solubility increase with pressure, 2) calcite solubility increase with salinity, 3) calcite solubility decrease with temperature, 4) CO_2 solubility in aqueous solution increase with pressure, 5) CO_2 solubility decrease with increasing salinity, and 6) CO_2 solubility decrease with increasing temperature. The most significant factors are the increase in CO_2 gas solubility with increasing pressure, and decreasing CO_2 gas solubility with increasing temperature and salinity. At 1,800 psi and 38°C in a solution with an ionic strength of 50,000 mg/L (Table 1, O'Conner and Rush 2005), the CO_2 gas solubility is calculated at 53.9 g/L (Jarrell et al. 2002; Crawford et al. 1963). The high salinity resulted in a 22% decrease in CO_2 gas solubility. In contrast, the CO_2 gas solubility at 1 atmosphere and 38°C is 21.1 mg/L. Therefore, the CO_2 gas solubility in subsurface conditions (1,800 psi, 38°C, 50,000 mg/L salinity) is 2,567x higher than at 1 atmosphere, 38°C, and low ionic strength.

In addition, total carbonate ion concentration increases significantly with increasing pressure (Ingle 1975), increases slightly with increasing salinity, but decreases slightly with increasing temperature (Garrels and Christ 1965). More specifically, the calcite solubility product increases by 2.9x at 5,000 psi relative to atmospheric pressure, calcite solubility increases about 1.5x as the ionic strength increases to 2 mol/L, and calcite solubility decreases <20% as the temperature increases from 15°C to 35°C.

Although the total carbonate ion concentration is expected to increase significantly at high pressure, when pressure is reduced in the sample container during sampling, there is significant outgassing of CO_2, and carbonate solubility measurements are not precise. It is possible that dilution water could be added to the high-pressure system just before sampling to maintain solubility even when the sample is depressurized. Because drill cuttings were available 1.5 years before solid core material (from both the upper Mount Simon Sandstone and Elmhurst Formation), $scCO_2$/brine/sandstone geochemical experiments were conducted with crushed drill cuttings for time periods ranging from 0 to 416 days (10,000 hours), and solid core material to 141 days (3,400 hours). Reaction experiments were conducted at 1,800 psi and 38°C with different $scCO_2$/brine saturations ranging from 10, 50, 75, 90, and 98% $scCO_2$ saturation, because reactions may be affected by differing pH conditions (i.e., higher $scCO_2$ concentration leads to lower pH in the brine). Experiments were conducted with the upper Mount Simon Sandstone (3,429- to 3,449-ft depth) and Elmhurst Formation (3,982-ft depth). Major cation and anion analysis are reported for crushed rock experiments (Figure 3.15) and intact core experiments (Figure 3.16).

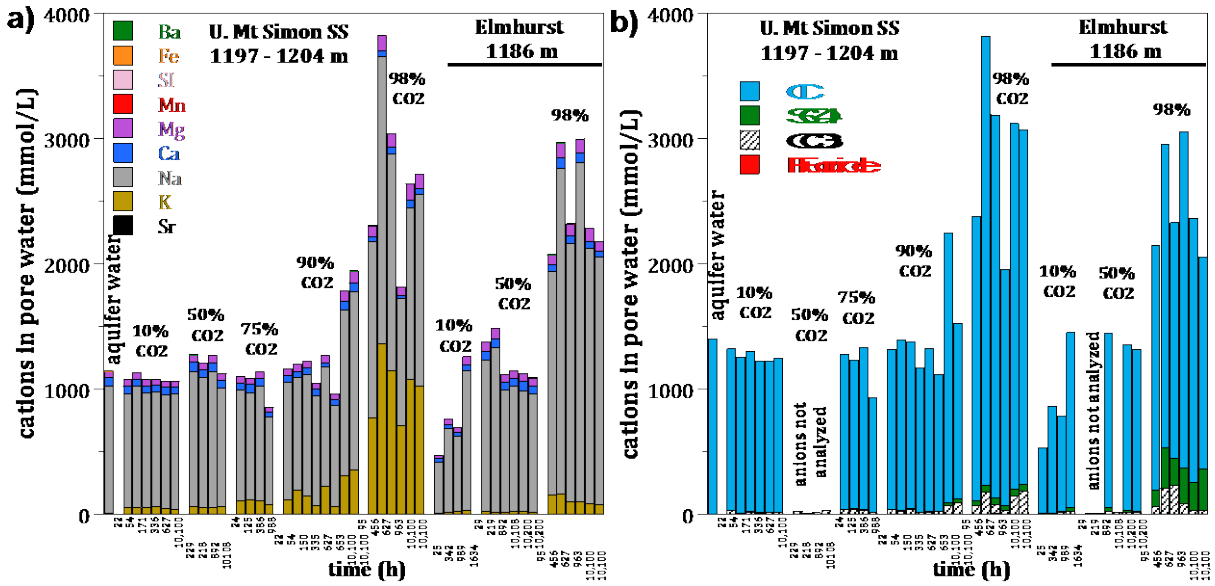

Figure 3.15. Major cation (a) and anion (b) changes in Mount Simon or Elmhurst Formations with different CO_2/brine mixtures over time (x-axis) using crushed core material. Groupings are different percentage of CO_2 with a balance of brine (e.g., 10% CO_2 is 90% brine).

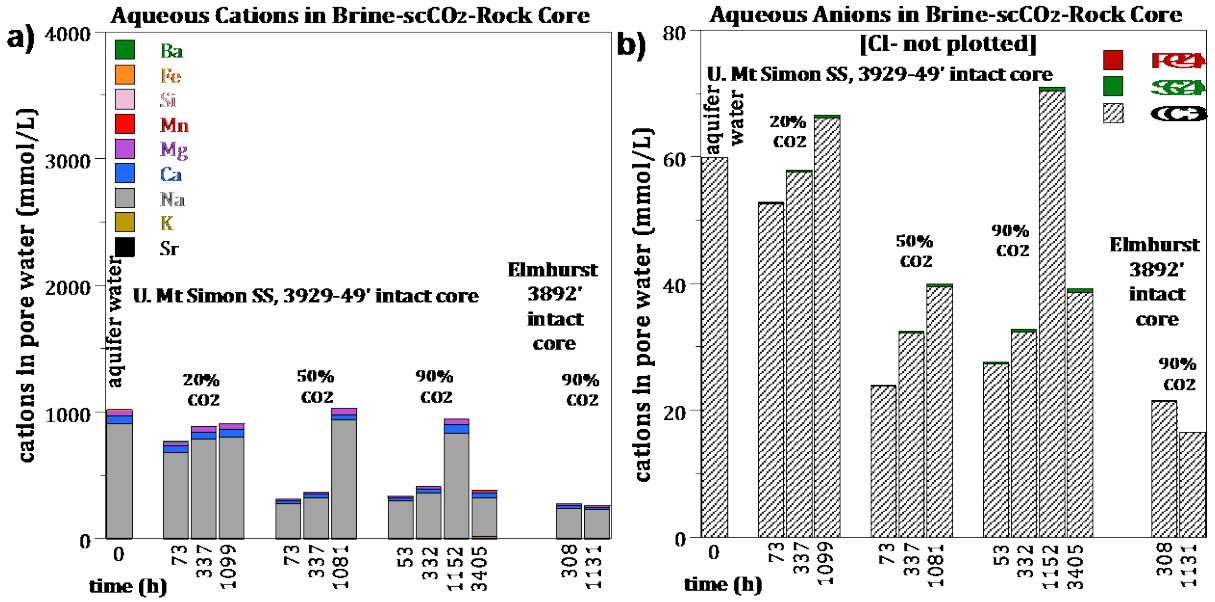

Figure 3.16. Major cation (a) and anion (b) changes in Mount Simon or Elmhurst Formations with different CO_2/brine mixtures over time (x-axis) using intact solid core material. Groupings are different percentages of CO_2 with a balance of brine (e.g., 20% CO_2 is 80% brine).

In $scCO_2$-brine systems (at different ratios), reactions over time with the Mount Simon and Elmhurst Formations show significant major cation and trace-metal changes, which are summarized as follows:

- minor aqueous ion changes at 10, 20, 50, and 75% $scCO_2$ saturation, even after 1.2 years

- greatest aqueous ion changes are in the 98% CO_2/2% water systems, with nearly no major ion effects at <90% CO_2 (Figure 3.15)
- at 98% CO_2/2% water, Na+ and Cl- increase from 1,000 mM to 2,000−4,000 mM (same for Mount Simon Sandstone and Eau Claire Shale). This is likely a salting-out phenomenon, as noted by others, where ions in the brine are left behind (precipitate) as the scCO_2 displaces the water (Figure 3.15a and Figure 3.15b) and CO_2 slowly partitions into the water, potentially lowering mineral solubility.
- at 98% CO_2/2% water, K+ increases from 3.6 mM to 1,300 mM (Mount Simon Sandstone, 300x) and to 152 mM (Eau Claire Shale, 42x increase). This may be indicative of mineral-phase dissolution in both formations (with more in the Mount Simon Sandstone).
- at 98% CO_2/2% water, sulfate increases from 0 mM to 200 mM (Mount Simon Sandstone) or 500 mmol/L (Eau Claire Shale), which may be indicative of dissolution of mineral phases such as gypsum (Figure 3.15b).
- at 98% CO_2/2% water, Ca2+ decreases (Figure 3.15a) from 67 mM to 20 mM, which may be indicative of precipitation.
- at 98% CO_2/2% water, Mg2+ increases from 53 mM to 120 mM (Figure 3.15a), which may be indicative of mineral dissolution.

Because Na+, K+, Cl-, and CO_3^{-2} ions dominate the solution, changes in minor ions are difficult to evaluate, so additional plots are provided with selected cations removed. Additional plots of anions without Cl- and CO_3^{-2} are also provided (Figure 3.17).

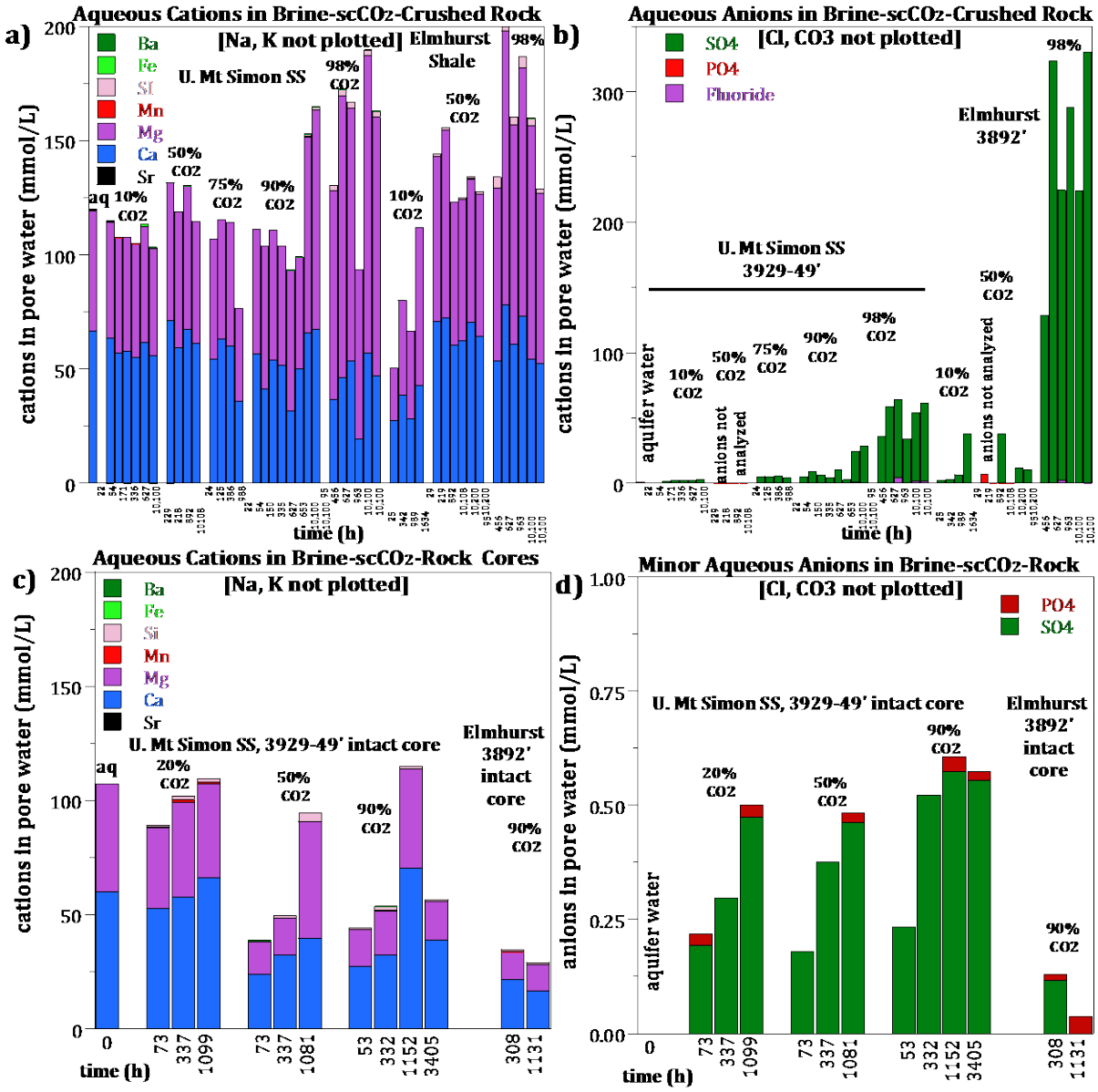

Figure 3.17. Major cation (a) and anion (b) changes in Mount Simon or Elmhurst Formations with different CO_2/brine mixtures over time (x-axis) using crushed core material (a, b) or solid cores (c, d). Major cations except Na+ and K+ are shown (a, c), and major anions except Cl- and CO_{3-2} are shown (b, d).

The relatively constant Ca/Mg ratio is easily observed over a wide range of brine/$scCO_2$ saturations (Figure 3.17a, c), with a moderate (< 50%) increase over time for only the highest $scCO_2$ saturation (98%). Cation concentrations for solid rock cores were lower than corresponding crushed rock experiments, likely indicating additional surface area exposure for the crushed rock. For anions, the sulfate concentration increase over time is clearly observed in all experiments, and was very significant for the Elmhurst Sandstone/Shale samples (Figure 3.17b, d). Dissolution of mineral phases K-feldspar, albite, smectite, and anorthite predicted in a long-term modeling study (White et al. 2005) also showed increases in Mg^{2+}, K^{+}, and SO_4^{2-}. Changes in trace ion concentrations are described in Section 3.4.

To gain further insights into the dynamics of the chemistry, time-resolved plots of the major ions were made for the batch experiments with cuttings performed at 2000 psi and 35°C. The measured carbonate concentration at different water/CO_2 mixtures (Figure 3.18a) shows an increase from 0.82 mmol/L (initial concentration in brine) to 173 mmol/L with increasing CO_2/brine ratio. This 210x increase in carbonate for high CO_2/brine relative to the carbonate initially present in the brine (blue circle, Figure 3.16b) is less than the predicted 25,000x increase from simulations probably as a result of outgassing of CO_2 during depressurization. After an initial rise following addition of the water/CO_2 mixture, most of the experiments showed a decrease in the carbonate concentration over hundreds of hours, implying precipitation was occurring (although this would have to be confirmed by analysis of solids to identify precipitate coatings on grains). In contrast, high scCO_2 experiments in the Elmhurst Formation showed an increase in carbonate and Mg. The calcium concentration (Figure 3.18b) also showed a decrease in concentration over the same hundreds of hours time scale. Magnesium concentrations (Figure 3.18c) showed little change over time, except for the 97% scCO_2 experiments, which showed a 3x increase. Ferrous iron can precipitate with carbonate (siderite), but because the total iron present initially in water is so low (0.3 mmol/L) relative to the carbonate concentration (10 to 100 mmol/L), there is likely little impact on the overall carbonate solubility. Total iron concentrations were generally less than detection limits (Figure 3.18d), because ferric iron solubility is <1 micromolar at this pH, and in this system containing oxygen, ferrous iron will oxidize.

The aqueous sodium concentration could increase as a result of mineral dissolution because this cation is typically not present in many secondary precipitates that form. Long-term simulations (White et al. 2005) indicate that Na could increase as a result of albite ($NaAlSi_3O_8$) dissolution. Although experimental data (Figure 3.19a) showed no sodium increase in most of the experiments, a significant increase was measured for the high scCO_2 concentration (97%) experiments.

The aqueous strontium concentration increased as a function of the amount of CO_2 added (Figure 3.19b), indicating that strontium may be desorbing from the surface or dissolved from (Ca, Sr)carbonates. The aqueous K concentration also increased in response to higher CO_2 concentrations (Figure 3.19c). In addition to the rapid initial K+ increase (likely desorption in <20 hours), there was a slow K+ increase over hundreds of hours, which is likely indicative of dissolution (K-feldspar as indicated by White et al. [2005]; see Section 3.3.5). Aqueous manganese, though initially not present in the brine, shows an increase in all brine/CO_2 ratios (<100 hours) from desorption or dissolution (Figure 3.19d), then a decrease in concentration likely due to precipitation by 1,000 hours.

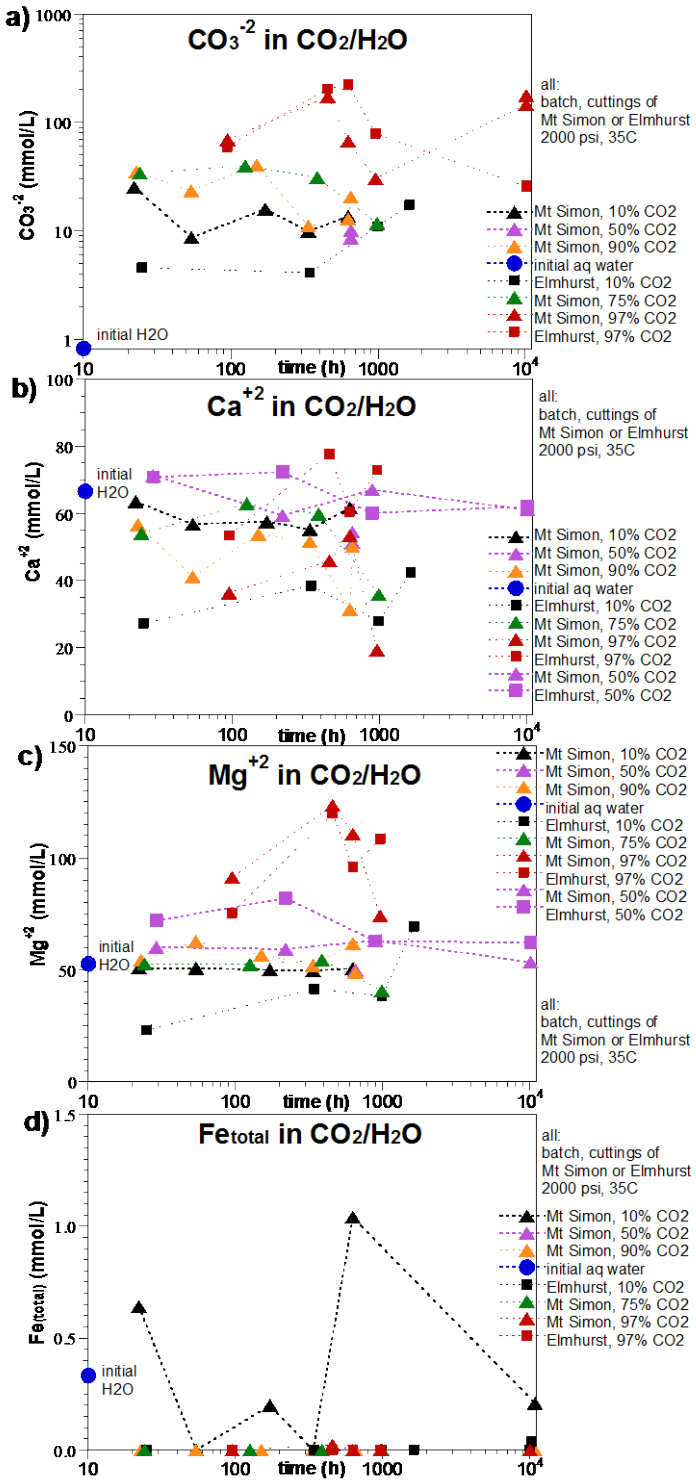

Figure 3.18. Experimental measurement of ion changes in Mount Simon or Elmhurst porous media systems with different CO_2/brine mixtures.

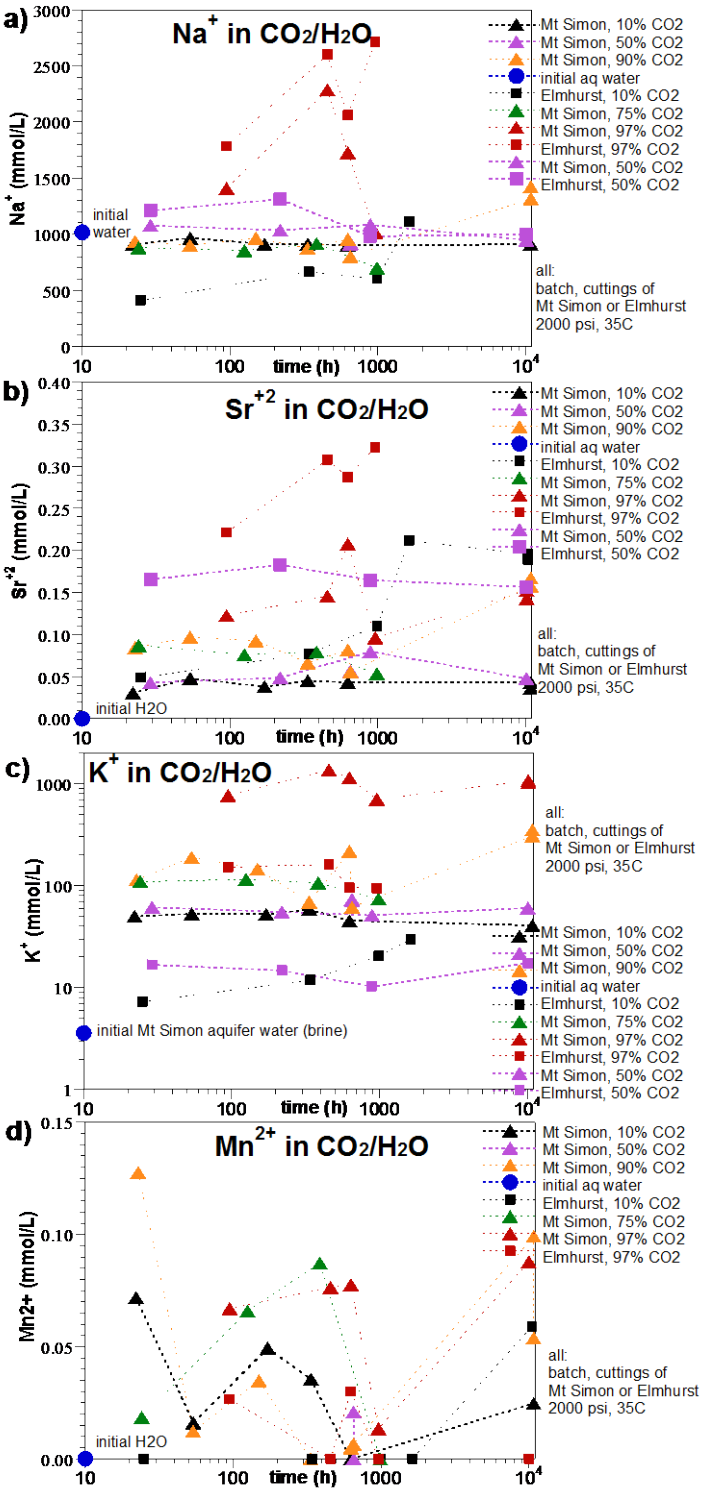

Figure 3.19. Experimental measurement of cation changes in Mount Simon or Elmhurst porous media systems with different CO_2/brine mixtures.

At 90% CO_2 and 98% CO_2, aqueous silica increases from 0.4 mM to 5.5 mM (Eau Claire shale) or 3 mM (Mount Simon Sandstone) slowly (i.e., increases observed after months to a year; Figure 3.20a). Aqueous silica measurements in the brine/CO_2 systems (Figure 3.20a) are indicative of leaching due to dissolution of multiple formation minerals (albite, smectite, anorthite, K-spar). For both silica and aluminum, most measurements are below detection limits, because of the presence of high Na and Cl in the brine (i.e., difficult to analyze low concentrations when other ions are present in very high concentrations). Aluminum is not initially present in the brine, and most analyses results from the earlier work with crushed core material are below detection limits (Figure 3.20b). Additional experiments were conducted with inductively coupled plasma (ICP) analysis targeting Al measurements (Figure 3.21). These experiments showed low Al concentrations (i.e., 0.1 mmol/L) are present as a result of $scCO_2$ addition to the brine/core and the subsequent mineral-phase dissolution over a few hundred hours. Silica is present in higher concentrations (about 1 mmol/L) over a shorter time scale, suggesting dissolution sources of Si and Al are not the same (i.e., not the dissolution of a 1:1 or 2:1 clay). A plot of the Si/Al ratio over time (Figure 3.21c) confirms the dominance of early aqueous Si input from dissolution of a non-Al phase, then later precipitation of Si (Figure 3.21b). The slight increase in Al in 100s of hours had little influence on the Si/Al ratio, which ranged from 40 to 100 (short times), then decreased to 20 by 1,000s of hours. The ratio is indicative of little influence of the Si from 1:1 or 2:1 clays.

Aqueous Na+ and Cl- are not expected to change with the introduction of $scCO_2$ at <75% $scCO_2$ (Figure 3.20c), so they can be used as a tracer of potential experimental artifacts. For these conditions, the lack of change for both Na+ and Cl- demonstrates that there are few experimental sampling artifacts in the systems used. If there were systematic errors introduced during dilution and sampling, there may be systematic differences in reported data for these ions as a function of the ratio of CO_2/brine.

Although aqueous sulfate was not expected to change, increases in sulfate concentration were observed as a direct function of the amount of CO_2 added (Figure 3.20d). Sulfate and magnesium (Figure 3.18c) increase similarly, although calcium decreases (Figure 3.18b), possibly indicative of dissolution of a specific mineral phase. The carbonate solubility in brine is certainly a function of pH, but also controlled by Mg 2+ and Na+ concentrations, and gypsum solubility (Garrels and Christ 1965). Finally, barium, which was not initially present in the synthetic brine, increased quickly (10s of hours) due to desorption/dissolution, Figure 3.21a), then over 100s to 1,000s of hours it decreased in aqueous concentration due to precipitation.

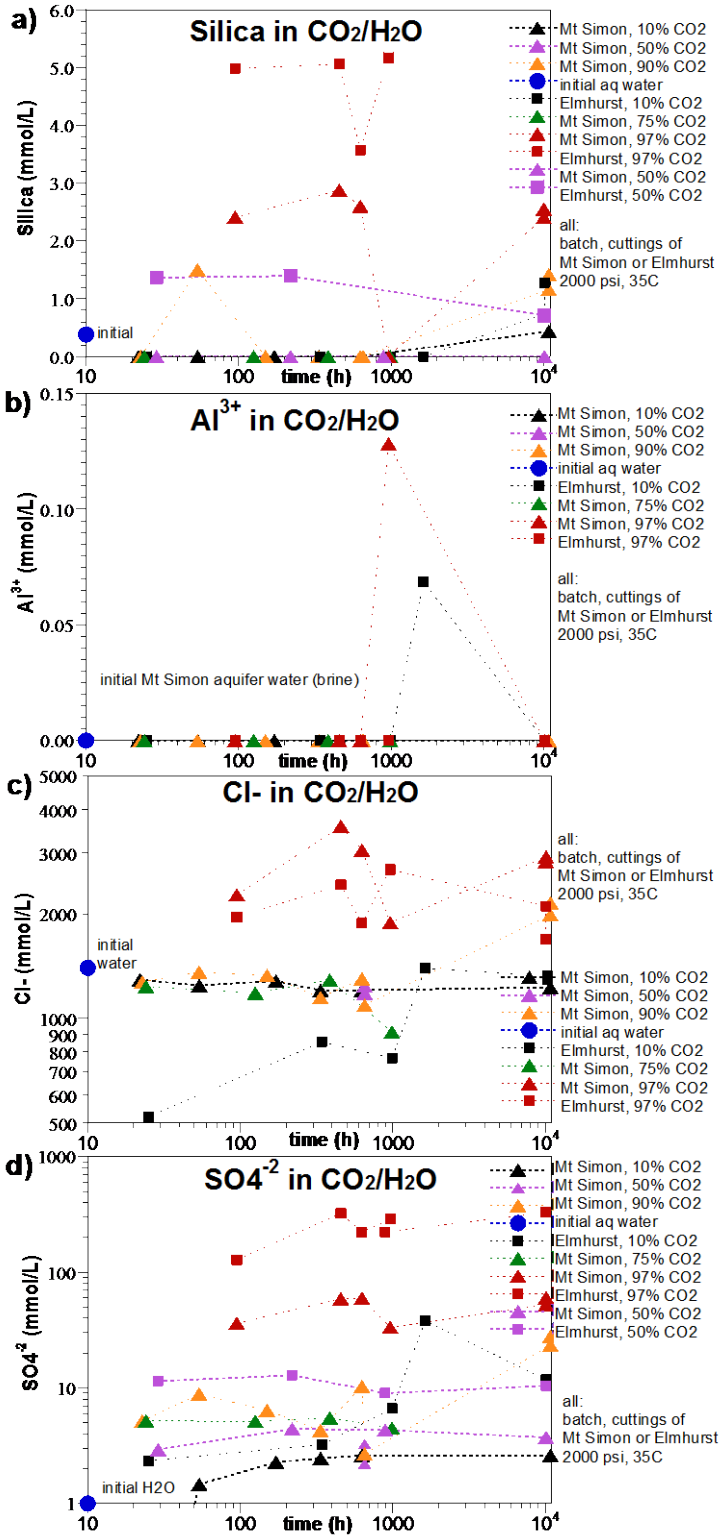

Figure 3.20. Experimental measurement of silica (a), aluminum (b), chloride (c), and sulfate (d) changes in Mount Simon or Elmhurst porous media systems with different CO_2/brine mixtures.

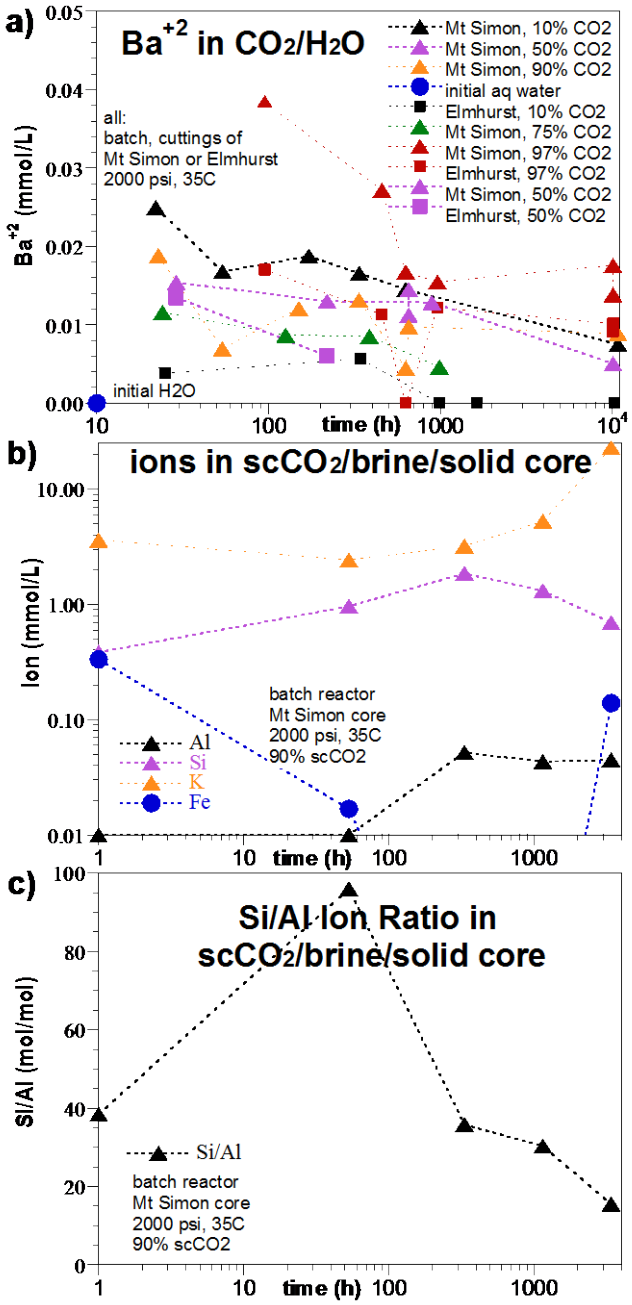

Figure 3.21. Experimental measurement of a) Si, Al, K, Fe for 90% $scCO_2$/10% brine reacting with upper Mount Simon core, and b) Si/Al ratio.

3.3.3 Trace-Metal Mobility Changes Caused by $scCO_2$ Injection

Trace metals present in the $scCO_2$ injection stream or as a result of desorption or dissolution of mineral phases are present at such low concentrations that any dissolution or precipitation that occurred likely had no influence on $scCO_2$ injectivity due to the small volume of precipitate change. The interest in trace metals is related to the potential for degradation of water quality within overlying aquifers in the

event of an unforeseen leak. Macroelements present in the fly ash include Al, C, Ca, Cl, Fe, Mn, N, Na, P, S, Ti, and K. Particulate components (trace elements) that may be present in fly ash, even in advanced coal plants, include As, B, Cr, F, Mn, Ni, Pb, Hg Se, V, and Zn. The brine chemistry of the upper Mount Simon aquifer includes Na, Ca, Fe, Mn, K, Si, Cl, and F (Table 3.2). Most experiments were conducted with $scCO_2$, core material (intact or crushed), and brine chemistry that included only the major aqueous components described above. Some experiments additionally included the trace elements (described above) that are potentially injected with the $scCO_2$ to characterize the fate of those metals (Table 3.4). It is hypothesized that metals present as cations (in the brine or $scCO_2$ or desorbed or from mineral dissolution) will remain mobile or be mobilized as the $scCO_2$ creates an acidic environment. In addition, metals present as oxyanions (Cr, As, Mn) are likely to decrease as the system acidity increases. Finally, while the upper Mount Simon aquifer is presumed initially to be anoxic (or reducing), trace-gas components are likely to include other trace gases (2% N2, Ar), 0.12% NO_x (NO, NO_2), 0.12% SO_x (SO_x), 0.002% O_2, and 0.002% water vapor (Table 3.5). Introduction of NO_x and SO_x may simulate nitrate- or sulfate-reducing microbial activity (with a carbon source). Although the aquifer is likely reducing, large $scCO_2$ injection with O_2 may eventually overwhelm aquifer reductive capacity so there may be aerobic microbial activity (see Section 2.5) or cause changes in metals mobility. Redox reactive metals such as Fe, As, and Mn are more mobile in a reducing environment, and will be less mobile (precipitate) in an oxic environment.

For systems that contained only major cations in the brine solution and either crushed drill cuttings or intact core (i.e., no trace metals added, Figure 3.22a, b), a significant increase in silica was observed for high $scCO_2$ systems for both the Mount Simon Sandstone and Elmhurst Shale. In addition, Sr, Ni, and Mn were observed to increase. For low CO_2 saturations (10% $scCO_2$/90% brine), the aqueous concentrations of Fe and Ni increased to a greater extent than in systems with higher $scCO_2$ fraction. For systems that contained major cations in the brine solution and additionally trace metals (list described above) that may be present in the injecting $scCO_2$ stream (Figure 3.18c, d), trace metals observed to increase included Fe, Ba, Mn, Sr, Ni, Sn, , Bi, Cu, Li, P, and Zn with a rapid increase in aqueous Fe and Zn. Trace metals observed to decrease in concentration include Co and Pb. Metals present as oxyanions (Cr, As, Mo) were below detection limits in all systems (i.e., precipitated).

Mercury is a volatile product of coal combustion, so it is also found in $scCO_2$. In rock core/brine/$scCO_2$ experiments in which 688 ug/L Hg was added with other trace metals (Figure 3.22d), measurements for Hg by ICP were all below detection limits. Additional analysis was conducted on samples using ICP-mass spectrometry (MS), which showed that the initial Hg concentration (688 ug/L) injected in the brine decreased to below detection limits (<12.5 ug/L) when reacted with rock core and $scCO_2$.

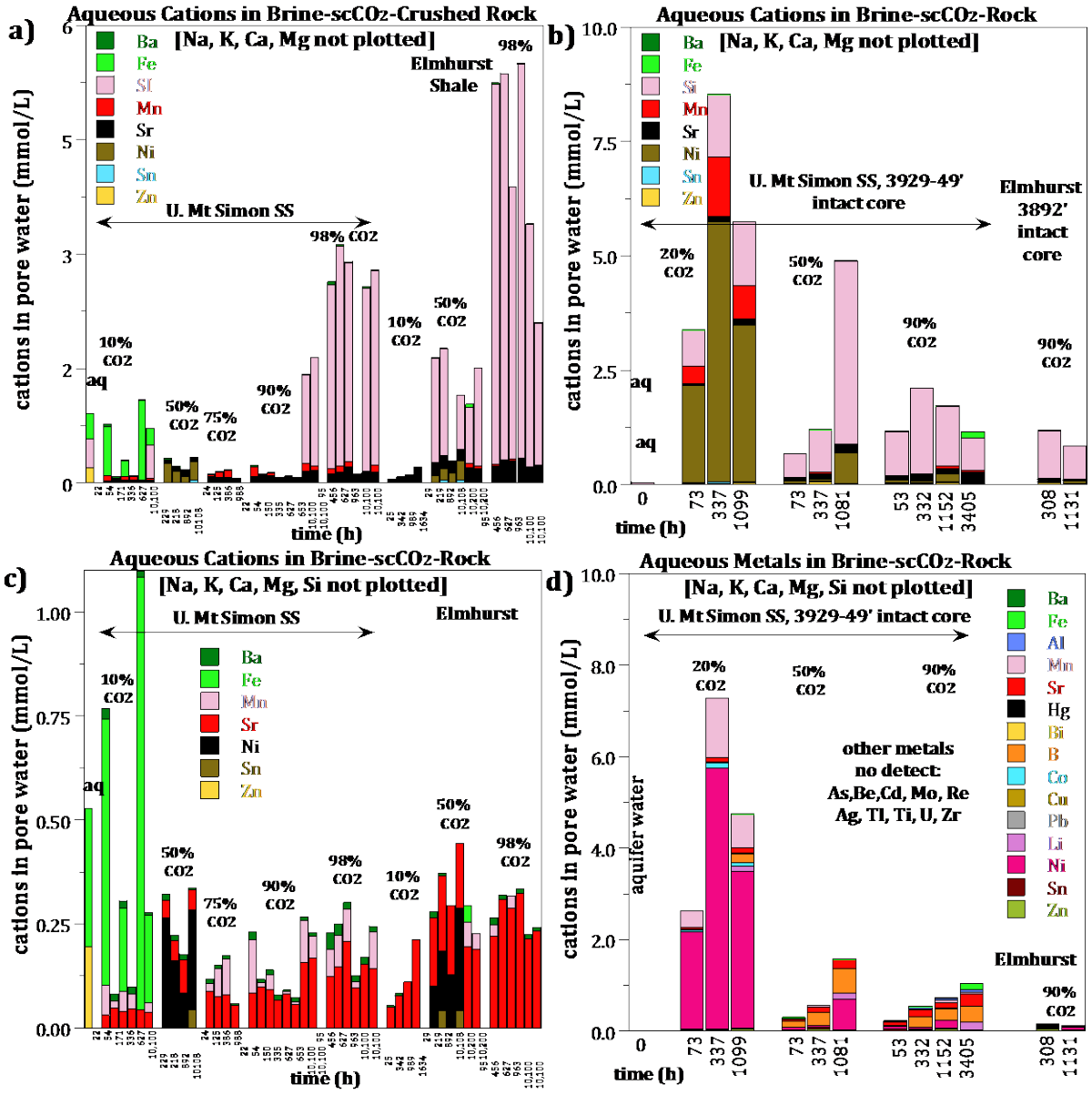

Figure 3.22. Trace metals in aqueous solution in different $scCO_2$/brine/rock systems: a) major cations only added to brine, crushed rock; b) major cations only added to brine, intact rock core; c) major cations and trace metals added to brine, crushed rock; and d) major cations and trace metals added to brine, intact rock core.

3.3.4 Short-Term Precipitation by Solid-Phase Analysis

Analysis of aqueous ions (Section 3.3) showed that mainly at high $scCO_2$/brine ratios where significant acidification of the sandstone occurred, some metals present as cations increased in aqueous concentration and some present as anions decreased in aqueous concentration. Solid-phase analysis of core material by electron microprobe analysis of several samples reacted with 98% $scCO_2$/2% brine at 38°C and 1800 psi for 1.2 years was conducted to evaluate the formation of 1) significant precipitates that could alter the formation permeability, and 2) minor precipitate phases that confirm the fate of specific

ions that decrease in aqueous solution concentrations. Solid phases identified in this treated sample were compared to solid-phase analysis conducted on untreated core (Section 3.1.2). Brine is initially poorly displaced by the injecting $scCO_2$ in laboratory experiments respresenting near-injection−well conditions, even after 100 pore volumes of $scCO_2$ injection, likely due to the relatively short duration of the experiment not allowing for sufficient carbonate dissolution into aqueous solution (see Section 3.2). However, once a steady-state residual water content is achieved, slow partitioning of water into the $scCO_2$ (limited solubility) will continue to dewater the injection zone. As water partitions into the $scCO_2$, ions left eventually become supersaturated and precipitate. This "salting-out" phenomenon has been observed by others with NaCl precipitates (Gaus et al. 2008). Electron microprobe analysis of the $scCO_2$/brine-treated sandstone in this product shows extensive formation of small NaCl crystals on silica (Figure 3.23a), KCl crystals on silica (Figure 3.23b), and KCl crystals on calcite (Figure 3.23b), likely the result of salting out. Other minor precipitate phases identified include an iron oxide (likely hematite, Figure 3.23c), forsterite (or talc) on calcite (Figure 3.23d), and a Pb oxide precipitate (Figure 3.23d).

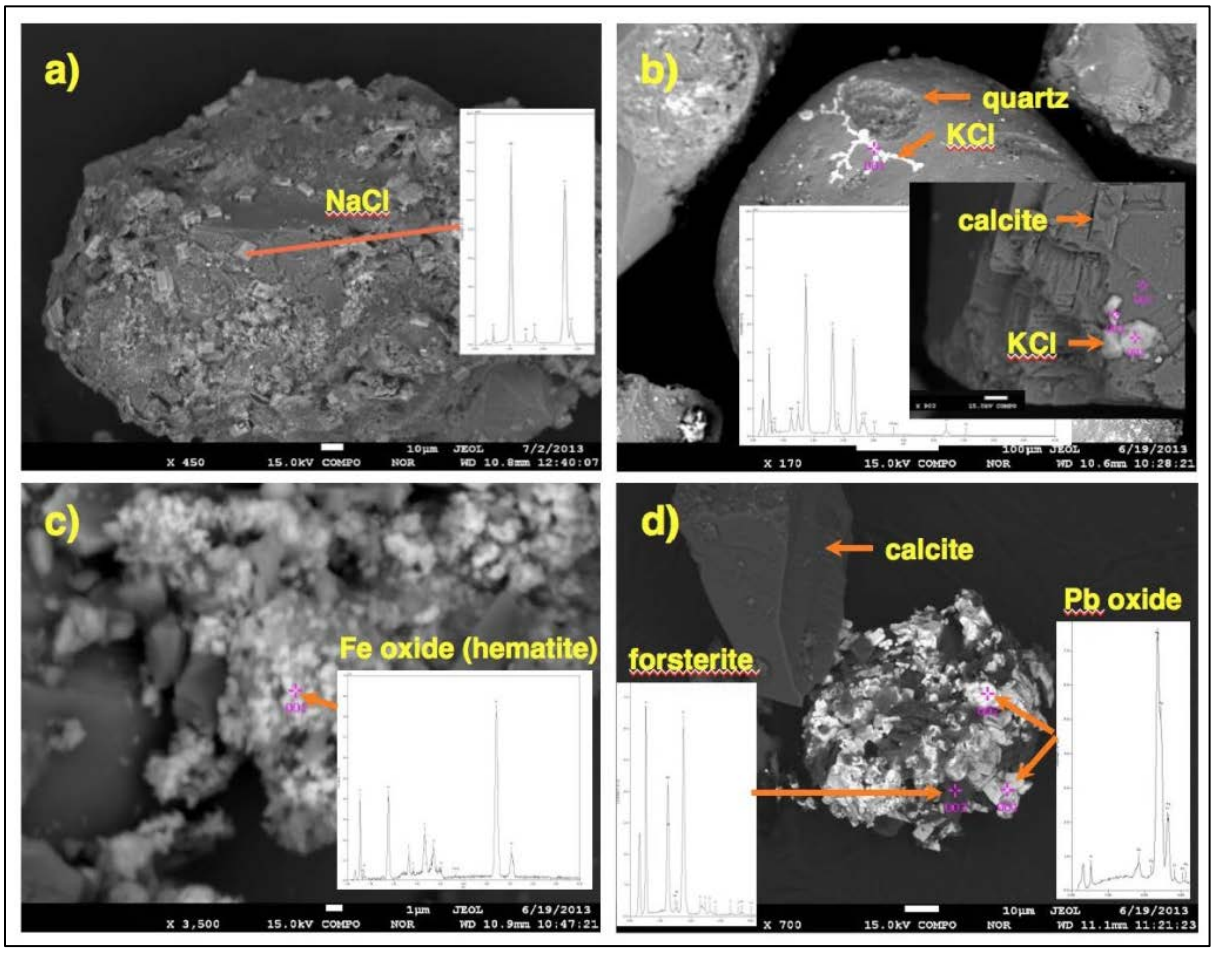

Figure 3.23. Electron microprobe analysis of upper Mount Simon Sandstone treated with 98% $scCO_2$ and 2% brine at 1,800 psi and 38°C for 1.2 years showing the formation of the following precipitates: a) NaCl, b) KCl on quartz and calcite, c) unidentified iron oxide, and d) forsterite on calcite.

3.3.5 Long-Term Predicted Carbonate and Other Mineral Precipitation

Laboratory experiments described in previous sections can be used to characterize short time-scale processes such as $scCO_2$ displacement of brine. Simulations presented in this section are conducted by others in similar (but not the same) sandstone formations to show likely longer term processes that ultimately sequester liquid CO_2 into carbonate minerals. Over the time scale of injection (20 years), sequestration of $scCO_2$ occurs by stratigraphic trapping, meaning the $scCO_2$ migrates upward through the reservoir due to buoyancy, but advection of the $scCO_2$ into low-permeability confining zone materials is extremely slow and thus the injected $scCO_2$ is contained within the reservoir. Over the time scale of hundreds to thousands of years, carbonate minerals form, trapping increasing amounts of $scCO_2$ in solid phases (shown conceptually in Figure 3.24). The time scale and minerals involved are site-specific.

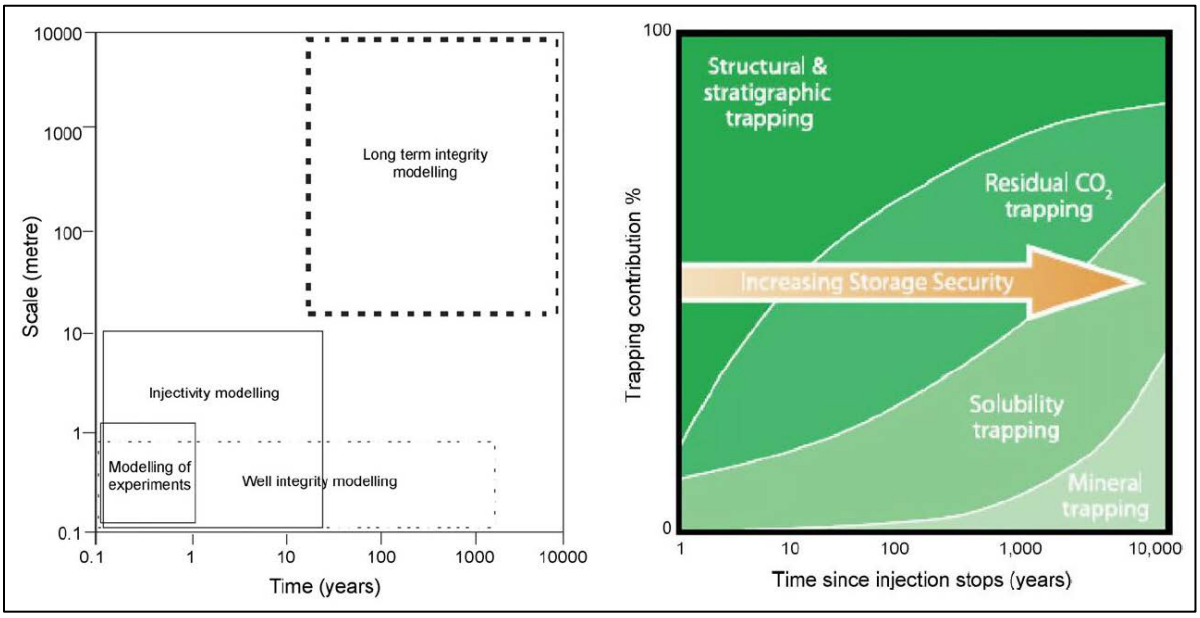

Figure 3.24. Long-term fate of injected $scCO_2$ with a conceptual approach of a) physical and temporal time scale of experiments versus field system, and b) temporal evolution of differing mechanisms trapping C mass over time (from Gaus et al. 2008).

Multiphase modeling with geochemical reactions was not conducted in this study, but some insight is gained from the results of a simulation study in a similar sandstone/shale/brine geochemical environment (White et al. 2005). In this study, $scCO_2$ was injected over a 30-year period, into the marine-deposited White Rim Sandstone, which is capped by a thick (700-m) Mancos Shale composed of interbedded shale and sandstone. The ChemTOUGH model used (White et al. 1995) is based on TOUGH2, with chemical reactions at equilibrium or described by a general kinetic rate law. Simulations had constant $scCO_2$ saturation (to brine ratio) using simplified reservoir mineralogy with 15 minerals (Table 3.6). Simulation of these minerals in contact with a constant percentage of $scCO_2$ and no flow showed the following mineral changes: 1) rapid acidification and dissolution of quartz, Na-smectite, albite, and K-feldspar over hundreds to thousands of years (Figure 3.25), and 2) eventual pH neutralization with precipitation of kaolinite, calcite, and dawsonite. Both calcite and dawsonite contain carbonate. Even though geochemically this site is generally similar to the FutureGen 2.0 storage site, the injection depth, bedding inclination, and fracture network structure are different, so there are few similarities in $scCO_2$/geochemical transport results in this study that are applicable to the Future Gen 2.0 storage site.

Table 3.6. Minerals used in White et al. (2005) simulations.

Quartz	SiO_2
K-feldspar	$KaAlSi_3O_8$
Kaolinite	$Al_2Si_2O_5(OH)4$
Calcite	$CaCO_3$
Dolomite	$CaMg(CO_3)_2$
Siderite	$FeCO_3$
Illite	$K_{0.6}Mg_{0.25}Al_{1.8}(Al_{0.5}Si_{3.5}O_{10})(OH)_2$
Albite-low	$NaAlSi_3O_8$
Smectite-Na	$Na_{0.290}Mg_{0.26}Al_{1.77}Si_{3.97}O_{10}(OH)_2$
Anorthite	$CaAl_2Si_2O_8$
Dawsonite	$NaAlCO_3(OH)_2$

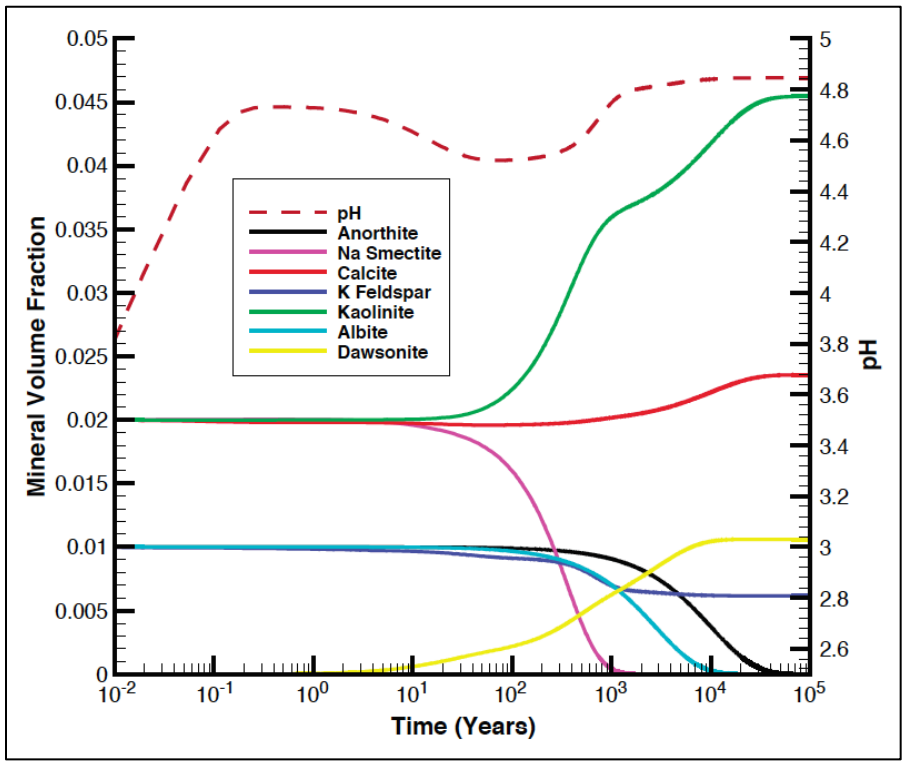

Figure 3.25. Long-term mineral dissolution and precipitation in a sandstone/shale system with the injection of $scCO_2$ (simulation results from White et al. 2005).

3.4 Permeability Change from $scCO_2$-Brine-Sandstone Interactions

Investigation of the measured change in permeability, the movement of iron oxide particulates, and the potential for microbial biomass growth to decrease permeability is discussed in the following sections.

3.4.1 Measured Pressure Change and Implications to Permeability

At field scale, as the $scCO_2$ saturation increases and brine saturation decreases, the equivalent hydraulic conductivity of the formation will increase because of the significantly lower viscosity of the $scCO_2$. Although this fluid change is likely to dominate the overall hydraulic response, a study was conducted to investigate whether the formation of precipitates (or movement of iron oxide particulates) have the potential to reduce formational permeability to some extent. In this study, hydraulic conductivity was measured using water as the fluid to assess whether sandstone permeability would change appreciably due to mineral-phase dissolution/precipitation and/or particulate advection.

The hydraulic conductivity of 17 intact cores (upper Mount Simon, lower Mount Simon, Eau Claire Sandstone) were measured at four flow rates prior to any $scCO_2$ injection (results in Section 2.1.2), then measured after experiments conducted with different $scCO_2$/brine mixtures and different durations (Table 3.7). An additional 10 intact cores were used to measure iron oxide particulate movement (see Section 3.4.2), because observed hydraulic conductivity changes occurred within the first few pore volumes after extended no-flow periods and were accompanied by iron oxide particles in the outlet. For experiments >100 hours, there was an increase in the pressure in the core correlated with a) increasing reaction time of $scCO_2$/brine/core, b) increasing percentage of $scCO_2$ relative to brine, and c) increasing injection amount (i.e., number of pore volumes). The pressure increase could be caused by a) precipitation (see Section 3.0), b) microbial growth (see Section 3.4.3), or c) iron oxide particulate movement. While NaCl and KCl precipitate formation has been observed and is predicted, over the <1.5 years of the laboratory experiments, the volume of pore space occupied by these precipitates is small. Similarly, formation of other precipitates has been observed including hematite, forsterite/talc, and a Pb oxide (Section 3.3.5), but none is present in significant mass. Microbial biomass growth is characterized in Section 3.5, and the calculated growth effect on pore space calculated in Section 3.4.3 shows an insignificant change. Because the influence of precipitates and microbial growth was small and iron oxide particulate movement significant, the apparent decrease in hydraulic conductivity was likely caused by the iron oxide particles. It should be noted that an increase in pressure could be the result of a real decrease in hydraulic conductivity of the sandstone or could be an experimental artifact of iron oxide particles partially clogging the outlet frit. Because significant (but inconsistent) amounts of iron oxide particulates were observed on the outlet frit upon taking columns apart, it is likely increases in pressure were caused by outlet frit clogging. If columns were built with multiple pressure measurement ports along the length of the column, then there would be clear evidence of potential changes in the formation permeability exclusive of the outlet frit.

Table 3.7. Measured change in brine hydraulic conductivity after $scCO_2$ experiments.

#	Formation	depth (ft)	core orientation	final CO_2 (%)	time (h)	H_2O mean K_{sat} (cm/sec)	H_2O std dev K_{sat} (cm/sec)	K_{sat} change* (%)
B1	upper Mt Simon	3946.5	vertical	38.5	73	9.19E-05	4.555E-06	43.83
B2	upper Mt Simon	3949.7	vertical	14.9	336.8	1.17E-06	3.223E-07	-83.90
B3	upper Mt Simon	3949.7	vertical	no flow				
B4	upper Mt Simon	3946.5	vertical	23.7	1099.4	9.26E-07	4.023E-07	-93.21
B5	upper Mt Simon	3949.7	vertical	58.3	72.3	1.6E-06	6.047E-08	15.49
B6	upper Mt Simon	3949.7	vertical	70.9	334.8	2.73E-07	1.564E-07	-77.91
B7	upper Mt Simon	3931.7	horizontal	82.6	1081.5	2.16E-07	1.062E-07	-76.35
B8	upper Mt Simon	3931.7	vertical	70.6	53.5	1.88E-06	2.681E-07	-53.79
B9	upper Mt Simon	3931.7	vertical	74.9	331.7	1.45E-06	6.166E-07	-90.90
B10	upper Mt Simon	3931.7	vertical	73.2	1152.5	2.14E-06	2.42E-07	-39.01
B11	lower Mt Simon	4405.0	vertical	68.2	1152.5	3.86E-07	1.432E-07	-76.35
B12	lower Mt Simon	4405.0	horizontal	no flow				
B13	Eau Claire SS	3884.2	vertical	77.2	308.3	5.91E-07	3.589E-07	-94.72
B14	Eau Claire SS	3884.2	horizontal	87.7	1131	1.77E-05	9.395E-07	78.06
B17	upper Mt Simon	3929.1	vertical	87.7	1131	1.49E-07		58.98

* + = higher Ksat after $scCO_2$ injection, - = lower Ksat after$scCO_2$ injection

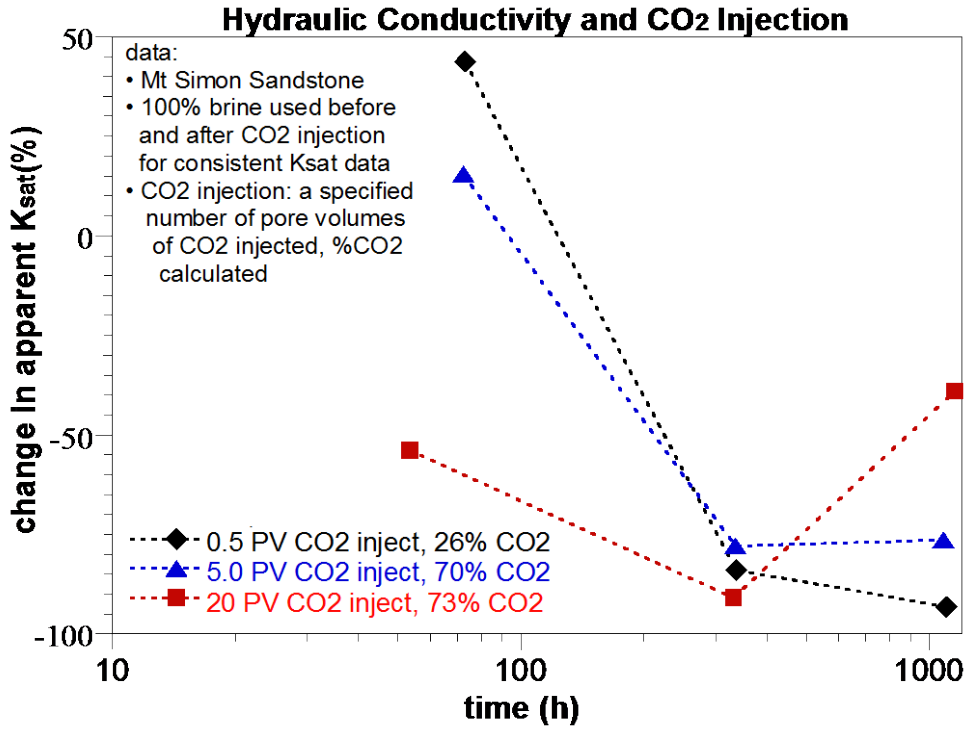

Figure 3.26. Change in hydraulic conductivity of upper Mount Simon Sandstone as a result of $scCO_2$/brine/core reactions resulting in precipitation or iron oxide particulate movement.

3.4.2 Iron Oxide Particulate Movement

The mobilization of iron oxides from the upper Mount Simon Sandstone core due to injection of $scCO_2$ was investigated because of its potential to change formation permeability. The acidification of

formation materials by contact with $scCO_2$ results in dissolution of some of the ferric oxides (i.e., the 0.76% hematite, Section 3.1.1), which may precipitate downgradient. In addition, dissolution could result in the movement of hematite particulates/colloids, potentially clogging downgradient pores. Experiments were conducted using varying amounts of acidification (i.e., higher $scCO_2$/brine ratio results in a lower pH), a range of reaction times, and different injection fluids (i.e., brine or $scCO_2$) to evaluate the total particulate mass moving downgradient. Experiments consisted of intact upper Mount Simon Sandstone cores with no end frits (which could capture some of the particulates) connected to a second column filled with glass beads and 1-µm outlet frit. The particulate weight was measured by the increase in mass of the glass bead column.

For intact cores filled with different initial $scCO_2$/brine solutions, no reaction time, and injection of brine (i.e., fairly unrealistic given the short reaction time for the $scCO_2$/brine/core), the mass of solids measured downgradient of the column (i.e., either movement of particulates or formation of iron oxide precipitates) was 5 to 16 mg/g of core material after 1 pore volume and 5 to 45 mg/g after 15 pore volumes (Figure 3.24a). For this case, higher fractions of initial $scCO_2$ saturation resulted in less particulate movement, which was unexpected for such a small $scCO_2$/brine/sandstone reaction time. The observed response may have been caused by the fact that brine was transported through only a fraction of the core, because there is 30−60% residual $scCO_2$ saturation in the 1 to 15 pore volume range (Figure 3.11).

In another series of experiments with intact cores, the $scCO_2$/brine/sandstone reaction time was increased to 500 hours (but still using brine as the injecting fluid), based on measured change in hydraulic conductivity being larger at times greater than 100 hours (Figure 3.26). These experiments showed that increasing the fraction of $scCO_2$ initially in the core increased the solids mobilization (Figure 3.27b). Finally, experiments were conducted in which the fractions of solids mobilized by brine injection versus $scCO_2$ injection were compared (Figure 3.27c). This showed that injecting $scCO_2$ mobilized significant amounts of iron oxide particulates (or mobilized aqueous iron that subsequently precipitated), with 50 mg/g core after 1.5 pore volumes, 60 mg/g core after 10 pore volumes, and 180 mg/g after 100 pore volumes (cumulative solids mass, red data in Figure 3.27c). It should be noted that injection of 100 pore volumes of $scCO_2$ took 10 hours to inject, which increases the reaction time for carbonate to partition from the $scCO_2$ into the brine when compared with smaller pore volume injections. One likely experimental artifact is that these 1-in.-diameter cores have some loose iron oxide coatings at the outer edge of the drilled core. Injection of brine into brine-filled cores (i.e., no contact with $scCO_2$; black triangles in Figure 3.27c) showed some particulate movement after 1 pore volume (50 mg/g), which increased only slightly after 100 pore volumes (65 mg/g). Because this is considered background particulate movement, a realistic mass of iron oxide particulate movement from the injection of $scCO_2$ is the total observed minus this background value (i.e., 10 mg/g after 1 pore volume, 30 mg/g after 10 pore volumes, and 115 mg/g after 100 pore volumes of injected $scCO_2$).

Particulate transport experiments showed some increase in iron oxide mass transported as a result of $scCO_2$ injected, but it was not possible to separate whether the particle movement causes actual formation permeability decrease or just end frit clogging in the 1D cores (i.e., experimental artifacts). Although there was evidence of particulate movement observed in these 1D columns (i.e., linear flow systems), it is likely that this effect would be less significant at the field scale because of the radial flow system associated with well injection. Any particulate movement near the injection well would advect particles into an ever-increasing volume further away from the injection well, so this effect would likely to have less impact on field-scale hydraulic conductivity than was measured in this laboratory study.

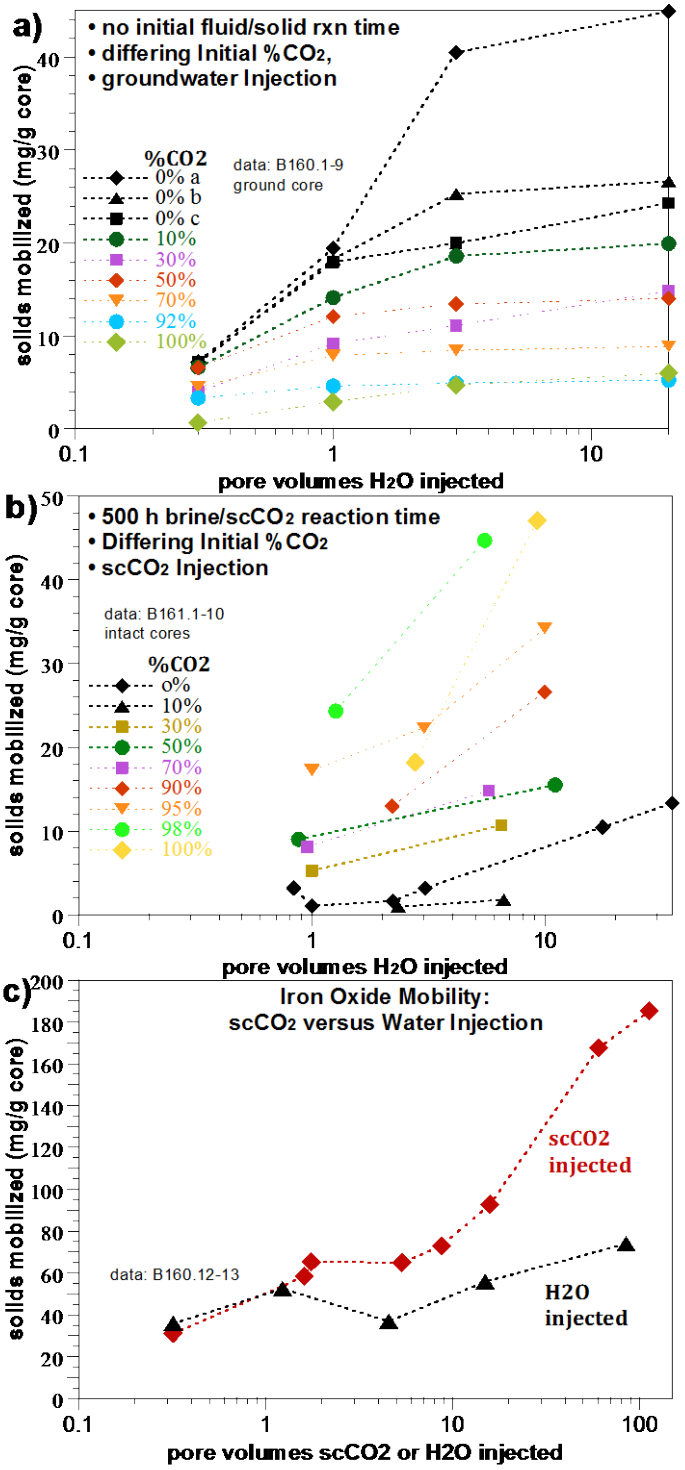

Figure 3.27. Transport of particulates or precipitates out of upper Mount Simon Sandstone core material with a) no reaction time and brine injection, b) 500-hour reaction time and brine injection, and c) variable reaction time and brine or scCO$_2$ injection.

3.4.3 Potential of Microbial Biomass Growth to Decrease Permeability

Anaerobic microbial growth can be expected to occur when $scCO_2$ is injected into the anaerobic aquifer at field scale. Measured anaerobic microbial biomass growth after 1,300 hours in $scCO_2$/brine/Mount Simon core systems was 23.5 times ($9.39 \pm 4.07 \times 10^6$ cells/g) the untreated biomass ($4.02 \pm 4.01 \times 10^5$ cells/g), as described in detail in Section 3.5 (Table 3.8). Aerobic microbial growth may occur in a zone near the injection wells, because the small amount of injected oxygen will eventually oxidize any reduced aqueous and solid phases present. Measured aerobic microbial biomass growth after 1,300 hours in $scCO_2$/brine/Mount Simon core systems was 14 times ($5.64 \pm 3.05 \times 10^6$ cells/g) the untreated biomass. Given an average cell density of 2.8×10^{-13} g/cell (Bailey and Ollis 1986), the untreated biomass is 1.1×10^{-7} g cells/g sandstone, and would occupy approximately 0.004% of the pore space (assuming 17% porosity; Cunningham and Characklis 1991). The maximum observed biomass increase in a field-realistic system ($9.39 \pm 4.07 \times 10^6$ cells/g in an anaerobic system) would occupy 0.09% of the pore space, which is a significant increase, but still too small to influence permeability (Cunningham and Characklis 1991). With a continuous influx of microbial nutrients, biomass could potentially continue to increase, near the injection well, so nutrients will generally not be transported downgradient (i.e., no downgradient growth [Taylor and Jaffe 1990]). In addition, microbes generally attach to mineral surfaces by a variety of mechanisms, but can be sheared off with high velocities and high-ionic−strength solutions. As microbes occupy a substantial fraction of the pore space, fluids traveling through the remaining pore space will be moving at a higher velocity, which eventually exceeds the microbe-surface attachment strength and additional growth at that location does not occur (Cunningham and Characklis 1991).

3.5 Anaerobic and Aerobic Microbial Growth with $scCO_2$ Injection

Injection of $scCO_2$ with minor components (O_2, NO_x, SO_x) changes the geochemical conditions in the upper Mount Simon Sandstone aquifer, by decreasing pH, increasing carbonate, dissolving some mineral phases (Mg^{2+}, K^+, and SO_4^{2-} concentrations), precipitating some salts (NaCl, KCl), and changing the reducing conditions to oxic conditions. Trace metals Ba, Sr, Ni, Sn, and Mn also increase, as a result of desorption (in the slightly acidic conditions) or mineral dissolution. If microbes are present in this injection zone, the change in geochemical conditions could stimulate growth, but only if O_2 for aerobes or CO_2 for methanogens, nutrients, and needed trace metals are present. It is hypothesized that the $scCO_2$itself does not stimulate aerobic microbial growth (no O_2 present), but the minor components in the injection stream (O_2, NO_x, SO_x) might stimulate aerobic microbial growth, because oxygen and nitrogen are electron acceptors. Methanogenesis may be stimulated by the introduction of just the $scCO_2$, although the extreme geochemical conditions of two-fluid phases may limit growth. Trace metals are also used for microbial enzymatic pathways, so addition of bioavailable metals could also increase microbial growth to some extent. Therefore, experiments were conducted to quantify 1) microbial biomass population in the upper Mount Simon Sandstone (3,918- to 4,200-ft depth), 2) influence of the addition of $scCO_2$ alone (no minor components) on microbial growth, and 3) influence of the addition of $scCO_2$ with minor components on microbial growth.

3.5.1 Materials and Methods

This section describes the materials and methods used in laboratory studies of anaerobic and aerobic microbial growth resulting from $scCO_2$ injection.

3.5.1.1 Core and Solutions

Methods were developed to extract microbes aseptically from the Mount Simon Sandstone core from a 3,928-ft depth. The 4-in.-diameter core (by 6-in. length) was processed inside a microbial hood (HEPA filtered), which filters outside air and significantly decreases the introduction of microbes from other sources. First, the core was split into 1/4-in.-thick disks along natural bedding planes, then the outer 1/2 in. of core was removed, because it may have been contaminated with ex situ microbes. These operations were conducted using a sterilized chisel, hammer, and steel plate. The core pieces were then subdivided into 1/2-in.-diameter by 1/8–in.-thick pieces, which were used in experiments. Initial experiments were conducted using crushed core, but biomass counting was not possible because the significant mass of iron oxide particulates that accumulate on the microbial filter prevents counting microbes.

A synthetic brine solution was used to simulate the Mount Simon aquifer water (O'Connor and Rush 2005) that consisted of 23,400 mg/L Na, 49,600 mg/L Cl, 2,670 mg/L Ca, 18.6 mg/L Fe, 1,280 mg/L Mg, 141 mg/L K, 10.8 mg/L Si, 120 mg/L CO_3, and 83.3 mg/L F (Table 3.2). Additional trace metals present in just fly ash were also included in some experiments: Mn, Co, Ni, B, Mo, PO_4 (2.1E-6 mol/L), Zn, AsO_4, Cr, Pb, V(III), and Hg (Table 3.3). This solution was vacuum filtered through a 0.2-µm filter before using it in microbial experiments. Two different $scCO_2$ gases were used that included 100% CO_2 (for methanogenesis biostimulation), and a mixed gas containing 97% CO_2, 2% inert gas (N_2), and 1% oxygen (for aerobic biostimulation). In some experiments, the 100% CO_2 was used, and in other experiments, the mixed gas was used, but with additional gases (SO_x and NO_x). A source of pure SO_2 gas was added (as 0.2% by volume) from a separate gas tank. NO_x (a mixture of NO_2 and NO, as separate gases, as these gases react with each other) was not available at the time of the experiments. However, as these gases result in some nitrite (NO_2-) in solution in addition to the dissolved gases, 10 mg/L nitrite was added to experiments.

3.5.1.2 Growth Experiments

Microbial experiments consisted of reacting core chips (which contained microbes) with the mixture of aquifer brine, $scCO_2$, and trace components in a high-pressure reactor at 1,500 psi (and 38°C) for 770 hours before analysis of the microbial biomass. The control experiment consisted of mixing 20 g of core chips with 11.8 mL of brine, with no CO_2 or other trace components added (i.e., this represents conditions in the aquifer with no injection). Because it was hypothesized that minor components and not the $scCO_2$ could cause growth, experiments were compared that contained only $scCO_2$ to experiments with $scCO_2$ and other trace components. The two brine/CO_2 control experiments (i.e., no additional gases or other trace components) were conducted with 50% brine/50% CO_2 or 2% brine/98% CO_2. In previous geochemical experiments, high $scCO_2$ concentration experiments showed the most significant changes, so these microbial experiments were conducted at higher CO_2 concentrations, as additional ferric iron (which can be a microbial electron acceptor) dissolves from sediment. Four experiments conducted with brine/CO_2 with additional components were at the following brine/CO_2 ratios: 1) 90% brine/10% CO_2, 2) 50% brine/ 50% CO_2, 3) 10% brine/90% CO_2, and 4) 2% brine/98% CO_2. One additional growth experiment was conducted that included supplying the in situ microbes with all necessary growth nutrients, in order to test whether there actually is a viable microbial population. The growth medium consisted of a carbon source (5 mg/L lactate), trace metals (Fe, Mg, Na, K, Mn, Mo, Co, Ni, SO_4, Zn), a P source (0.7 mg/L PO_4), a N source (50 mg/L NO_3), amino acids (arginine, serine, glutamic acid), and

vitamins (biotin, folic acid, pyridoxine, thiamine, nicotinic acid, pantothenic acid, vitamin B12, aminobenzoic acid, and thioctic acid.

Time is a factor for microbial growth, because microbes that have been dormant for a very long time require hundreds of hours (or more) to gear up enzymatic pathways for the electron-transfer reactions that result in growth. Ideally, experiments should be conducted at times ranging from tens to thousands of hours, but in this initial series of experiments, to limit the number of experiments, a single time period (770 hours) was used to compare results in all experiments.

3.5.1.3 Biomass Enumeration

As microbes sorb (or attach) strongly to sediment surfaces, the procedure for counting the microbial population involves 1) use of a high-ionic−strength solution and shear forces to detach microbes from the core pieces, 2) mixing the solution with a DNA stain, 3) filtering a specified amount of the solution containing fluorescent-DNA-stained microbes onto a microbial filter, and 4) counting the microbial population. The phosphate-buffered saline solution consisted of 0.798 mol/L Na_2HPO_4 and 0.15 mol/L NaH_2PO_4 at pH 7.5. The core pieces (2 g) were mixed with 20 g of the phosphate solution. A preliminary series of experiments was conducted at different sediment/phosphate solution ratios to determine a mixture that worked best. A DAPI (4',6-diamidino-2-phenylindole) fluorescent DNA stain (250 µL in 20 mL) was then added to the solution. This core/phosphate solution was reacted for 30 minutes in the dark (DAPI stain is light sensitive), then vortexed for 1 minute to create high shear conditions to detach microbes from the sediment surface (along with the high-ionic−strength phosphate solution). Then, 2 mL of this solution was filtered onto a microbial filter, which consisted of a Whatman 25-mm GF backing filter and 25-mm black polycarbonate microbial filter (0.2 µm) (from General Electric 1215609 or Nucleopore PCMB). Four milliliters of filtered deionized water were then washed onto the vacuum filter system to remove excess DAPI stain that is not attached to microbes. The filter was then mounted onto a glass slide; citifluor was added and a cover plate. Slides were counted immediately or stored at -80^{o}C before counting.

Counting the number of microbes involved of the use of a specialized fluorescent light microscope at 1,000x. At the correct dilution, the field of view showed <100 microbes, which were manually counted. A total of 10 different fields were counted to obtain a statistical distribution of the counts. If the microbial density was too high, a 10x and 100x dilution from the original extraction solution was used on a different filter. In some cases, microbes clumped, which made counting individual microbes more difficult. Counting the microbes was also more difficult because of the presence of substantial amounts of iron oxide particles on the filter. In many natural systems, the total biomass consists of a range of different types of microbes, which can be of different sizes and shapes (that are also difficult to count). In this case, qualitatively, there were few different types of microbes, although an actual identification of the types of microbes present has not been conducted.

3.5.2 Results

3.5.2.1 Microbial Biomass in the Untreated Mount Simon Core

The microbial biomass measured in the Mount Simon Sandstone at the 3,928-ft depth was 4.02 ± 4.01 x 10^5 cells/g (n = 10,Table 3.8). This value is within the range previously reported for marine-deposited

sediments, but higher than reported for an arid fluvial-laid subsurface sediment. In a study of sandstone and shale marine deposits in New Mexico from the late Cretaceous period (120−135 Myr) at a 450- to 750-ft depth, or similar depositional environment to the Mount Simon Sandstone and Eau Claire Shale, microbial biomass averaged 3×10^7 to 2×10^8 cells/g (Ringelberg et al. 1997), using a conversion of 20,000 to 30,000 cells/pmol of phospholipid fatty acids (Green and Scow 1999; Zink et al. 2008). For comparison, because the Mount Simon Sandstone was a marine depositional environment, current sediments from deep Pacific ocean cores (12,000-ft water depth, 150-ft to 300-ft depth into sediment) averaged 10^6 to 10^7 cells/g, while ocean floor sediments (i.e., at the sediment/water interface) averaged 10^8 cells/g (Inagaki et al. 2006). In the arid northwest at Hanford Site (Washington State), surface soils contained 10^8 cells/g, which decreased to 10^2 to 10^3 cells/g by a 40 ft depth (Szecsody et al. 2009). In a study of fluvial sediments from the same site at Hanford at a 570-t to 712-ft depth, microbial biomass measurements were 10^4 to 1.3×10^5 cells/g (Ogram et al. 1995).

To demonstrate that the cells are viable, a second sample of brine included a microbial growth medium, which contained electron acceptors, trace metals, vitamins, and amino acids (described in the experimental Section 3.5.1). This medium addition resulted in 540x growth in 770 hours to a cell count of $2.16 \pm 0.05 \times 10^8$ cells/g (Table 3.8). No attempt was made to evaluate which nutrients the cells were lacking, but this demonstrates that if the limiting nutrients are added to this deep subsurface microbial population, significant growth can occur.

Table 3.8. Microbial biomass enumeration in untreated and $scCO_2$/brine-treated Mount Simon Sandstone core samples.

experiment type	time (h)	cell counts (cells/g)	std dev, cells (cells/g)	treated/ untreated growth
no additions	0	4.02E+05	4.01E+05	1.000
anaerobic/methanogenesis	16.3	2.02E+06	1.46E+06	5.04
anaerobic/methanogenesis	71.1	2.30E+06	1.37E+06	5.71
anaerobic/methanogenesis	364.2	2.48E+06	1.90E+06	6.18
anaerobic/methanogenesis	430.3	3.02E+06	1.81E+06	7.52
anaerobic/methanogenesis	597.8	1.69E+06	1.06E+06	4.20
anaerobic/methanogenesis	768.2	4.49E+06	6.19E+06	11.2
anaerobic/methanogenesis	1293	9.39E+06	4.07E+06	23.4
anaerobic/methanogenesis	2212	6.94E+06	4.47E+06	17.3
aerobic (O_2, NO_x, SO_x)	16.3	1.61E+06	1.22E+06	4.00
aerobic (O_2, NO_x, SO_x)	71.1	1.37E+06	6.94E+05	3.42
aerobic (O_2, NO_x, SO_x)	364.2	1.13E+06	1.29E+06	2.81
aerobic (O_2, NO_x, SO_x)	430.3	1.31E+06	9.37E+05	3.26
aerobic (O_2, NO_x, SO_x)	597.8	2.17E+06	1.21E+06	5.40
aerobic (O_2, NO_x, SO_x)	768.2	3.36E+06	4.74E+06	8.35
aerobic (O_2, NO_x, SO_x)	1293	5.64E+06	3.05E+06	14.0
aerobic (O_2, NO_x, SO_x)	2212	3.76E+06	2.94E+06	9.36
aerobic (O_2, P, N, S, amino acids, metals)	768	2.16E+08	4.90E+06	538

3.5.2.2 Anaerobic Microbial Growth in Brine/CO_2 Solutions

In different mixtures of brine and $scCO_2$ only (with no other gases or trace metals), anaerobic microbial growth was observed that correlated with higher $scCO_2$ concentration only (no additional trace metals; Figure 3.28, untreated point and green triangles;Table 3.8). Only two CO_2 saturations were evaluated, 50% and 98% $scCO_2$. In each case, microbial plate counts were done on 10 locations of the slide, so the order of magnitude increases from $4.02 \pm 4.01 \times 10^5$ (0% $scCO_2$) to $1.71 \pm 1.08 \times 10^6$ (50% $scCO_2$) to $4.49 \pm 0.62 \times 10^6$ cells/g (98% $scCO_2$) were statistically different and represent a trend relative to the untreated sample ($4.02 \pm 4.01 \times 10^5$ cells/g). Anaerobic growth as a function of the fraction of $scCO_2$ with additional trace metals was similar (Figure 3.28a, brown squares), but with slightly less growth. Whether this observed microbial growth is caused by methanogenesis requires proof by consumption of the CO_2 (which would be very difficult to measure a very small decrease in the high $scCO_2$ concentration) or production of methane and H_2 (which is possible to measure).

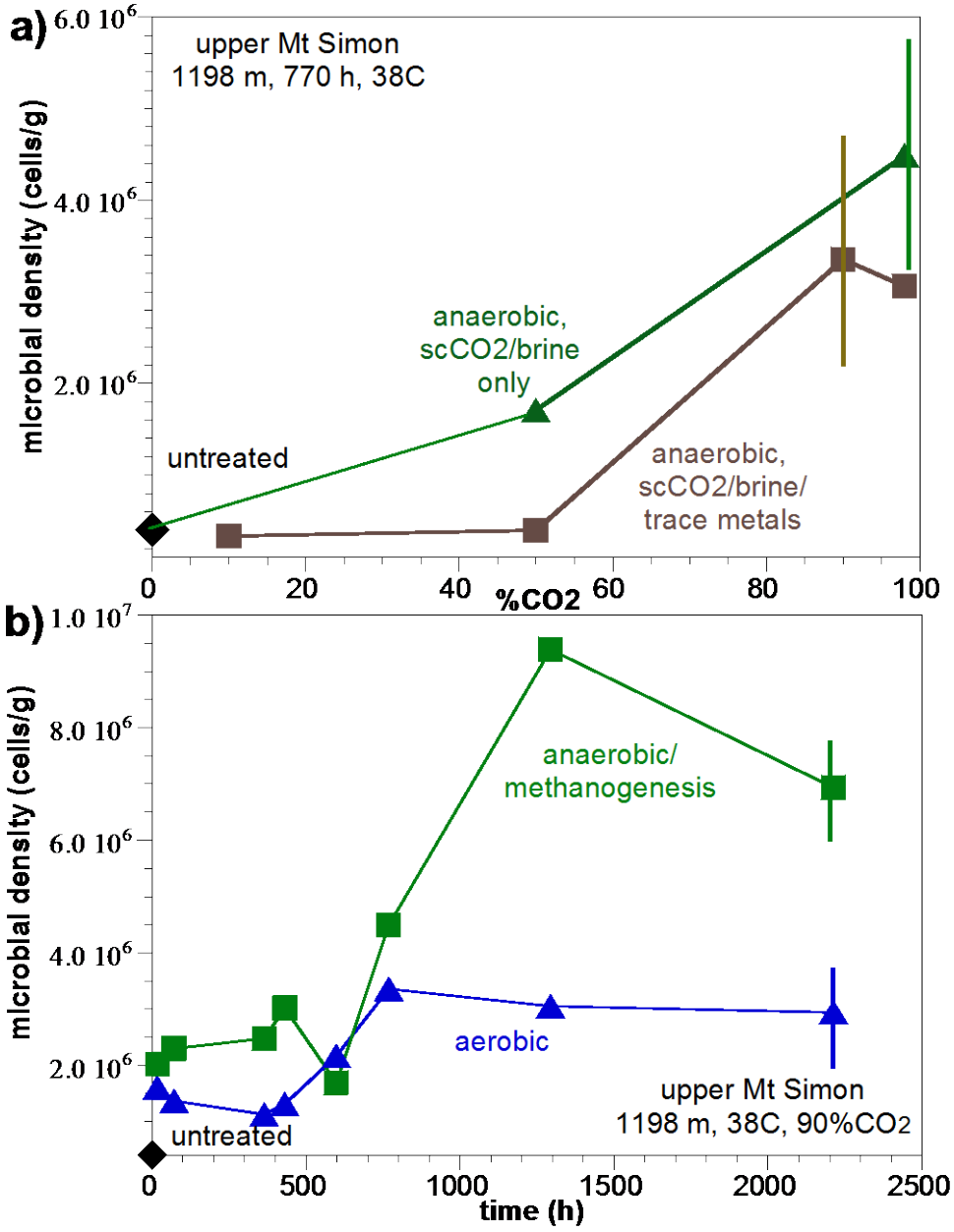

Figure 3.28. Influence of additions of $scCO_2$ and minor gas/trace metals on microbial growth at 38°C a) as a function of fraction $scCO_2$ and trace metals in an oxic system (all at 770 hours), and b) as a function of time in aerobic and anaerobic systems. Vertical bars on points represent ± standard deviation.

It is possible that the anaerobic microbial growth effect is indirect. Higher $scCO_2$ concentrations acidify the system and desorb heavy metals from clay, iron oxide, and other mineral surfaces, and also cause dissolution of some of the ferric oxides. Trace metals may, therefore, be more bioavailable and promote more rapid microbial growth (i.e., used in microbial enzymatic pathways). In addition, ferric iron is used as an electron acceptor by iron-reducing microbes, so dissolution of ferric oxides may increase electron acceptor bioavailability. The total ferric oxide content is significant, because X-ray

diffraction of the Mount Simon Sandstone 3,928-ft depth indicated 96.2% quartz, 1.84% mica (mainly muscovite), 1.23% mullite, and 0.76% hematite (Fe_2O_3). The significant amount of bioavailable ferrous iron from hematite dissolution could be used by iron-reducing bacteria (if present), for example.

Additional experiments were conducted to evaluate microbial growth in anaerobic Mount Simon core systems over time (Figure 3.28b, green squares). Microbial growth by 500 hours was 7.5x (i.e., minimal), but by 1,300 hours it was 23.5x, and then it leveled off by 2,300 hours, possibly indicating limiting nutrients. These time-course experiments contained trace metals and trace-gas components (NO_x, SO_x) likely to be in the $scCO_2$ injection stream (but not the O_2). Given that the upper Mount Simon Sandstone aquifer is likely under reducing conditions (with the 18.6 mg/L total iron likely ferrous iron, Table 3.2), injection of a small fraction of oxygen (2E-5%, Table 3.4) would not be enough to alter the anaerobic/reducing conditions and the oxygen would likely be completely consumed in most areas of the aquifer. The result of 23.5x biomass increase by 1,300 hours as a result of $scCO_2$ addition is significant, but not enough to influence permeability (see Section 3.4.3).

3.5.2.3 Aerobic Microbial Growth in Brine/CO_2 Solutions

Near the injection well, the mass of injected oxygen will be greater than the reductive capacity of the aquifer (ferrous iron in aqueous solution and any reduced Fe or Mn surface phases), so oxic microbial growth was also investigated. In general, aerobic microbial growth (blue triangles, Figure 3.28b) was less than anaerobic microbial growth (green squares, Figure 3.28b) at all time periods. After 500 hours, aerobic microbial growth was 3.3x. It increased to 7.6x after 1,300 hours and leveled off thereafter. Images of the microbial plates are shown for 10%, 50%, and 90% $scCO_2$ (with trace component addition, Figure 3.29). Qualitatively, there are more cells at higher $scCO_2$ concentrations (individual cells are the small rod-shaped blue fluorescent shapes). The actual cell counts are the result of counting 10 different locations.

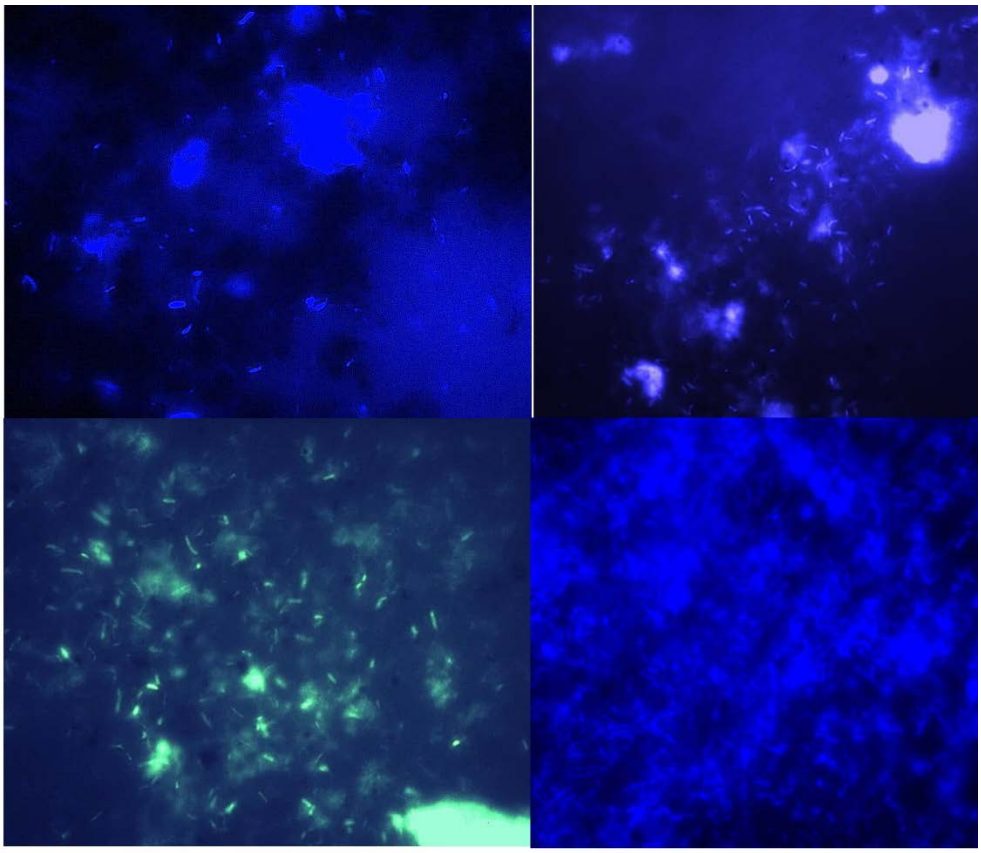

Figure 3.29. Influence of additions of $scCO_2$ and minor gas/trace metals on microbial growth after 770 hours at 38°C: a) 10% CO_2, b) 50% CO_2, c) 90% CO_2, and d) 0% CO_2, but growth media.

3.5.3 Implications of Microbial Growth

A preliminary series of experiments were conducted to quantify 1) the microbial biomass in the Mount Simon Sandstone, 2) the viability of the in situ microbial consortium to grow by methanogenesis (i.e., just $scCO_2$ addition), and 3) the influence of $scCO_2$, O_2, SO_x, NO_x, and trace-metal additions on aerobic microbial growth. Results show that there is a significant microbial population in these sediments ($4.02 \pm 4.01 \times 10^5$ cells/g), likely due to the marine depositional environment, because these cell counts are similar to those found in other modern ocean sediments or similar Paleozoic (i.e., 110 million year old) sandstone/shale deposits in the deep subsurface. The cells are viable, because 540x growth was observed by 770 hours (at 38°C) if a microbial growth media was added to the brine. Four realistic additions (i.e., $scCO_2$ and $scCO_2$ with trace gas/metals in anaerobic and aerobic systems) for the FutureGen 2.0 storage site were used to evaluate the potential for anaerobic and aerobic microbial growth due to the $scCO_2$ injections. Addition of $scCO_2$ alone (with no minor gas components or trace metals) resulted in 11x microbial growth directly in response to the fraction of CO_2 added. This result is consistent with (but does not prove) methanogenesis occurring where the in situ microbial population is using CO_2 (i.e., carbon is the electron acceptor in this case) for methane production. The presence of oxygen would actually inhibit methanogenesis. The addition of $scCO_2$ with trace-gas components (oxygen, SO_x, NO_x) and heavy metals also increased microbial growth 10x, but only at high $scCO_2$ concentrations. At 50% brine/50% $scCO_2$, there was no growth in the system with trace gas/metals in

contrast to 4x growth in the system with no trace components (i.e., anaerobic growth occurred in a wider range of conditions than aerobic growth).

Overall, the 23.5x growth observed by 1,300 hours was minor and would have no influence on permeability in the Mount Simon Sandstone. Future experiments planned in a related project (Rick Colwell, Oregon State University) will include the following:

- time-dependent anaerobic and aerobic growth experiments
- measurement of CH_4 and H_2 in anaerobic experiments
- anaerobic experiments with a methanogen inhibitor
- measurement of total organic and inorganic carbon in the sediment
- identification of microbial type to determine if in situ or from contamination.

If microbial growth continues over time, then it may be useful for microbial characterization to classify the types of microbes present (i.e., archaeal diversity by phylogenetic analysis of 16S rRNA gene sequences). Microbial biomass counting (shown in Figure 3.29) qualitatively indicates mainly few different shapes of microbes. This could be useful at field scale, because a single type of microbe is more easily controlled than a consortium (i.e., wide range of different types of microbes). It should also be noted that while every effort was made to conduct experiments aseptically, drilling fluids (containing surface microbes) could have circulated into the core during drilling/core recovery. Classification of the types of microbes would identify whether the microbes are common for the deep subsurface or likely from surface contamination. If there was significant surface microbial contamination of the cores, then microbial growth results shown are not representative of subsurface conditions.

4.0 Geohydrologic Monitoring Considerations

A modeling study was conducted to determine whether pressure measurements from reservoir monitoring wells can be used to infer the spatial extent of $scCO_2$ during evolution of the $scCO_2$ plume. This monitoring concept relies on the fact that pressures measured in the injection wells and reservoir monitoring wells will tend to decrease (or increase less over time) as the plume of lower viscosity and density $scCO_2$ grows. At the same time, increasing $scCO_2$ saturations will increase the relative permeability of the injection zone formation materials across the region where $scCO_2$ is present. The resulting change in hydraulic conductivity may result in appreciable changes in hydraulic response during the periodic injection stoppage/restart operations associated with power plant maintenance outages. Any observed asymmetry in these pressure responses might also be used as a corroborative measure of asymmetrical CO_2 plume development.

The preliminary scoping-level modeling study described in this section uses a simplified hydrostratigraphic domain and structure to assess the impact of increasing $scCO_2$ plume size on pressure responses in the SLR monitoring wells at the FutureGen 2.0 site that result from annual power plant maintenance outages and associated pressure fall-off in the injection wells. The sections below include a literature review of studies that focused on CO_2 injection using horizontal well(s), a description of the FutureGen 2.0 reservoir response modeling evaluation framework, and results from this initial modeling effort.

4.1 Literature Review of Horizontal CO_2 Injection Well Simulation

A review of the scientific literature was conducted to identify studies that simulated CO_2 injection using one or more horizontal wells. Table 4.1 highlights 11 studies that matched these search criteria. These studies varied widely in research scope, leading to variations in hydrologic, operational, and time frame considerations for each paper. Almost all of the studies focused on optimizing CO_2 storage capacity in various geologic strata, enhancing hydrocarbon production through enhanced gas recovery or coal-bed methane production, or a combination of both. While each study had different research objectives, only four different types of numerical reservoir simulators were used: four studies used Schlumberger's ECLIPSE with its CO_2 module CO2STORE (Schlumberger 2010), three used Computer Modeling Group's (CMG's) GEM program (CMG 2009), three used Lawrence Berkeley National Laboratory's (LBNL) TOUGH2 with modules FLAC, REACT, and ECO2N (Pruess et al. 1999; Rutqvist and Tsang 2003; Pruess 2005; Xu et al. 2014), while the remaining paper used CODE_BRIGHT (Vilarrasa 2010a, b).

Most of the simulations examined regional-scale areas, from tens to thousands of square kilometers in area. Two studies specifically examined existing CCS project areas at In Salah, Algeria, and the offshore site near Sleipner, Norway; all other studies focused on generalized or site-specific (but not with an active CCS project) settings, such as German sedimentary basins or Wyoming coal seams. For grid spacing, five studies used uniform grid spacing for the study area, generally on the tens to hundreds of meters scale for grid block dimensions. Others used non-uniform grid spacing, with a higher refinement near the injection well, gradually coarsening toward model boundaries. Some of these grid refinements were calculated logarithmically while others were simply coarsened at specific spatial intervals. Discretization for studies that used non-uniform spacing ranged from 0.003 to 3.5 m at the injection well.

The reservoir depth studied was based on the stated research goals for each paper. For example, Dutta and Zoback (2012) focused on a production coal seam 290 m deep while conducting optimization studies for CO_2 injection and methane production. Reservoir depths in simulations that injected CO_2 into saline aquifers ranged from 700 to 3,000 m, while the remaining studies (focusing on enhancing hydrocarbon recovery) considered depth ranges from 420 to 2,438 m. Reservoir characteristics were model-specific; a majority of studies assigned deterministic values for different parameters. Three studies populated model porosity and permeability values based on sequential Gaussian simulations of log-normally distributed data (Cameron and Durlofsky 2012), or from well logs (Dutta and Zoback 2012; Pham et al. 2013).

Table 4.1. Overview of literature review results for CO_2 horizontal well injection simulations.

	Cameron and Durlofsky 2012	Jadhawar and Sarma 2012	Liu et al. 2013	Mitiku and Bauer 2013	Okwen et al. 2011
Simulator Name	ECLIPSE/CO2STORE	CMG GEM	CMG GEM	ECLIPSE/CO2STORE	TOUGH2 ECO2N
Simulator Type	Numerical reservoir simulator option in ECLIPSE	EOS compositional simulator	EOS compositional simulator	Numerical reservoir simulator option in ECLIPSE	Numerical non-isothermal, multicomponent simulator
Geographic and Geologic Setting	Generic (Saline Aquifer/Sandstone)	Generic (Oil Reservoir/Sandstone)	Illinois Basin, USA (New Albany Shale)	Northern Germany (Bunter Sandstone)	Generic (Saline Aquifer/Sandstone)
Model Area or Volume	11.58 km^3	15.29 km^3	0.009 km^3 (62 ac)	1,827 km^3	1,000 km^3
Grid Dimensions	39 × 39 × 8 (15 × 15 × 8 central portion with injection wells)	50 × 30 × 10	Logarithmically spaced, local grid refinement, dual-permeability	Not specified	65 × 65 × 10
Grid block size, m	434 × 434 × 12 (central portion)	182.88 × 121.92	Logarithmically increasing outwards from 0.003 at injection well	Vertical discretization: 3.5 (injection zone) to 500 (model boundaries). Horizontal discretization: 220 x 200 (within anticline area) to 1,100 x 500 (model boundaries)	Non-uniform discretization: Smaller size grid blocks closer to injection well, coarser far away from well
Top of Reservoir Depth, m	Not specified	2,438	420	3,000	1,200
Reservoir Porosity, %	23 (mean)	22	10-14	13	12
Reservoir Permeability	67 mD (median)	1,200 mD	150 nD	50 mD	1e-13 m^2
K_v/K_h	0.1	1	Not specified	0.1	0.001-0.5 (sensitivity studies)
Temperature, °C	40	137.22	30	94	45
Reservoir Pressure, MPa	17	16.2	Not specified	Not specified	12-13
Injection Rate	5 MMT/yr	5.48e8, 1.21e9 MMscf/yr	1.03e6 m^3/yr	1.185 MMT/yr	1.58e9 - 8.08e9 kg/yr
Injection Time Frame, years	30	130	5	50	50
Simulation Time Frame, years	1,000	130	30	1,000	50
Horizontal Well Length, km	1.304	Not specified	1.28	1.0, 2.2, 3.3, 10.12 (sensitivity studies)	1-4 (sensitivity studies)
# of Horizontal Wells	4 (sensitivity studies)	5-12 (sensitivity studies)	2	1-4 (sensitivity studies)	1
Well Spacing, km	Not specified	0.732 - 2.012 (sensitivity studies)	0.329	5-7.48 (sensitivity studies)	

Table 4.1. (contd)

	Pham et al. 2013	Dutta and Zoback 2012	Rutqvist et al. 2010	Vilarrasa 2014	Zhang et al.2011	Sobers et al. 2013
Simulator Name	ECLIPSE/CO2STORE	CMG GEM	TOUGH-FLAC	CODE_BRIGHT	TOUGHREACT	ECLIPSE
Simulator Type	Numerical reservoir simulator option in ECLIPSE	EOS compositional simulator	LBNL numerical geomechanical simulator	Finite element numerical code	Reactive transport numerical simulator	Numerical reservoir simulator
Geographic and Geologic Setting	Offshore Norway (Utsira/Skade Sandstones)	Campbell County, WY (Wyodak Coal Seam)	In Salah, Algeria (Sandstone)	Generic (Saline Aquifer/Sandstone)	Generic (Carbonate Formation)	Trinidad and Tobago (Sandstone)
Model Area or Volume	1,600 km^2 (with log-based varying depths)	23.09 km^2 (with log-based varying depths)	400 km^3	36 km^2	7.47 km^3	0.09 km^2
Grid Dimensions	Not specified	48 × 48	Not specified	Not specified	20 × 20 × 19	100 × 30 × 50
Grid Block Size, m	500 × 500 and 200 × 200 (separate simulations)	100 × 100	Finer toward injection wells, coarsens at further distances	Horizontal: 0.1 to 400 from injection well to model boundaries. Vertical: 5 to 25 from injection zone toward model boundaries	300 × 415 × 8	10 × 3 × 2
Top of Reservoir Depth, m	700 to 900	260	1,810	1,500	Not specified	1,238
Reservoir Porosity, %	30-35 (Generated from logs)	Gaussian geostatistical gridding	15-20	10	18	26
Reservoir Permeability	Generated from logs	Gaussian geostatistical gridding	1.3e-14 m^2	1e-13 m^2	25 mD	525 mD
K_v/K_h	0.01, 0.1	Not specified	Not specified	Not specified	Not specified	0.1
Temperature, °C	37	Not specified	90	54.5	102	81.7
Reservoir Pressure, MPa	8.5	1.825	17.9	34.5	22.5	27.4
Injection Rate	From 7 MMT/yr to 1 MMT/yr over 50 years	0.737 million tons/yr	5,475 MMscf/yr	2 MMT/yr	6.31e8 kg/yr	1.83e7 m^3/yr (2.2e5 total tonnes)
Injection Time Frame, years	50	20	3	20	1	
Simulation Time Frame, years	8,000	20	3	20	1	
Horizontal Well Length, km	Not specified	0.6	Not specified	1-8 (sensitivity studies)	0.5	<0.15
# of Horizontal Wells	1-5 (sensitivity studies)	1	3	1	1	2

Injection time frames varied greatly for the studies, depending on research goals, and overall simulation times ranged from 1 to 8,000 years. For example, Zhang et al. (2011) modeled 1 year of CO_2 injection in a carbonate reservoir to determine near-well, short-term effects of geochemical reactions. Other models focused on a set period of injection (20−50 years), coupled with a period without injection to allow for injected CO_2 equilibration. For injection rates, units used to quantify the injection rate per year were million metric tons (MMT), million tons, kilograms (kg), cubic meters (m^3), and million standard cubic feet (Mscf). Two studies (Dutta and Zoback 2012; Sobers et al. 2013) sought to quantify the maximum injection rate based on their simulation times and did not have a pre-defined set injection rate, resulting in rates that equated to 0.737 million tons/year and 1.87e7 m^3/yr, respectively.

The horizontal well lengths and number of wells also varied based on goals of the respective study. Three studies focused on varying well lengths as a means of optimizing CO_2 injection, while the remaining studies featured well lengths less than 0.6 km, or at or near 1.3 km. Four studies varied well number and position either through numerical optimization or pre-assigned sensitivity scenarios, while the remaining studies used a fixed number of horizontal wells.

4.2 Preliminary Reservoir Response Model Description

The numerical model being applied in this analysis is the STOMP-CO_2 simulator (White et al. 2012). A simplified domain and hydrostratigraphic structure was developed as a rough approximation of the site for these initial simulations to help identify important processes and potential responses from the $scCO_2$ injection. These simplifications allow the use of relatively fine grid spacing but with shorter run times. The model domain used a 1/4 symmetry approach (see Figure 4.1) with a horizontal injection well along the diagonal (x = y) to roughly approximate one of the four injection wells at the FutureGen 2.0 site (similar to reduced-domain studies of five-spot problems). The model simulates one of the short horizontal wells (northeast or northwest quadrant), which was chosen because of the proximity of these laterals to the SLR monitoring wells.

Construction of this numerical model used the following data sources and assumptions:

- Constant thicknesses were specified for each layer based on the model used in the UIC permit application (Alliance 2013, Table 3.8), but ignores the slight dipping structure at the site. A truncated vertical domain (bottom of Mount Simon to top of the Lombard Member of the Eau Claire) was used.
- Some high permeability layers in the model used in the UIC permit application, including the injection layer and a few high permeability layers above and below the injection layer, have also been subdivided in thinner layers but with the same properties.
- Layer properties for permeability and porosity are the same as the model used in the UIC permit application (Alliance 2013, Table 3.8), but the Brooks and Corey relative saturation parameters for $scCO_2$ and brine are based on analysis of the CoreLabs Mercury Injection data (Rockhold et al. 2014).
- The CO_2 mass injection rate from the model used in the UIC permit application was scaled to an annual cycle of 0.9 years of injection followed by 0.1 year shut-in for 10 years (i.e., 110% of the rate during 0.9 years) to maintain same annual mass.
- No injection occurs in the vertical or curved portions of the well. The 1,500-ft length of the horizontal perforated portion of the well, starting at a 330-ft radius from centroid of injection well

heads to 1,830-ft radius, was implemented using the STOMP-CO_2 Coupled Well model (White et al. 2012).

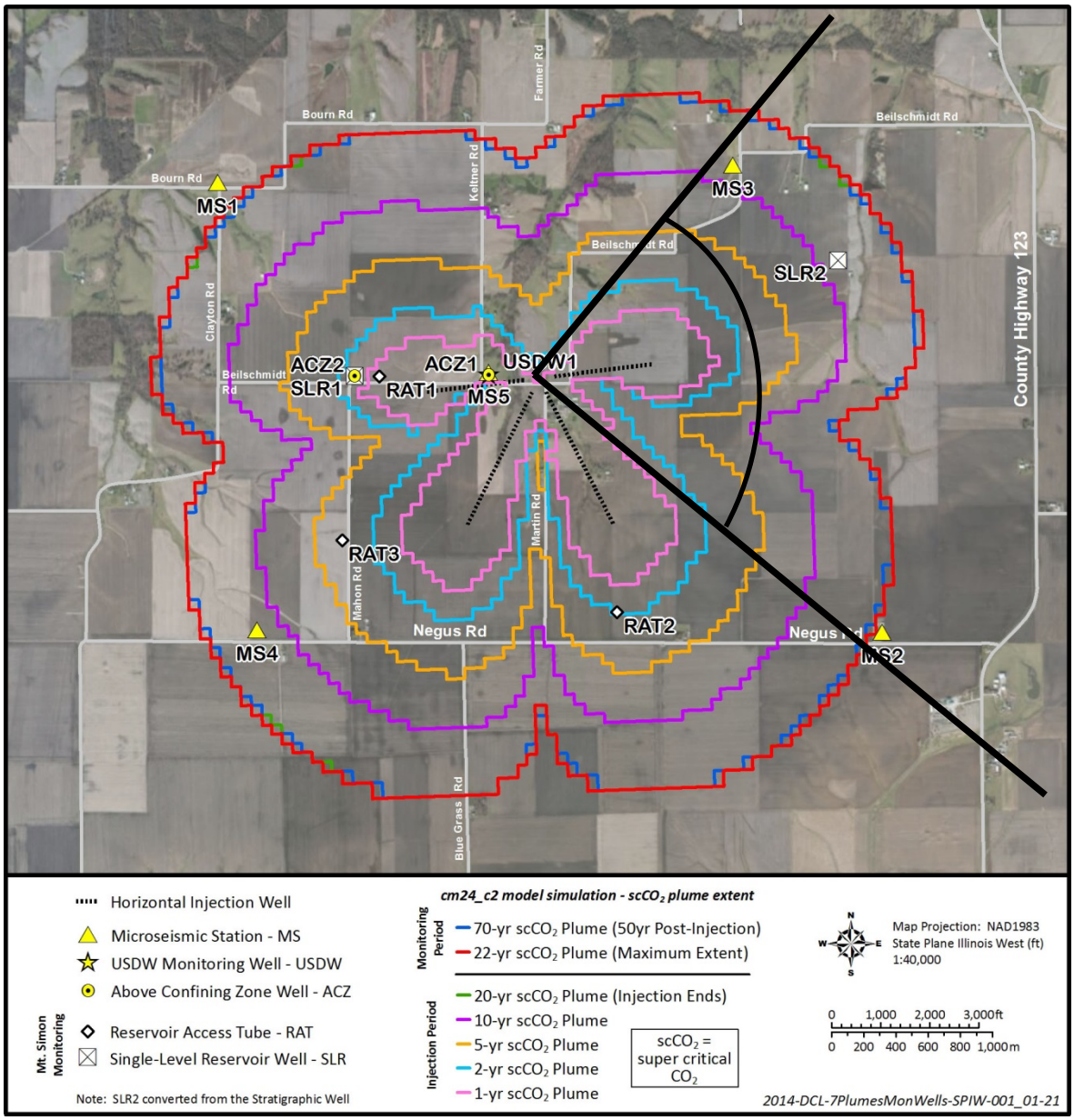

Figure 4.1. Schematic diagram showing 1/4 model symmetry domain approximation (heavy black lines).

4.2.1 Model Grid

Model units are in feet. X and Y coordinates are relative to (0,0) at the origin (i.e., the centroid of the injection wells). Z coordinates are increasing upwards, and the bottom of the Mount Simon Sandstone layer (4,418 ft bgs) has a Z-coordinate of 0.0.

Scoping simulations were conducted to determine the X and Y grid spacing around the horizontal well. These tests included 200-ft, 50-ft, 30-ft, and 20-ft X and Y grid spacing extending from the origin

of the domain to slightly past the horizontal well terminus. Additional simulations were conducted to vertically subdivide the permeable layers around the injection well. Results of these tests are described in Section 4.3.1. A 30-ft x 30-ft grid was selected around the injection well, with vertical subdivision of the permeable layers around the injection well based on the grid spacing tests. The model grid constructed for these initial scoping simulations (see Figure 4.2 and Figure 4.3), has 99 X nodes, 99 Y nodes, and 43 Z nodes (421,443 total nodes) with variable X and Y grid spacing (using an increasing scheme to give a total length of 195,000 ft). Figure 4.3 shows the X and Y grid spacing, as follows:

- 30 ft spacing for 1,500 ft
- 50 ft spacing for 1,000 ft
- 100 ft spacing for 500 ft
- 200 ft spacing for 3,000 ft
- 500 ft spacing for 1,000 ft (not shown in Figure 4.2 and Figure 4.3)
- Five additional nodes (also not shown in Figures 4.2 and 4.3) of increasing spacing to extend the domain to its full extent (1,000-, 2,000-, 5,000-, 10,000-, 20,000-, 50,000-, and 100,000-ft spacing).

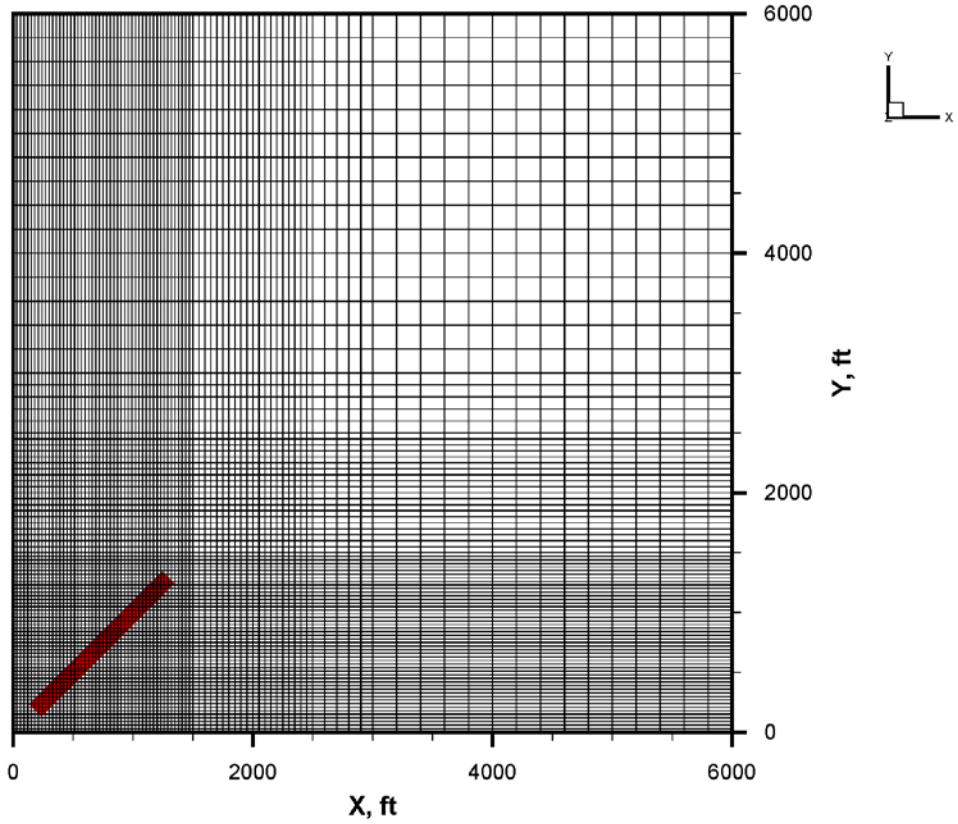

Figure 4.2. Plan view of the preliminary reservoir response model grid geometry in the X and Y directions showing the injection well perforated zone in red. Note: The last seven nodes in the X and Y directions are not here so that the grid refinement near the injection well is visible. The injection well width is not to scale.

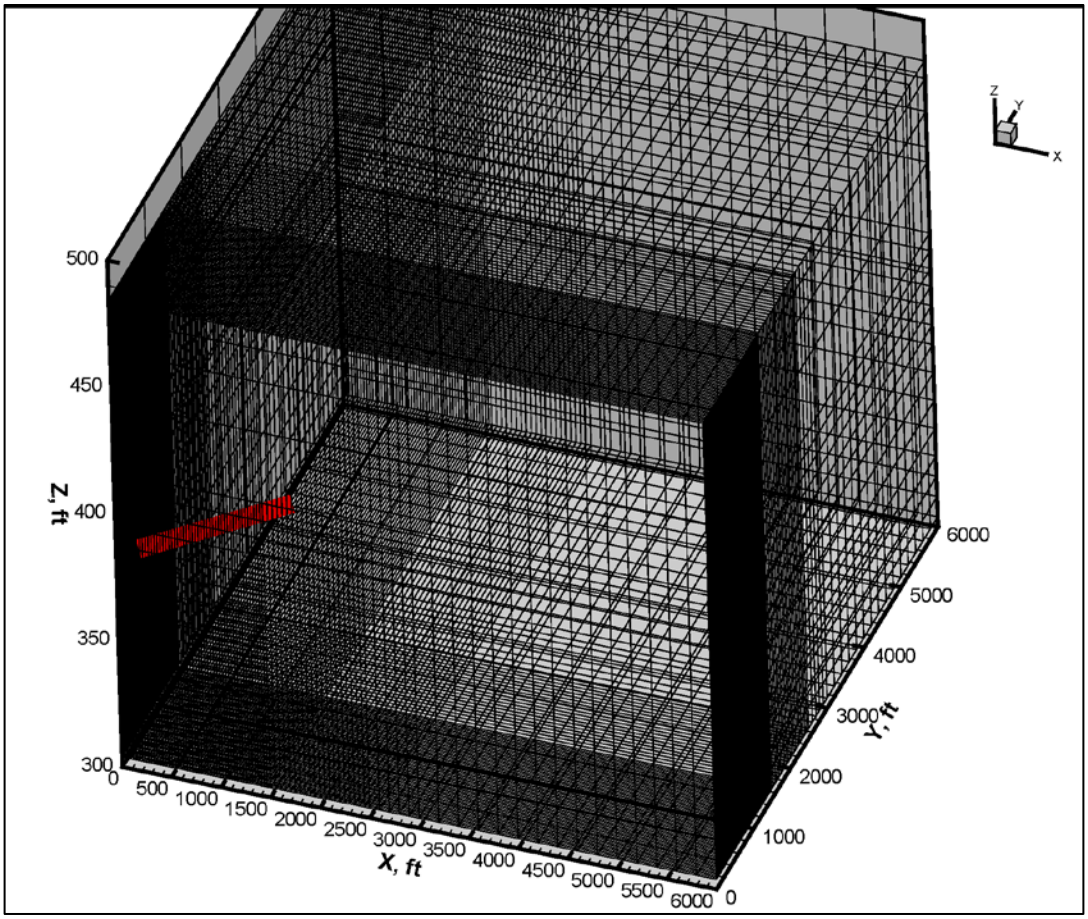

Figure 4.3. Perspective view of the preliminary reservoir response model grid geometry for the X-, Y- and Z-directions showing the injection well perforated zone in red. Note: The last seven nodes in the X- and Y- directions are not here so that the grid refinement near the injection well is visible. The injection well width is not to scale.

The Z-direction grid spacing for the model is based on the layering in the model used in the UIC permit application shown in Table 4.2 (from Alliance 2013, Table 3.8), and extends from the bottom of the Mount Simon unit to the top of Lombard member of the Eau Claire unit. The total thickness is 839 ft, as shown in Figure 4.4. The high permeability layers near the injection interval were subdivided as follows (with layer designations fromTable 4.2):

- Mount Simon 8: 8−ft layers (3)
- Mount Simon 9: 11−ft layers (2) – only used 2 layers because properties are the same as Mount Simon 10
- Mount Simon 10: 11−ft layers (2)
- Mount Simon 11: 7.7−ft layers (3) (injection zone)
- Mount Simon 12: 7−ft layers (3).

In addition, some adjacent layers away from the injection interval were lumped together for this initial scoping-level simulation to reduce the number of nodes:

- Mount Simon 1 and 2
- Mount Simon 4 and 5
- Lombard 12 and 13.

The final layering is shown on the STOMP grid in Figure 4.5. The layer numbers differ slightly from Figure 4.4 and Table 4.2 because of the combining of layers, as discussed above.

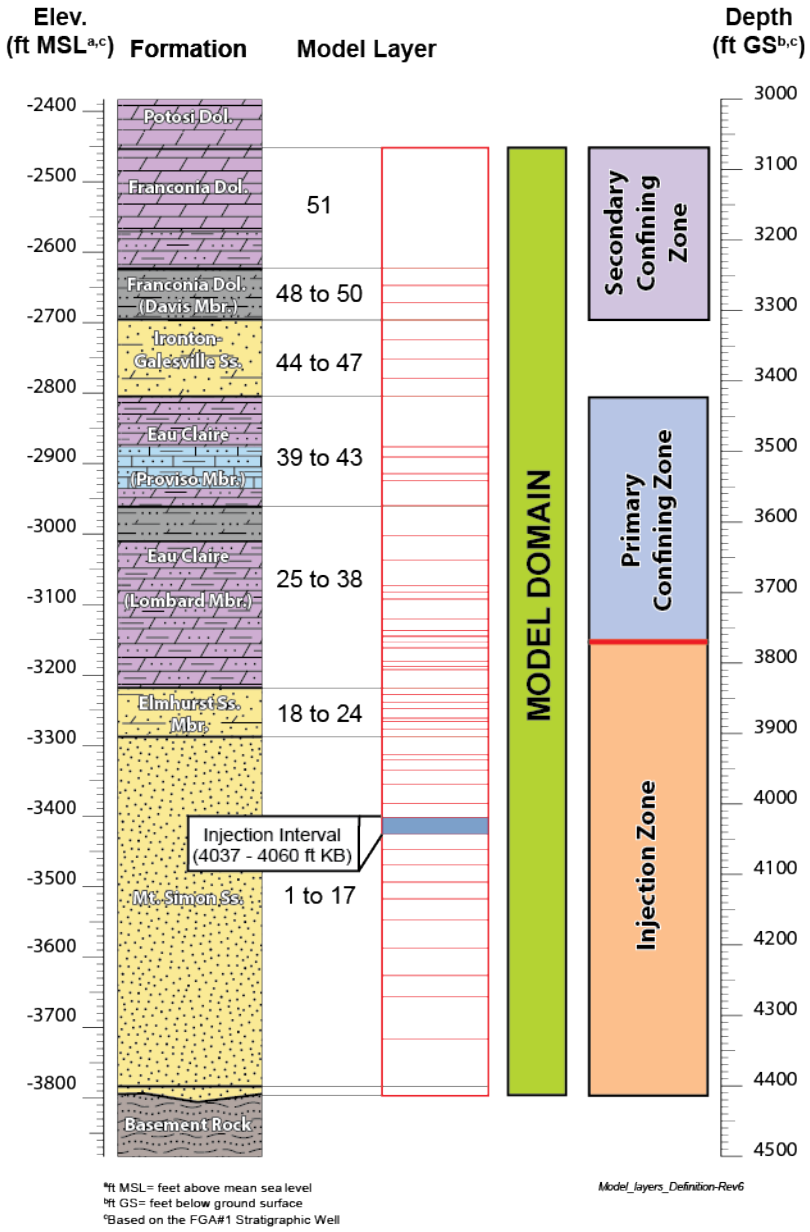

Figure 4.4. Division of stratigraphic layers and layering in the model used in the UIC permit application (modified from Alliance 2013).

Table 4.2. Summary of the hydrologic properties assigned to each layer used in the model for the UIC permit application (from Alliance 2013, Table 3.8).

	Model Layer	Top Depth (ft bkb)	Top Elevation (ft)	Bottom Elevation (ft)	Thickness (ft)	Porosity	Horizontal Permeability (mD)	Vertical Permeability (mD)	Grain Density (g/cm3)	Compressibility (1/Pa)
Primary Conf. Zone	Franconia	3086.00	-2453	-2625	172	0.0358	5.50E-06	3.85E-08	2.82	7.42E-10
	Davis-Ironton3	3258.00	-2625	-2649	24	0.0367	6.26E-02	6.26E-03	2.73	3.71E-10
	Davis-Ironton2	3282.00	-2649	-2673	24	0.0367	6.26E-02	6.26E-03	2.73	3.71E-10
	Davis-Ironton1	3306.00	-2673	-2697	24	0.0218	1.25E+01	1.25E+00	2.73	3.71E-10
	Ironton-Galesville4	3330.00	-2697	-2725	28	0.0981	2.63E+01	1.05E+01	2.66	3.71E-10
	Ironton-Galesville3	3358.00	-2725	-2752	27	0.0981	2.63E+01	1.05E+01	2.66	3.71E-10
	Ironton-Galesville2	3385.00	-2752	-2779	27	0.0981	2.63E+01	1.05E+01	2.66	3.71E-10
	Ironton-Galesville1	3412.00	-2779	-2806	27	0.0981	2.63E+01	1.05E+01	2.66	3.71E-10
Primary Confining Zone	Proviso5	3439.00	-2806	-2877	71	0.0972	1.12E-03	1.12E-04	2.72	7.42E-10
	Proviso4	3510.00	-2877	-2891	14	0.0786	5.50E-03	5.50E-04	2.72	7.42E-10
	Proviso3	3524.00	-2891	-2916	25	0.0745	8.18E-02	5.73E-04	2.77	7.42E-10
	Proviso2	3548.50	-2916	-2926	10	0.0431	1.08E-01	7.56E-04	2.77	7.42E-10
	Proviso1	3558.50	-2926	-2963	38	0.0361	6.46E-04	4.52E-06	2.77	7.42E-10
	Lombard14	3596.00	-2963	-3003	40	0.1754	5.26E-04	5.26E-05	2.68	7.42E-10
	Lombard13	3636.00	-3003	-3038	35	0.0638	1.53E-01	1.53E-02	2.68	7.42E-10
	Lombard12	3671.00	-3038	-3073	35	0.0638	1.53E-01	1.53E-02	2.68	7.42E-10
	Lombard11	3706.00	-3073	-3084	11	0.0878	9.91E+00	9.91E-01	2.68	7.42E-10
	Lombard10	3717.00	-3084	-3094	10	0.0851	1.66E+01	1.66E+00	2.68	7.42E-10
	Lombard9	3727.00	-3094	-3121	27	0.0721	1.00E-02	1.00E-03	2.68	7.42E-10
	Lombard8	3753.50	-3121	-3138	17	0.0663	2.13E-01	2.13E-02	2.68	7.42E-10
	Lombard7	3770.50	-3138	-3145	8	0.0859	7.05E+01	7.05E+00	2.68	7.42E-10
	Lombard6	3778.00	-3145	-3153	8	0.0459	1.31E+01	1.31E+00	2.68	7.42E-10
	Lombard5	3785.50	-3153	-3161	9	0.0760	4.24E+02	4.24E+01	2.68	7.42E-10
	Lombard4	3794.00	-3161	-3181	20	0.0604	3.56E-02	3.56E-03	2.68	7.42E-10
	Lombard3	3814.00	-3181	-3189	8	0.0799	5.19E+00	5.19E-01	2.68	7.42E-10
	Lombard2	3821.50	-3189	-3194	5	0.0631	5.71E-01	5.71E-02	2.68	7.42E-10
	Lombard1	3826.50	-3194	-3219	26	0.0900	1.77E+00	1.77E-01	2.68	7.42E-10

Table 4.2. (contd)

	Model Layer	Top Depth (ft bkb)	Top Elevation (ft)	Bottom Elevation (ft)	Thickness (ft)	Porosity	Horizontal Permeability (mD)	Vertical Permeability (mD)	Grain Density (g/cm3)	Compressibility (1/Pa)
Injection Zone	Elmhurst7	3852.00	-3219	-3229	10	0.1595	2.04E+01	8.17E+00	2.64	3.71E-10
	Elmhurst6	3862.00	-3229	-3239	10	0.1981	1.84E+02	7.38E+01	2.64	3.71E-10
	Elmhurst5	3872.00	-3239	-3249	10	0.0822	1.87E+00	1.87E-01	2.64	3.71E-10
	Elmhurst4	3882.00	-3249	-3263	14	0.1105	4.97E+00	1.99E+00	2.64	3.71E-10
	Elmhurst3	3896.00	-3263	-3267	4	0.0768	7.52E-01	7.52E-02	2.64	3.71E-10
	Elmhurst2	3900.00	-3267	-3277	10	0.1291	1.63E+01	6.53E+00	2.64	3.71E-10
	Elmhurst1	3910.00	-3277	-3289	12	0.0830	2.90E-01	2.90E-02	2.64	3.71E-10
	MtSimon17	3922.00	-3289	-3315	26	0.1297	7.26E+00	2.91E+00	2.65	3.71E-10
	MtSimon16	3948.00	-3315	-3322	7	0.1084	3.78E-01	3.78E-02	2.65	3.71E-10
	MtSimon15	3955.00	-3322	-3335	13	0.1276	5.08E+00	2.03E+00	2.65	3.71E-10
	MtSimon14	3968.00	-3335	-3355	20	0.1082	1.33E+00	5.33E-01	2.65	3.71E-10
	MtSimon13	3988.00	-3355	-3383	28	0.1278	5.33E+00	2.13E+00	2.65	3.71E-10
	MtSimon12	4016.00	-3383	-3404	21	0.1473	1.59E+01	6.34E+00	2.65	3.71E-10
	MtSimon11 *(injection Interval)*	4037.00	-3404	-3427	23	0.2042	3.10E+02	1.55E+02	2.65	3.71E-10
	MtSimon10	4060.00	-3427	-3449	22	0.1434	1.39E+01	4.18E+00	2.65	3.71E-10
	MtSimon9	4082.00	-3449	-3471	22	0.1434	1.39E+01	4.18E+00	2.65	3.71E-10
	MtSimon8	4104.00	-3471	-3495	24	0.1503	2.10E+01	6.29E+00	2.65	3.71E-10
	MtSimon7	4128.00	-3495	-3518	23	0.1311	6.51E+00	1.95E+00	2.65	3.71E-10
	MtSimon6	4151.00	-3518	-3549	31	0.1052	2.26E+00	6.78E-01	2.65	3.71E-10
	MtSimon5	4182.00	-3549	-3588	39	0.1105	4.83E-02	4.83E-03	2.65	3.71E-10
	MtSimon4	4221.00	-3588	-3627	39	0.1105	4.83E-02	4.83E-03	2.65	3.71E-10
	MtSimon3	4260.00	-3627	-3657	30	0.1727	1.25E+01	1.25E+00	2.65	3.71E-10
	MtSimon2	4290.00	-3657	-3717	60	0.1157	2.87E+00	2.87E-01	2.65	3.71E-10
	MtSimon1	4350.00	-3717	-3799	82	0.1157	2.87E+00	2.87E-01	2.65	3.71E-10

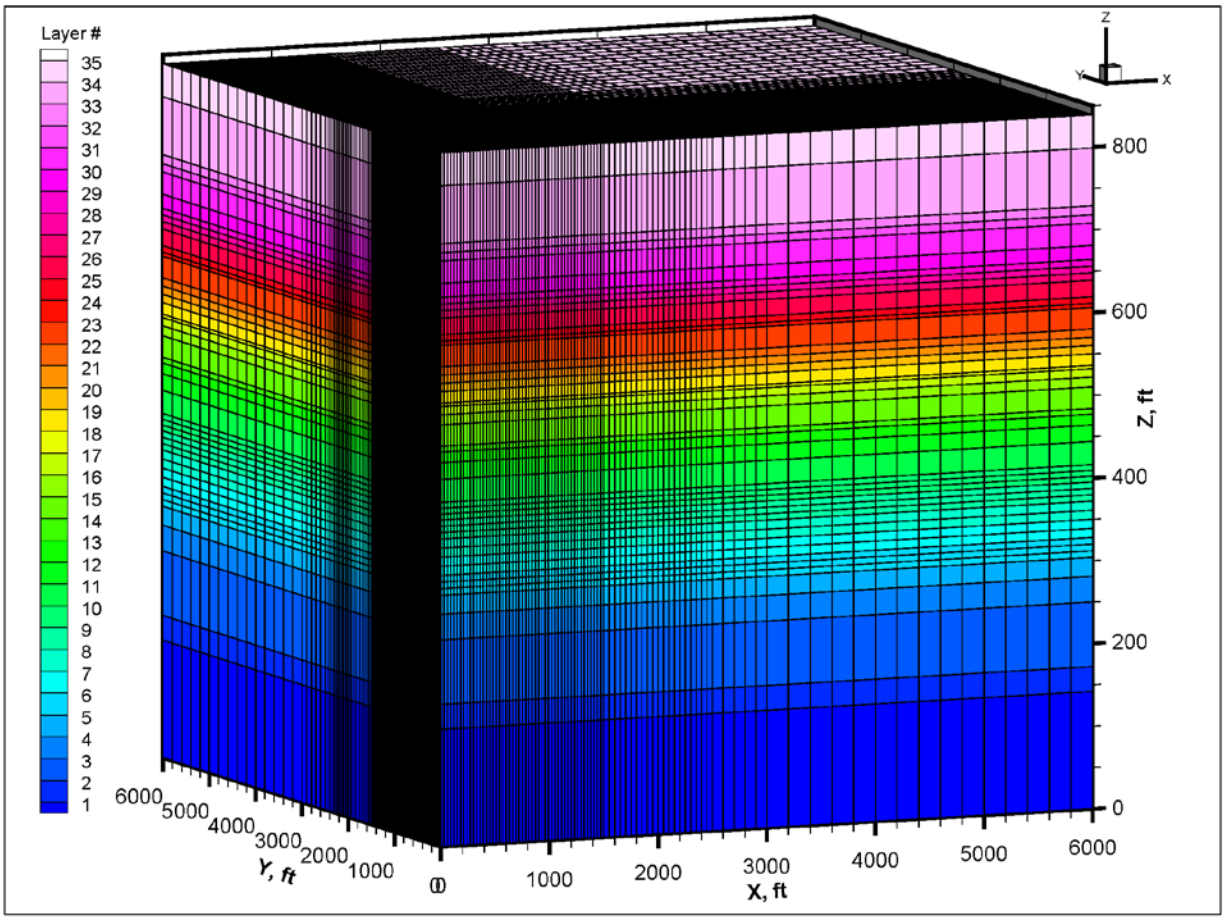

Figure 4.5. Three-dimensional model domain and layer numbers for the preliminary reservoir response model. Note: The last seven nodes in the X- and Y- directions are not here so that the grid refinement near the injection well is visible.

4.2.2 Initial and Boundary Conditions

The STOMP-CO2 simulator calculated initial hydrostatic pressure conditions for the domain based on the following conditions:

- specified pressure at a single vertical location: 1,790.2 psi at Z = 383.5 ft (middle of injection interval)
- temperature: 96.6°F at Z = 510 ft (top of Mount Simon), Z gradient: -0.00672°F/ft
- specified salt mass fraction (constant): 0.0475.

This is the same approach and parameter values for specifying the initial conditions that were applied for the model used in the UIC permit application (Alliance 2013).

The boundary conditions are as follows:

- No-Flow at the bottom of the domain (Z=0) (i.e., the bottom of the Mount Simon unit)

- No-Flow on the Y=0 Vertical Plane
- No-Flow on the X=0 Vertical Plane
- Constant Head at Initial Conditions at the $X=X_{max}$ Vertical Plane
- Constant Head at Initial Conditions at the $Y=Y_{max}$ Vertical Plane
- ($Z=Z_{max}$) Horizontal Plane: No-flow boundary. Note: Also ran a case with a Dirichlet boundary at Initial Conditions during grid space testing and results were similar to the no-flow boundary.

4.3 Preliminary Reservoir Response Simulation Results

4.3.1 Grid Spacing Tests

Grid spacing test simulations were conducted for XY node spacing in the vicinity of the injection well (ranging from 200 ft to 20 ft from the injection well). Selected tests also investigated vertical refinement, as discussed in Section 4.2.1, and the variation in the saturation/relative permeability parameters from the values used in the UIC permit application modeling.

Results of the different grid spacing tests are shown in Figure 4.6 for the simulated injection well pressure buildup and Figure 4.7 for the $scCO_2$ saturations near the end of the injection well. As discussed below, both pressure and $scCO_2$ saturation need to be considered when interpreting changes in simulated responses related to grid spacing.

Pressure buildup for the 50-ft node spacing case was higher than the 200-ft node spacing case because of the smaller nodal volumes along the well. However, these increases in pressure are smaller than they would be otherwise because higher near-well $scCO_2$ saturations in the 50-ft case cause increases in $scCO_2$ relative permeability. The 50-ft case that included vertical refinement in the injection interval (further decreasing the nodal volumes) had even higher $scCO_2$ saturations and the injection pressure was lower than for the 200-ft case. The 30-ft XY node spacing case with vertical refinement continued this trend of higher $scCO_2$ saturations and lower injection well pressures.

Two other cases were simulated using alternative saturation/relative permeability parameters that differed from those used in the UIC permit application and were derived from mercury injection measurements on cores obtained from the initial stratigraphic borehole (Rockhold et al. 2014). Not all the layers had core samples, so the properties were selected from the closest cores based on permeability and porosity measurements. Comparing the results of the two 30-ft XY grid spacing cases, the alternative saturation/relative permeability parameters resulted in slight lower simulated saturations and higher well pressures.

A 20-ft XY grid spacing case incorporating the alternative saturation/relative permeability parameters was also run to evaluate the adequacy of the 30-ft grid spacing case. This simulation was only run for 5 years. The simulated injection pressures were very similar between the 30-ft and 20-ft cases, as shown in Figure 4.6. The $scCO_2$ saturations were initially higher for the 20-ft case, but became close to those for the 30-ft case after about 4 years as shown in Figure 4.7.

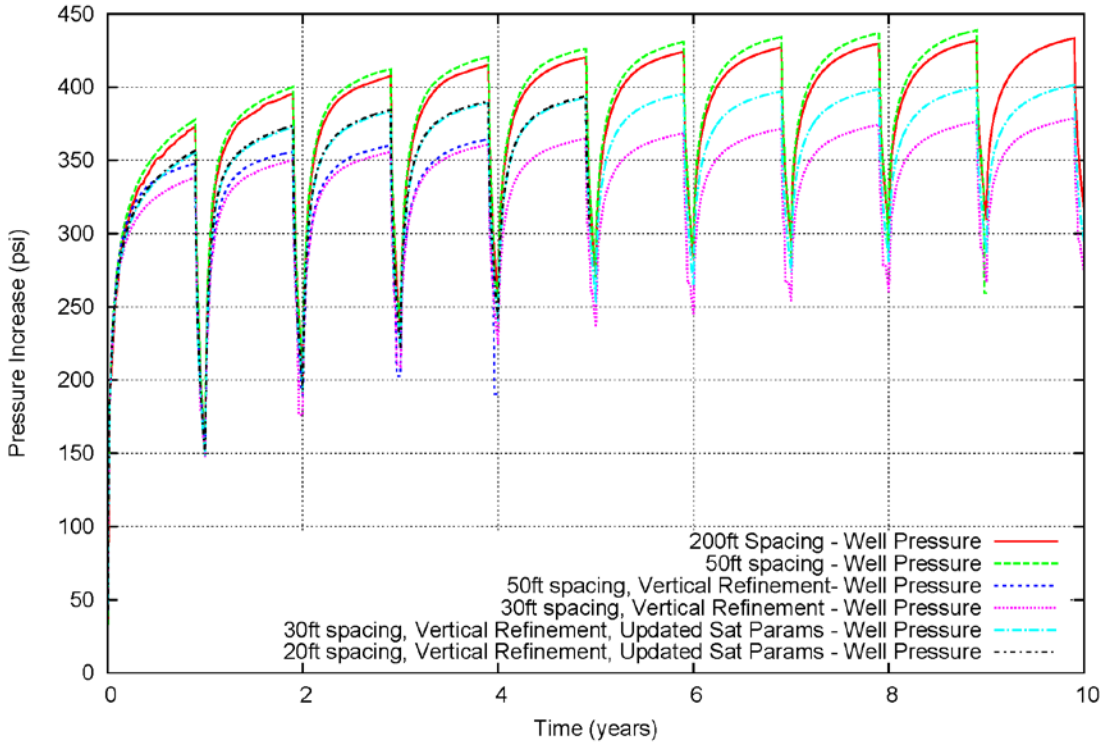

Figure 4.6. Comparison of simulated injection well pressure buildup response for models using different grid spacing.

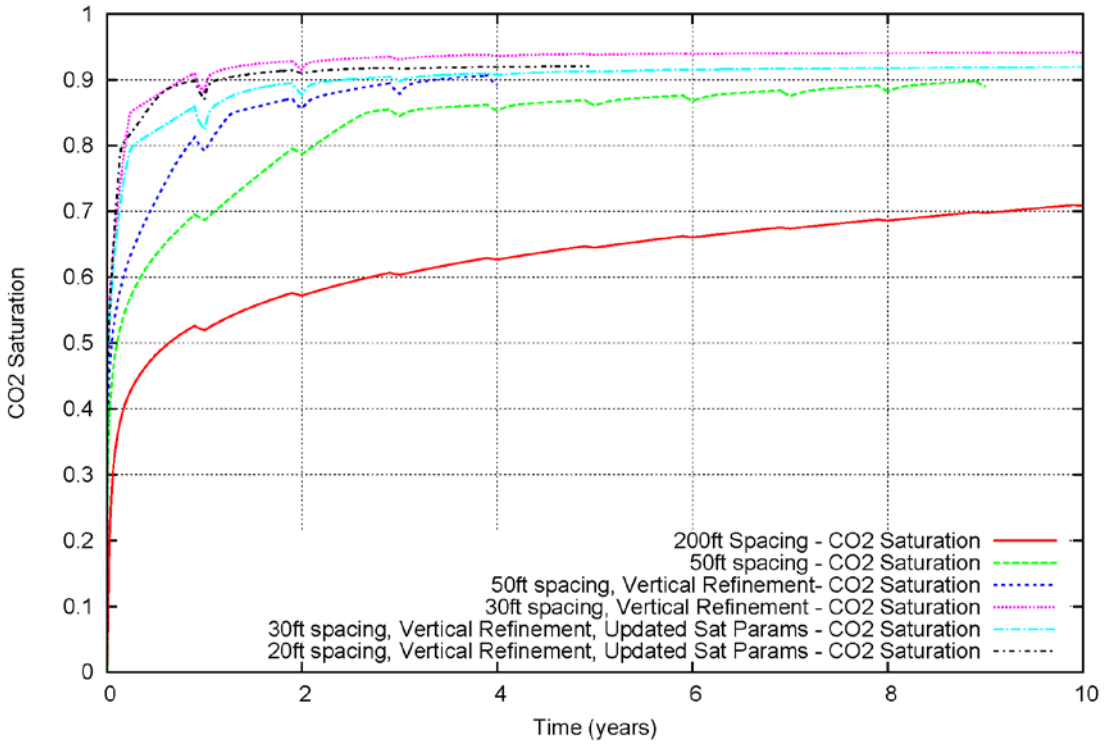

Figure 4.7. Comparison of $scCO_2$ saturations for models using different grid spacing. Nodes selected for comparison were near the end of the injection well.

4.3.2 Simulation Results

Based on the results of the grid testing discussed above, the 30-ft XY grid spacing case with vertical refinement and updated saturation/relative permeability parameters (as discussed in Section 4.3.1) was selected as the nominal case for use in this preliminary modeling evaluation. The 30-ft XY grid spacing case had similar well pressure responses and only slightly lower initial $scCO_2$ saturations than the 20-ft XY grid spacing case, but with much faster runtimes.

4.3.2.1 Simulated Pressure

Figure 4.8 shows the simulated pressure buildups for the injection well and at two distances from the domain origin to represent the distances to SLR#1 (3,610 ft) for the northwest horizontal well section and SLR#2 (6,580 ft) for the northeast horizontal well section. Both aqueous and $scCO_2$ pressures are plotted, and the results are similar because the simulated free-phase $scCO_2$ did not arrive at these locations for the 10-year duration of this simulation. The simulated pressures in Figure 4.8 (and in Figure 4.9, which shows the same data but only includes the SLR wells) show the responses with the peaks and troughs, representing the annual cycle of 0.9 years of injection and 0.1 years of shut-in. The peak responses over this time period show initial increases in the magnitude of pressure during each cycle; however, the increases get smaller for each cycle. In addition, the amplitudes (i.e., difference between peak and trough) get smaller for each cycle.

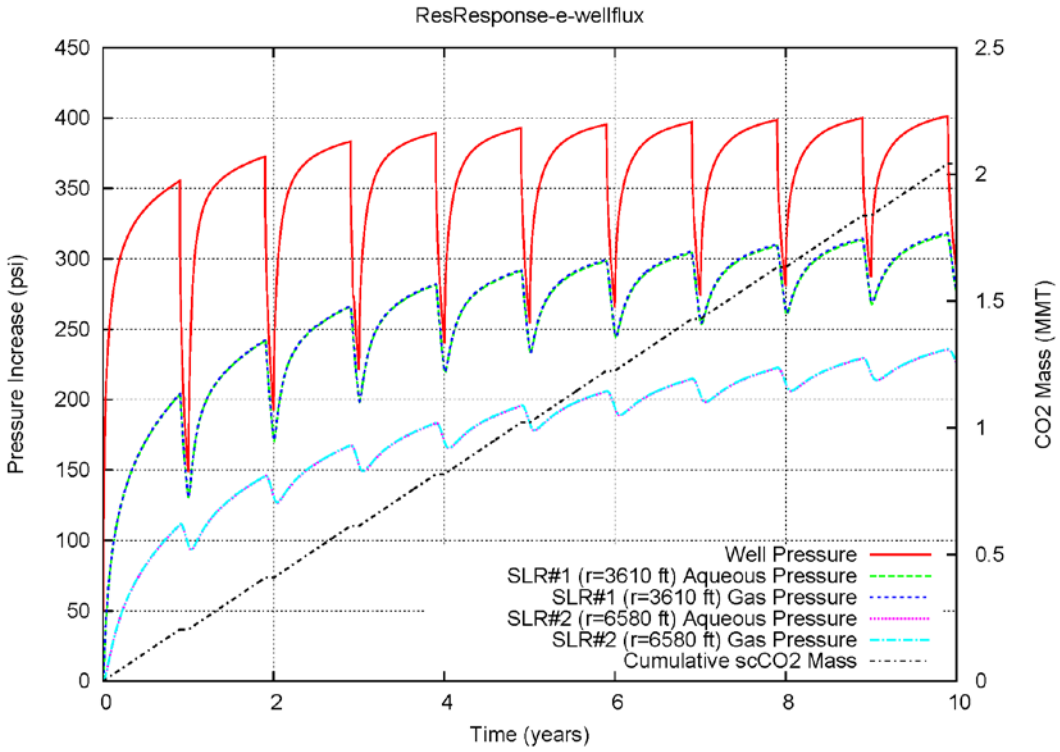

Figure 4.8. Simulated pressures for the nominal case for the injection well and SLR wells. Also shown (on the secondary Y-axis) is the cumulative injected $scCO_2$ mass.

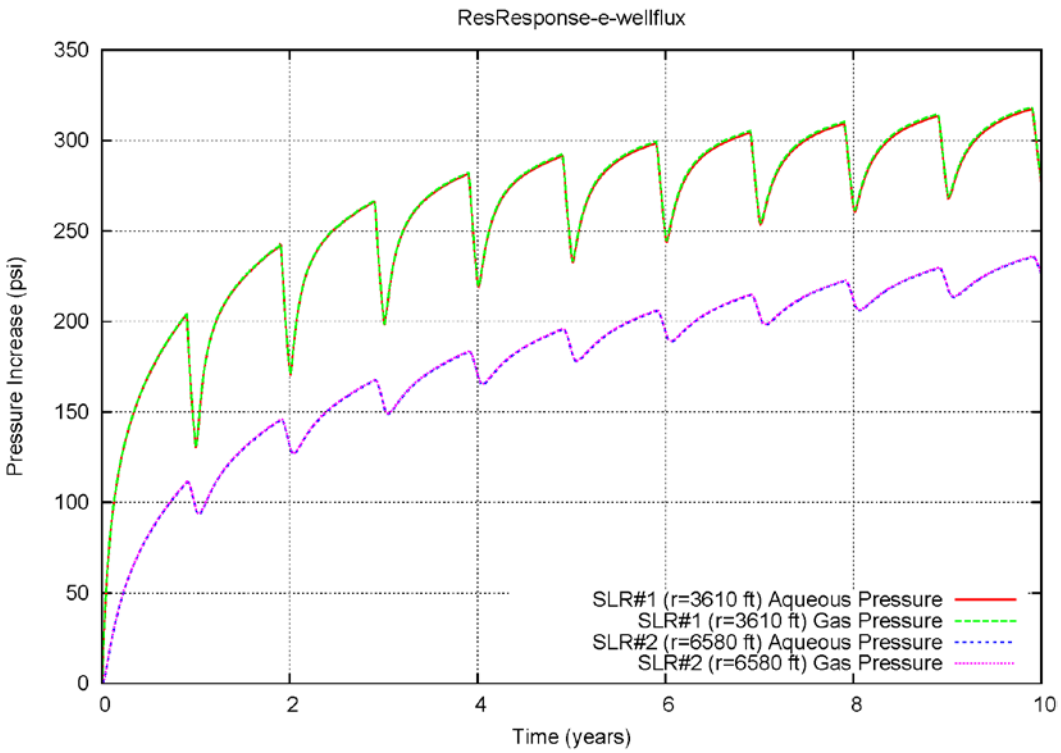

Figure 4.9. Simulated pressures for the nominal case for the SLR wells.

4.3.2.2 $scCO_2$ Saturations and Flow Field

Figure 4.10 shows the development of $scCO_2$ saturations during the simulation period. Iso-surfaces of $scCO_2$ saturations at selected values are shown for 0.9, 4.9, and 9.9 years. These iso-surfaces are sliced along the X = Y plane to show the interior of the plume (the plumes are symmetrical along this plane). The injection well is at an elevation of 383 ft, which corresponds to the maximum radial extent of the iso-surfaces and the highest $scCO_2$ saturations. The plume also spreads out vertically with the maximum vertical extent near the toe-end of the horizontal injection well, and extends higher above the well than below due to buoyancy and the greater permeabilities in the upper part of the Mount Simon unit. The $scCO_2$ plumes are also shown for these time periods as contoured values for horizontal slices taken at three vertical positions in Figure 4.11. The vertical positions are at elevations of 313 ft, 383 ft (i.e., at the injection well Z value), and 453 ft. Figure 4.11 more closely shows the difference between the vertical spreading because the plane above and below the injection well plane are the same distance. These plots show that the $scCO_2$ saturations exceed 0.8 along the injection well for this case (also see Figure 4.7).

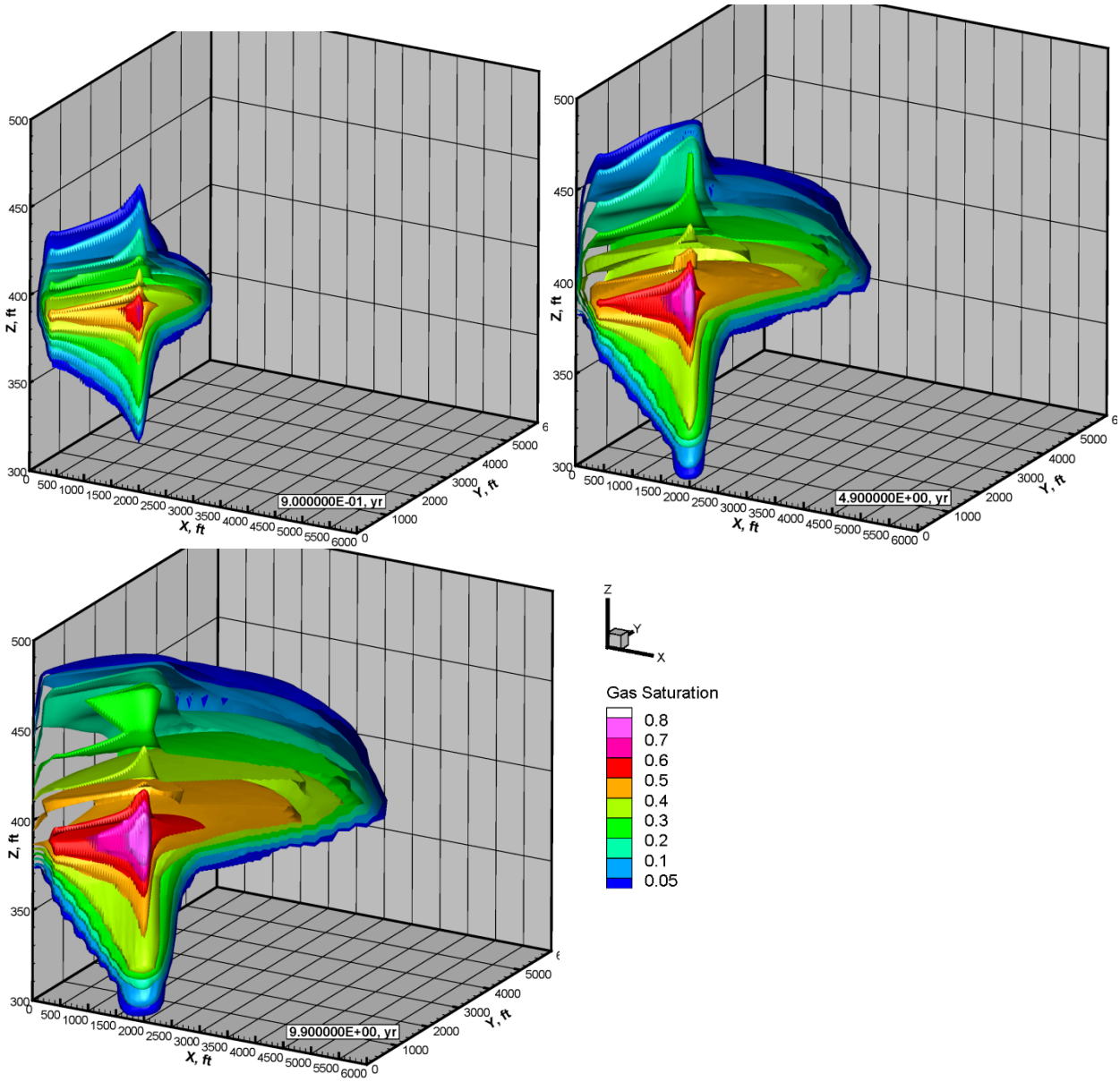

Figure 4.10. Simulated $scCO_2$ saturation iso-surfaces at three separate time periods: 0.9, 4.9, and 9.9 years. Iso-surfaces are blanked in front of the Z plane along the X=Y coordinates for visualization of the interior (symmetrical).

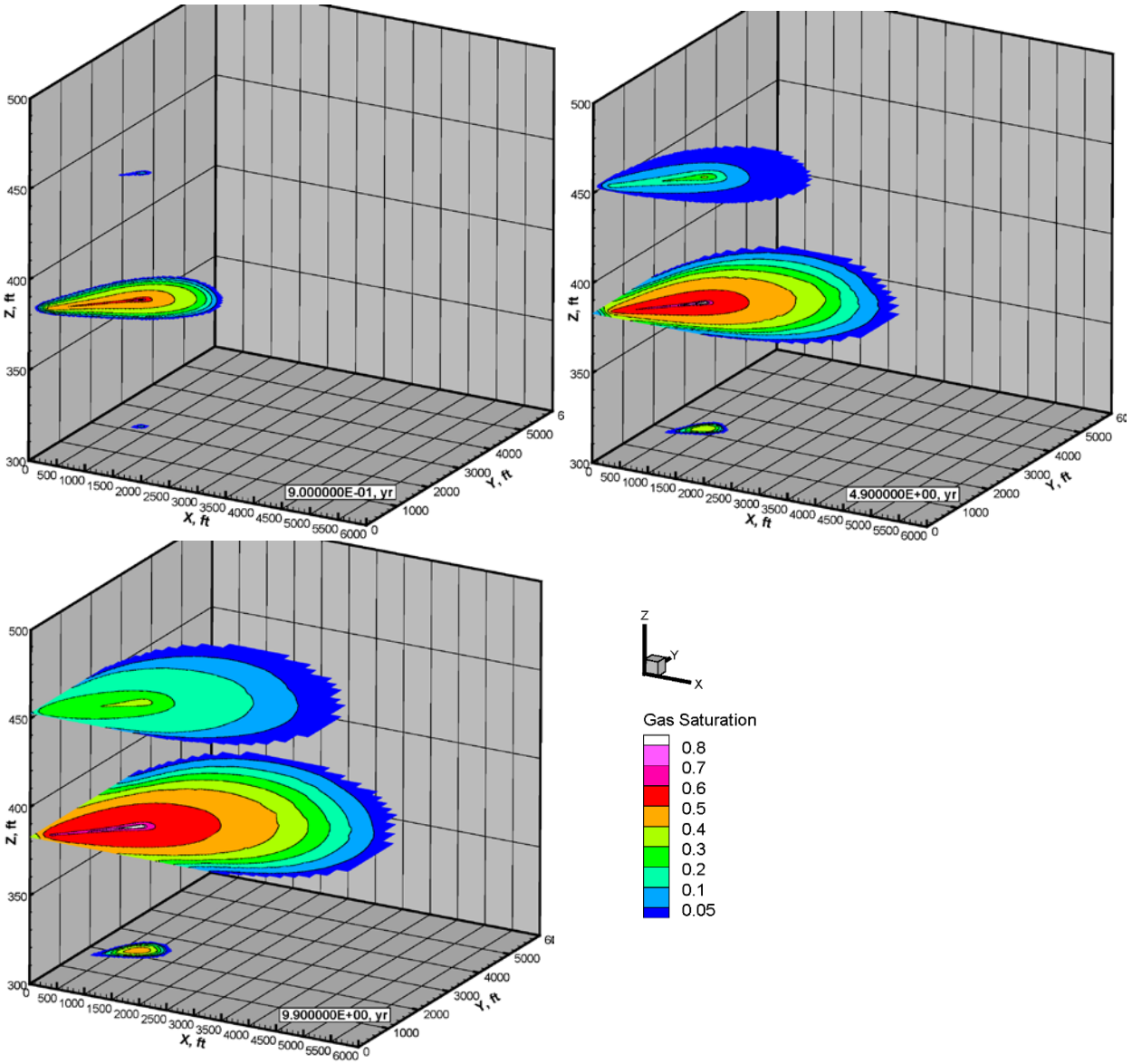

Figure 4.11. Simulated $scCO_2$ saturation contour plots at three different Z planes (Z = 313, 383, and 353 ft) for three different time periods (0.9, 4.9, and 9.9 years). The horizontal injection well is at Z = 383 ft.

Figure 4.12 shows the same iso-surfaces of $scCO_2$ saturations as Figure 4.10, but with the $scCO_2$ velocity vectors superimposed. As shown in Figure 4.12, the highest velocities are near the toe-end of the horizontal well, which corresponds with the larger plume growth in that area. Figure 4.13 shows the $scCO_2$ fluxes over time from the injection well separated into six different segments. The last 1/6 of the injection well has a significantly higher flux than the other segments. This outer portion of the lateral represents roughly the same flux as the five other segments combined. This effect is due to the greater reservoir pressure buildup near the heel of the horizontal injection wells because of the superposition of pressures from all four of the radial horizontal injection wells, which is approximated in these simulations by the no-flow boundaries on the sides of the domain.

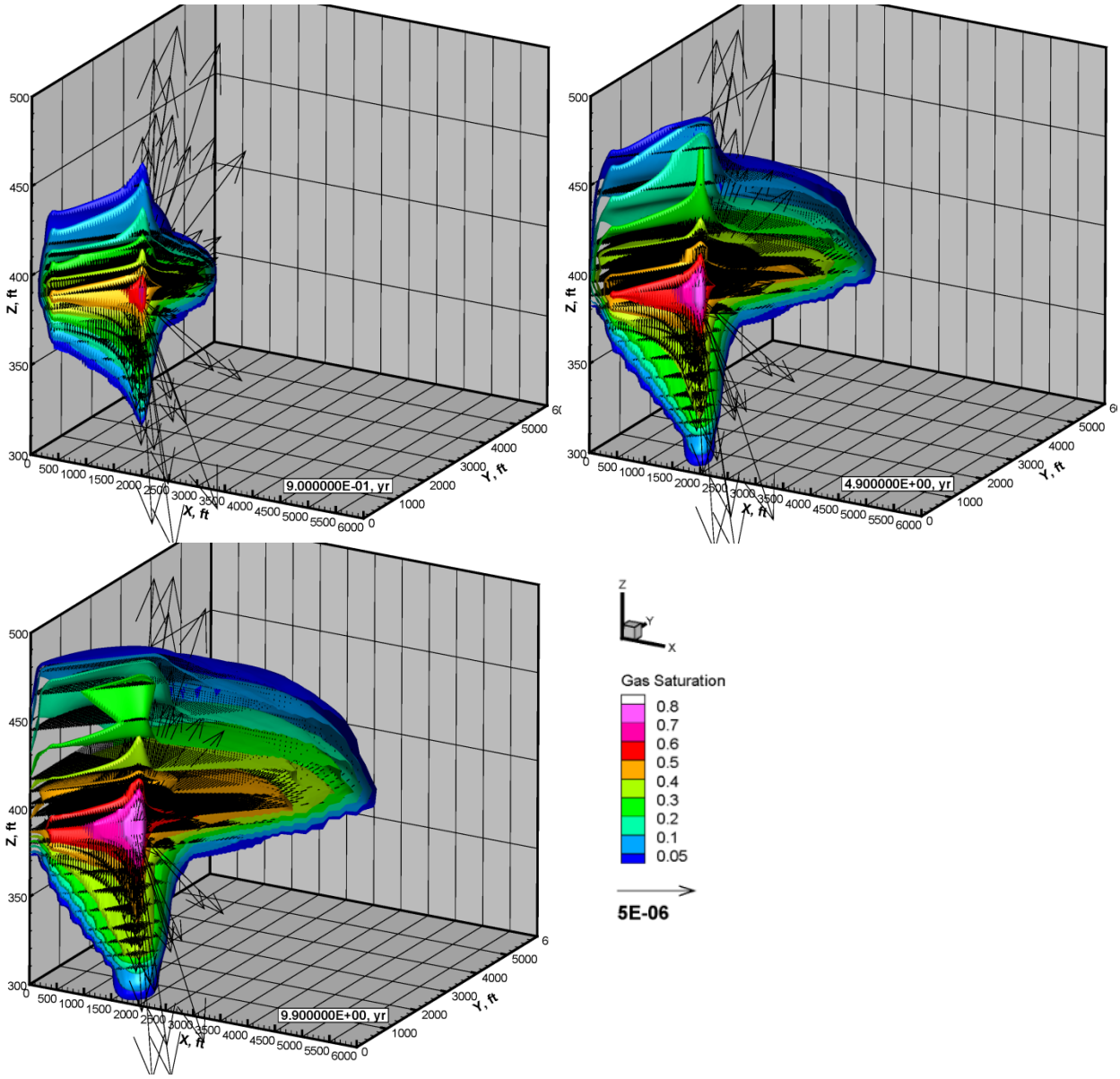

Figure 4.12. Simulated $scCO_2$ saturation iso-surfaces and $scCO_2$ velocity vectors at three separate time periods: 0.9, 4.9, and 9.9 years. Iso-surfaces are blanked in front of the Z plane along the X=Y coordinates for visualization of the interior (symmetrical).Note that the largest velocities occur toward the end of the horizontal well. Velocity vector units are m/s.

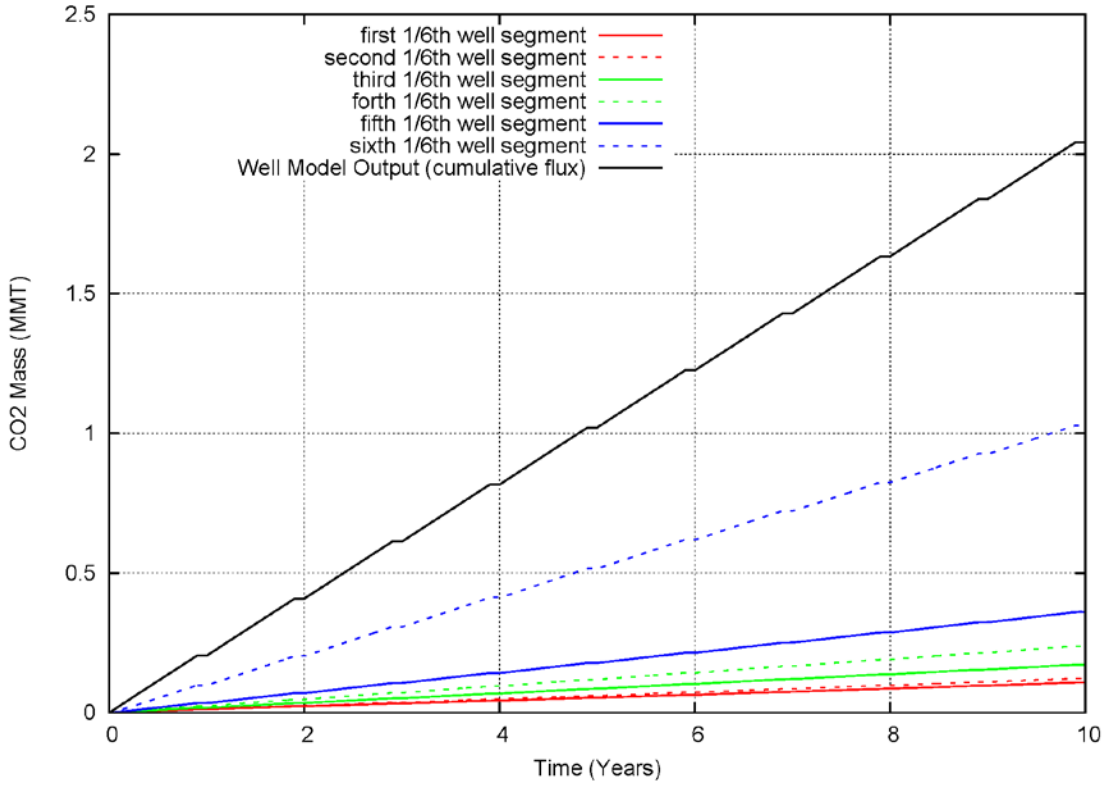

Figure 4.13. Cumulative $scCO_2$ fluxes along 1/6 length segments of the injection well (labeled sequentially first through sixth going from heel to toe) and total cumulative flux for the injection well.

4.4 Discussion of Preliminary Reservoir Response Model Results

A primary objective of this modeling effort was to determine whether pressure measurements in the reservoir monitoring wells (SLR #1 and SLR #2) could provide information about the spatial extent, symmetry, and evolution of the $scCO_2$ plume. Results from the preliminary simulations are inconclusive but show that while the peak pressures during each annual cycle were still increasing over the 10-year simulation period, the increases were becoming smaller as the simulation progressed and the amplitude of pressure cycles were also reduced. Additional simulations using updated material properties from future site characterization activities (e.g., specific storage) and sensitivity cases are needed to further investigate the potential of this response for providing supplemental information about plume evolution under site-specific conditions. Brine-only injection simulations are also planned to evaluate what the pressure responses would be when there are no relative permeability effects.

One significant finding resulting from these preliminary simulations was the demonstration that higher flux rates occur toward the end of the horizontal lateral. This may be useful in optimizing the injection design once additional site characterization data are available from upcoming drilling/reservoir characterization activities.

The approach and preliminary simulation framework described here will be updated as additional site information becomes available. This modeling effort will also include further sensitivity studies, extension of the lateral rectangular domain of the model to determine the impact of the outer boundaries

on the plume shape, and extending the simulation time to 20 years. The impacts of longer horizontal wells on the pressure responses in the monitoring wells, such as those planned for the southeast and southwest quadrants, may also be evaluated.

5.0 Geochemical Monitoring Considerations

This section discusses both aqueous- and gas-phase geochemical monitoring considerations, including the relative benefit of using intrinsic geochemical signals versus co-injected tracers as indicators for early leak-detection. Based on an integrated evaluation of these monitoring considerations, a summary of the geochemical monitoring approach that will be used at the FutureGen 2.0 storage site is presented.

5.1 Description of the Monitoring Concept

As described in Section 2.0, monitoring typically operates in two distinct modes—detection and assessment. The primary goal of the *detection* mode is to identify whether or not a leak is occurring. Secondary goals are to identify any leakage as early as possible in the process and at minimal cost. The primary goals of the *assessment* mode, on the other hand, are to determine the size of a leak and to support any required mitigation efforts.

Geochemical monitoring involves spatially and temporally resolved measurement of chemical parameters that directly or indirectly indicate the local influence or presence of the injected CO_2 in the aqueous or gas phase. Any indicators of brine migration present in aqueous-phase monitoring are also of interest. Because of the relatively small subsurface volumes they can economically access, geochemical monitoring technologies are generally of limited use in detection-mode monitoring. In assessment-mode monitoring, however, geochemical monitoring is essential.

Examples of the types of geochemical parameters measured in the aqueous phase include pH, specific conductance, and concentrations of solutes such as inorganic carbon and trace metals. Parameters measured in the gas phase, which encompasses gas present in soil pores, the near-surface atmosphere, and dissolved in surface water or groundwater, include the concentrations and isotopic signatures of CO_2, oxygen (O_2), methane (CH_4), and any tracer gases co-injected with the CO_2. The main focus of this section is the geochemical monitoring of aquifers and soil gas, but the conclusions also apply generally to geochemical monitoring of surface waters and the atmosphere.

Two general approaches can be taken in geochemical monitoring. The first involves measurements of intrinsic geochemical signals, such as changes in pH and dissolved metals in the aqueous phase and changes in the relative compositions, both chemical and isotopic, of soil gases. This approach relies on chemical interactions between the stored CO_2 and the subsurface or on innate differences in the isotopic chemistry of stored and natural CO_2, to produce changes in the composition of aquifers and gases that can be interpreted as leakage signals. The second approach involves the co-injection of a tracer compound with the CO_2 and subsequent measurements to determine whether any of the tracer-tagged injectate has leaked. Initial leakage of CO_2 could be inferred from the tracer results, and subsequently verified by direct measurements. This approach, while seemingly more straightforward, assumes some knowledge of and consistency in the relative transport behavior of the tracer compound and the stored CO_2. In the following sections we discuss the concepts involved in both approaches, and then discuss how they might be implemented for monitoring of the aqueous and gaseous phases in the subsurface.

5.2 Aqueous-Phase Monitoring Considerations

If any unforeseen leakage of CO_2 or brine from the injection zone were to occur, the first monitoring interval affected would be the aquifer located directly above the primary confining zone (Ironton Sandstone). Although initial detection would likely be based on changes in observed pressure response, aqueous geochemical monitoring would help confirm the leak and constrain the estimates of its size during the leak assessment stage. In this section we discuss the intrinsic geochemical signals initiated by such a leak as well as the types of co-injected tracers that could be used. We conclude with our evaluation of these aqueous-phase monitoring approaches and selection of the most appropriate approach for the FutureGen 2.0 project.

5.2.1 Intrinsic Signals

The types of intrinsic geochemical signals generated by the release of CO_2 from the storage zone into aquifers above the confining zone include changes in the chemical and isotopic composition of the groundwater. Chemical changes include increases in the concentrations of total dissolved solids (TDS), dissolved trace metals, dissolved noble gases, and carbonate species, as well as a decrease in the pH. A shift in the redox potential toward more oxic values would also be expected as a result of the entrainment of oxygen in the injected CO_2. If the release also (or instead) involves leakage of saline reservoir fluids from the storage zone, increases in the concentrations of sodium and chloride will occur if ambient salinity in the injection zone is appreciably higher than that in the ACZ. If the release involves the migration of free-phase CO_2 (i.e., CO_2 not dissolved in aquifer fluids) into the ACZ a decrease in specific conductivity would be observed because of the displacement of the water. Thus, with the exception of the redox potential and dissolved noble gases, all of these chemical signals should alter the specific conductivity of the aquifer, and this simple measurement, which can be performed on small sample sizes, provides a robust and sensitive indicator of whether or not leakage has occurred. Compositional measurements of aquifer fluids for trace metals, dissolved noble gases, carbonates, pH, redox potential, and sodium and chloride ions serve as confirmatory information that is useful during the assessment stage of monitoring.

Isotopic changes rely primarily on differences between the isotopic composition of carbon (^{14}C, ^{13}C, and ^{12}C) present in the injectate and the pre-existing carbon in the ACZ zone fluids. Isotopic measurements of other nuclides such as oxygen (^{18}O, ^{16}O) can also be of value, particularly when entrained O_2 is present in the injectate. Isotopic shifts in noble gas composition (e.g., $^{3}He/^{4}He$, $^{20}Ne/^{22}Ne$, $^{21}Ne/^{22}Ne$, $^{38}Ar/^{40}Ar$) also occur in response to the release of radiogenic isotopes (^{4}He, ^{21}Ne, ^{22}Ne, and ^{40}Ar) trapped in minerals that are subsequently dissolved by contact with CO_2. Recently, field measurements of $^{13}C/^{12}C$ ratios in CO_2 and methane isolated from groundwater or in soil gas have become practical with the advent of off-axis integrated cavity output laser spectrometers (McAlexander et al. 2011; Mortazavi et al. 2013) and there is some hope that the sensitivity can be enhanced to allow $^{14}C/^{12}C$ ratios to be determined in the field as well (Marino et al. 2011). Ambient differences in the carbon isotopic composition between the injection and ACZ fluids, and that of the CO_2 injection stream, may provide an isotopic signature that could be used as an indicator of the presence of injected CO_2.

5.2.2 Co-Injected Aqueous Tracers

Two major classes of aqueous tracers, hydrophobic and hydrophilic, can be co-injected with CO_2. The hydrophobic tracers are generally perfluorinated compounds such as perfluoro-1,2-dimethylcyclohexane (PDCH), perfluorotrimethyl-cyclohexane (PTCH), and perfluorodimethyl-cyclobutane (PDCB). As discussed in Section 4.3, each of these perfluorinated tracer (PFT) compounds is highly soluble in $scCO_2$ and has been previously injected with CO_2 in field studies (e.g., Wells et al. 2007, 2010, 2013). Subsequent transport of CO_2 and PFTs varies significantly, however, because of the widely disparate solubilities of these compounds in water. In contrast to CO_2, PFTs have very limited aqueous solubilities and rapidly partition into hydrophobic solid phases (e.g., coal seams, soil organic matter, very dry clay minerals) or into the gas phase at aqueous/gaseous phase boundaries. Gas-phase partitioning of PFTs is generally helpful to monitoring, because it means that, in most instances, PFTs will provide an early warning signal (e.g., Senum et al. 1997; Wells et al. 2007; Zhong et al. 2014). Another class of hydrophobic tracers that has been used is SF_6 and various substituted versions (e.g., SF_5CF_3; Matter et al. 2011). These behave similarly to PFTs although they seem slightly less prone to interactions with sediment surfaces because of their compact size (Zhong et al. 2014). As discussed in Section 5.3, intrinsic signals from trapped noble gases released by reaction of CO_2 with minerals also provide early warning, so the main benefit of using PFTs or SF_6 tracer compounds would be removal of any ambiguity with respect to the source of the leak.

Because, like CO_2, they are reasonably soluble in water, hydrophilic tracers avoid some of the differential transport issues associated with the hydrophobic tracers. Examples of hydrophilic tracers include naphthalene sulfonates such as 2-naphthalene sulfonate, 2,7-naphthalene sulfonate, and 1,3,6-naphthalene trisulfonate (Rose et al. 2001), and fluorinated benzoic acids such as pentafluorobenzoic acid (PFBA), 2,6-difluorobenzoic acid, and 2,3-difluorobenzoic acid (Flury and Wai 2003; Stetzenbach et al. 1982). These tracers have limited volatility so they are measured as aqueous constituents. However, they also have significantly greater affinities for hydrophobic solid phases than does CO_2, and thus some transport retardation would be expected in sediments with high organic-matter contents.

5.2.3 Evaluation of Aqueous-Phase Monitoring Approaches

An evaluation of the intrinsic and tracer-based monitoring approaches indicates that *the intrinsic approach will provide the required sensitivity to support a viable early-leak−detection capability in the aqueous phase*. Aside from unambiguous identification of the source of a leak, little additional information for assessment purposes would be gained from the co-injection of aqueous tracers. Tracers are generally used to interrogate the subsurface during site characterization activities or as a means of tracking injectate migration when the signal provided by the injection solution is difficult to detect. For the case of commercial-scale−$scCO_2$ injection, identifying first arrival of the injectate should not represent a significant technical challenge. In addition, limitations associated with the use of co-injected aqueous tracers need to be considered. From a brine-migration perspective, an aqueous tracer would be most useful if it were added to the injection zone prior to the start of CO_2 injection so that it was present within the reservoir prior to the start of CO_2 injection, otherwise the incremental improvement in early-leak−detection capability would be relatively small. From a CO_2 release detection perspective, uncertainties in the relative transport properties of the aqueous tracers and CO_2 would need to be considered. If unambiguous identification of the CO_2 source became the primary criterion, then either of

the types of hydrophilic tracers discussed (sulfonated naphthalenes or fluorinated benzoic acids) would suffice for pre- or co-injection.

5.3 Gas-Phase Monitoring Considerations

Although the solubility of CO_2 in groundwater is large compared to most gases, it is finite. With continued leakage, saturation levels would be reached in the aquifers above the confining zone and a separate CO_2-dominated gas phase could form. Migration of this gas phase through soil pores and sediment fractures could eventually result in a change in gas-phase concentration near the surface. This section focuses on the measurement of this primary signal (CO_2 together with any co-injected tracer gases), as well as any secondary signals resulting from the influence of CO_2 on other subsurface gas concentrations.

Given that the subsurface is mostly saturated with water, subsurface gas-phase monitoring is largely confined to the top few meters of soil. Our discussion thus centers on soil-gas measurements, although similar measurements can be made on gases exsolved from groundwater. And, as with the aqueous monitoring discussed in Section 5.2, the discussion of gas-phase monitoring follows two major approaches: 1) measurement of intrinsic signals associated with a CO_2 leakage response, and 2) measurement of concentrations of appropriate tracer gases that would be co-injected with the CO_2. The section ends with an evaluation of the two approaches and recommendations for the best practices to follow for gas-phase monitoring.

5.3.1 Intrinsic Signals

This section focuses on intrinsic signals that can be used as indicators of a CO_2 leakage response. Co-injected tracers are discussed in Section 5.3.2.

5.3.1.1 Carbon Dioxide

The primary intrinsic signal comes from changes in the concentration and isotopic composition of CO_2. Isolation and measurement of this signal comes with many complications, however. Typical instrumental measurement sensitivity is on the order of 0.1−1 ppmv, whereas background levels in the atmosphere are around 400 ppmv and have diurnal fluctuations of as much as 50 ppmv during the growing season when photosynthesis activity is high (Chandra and Joshi 2002; Massen et al. 2007). Concentrations of CO_2 in soil gas range from 10 to 50 times greater than those in the atmosphere, because of respiration by soil microorganisms and plant roots, and also exhibit a diurnal cycle. Moreover, this large reservoir of CO_2 in soil gas is also affected by wind, which exhibits a pumping action on the soil that can cause dramatic changes in CO_2 levels, and the wind effect is further modified by the rainfall events that alter the connectivity of the air-filled pores in the soil (Amonette et al. 2010, 2013). Because of these relatively large fluctuations in background levels, only very large fluxes of CO_2 are likely to be identified through direct measurements of CO_2 concentrations in soil gas.

Somewhat better success is possible using measurements of the isotopic composition of carbon in the CO_2. Because of cosmic radiation (and the residue from atmospheric nuclear testing), about 1 carbon atom in a trillion atmospheric CO_2 molecules is the radioactive ^{14}C isotope. This carbon decays at a half-life of about 5,730 years such that CO_2 derived from fossil sources (i.e., that which will be injected into

the storage site) has essentially no ^{14}C. Thus, measurements of the $^{14}C/^{12}C$ ratio in the CO_2 in soil gas can indicate whether or not leakage from the storage site is occurring. Instrumental sensitivity is about 1,000 times better than the natural abundance, so that a change in $^{14}C/^{12}C$ ratio of about 0.1% can be measured. Unfortunately, CO_2 in soil gas that is derived from fossil carbon deposits, rather than from combustion of fossil carbon fuel, is also essentially depleted in ^{14}C, so an observation of a drop in the $^{14}C/^{12}C$ ratio still contains some ambiguity regarding the source. Nevertheless, such an observation, particularly if a departure from an established baseline, strengthens the case for leakage and serves as the basis for more detailed measurements.

5.3.1.2 Light Hydrocarbons

Methane and other light hydrocarbons could be released if leaked CO_2 displaces them from the porous subsurface matrix in which they are trapped. For example, such a release would be likely to occur if, as it diffuses toward the surface, a plume of CO_2 encounters a layer of coal. Just as in the production of natural gas from coal beds (i.e., coal-bed methane), mass action would cause the CO_2 to displace these light hydrocarbon gases and a rise in their concentration would be seen in the soil gas prior to any increase in CO_2 concentration. Although suggestive of leakage, observations of increases in methane levels are further complicated by the presence of methanotropic and methanogenic microbes in the soil and lower strata that can affect methane levels. Although deeper strata tend to be methanogenic, soils act as methane sinks (i.e., are dominantly methanotropic) and, as a result, an increase in methane levels in soil gas, coupled with a subsequent decrease in the $^{14}C/^{12}C$ ratio in both CO_2 and methane, would be evidence of a leakage signature that would be sufficient to trigger further measurements.

5.3.1.3 Noble Gases

When CO_2 dissolves in water, carbonic acid is produced, which in turn reacts to dissolve simple oxides present in geologic materials. These oxides typically contain some products of uranium decay and related secondary decay reactions, such as ^{4}He (alpha particles), ^{21}Ne, and Rn gas, that are trapped in the mineral lattice. Dissolution of the lattice releases these noble gases. Because these gases cannot react or be trapped, once freed from the oxide cages in which they were formed, they migrate readily in the subsurface. As a consequence, if any unforeseen leakage through the primary confining zone does occur, these gases would be expected to migrate to shallower monitoring intervals (and could eventually reach the surface) ahead of (and/or along with) the CO_2. If, relative to baseline levels and background sites, an abnormally large concentration of ^{4}He, ^{21}Ne, or Rn is observed, CO_2 leakage is highly likely to be occurring in deeper strata.

5.3.1.4 Metabolic Mass-Balance Monitoring

In contrast to monitoring of specific gas concentrations in isolation, metabolic mass-balance monitoring examines the concentration trends between metabolically related gases present at or near the surface (Romanak et al. 2012; Johnson and Rostron 2012). The method assumes that there is a fixed inverse relationship between the concentration of O_2 and the concentration of CO_2 because of the consumption of O_2 during respiration by organisms in the soil. Increases in CO_2 concentration caused by organismal respiration are exactly matched by decreases in O_2 concentration (Figure 5.1a). If, on the other hand, the CO_2 concentration is increasing for any other reason and no metabolic consumption of O_2 is occurring, then the concentration of O_2 decreases by only one-fifth of the CO_2 increase as expected for

simple dilution. A similar inverse relationship exists between non-metabolic gases such as N_2 and Ar and CO_2. If CO_2 concentrations increase due to metabolic activity (i.e., at the expense of O_2), then the concentrations of N_2 and Ar do not change (Figure 5.1b). Otherwise, they decrease in proportion to their initial concentration as expected for simple dilution.

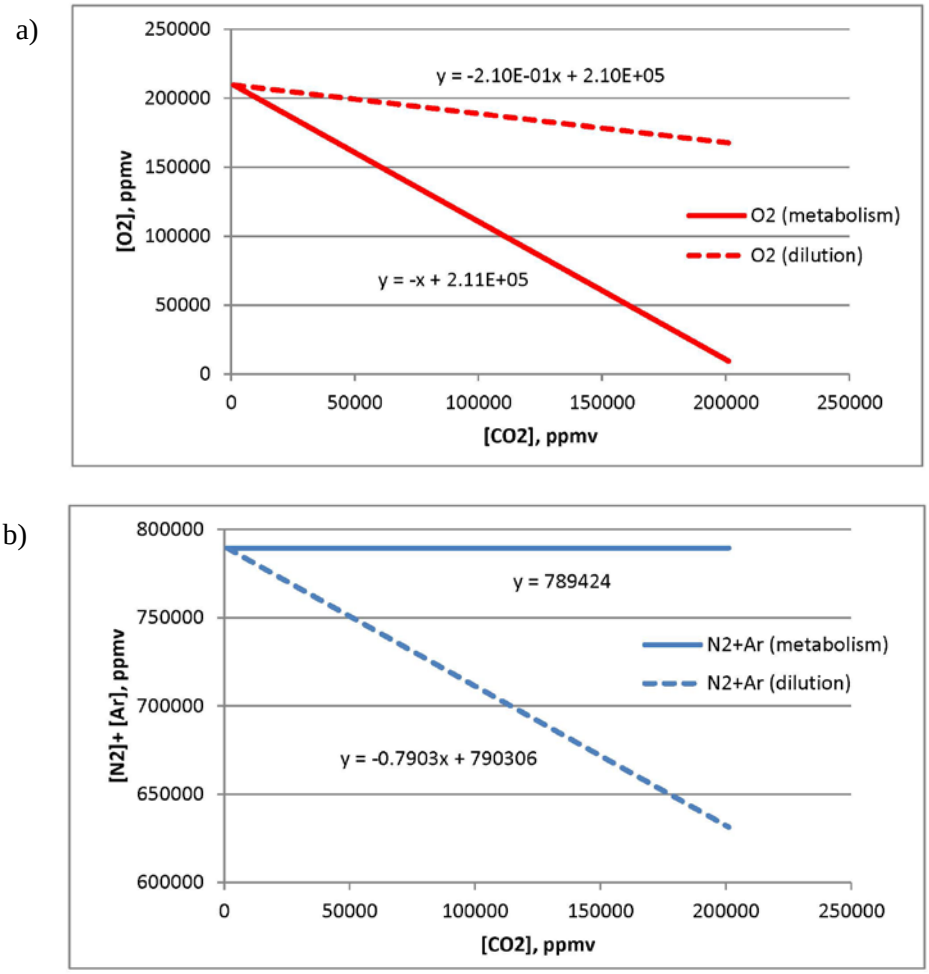

Figure 5.1. Theoretical response curves for soil-gas concentrations of a) O_2 and b) N_2+Ar in response to different levels of CO_2 generated by metabolic or dilution mechanisms. Solid lines indicate the trends expected for metabolic production of CO_2 at the expense of O_2. Dashed lines indicate the trends expected for a dilution mechanism produced by leakage of CO_2 from the storage site.

Just as O_2 is a terminal electron receptor for aerobic respiration with the resultant production of CO_2, CO_2 itself may be reduced to yield CH_4 during methanogenic bacterial metabolism (the reverse occurs during methanotrophic bacterial metabolism). Thus, a relationship between CO_2 and CH_4 similar to that for O_2 and CO_2 shown in Figure 5.1a also exists, and monitoring of CH_4, CO_2, and O_2 concentrations may prove useful for fine-grained soils where occasional anoxic conditions occur due to water saturation.

In practice, metabolic mass-balance monitoring involves measuring the concentrations of at least three gases (CO_2, O_2, and a major non-metabolic gas such as N_2 or Ar) on the same sample, and then

repeating this measurement protocol at multiple points in time. From the variations in concentrations of the three gases, response curves for O_2 and the non-metabolic gas relative to the concentration of CO_2 are obtained. Comparison with the theoretical response curves shown in Figure 5.1 indicates whether dilution or metabolism is the dominant mechanism in play. If evidence suggests that dilution is the major mechanism, then leakage is probable and further investigation is needed. As shown in Figure 5.2, the metabolic mass balance approach was used successfully at the Weyburn injection site to help establish the metabolic provenance of the CO_2 emissions measured there (Johnson and Rostron 2012).

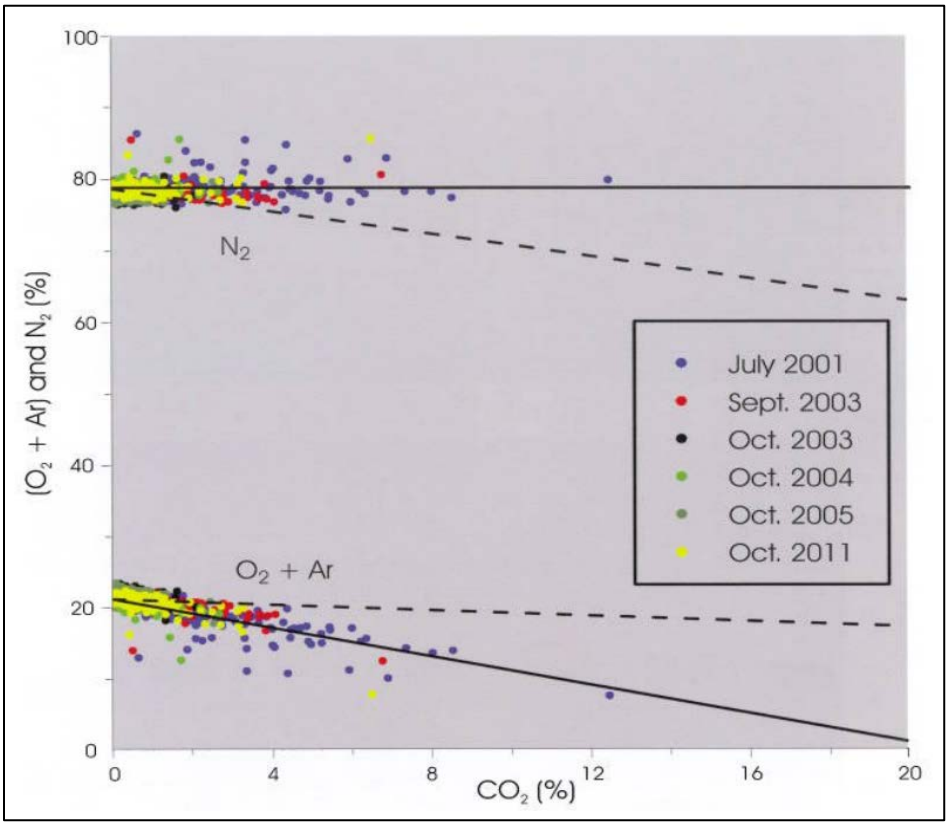

Figure 5.2. Scatter plots of N_2 and (O_2 + Ar) levels versus CO_2 levels for soil-gas samples collected from the Weyburn injection site. The solid lines indicate the trend expected for biogenic CO_2 production, and the dashed lines the trend expected for the addition of CO_2 leaked from the geologic formation. This figure was reproduced from Table 4-10 of Johnson and Rostron (2012).

5.3.2 Co-Injected Gaseous Tracers

In this section we focus on an "active" monitoring approach in which gaseous tracers are co-injected with CO_2 into the injection zone. In addition to providing unambiguous identification of the source of a potential leak, the approach relies on the prospective tracers being reasonable proxies for CO_2 in terms of their transport behavior in the subsurface. In the next several subsections, we introduce the potential gaseous tracers considered and discuss their geochemical behavior and the analytical methods used to measure their concentration.

5.3.2.1 Gaseous Tracers Considered

The following sections present a description of all the gaseous tracers that were considered in the evaluation. Analytical approaches for each of the potential tracers are listed in Table 5.1.

Table 5.1. Analytical methods and limits of detection for selected tracers.

Tracer	Analytical Method[(a)]	Limit of Detection	Sorbent Type	Reference
SF_6	GC-ECD	.6 ppt ±1.0%	Activated Carbon	Geller 1997
$^{13}CO_2$	CRDS	100 ppm ± 10 ppb	NA	Datasheet (www.picarro.com)
	Off-Axis Integrated Cavity Output Spectroscopy	150 ppm ± 0.2 ppb		Datasheet (www.lgrinc.com)
Kr	GC-MS (Adsorption onto solid)	10 ppb	Zeolite/ Silver Mordenite	Monson 1982
Ar	GC-TCD	2E-6 g	Zeolite	Lasa 2002
^{222}Rn	Solid-state planar Si detector	$7x10^{-20}$ L tracer/L air (0.1 pCi/L)	NA	RAD7 detector specifications, Durridge Company, Inc.
PFTs	GC-ECD	≤ 1 ppq (10^{-15} L tracer/L air)	Activated Carbon	Dietz 1986, Nazzari 2012, Watson et al. 2007
$^{14}CO_2$	LSC AMS OGS SCAR	ppt range Ratio of 10^{-15}[(b)] Ratio of ~10^{-12}[(b)] Ratio of 10^{-14}[(b)]	CO_2 Specific (Ascarite II or CaO)	Bachelor 2008 CAIS[(c)] Murnick 2008, Persson 2013 Galli 2011

(a) Analytical Methods: GC-ECD = gas chromatography with electron-capture detector; CRDS = cavity ringdown spectroscopy; GC-MS = gas chromatography with mass spectrometer; GC-TCD = gas chromatography with thermal conductivity detector; LSC = liquid scintillation counting; AMS = accelerator mass spectrometry; OGS = optogalvanic spectroscopy; SCAR = saturated-absorption cavity ringdown spectroscopy.
(b) Ratio of ^{14}C to ^{12}C
(c) Center for Applied Isotope Studies (University of Georgia)

Sulfur Hexafluoride

Sulfur hexafluoride (SF_6) is a conservative gaseous tracer (Dietz 1986). Conservative gaseous tracers are considered to be stable and thus SF_6 is not expected to decompose while in the subsurface. Klusman (2011) suggests however that SF_6 may not be completely conservative. It is probably reasonable to rate the stability of this tracer as moderate to high. The ambient level for SF_6 is in the low parts per trillion range (Dietz 1986). Myers (2013) reports its ambient value at approximately 7 ppt and Geller (Geller et al. 1997) report a value of about 4 ppt. Because the background level of SF_6 is in the parts per trillion range, large quantities will be needed. The need for large quantities will drive up the cost of SF_6, which was the most expensive of the conservative gaseous tracers studied by Dietz in 1986. Also, in terms of environmental impact, SF_6 is one of the more potent greenhouse gases (GHGs). According to the Intergovernmental Panel on Climate Change, the global warming potential (GWP) for SF_6 is 23,900 (Forster 2007), meaning that, per unit mass, it is nearly 24,000 times more potent a GHG than CO_2. The GHG potency of SF_6 means that it can only be injected at low levels and no substantial leakages can occur.

Sulfur hexafluoride can be sampled by pulling air through a series of scrubbing tubes and passing it through a Nafion dryer, followed by analysis with gas chromatography with an electron-capture detector (GC-ECD) (Geller et al. 1997). Geller et al. (1997) also reported an estimated detection limit of 0.6 ppt and a relative precision of ± 1.0% while using this method. Continuous sampling with this method could be a possibility; however, it would be challenging to have a GC-ECD deployed in the field. Sample analysis will be easier to control if it is completed in a laboratory or mobile facility. The cost of sampling and analysis depends on the sampling frequency, number of locations sampled, and the instrumentation available.

Carbon-13 CO_2 ($^{13}CO_2$)

Isotopically labeled compounds have the potential to work well as tracers. By artificially altering the natural abundance of various isotopomers in the injected stream, anomalies at the surface in these ratios would be indicative of leakage. Altering the ratios of $^{13}CO_2$ to $^{12}CO_2$ (δ-$^{13}CO_2$) is an attractive option because of the high degree of mimicry that use of $^{13}CO_2$ would afford. As mentioned previously, $^{13}CO_2$ should mimic the sequestered CO_2 very well but detection of isotopically distinct CO_2 is much less sensitive than for other tracers (Myers 2013). Background levels for $^{13}CO_2$ in ambient conditions are approximately 1.0% of all CO_2 or about 4 ppm (Marino et al. 2011; Whiticar 1996). Because this background level is moderately high, a large quantity of $^{13}CO_2$ would need to be injected in order to detect an anomalous δ-$^{13}CO_2$ near the surface after accounting for an estimated 2 to 3 orders of magnitude of dilution. This isotopically distinct CO_2 will be extremely expensive because of the large quantities needed. We estimated that 570,000 L of $^{13}CO_2$ would be needed to make the $^{13}C/^{12}C$ ratio distinct from the ambient ratio. If we also estimate about $100/L for the $^{13}CO_2$ then it would have an annual cost of around $57,000,000. The environmental impact of this tracer would be the same as CO_2 and, because it is a stable isotope, there is no concern about radiological hazards.

Sampling for distinct isotopic ratios of CO_2 would include adsorption or dissolution in a sorbent material if pre-concentration is necessary. A variety of sorbents could be used for pre-concentration, either liquid (e.g., aqueous NaOH) or solid (e.g., CaO). One requirement for sorbent selection is to ensure that the tracer can be desorbed for subsequent analysis by mass spectrometry. Some analytical methods would allow for direct analysis of a collected gas sample without pre-concentration. These methods include laser-based spectroscopic methods such as optogalvanic spectroscopy (Marino 2011), cavity ringdown spectroscopy (CRDS), and off-axis integrated cavity output spectroscopy. Commercial, field-deployable implementations of the CRDS and off-axis laser-spectroscopic technologies are available with detection limits reported in the part per billion range and the ability to do stable-C isotopic ratios for both CO_2 and CH_4.

Noble Gases

Noble gases are good options for tracers. Because they are inert gases, they have high stability and should not be delayed in the subsurface strata—thus remaining near the front or slightly ahead of the plume. Modeling will be required to better estimate the elution rate of the noble gases compared to that of the sequestered CO_2. The background levels for the noble gases will be higher than some other tracers. The background level will vary depending on the specific gas chosen. For a lower background level, an isotope with low natural abundance could be chosen. Noble gases are not GHGs and will not harm the environment. The extremely low environmental impact of using noble gases is their biggest advantage.

However, the availability of noble gases is fairly limited, especially for rare isotopes. Noble gases would not likely be readily available for several commercial sized projects. Associated with the low availability is the extremely high cost of noble gases, which makes their use largely impractical. Helium (He) and radon (Rn) are two noble gases that could be released from the interaction of slightly acidic CO_2 with subsurface formation materials. If they are released they could potentially migrate to the surface and signal leakage, because there would be an anomalous increase in their levels over normal background levels.

Many of the noble gases can be analyzed using gas chromatography with mass spectrometric detection (GC-MS). The detection limits for the noble gases are moderately high, but again will vary depending on the gas/isotope chosen. The noble gases can be adsorbed onto a zeolite for sampling and pre-concentration. Hydrogen mordenite and silver mordenite, in particular, have been shown to be effective zeolitic adsorbents for the noble gases (Monson 1982; Scheele et al. 2002). As far as sampling and the other criteria, He and Rn will be comparable to the other noble gases. Table 5.2 summarizes the various noble gas tracer candidates with respect to the selection criteria.

Table 5.2. Comparison of noble gas tracers.

Criterion	He	Ne	Ar	^{38}Ar	Kr	^{78}Kr	Xe	^{222}Rn
Type of Tracer[(a)]	Nat	Inj	Inj	Inj	Inj	Inj	Inj	Nat
Cost/Avail.	---	very high	high	very high	high	very high	very high	---
Background	5 ppm[1]	15 ppm[1]	0.93%	5.8 ppm	1 ppm	4.0 ppb	50 ppb[1]	$1.0x10^{-6}$ ppq[1]
Method	GC-MS	GC-MS	GC-TCD	GC-MS	GC-MS	GC-MS	GC-MS	Solid-state Si Detector
Detection Limit	1 ppb	1 ppb	15 ppb	15 ppb	800 ppt	800 ppt	1 ppb	$7x10^{-20}$
Sampling			AgZ[(b)]	AgZ	AgZ	AgZ*	AgZ	NA

(a) Nat = "natural", Inj = "co-injected"
(b) Weast 1983
(c) AgZ = sorption on silver mordenite.

Argon (Ar) was considered as a potential injected tracer for the project. The mimicry for Ar was classified as moderate to low, because the CO_2 will behave differently in the subsurface. This is due to the differences in the chemical reactivity of the two different compounds given the aqueous solubility of CO_2 and its activity as an acid. In addition, the background level for Ar is the highest of all the potential tracers considered for this project. Argon's ambient levels are 0.93% (Dietz 1986; Myers et al. 2013). To concentrate the plume with enough Ar to be differentiated from the ambient conditions, an excessive amount of Ar would be needed. To find a way to use less Ar, we looked at the different stable isotopes of Ar. The stable isotope with the lowest ambient background level was ^{38}Ar (Berglund and Wieser 2011). This specific isotope has an ambient level of 5.8 ppm, roughly three orders of magnitude higher than SF_6.

One method for detecting Ar is gas chromatography with a thermal conductivity detector (GC-TCD) (Lasa et al. 2002). This method has a reported absolute limit of detection of 2 μg (Lasa et al. 2002). Another method, diode laser adsorption spectrometry (DLAS), used neon as a carrier gas and was

reported to have a detection limit of 15 ppb (Uhl et al. 2001). ^{38}Ar has a prohibitive cost and is not readily available. A cost estimate is $45,500 for 1 L of the isotope (Icon Isotopes).

Krypton (Kr) would have a stability and mimicry very similar to that of Ar. However, one of the major advantages of Kr over Ar is the background concentration, which is about 1 ppm (Monson 1982; Myers et al. 2013). This is significantly lower than Ar, but we still considered less-abundant stable isotopes for Kr so that less has to be injected with the CO_2. The stable isotope with the lowest ambient concentration is ^{78}Kr; it has an ambient level of 4.0 ppb (using 1.14 ppm for atmospheric Kr and a natural abundance for ^{78}Kr of 0.35518 % [Berglund and Wieser 2011]). GC-MS is one method for analyzing Kr. Monson (1982) uses a method where a 10-ppb detection limit for Kr is necessary. Uhl et al. (2001) also analyzed Kr using DLAS and reported a detection limit of 800 ppt. As with ^{38}Ar, the cost and availability of ^{78}Kr are prohibitive. The estimated cost based on a single supplier inquiry is $59,500 for 3 L of ^{78}Kr (Icon Isotopes).

Helium is a noble gas that could be a natural tracer. As the sequestered CO_2 interacts with various components of the subsurface, He is one of the possible gases that could be released. This would increase the amount of He migrating up to the surface leading to an anomalous increase in the soil-gas levels. Such an anomaly would be indicative of possible leakage.

Similarly, ^{222}Rn would be considered a natural tracer. It could be released from the subsurface much like He. Detecting a significant increase in Rn concentration may also be indicative of possible leakage.

Perfluorocarbons

Perfluorocarbon tracers (PFTs) are cycloalkanes with four to six member rings that are fully substituted with fluorine (Watson et al. 2007). Perfluorocarbon tracers are chemically inert and have no biological effects (Nazzari et al. 2012; Dietz 1986). With these properties, PFTs are highly stable compounds that will not be broken down in the subsurface and thus would be classified as conservative gaseous tracers. The PFTs will be less soluble in subsurface aqueous phases than CO_2, resulting in a faster elution time to the surface. This would allow the monitoring program to detect possible leakage before CO_2 reaches the monitoring station (Wells et al. 2007). Although PFTs are less soluble in aqueous phases, they might have stronger surface interactions with soil, coal, or other subsurface strata resulting in the partial or complete delay of elution (Watson and Sullivan 2012). Modeling needs to be completed to better estimate the elution rate of the PFTs compared to that of leaked CO_2. If the PFTs are projected to elute before the plume, it is important to have an idea about the distance between the PFTs and the plume. It is also important to establish that the PFTs do not fall behind the plume during leakage.

In terms of environmental impact, PFTs are potent GHGs. They have a GWP of 14,740 but they do not contribute to ozone depletion (Watson and Sullivan 2012; Watson et al. 2007). At the current release rates associated with their use as tracer gases, the environmental impact for PFTs is negligible, but they should only be used for research purposes (Watson and Sullivan 2012; Watson et al. 2007). In a commercial sequestration project, PFT use raises the concern about accidental release of large quantities from pre-injection storage and handling, which could cause significant environmental harm. The availability of PFTs for sequestration projects is high because only small amounts are needed to provide detectable levels in the plume. For example, we estimate that about 0.5 kg of PFT would be needed to label a CO_2 plume at an injection rate of 1.3 MT of CO_2 per year. With the cost of PFTs being approximately $500 per kilogram, the annual cost for the tracer will be around $250. PFTs have been the

dominant tracer for a variety of applications during the past 30 years because of the small quantities required to show a significant difference from the ambient concentration.

A major advantage of PFTs is their extremely low background and detection limits. The background levels for PFTs are dependent on the specific compound, but are generally in the low parts per quadrillion range (Watson et al. 2007; Dietz 1986; Watson and Sullivan 2012). Using gas chromatography with electron-capture detection (GC-ECD), the detection limits for PFTs are in the femtomole range or 10^{-15} L of tracer/L of air (Watson et al. 2007; Nazzari et al. 2012; Dietz 1986; Watson and Sullivan 2012; Wells et al. 2007). As with the other tracers, PFTs are usually sampled and pre-concentrated onto a solid adsorbent. The adsorbent tubes are often placed 1 to 3 m into the soil, and when used passively they can sample up to 200 mL/day (Myers et al. 2013; Dietz 1986; Wells et al. 2007). With active sampling, the rate can be increased to 100 mL/min (Nazzari et al. 2012).

Radiocarbon Dioxide ($^{14}CO_2$)

Another possible isotopomer of CO_2 is radioactive $^{14}CO_2$. Carbon-14 is a weak beta emitter with a half-life of 5,730 years. Such a half-life will ensure stability of the tracer over the lifetime of the sequestration site. As with $^{13}CO_2$, one of the advantages of using $^{14}CO_2$ is its ability to mimic the injected CO_2 upon leakage (Bachelor et al. 2008; Lackner and Brennan 2009). With background levels around 1 ppt, $^{14}CO_2$ has the lowest natural abundance of the naturally occurring carbon isotopes (Murnick et al. 2008). In addition to low ambient background levels, the injected CO_2 will contain very little if any $^{14}CO_2$ because any ^{14}C in the source coal will have decayed long ago. This feature of the injected CO_2 would also allow $^{14}CO_2$ to be used as a natural tracer as well as an injected tracer. In the natural-tracer application, one could assay for an anomalous decrease in near-surface $^{14}CO_2$ levels because this would potentially be indicative of carbon leaked from the sequestration site. As an injected tracer, $^{14}CO_2$ would be used to increase the concentration beyond ambient levels. Detection of increasing ^{14}C levels near the surface would thus be indicative of leakage. The $^{14}CO_2$ background levels are also subject to environmental fluctuations similar to those of other forms of CO_2. The only known use of $^{14}CO_2$ as an injected tracer is at the CarbFix project in Iceland, where ^{14}C-labeled HCO_3^- is mixed into the aqueous CO_2 solution being injected into a basalt formation (Matter et al. 2011). The injected CO_2 reacts rapidly (<1 year) to precipitate carbonate minerals (Gislason and Oelkers 2014). The ^{14}C thus serves as a reactive tracer and changes in the ^{14}C content of aqueous and solid phases are contrasted with changes in the concentrations of two non-reactive tracers to facilitate understanding of the relative importance of the hydrologic and geochemical processes involved.

The $^{14}CO_2$ can be sampled directly from collected gas or by pre-concentration through partition onto a solid or into a liquid phase. One of the most prominent methods for analysis of $^{14}CO_2$ is accelerator mass spectrometry (AMS). AMS offers detection limits for $^{14}C/^{12}C$ ratios of 10^{-15}, which is three orders of magnitude lower than ambient levels. AMS can only be conducted at specialized facilities and will require that all samples be sent away for analysis. A typical such site (Center for Applied Isotope Studies, Athens, GA) charges a few hundred dollars per sample with turnaround times of 1 to 4 weeks. While AMS will be able to provide the smallest detection limits, it is not very cost- or time-effective if large numbers of samples are to be analyzed. To provide faster results, sample preparation processes are becoming automated to allow higher throughput (Turnbull et al. 2010). Another possible method for detecting radioisotopes including $^{14}CO_2$ is liquid scintillation counting (LSC). LSC would be more readily deployed near the sequestration site, would require some moderate sample preparation, but would

only have a detection limit in the parts per thousand range, which is very near background ambient levels (Bachelor et al. 2008).

Recent spectroscopic approaches are attempting to compete with AMS for precision, accuracy, and limit of detection, with the objective of providing rapid results using field-deployable instrumentation at a lower per-sample cost, excluding the initial cost of the instrumentation (Murnick et al. 2008). One of these methods, intracavity optogalvanic spectroscopy, initially reported detection limits of about 1 pmol for ^{14}C, which translates to an isotopic ratio of $^{14}C/^{12}C$ near 10^{-15} (Murnick et al. 2010, 2008). A recent publication however indicates that Murnick et al.'s limit of detection was overestimated by at least two orders of magnitude (Persson et al. 2013). These methods are able to use less sample, and obtain results within a couple orders of magnitude of the AMS result without the sample being destroyed upon analysis, thereby allowing the samples to be recycled and reanalyzed. An alternative laser-spectroscopic method is saturated-absorption cavity ringdown (SCAR) spectroscopy. This method reports a limit of detection within 1 order of magnitude of the AMS results and an analysis time of 1 hour (Galli et al. 2011). The optogalvanic and SCAR spectroscopic instrumentation would be able to be placed in a lab near the sequestration site to allow for more rapid processing of samples. For even faster turnaround, and eventually near-real-time detection, a field-deployable optogalvanic spectroscopy system is under development (Marino et al. 2011). Although the spectroscopic instruments do not currently have the reproducibility or reliability of AMS, they provide results significantly faster and with competitive limits of detection.

Although $^{14}CO_2$ is a radioactive compound, its low background and low detection limits would require only small quantities of tracer to be added annually. Nonetheless, the use of radiological tracers raises health and safety concerns, including the hazards perceived by the general public. Murnick et al. (2010) indicate that a person is allowed to inhale up to 200 mCi per annum. At the FutureGen 2.0 storage site, if $^{14}CO_2$ is co-injected with the sequestered CO_2 at double ambient levels, a total of 1,000−1,200 mCi would be needed annually. This means that a person would be allowed to inhale an estimated 20% of the tracer needed annually. If a large quantity of the $^{14}CO_2$ is released, it would most likely diffuse to safe levels by the time anyone would be inhaling the gas. It would also be necessary to allay public concern by educating concerned parties about how the low levels of the tracer compare to other radioactive doses commonly encountered in the general population. Accidental release of the tracer during storage of the tracer or during the process prior to co-injection is more of a safety concern and proper environmental health and safety (EH&S) procedures would need to be in place to ensure the safety of personnel and avoid site contamination. If $^{14}CO_2$ is chosen, testing must occur at every sampling point whenever a sample is taken throughout the project to ensure that there is no radioactive contamination. This additional monitoring for the contamination will consume a large amount of time and money throughout the lifetime of the project.

The cost and the availability of $^{14}CO_2$ remain the biggest impediment to the use of $^{14}CO_2$ as a tracer. One supplier, American Radiolabeled Chemicals (St. Louis, Missouri), could supply the required amount of tracer for around $65,000 annually, but this does not include the cost of ES&H and monitoring required of radiogenic materials.

5.3.2.2 Geochemical Behavior of Tracers

Phase Change

As CO_2 and tracers migrate through the subsurface they will potentially undergo multiple phase-transfer processes. Upon injection, the CO_2 stream will exist as a supercritical fluid with the tracer(s) dissolved therein. Initially, CO_2 will partially dissolve into the aqueous brine solution of the Mount Simon Sandstone Formation, and it will continue this dissolution process along the leading edge as the CO_2 plume develops. If there is an unforeseen release of CO_2 from the injection zone that migrates to shallower depth intervals where pressures are lower, CO_2 will interconvert into normal, as opposed to supercritical fluid, liquid phases, or the gas phase. These fluids can be contained in the pores of the formation and will percolate through them. As the CO_2 migrates to the surface during leakage processes, it will encounter a variety of pressure and temperature gradients as well as a variety of geologic formations, some containing aqueous phases. The CO_2 may experience differential mobility as it undergoes these phase-transfer processes. In addition, the CO_2 may become adsorbed onto the solid matrix of the various geologic strata encountered. An ideal tracer would need to mimic these phase-transfer steps or else differential migration rates will occur and the CO_2 and tracer will separate as they move upwards through the subsurface in a manner that is analogous to column chromatography. This would again result in the tracer lagging or leading the leaked CO_2.

The equilibrium tendency of a gas to dissolve into the aqueous phase is described by its Henry's law constant, with higher constants indicating that a greater fraction of the gas remains in the aqueous phase. Published values of the Henry's law constants for representative gases, along with the temperature sensitivity of these values, are given in Table 5.3.

Aqueous Solubility

Carbon dioxide and co-eluting tracers will interact with various aqueous phases in the subsurface including the brine phase in the Mount Simon Sandstone. In addition, the injected CO_2 will exist as a supercritical fluid phase in which tracers may have variable solubility. As the CO_2 and tracers migrate through the subsurface during leakage, they will dissolve to greater or lesser extents in the various fluid phases present. Carbon dioxide is reasonably soluble in water and can further ionize to form bicarbonates and carbonates. The ionic strength of the brine will further stabilize the formation of bicarbonate from aqueous CO_2. The values of Henry's law constants (Table 5.3) provide a good indication of the relative aqueous solubilities of CO_2 and a variety of tracer-related candidates in water at 298 K. Larger values are indicative of greater solubility at a given pressure. Any significant differences in solubility between CO_2 and the tracers will result in differential migration rates through the liquid phases—principally aqueous—which could result in the tracer leading or lagging any leaked CO_2. Many of the tracers considered above, except for the CO_2 isotopomers, will have more limited solubility in aqueous phases.

Adsorption

Limited work has been done to compare the adsorptive properties of gas-phase tracers on geologic media. Zhong et al. (2014) conducted a laboratory column study in which they compared transport of several PFTs with SF_6 and $^{13}CO_2$ in two unsaturated sediments and a laboratory sand at different

Table 5.3. Published values of Henry's Law constants for selected gases (Sander 1999).

Substance	k_H^{Θ}/[M/atm] 10^3	((-d ln k_H)/d(1/T))/[K]	Reference[(a)]
O_2	1.3 1.3 1.3 1.2	1500 1700 1500 1700	Wilhelm et al. 1977 Dean 1992 Lide and Frederikse 1995 Kavanaugh and Trussell 1980
SF_6	0.24	2400	Wilhelm et al. 1977
Ar	1.4 1.4	1100 1500	Morrison and Johnstone 1954 Wilhelm et al. 1977
Kr	2.4 2.5	1500 1900	Morrison and Johnstone 1954 Wilhelm et al. 1977
Rn	9.3	2600	Wilhelm et al. 1977
CO_2	34 34 35 32	2400 2600 2400	Wilhelm et al. 1977 Dean 1992 Lide and Frederikse 1995 Kavanaugh and Trussell 1980
OFCB[(b)]	0.25	~	Yaws and Yang 1992
CH_4	1.4 1.3 1.4 1.3	1700 1900 1600 1800	Wilhelm et al. 1977 Dean 1992 Lide and Frederikse 1995 Kavanaugh and Trussell 1980

(a) Sources are taken from Sander (1999).
(b) Octofluorocyclobutane: closest to PFT class of compounds

moisture contents. They found that in moist media the PFTs and SF_6 behaved similarly and could be considered conservative tracers. As the media dried, however, the higher molecular weight PFTs lagged SF_6 slightly, and in extremely dry sediments containing large quantities of smectite clay minerals, no breakthrough of PFTs was seen. The transport of CO_2 was essentially the inverse of these results. In dry media, CO_2 transported at essentially the same rate as SF_6, but when moisture was present, absorption of CO_2 into the water films slowed its progress through the medium.

These results highlight the question of how well gas-phase tracers mimic the transport of CO_2 through geologic media and suggest that in most instances (i.e., in moist sediments) the hydrophobic tracers would be transported at a more rapid rate through the sediments and thus provide an early warning of any leak. This assessment is supported by earlier work with PFTs by Senum et al. (1997) and Maxfield et al. (2005). As noted by Myers et al. (2013), however, using gas-phase tracer data to accurately infer the size of a leak would require a significant characterization and modeling effort.

5.3.3 Evaluation of Gas-Phase Monitoring Approaches

In this section we evaluate the sensitivity, range, cost, immediacy, robustness, and mimicry of the intrinsic-signal and injected-tracer approaches to monitoring of the gas phase. We conclude with recommendations of the best approach(es) for the FutureGen 2.0 project.

5.3.3.1 Sensitivity

Of the intrinsic-signal measurements, simple analysis for CO_2 levels is insensitive to leak identification because of the large ambient background levels and variability in those levels. Analytical sensitivity on the order of 0.1% is attainable for $^{14}C/^{12}C$ ratios, which may prove useful as part of a trend analysis and in helping to establish provenance of a CO_2 signal during assessment stage of monitoring. Analytical sensitivity for noble gases is on the order of parts per billion by volume (ppbv), except for ^{222}Rn, for which the exceptional sensitivity of 70 parts per sextillion is attainable. Because of its short half-life of 3.8 days, however, this analytical sensitivity to ^{222}Rn is of marginal value when transport times from a leakage location to the surface are on the order of months to years.

As implemented at the Weyburn site (Figure 5.2), metabolic mass balance monitoring is not a particularly sensitive technique for detecting whether a leak is occurring or not. From these field data, it can be seen that the difference in a 1% CO_2 level resulting from leakage compared to a 1% level resulting from metabolic processes is probably not statistically significant; if soil-gas concentrations exceed about 3% then it seems likely that leakage could be identified. Some of this lack of sensitivity stems from measurement of CO_2, O_2, and N_2 by different techniques on separate samples. However, the recent development of portable off-axis integrated cavity output laser spectrometers has allowed rapid, nondestructive, and robust analysis of CO_2, CH_4, and O_2 in the field at a sensitivity of 0.1% or better of typical ambient concentrations on the same gas sample (Los Gatos Research datasheet, www.lgrinc.com). Although not yet implemented in a field environment, this approach may eliminate much of the noise seen in the Weyburn data and improve detection sensitivity by an order of magnitude or better. Despite the relative insensitivity to initial leak detection, the metabolic mass balance approach is extremely useful in establishing the source of a CO_2 signal during the assessment stage of monitoring.

Of the co-injected tracers, PFTs afford the greatest sensitivity because of the extremely low detection limits and background levels. Using pre-concentration onto sorbents (CATS tubes) and a GC-ECD for analysis, the sensitivity and detection limit is better than any other method or tracer considered in this evaluation. Sulfur hexafluoride also uses GC-ECD methodology for analysis but detection limits are significantly higher than for PFTs. In addition, the background levels for SF_6 are many orders of magnitude higher than for PFTs. Noble gases including their distinctive isotopes principally use GC-MS for quantitation, which with standard approaches will have higher detection limits than GC-ECD. The combination of background levels and lower detection limits means that the sensitivity for noble gas tracers is generally poorer than for SF_6. Isotopically labeled CO_2 has variable sensitivity. The stable $^{13}CO_2$ isotope has a relatively high background level and is subject to large fluctuations because of metabolic, atmospheric, and subsurface processes. This results in a lower tracer sensitivity than several of the other possible tracers. The radiocarbon tracer $^{14}CO_2$ has relatively low background levels and low detection limits but a substantial amount would need to be injected annually to allow for detection of low-level leaks and those with large cross sections. Therefore, the sensitivity of this tracer is very good but not quite as good as PFTs.

5.3.3.2 Applicable Range

The applicable range is the range of leakage rates for which the monitoring approach is well suited to detect. As previously indicated, DOE sets the goal for leakage from CCS sites to be less than 0.01% per year of the total CO_2 stored over a 100-year project lifetime (Watson and Sullivan 2012). The metabolic mass balance monitoring system is unlikely to be sensitive enough to determine such a small quantity of

leakage but may serve as an inexpensive method to support evidence of larger volume leaks that should also be readily detected via early leak-detection monitoring in ACZ wells (see discussion in Section 7.0), as opposed to soil-gas monitoring approaches. We speculate that this method is capable of detecting a leak as small as a few percent provided the leak cross section is sufficiently small. Leaks of a few percent with large cross sections are likely not to be detected by this method. However, the ease of sampling and modest cost would allow for sampling at relatively high spatial resolution and frequency. Anomalous levels at a spatially localized area might aid in determining the source of the leak in the geologic feature when combined with other measurements.

5.3.3.3 Cost

A qualitative cost-performance ratio will measure how much each monitoring approach costs compared to its effectiveness at detecting the smallest possible classes of leaks. When estimating costs, several factors need to be considered. These factors include the annual cost of tracer and the costs associated with storage, handling, hazard monitoring, and injection of the tracer. Similarly, the number of samples analyzed, the costs associated with sampling and sample preparation, the total cost of analysis—amortized over the project duration—and the costs of instrument maintenance all should be considered.

A qualitative summary of the factors associated with cost-performance ratios for the soil-gas monitoring approaches described here are listed in Table 5.4. The most inexpensive option examined was the metabolic mass balance monitoring method. Associated costs include the purchase of instrumentation and sampling equipment as well as maintenance, but other costs associated with monitoring are low. This option is also the least sensitive, leading to an only moderate cost-performance ratio. For the co-injected-tracer approach, PFTs are a fairly inexpensive option as well. We estimate the annual cost of tracer to be currently a few hundred dollars because of the small quantities that are required. Capital and operational costs also would be associated with construction and maintenance of the tracer injection systems. Sampling requires sorbent tubes and either dynamic or static samplers. Samples must be analyzed in a lab-based instrument incurring a per-sample analysis cost or initial purchase of an instrument with certified staff to perform the analysis. The instrumentation and maintenance for PFTs, as well as SF_6, are more costly than for metabolic mass balancing. PFTs are also going to be the most sensitive option. Given these factors, PFT tracer-based monitoring has the lowest cost-performance ratio of the tracer approaches considered. Annual cost for use of SF_6 as a tracer will be significantly more than for use of PFTs because of the larger quantity needed for detection—due principally to the higher background levels. The instrumentation is the same for SF_6 and the PFTs so the performance difference lies in the sensitivity. Sulfur hexafluoride is less sensitive and more expensive than PFTs, resulting in a moderate level cost-performance ratio. The use of isotopically labeled tracers will also be more expensive, in some cases by significant amounts, and less sensitive than PFTs, although the sensitivity for $^{14}CO_2$ when analyzed by AMS approaches that of PFTs. Analysis of isotopic ratios by AMS has a per-sample cost that is currently several hundred dollars and sampling and pre-concentration may be necessary. Analysis of isotopes by GC-MS would have a similar but perhaps smaller per-sample cost. If many samples are analyzed then purchase of dedicated instrumentation might be more cost-effective. In general the use of isotopes involves a higher cost and a high to only moderate sensitivity. This results in cost-performance ratios that are moderate to high. Use of co-injected noble gas tracers is extremely expensive. The price for sufficient quantities of these tracers results in a cost-performance ratio that is prohibitively high.

Table 5.4. Comparison of cost and performance for intrinsic-signal and co-injected-tracer monitoring approaches.

Intrinsic Signal or Co-injected Tracer	Annual Tracer Cost, US$	Sampling Cost	Analysis Cost	Detection Limit	Leak Focus
$^{14}CO_2$	Intrinsic	High (AMS)	High (AMS)	10^{-15} $^{14}C/^{12}C$	High
^{4}He, ^{21}Ne	Intrinsic	Low	Moderate	1-10 ppb	Moderate
^{222}Rn	Intrinsic	Low	Low	10^{-20}	High
Metabolic Mass Balance	Intrinsic	Low	Low	ppb/ppm	High
SF_6	23,200	Low	Moderate	0.6 ppt	Moderate
$^{13}CO_2$	57,000,000	Low	Moderate	10 ppb $^{13}C/^{12}C$	High
Kr	11,900,000	Moderate	Moderate	10 ppb	Moderate
Ar	27,300,000	Moderate	Moderate	2 μg	Moderate
PFT	250	Low	Moderate	≤ 1 ppq	Low
$^{14}CO_2$	60,000	High (AMS)	High (AMS)	10^{-15} $^{14}C/^{12}C$	High

5.3.3.4 Immediacy

The immediacy of analytical results is important for selection of a soil-gas monitoring approach. If leakage is occurring, the sooner the leak can be detected, the sooner the problem can be mitigated. Metabolic mass balance and ^{222}Rn monitoring will provide the most immediate results. This is because it is possible to collect continuous data while still in the field using field-deployed instruments, but special installations would be needed to take measurements during the winter months. Significant leaks could be detected in this manner very readily with automated systems in the field. Isotopically labeled tracers will also provide moderately fast analysis times as long as AMS is not required. For the laser-spectroscopic-based techniques for determining isotopic ratios, field-ready analyzers are currently being developed and tested. If field-deployable analyzers are not available, the samples will need to be sent to a lab for analysis. If AMS is not used, analytical results for isotopic ratios can likely be determined within 24 hours to maybe a few days, depending on shipping time to the analytical lab. If AMS is used, it can take several weeks for results to become available. One lab we researched has typical 2- to 4-week turnaround times or 1-week expedited service available at higher sample costs. In general, immediacy for analysis of SF_6 and the PFT tracers will be comparable to that of the isotopic tracers. The GC-ECD analysis method requires lab-based instrumentation. The immediacy will again depend on transport time to the analytical lab. We estimate that typical results may be provided within 24 hours or up to a few days depending on the proximity of the lab to the injection site. Automated GC-ECD analysis in the field can also be performed with additional installation and maintenance costs and yield immediate results on the order of less than an hour.

5.3.3.5 Robustness

An approach is robust if it is subject to low variability and is resistant to broad changes in environment, handling, and application. Tracers are robust if they have high stability and if the background levels are subject to minimal fluctuations.

As implemented at the Weyburn injection site, the instrumentation used for metabolic mass balance analysis is rugged but involves multiple systems each subject to variability and requiring independent calibration. This approach is also subject to wide diurnal and seasonal fluctuations as well as to environmental and positional variation and thus likely has the highest variability of the approaches considered here. Furthermore it is likely that it will not be possible to collect some types of data during the winter months in central Illinois. However, with the arrival of portable off-axis integrated cavity output laser spectrometry, much of this variability could be eliminated by enabling analysis of all gases on a single soil-gas sample.

For the PFT tracers, dynamic or static sampling with sorbent tubes results in some variability because of sampling conditions and environmental differences between samples during transport to the analytical lab. The GC-ECD method is robust and highly reproducible. With their low background levels, the PFTs will only produce significant levels above the background if migration from the subsurface is occurring, thus minimizing the occurrence of false positives, although the potential for false positives associated with tracer injection operations and in-reservoir monitoring well sampling does exist. Some variability may occur with use of PFTs because of differential interactions with subsurface features as they migrate toward the surface. These interactions may vary spatially because of structural and environmental differences. PFTs have been found to be stable relative to the conditions of injection.

The sulfur hexafluoride tracer-based approach will be similar in robustness to the PFT tracer-based approach. However, with its significantly higher background level compared to the PFTs, it will be harder to detect leakage above ambient levels and the low signal-to-noise ratio will increase the variability of the results.

The noble gases are inert and therefore will not be lost throughout the subsurface and are likely to be less subject to differential interactions in the subsurface compared to PFTs. The high ambient levels of the noble gases within the atmosphere will result in lower signal-to-noise ratios and an increase in the variability of results. Quantitation by GC-MS is more subject to instrumental conditions and instrumental variability than GC-ECD. AMS approaches are highly reproducible, but sample preparation introduces variability to some degree. Laser-spectroscopic methods for radiocarbon isotope analysis do not have well-established estimates of their ruggedness, but initial reports (Marino et al. 2011) indicate that the variability may be significant.

5.3.3.6 Mimicry

In some respects, mimicry is the most important of the criteria. Clearly, mimicry is complete when direct measurements of CO_2 are made as, for example, in the metabolic mass balance approach. To the extent that the measured signal deviates from chemical similarity with CO_2 (e.g., the use of tracers having somewhat different transport properties), the degree of mimicry decreases.

Under ideal circumstances, the signal (whether intrinsic or co-injected tracer) would migrate through the subsurface at the same rate as the injected CO_2 but provide significant improvements in sensitivity as well as elimination of ambiguity with respect to source. However, significant value would be attached to the situation where the signal or tracer reaches the surface significantly before the plume, thus providing an early warning that leakage is occurring. It is also possible in this case that the CO_2 plume might never make it to the surface or that the leakage rate might be significantly overestimated. Failure of the tracer to travel at least as fast as the CO_2 plume is unacceptable because a leak would not be detected until a significant amount of the injected CO_2 had already escaped into the atmosphere.

The best co-injected tracers in terms of mimicry will be isotopically labeled CO_2. These will serve as a near-perfect mimic of the injected CO_2 as it migrates to the near-surface environment following a leakage event. Although noble gases, SF_6-based compounds, and PFTs are stable they may interact with different components of the subsurface matrix—particularly with coal seams—and be significantly retarded. Recent preliminary results from experiments conducted at PNNL indicate that the distribution coefficient for PFTs in coal is significantly different from CO_2. In such a situation, differential migration can occur—with the subsurface matrix functioning in a manner analogous to the packing in a chromatography column. As the mixture of CO_2 and tracer elute, they will become separated in the subsurface and arrive at the surface at different times. To ascertain the degree to which this may occur, it is necessary to experimentally determine the effective partition coefficients of each component with the various surfaces encountered and model the sum effect of these interactions upon plume migration to the surface. We anticipate that the carbon isotopes will provide optimal mimicry, and that the lighter noble gases will also be likely to migrate ahead of the CO_2 plume. Because of the presence of at least one coal seam in the geologic strata between the injection zone and the surface, it is difficult to say whether PFT- and SF_6-based tracers would precede or lag behind the CO_2 plume and this seriously constrains their usefulness for the FutureGen 2.0 project.

5.3.3.7 Recommended Gas-Phase Monitoring Approach

After evaluating and comparing the gas-phase monitoring approaches against multiple criteria, it is possible to make some conditional recommendations. Supporting these recommendations is the assumption that, because of limited spatial sampling, the primary value of geochemical monitoring is in assessment of the properties of a leak rather than in the initial detection of that leak. Thus, analytical sensitivity is of secondary value, and relatively insensitive methodologies, such as metabolic mass balance and isotopic dilution, are capable of providing the needed information.

With these assumptions in mind, *we recommend that monitoring of intrinsic gas-phase signals be implemented rather than co-injected gas-phase tracers*. Reasons for this include concerns about the different transport behaviors of co-injected tracers in the subsurface relative to CO_2, the loss of sensitivity near the wellbore because of inadvertent spillage during operations (as has been observed on some pilot-scale projects), the potential for false near-surface positives associated with in-reservoir monitoring well sampling activities, and the overall cost associated with the infrastructure required for co-injection of tracers.

One can envision a situation in which unambiguous identification of the injected CO_2 becomes the primary criterion and, as a result, many of the limiting issues associated with co-injected gas tracers become relatively less important. For this situation, a recommendation for a co-injected gas-phase tracer is in order. From a purely technical perspective, the ideal co-injected tracer is $^{14}CO_2$, which mimics CO_2

perfectly, has a low natural background, and a GWP of 1. Despite its use in at least one other sequestration project (Matter et al. 2011), operational and public-relations concerns stemming from its radioactivity, however slight, eliminate it from further consideration as a co-injected tracer. Co-injection of stable $^{13}CO_2$, is eliminated because of its high natural background and resulting lack of analytical sensitivity. Isotopes of the various noble gases (Ne, Ar, Kr, Xe) are also eliminated primarily because of cost and availability considerations. Sulfur hexafluoride, in addition to being the most powerful GHG known (100-year GWP = 23,900), has a relatively high background that limits its sensitivity, and so it too is eliminated. The perfluorinated cyclobutanes, cyclopentanes, and cyclohexanes, collectively referred to as PFTs, are also powerful GHGs (100-year GWPs > 7,500) that do not mimic CO_2 transport well because of their extremely low aqueous solubilities. However, they have extremely low atmospheric backgrounds, low cost/performance ratios, and an extensive track record in pilot-scale sequestration projects. Although their potential to be used on a large scale (i.e., by every CO_2 storage project) would likely lead to a decrease in their utility because of inadvertent leaks and consequent increases in atmospheric background, we nevertheless identify PFT compounds as the best potential co-injected gaseous tracers for the FutureGen 2.0 project, if their use becomes necessary.

5.4 Geochemical Monitoring for Leak Detection and Assessment

As discussed previously, monitoring can be divided into two distinct modes. The first is "detection" mode, which focuses on detecting a leak at the earliest possible opportunity. Its larger areal extent of detectability means this mode will most likely be primarily informed by changes in fluid pressure, although localized changes in aqueous geochemistry might also be detected. If a leak is detected, this would trigger a secondary "assessment" mode of monitoring wherein the focus would be on quantifying the rate and extent of the leak. This mode would continue to be informed by pressure data, but characterization of changes in aqueous geochemistry within the early leak-detection monitoring interval would likely play an increased role in the assessment.

Leaks can be classified according to the rate at which CO_2 is escaping the injection zone and migrating to shallower monitoring intervals. In addition, leaks will vary according to their cross-sectional area. Low leakage rates with large leak cross sections will be the most challenging to detect. However, given the current conceptual understanding of the FutureGen 2.0 storage site hydrogeology, this type of diffuse leakage is not expected. The most likely leakage scenario would be point-source leakage associated with locations within the region of highest pressure buildup where the primary confining zone has been somehow compromised. One potential source of increased leakage potential is associated with project-installed wells that penetrate the primary confining zone. Other potential sources include previously abandoned wells, tectonic structures, faults, and fracture zones. However, based on surveys of available information and site characterization activities conducted to date, there is no indication that these types of features exist in the vicinity of the FutureGen 2.0 storage site and thus, project-installed wells represent the most probable source of leakage potential. As such, early-leak−detection monitoring will be focused on regions of highest pressure buildup where project-installed wells penetrate the primary confining zone.

Based on the evaluation of aqueous- and gas-phase monitoring considerations discussed above, the geochemical monitoring program will initially rely on intrinsic and CO_2-related *aqueous* geochemical signals as the primary geochemical indicators of leakage response. Selection of the initial parameter list (see Table 5.5) was based on relevance for detecting the presence of fugitive brine and CO_2. The relative

benefit (and cost) of each analytical measurement will be evaluated throughout the construction and initial injection testing phase of the project to identify the analytes best suited to meeting project monitoring objectives under site-specific conditions. If some analytical measurements are shown to be of limited use and/or are cost-prohibitive relative to regulatory required parameters, they will be removed from the analyte list and not carried forward through the operational phases of the project. This selection process will consider the uniqueness and signature strength of each potential analyte and whether their characteristics provide for a high-value leak-detection capability.

The introduction of co-injected tracers will also be considered. An updated version of the monitoring, verification, and accounting upper layer transport (MVA-ULT) model that incorporates site-specific characterization data and baseline monitoring results will be used to assess early-leak−detection capabilities over a range of leakage scenarios. A preliminary evaluation is provided in Section 7.0. If future assessment indicates that intrinsic and/or CO_2-related geochemical signatures are unlikely to provide an acceptable degree of sensitivity to leakage through the primary confining zone, then addition of co-injected tracers may be implemented.

With respect to gas-phase monitoring, soil-gas composition (both geochemical and isotopic) and metabolic mass balance monitoring will be conducted to establish baseline conditions. In the event that deep early-detection monitoring indicates that a significant loss of containment has occurred, the need for establishing a long-term soil-gas monitoring program will be reevaluated.

Table 5.5. Aqueous sampling requirements for target parameters.

Parameter	Volume/Container	Preservation	Holding Time
Major Cations: Al, Ba, Ca, Fe, K, Mg, Mn, Na, Si,	20-mL plastic vial	Filtered (0.45 µm), HNO_3 to pH <2	60 days
Trace Metals: Sb, As, Cd, Cr, Cu, Pb, Se, Tl	20-mL plastic vial	Filtered (0.45 µm), HNO_3 to pH <2	60 days
Cyanide (CN-)	250-mL plastic vial	NaOH to pH > 12, 0.6 g ascorbic acid cool 4°C,	14 days
Mercury	250-mL plastic vial	Filtered (0.45 µm), HNO_3 to pH <2	28 days
Anions: Cl^-, Br^-, F^-, SO_4^{2-}, NO_3^-	125-mL plastic vial	Filtered (0.45 µm), cool 4°C	45 days
Total and Bicarbonate Alkalinity (as $CaCO_3^{2-}$)	100-mL HDPE	Filtered (0.45 µm), cool 4°C	14 days
Gravimetric Total Dissolved Solids (TDS)	250-mL plastic vial	Filtered (0.45 µm), no preservation, cool 4°C	7 days
Water Density	100-mL plastic vial	No preservation, cool 4°C	
Total Inorganic Carbon (TIC)	250-mL plastic vial	H_2SO_4 to pH <2, cool 4°C	28 days
Dissolved Inorganic Carbon (DIC)	250-mL plastic vial	Filtered (0.45 µm), H_2SO_4 to pH <2, cool 4°C	28 days
Total Organic Carbon (TOC)	250-mL amber glass	Unfiltered, H_2SO_4 to pH <2, cool 4°C	28 days
Dissolved Organic Carbon (DOC)	125-mL plastic vial	Filtered (0.45 µm), H_2SO_4 to pH <2, cool 4°C	28 days
Volatile Organic Analysis (VOA)	Bottle set 1: 3-40-mL sterile clear glass vials Bottle set 2: 3-40-mL sterile amber glass vials	Zero headspace, cool <6 °C, clear glass vials will be UV-irradiated for additional sterilization	7 days
Methane	Bottle set 1: 3-40-mL sterile clear glass vials Bottle set 2: 3-40-mL sterile amber glass vials	Zero headspace, cool <6 °C, clear glass vials (bottle set 1) will be UV-irradiated for additional sterilization	7 days
Stable Carbon Isotopes $^{13/12}C$ ($\delta^{13}C$) of DIC in Water	60-mL plastic or glass	Filtered (0.45 µm), cool 4°C	14 days
Radiocarbon ^{14}C of DIC in Water	60-mL plastic or glass	Filtered (0.45 µm), cool 4°C	14 days
Hydrogen and Oxygen Isotopes $^{2/1}H$ (δD) and $^{18/16}O$ ($\delta^{18}O$) of Water	60-mL plastic or glass	Filtered (0.45 µm), cool 4°C	45 days
Carbon and Hydrogen Isotopes (^{14}C, $^{13/12}C$, $^{2/1}H$) of Dissolved Methane in Water	1-L dissolved gas bottle or flask	Benzalkonium chloride capsule, cool 4°C	90 days
Compositional Analysis of Dissolved Gas in Water (including N_2, CO_2, O_2, Ar, H_2, He, CH_4, C_2H_6, C_3H_8, iC_4H_{10}, nC_4H_{10}, iC_5H_{12}, nC_5H_{12}, and C_6+)	1-L dissolved gas bottle or flask	Benzalkonium chloride capsule, cool 4°C	90 days
Radon (^{222}Rn)	1.25-L PETE	Pre-concentrate into 20-mL scintillation cocktail. Maintain groundwater temperature prior to pre-concentration	1 day
pH	Field parameter	None	<1 hour
Specific Conductance	Field parameter	None	<1 hour

HDPE = high-density polyethylene; PETE = polyethylene terephthalate; UV = ultraviolet.

6.0 Geophysical Monitoring Considerations

Geophysical monitoring methods are sensitive to subsurface changes that can occur because of fluid saturation or pressure changes resulting from CO_2 injection. These indirect monitoring technologies are a regulatory requirement, and at least one indirect methodology is needed for both CO_2 plume and pressure-front tracking. Geophysical monitoring methods considered for the FutureGen 2.0 storage site include electrical resistivity tomography, passive seismic, 2D and 3D surface seismic surveys, vertical seismic profiling, cross-well seismic imaging, time-lapse gravity, magnetotellurics and controlled-source electromagnetics, integrated deformation monitoring, and pulsed-neutron logging. The selection process considered the level of sensitivity, spatial resolution, installation and operational costs, the potential for interference with other monitoring activities, and the likelihood of local landowner acceptance.

Section 6.1 presents a brief summary of the geophysical monitoring technologies considered and associated findings. Section 6.2 presents the technical basis for each technology, and a detailed discussion of the technology screening and selection process is presented in Section 6.3. The metrics used in the screening process to identify the set of viable technologies that will be carried forward into the operational phases of the project include site-specific suitability and cost-effectiveness.

6.1 Summary of Geophysical Monitoring Technologies Considered

The primary objectives in geophysical monitoring are as follows:

- Track the development and evolution of the CO_2 plume and pressure front.
- Identify/characterize any asymmetry in pressure-front development.
- Identify and map areas of induced seismicity; this includes evaluating the potential for slip along any existing faults or fractures.
- Support assessment of any unforeseen leakage of brine or CO_2 from the reservoir.

In the following sections, the objectives, limitations and difficulties, experience gained at other CCS sites, and the findings from a technical evaluation performed to assess its suitability under site-specific conditions are presented for each geophysical monitoring technology considered.

6.1.1 Electrical Resistivity Tomography

Monitoring Objectives. Electrical resistivity tomography (ERT) has potential for detecting and quantifying $scCO_2$ saturation within a reservoir, which would be the primary objective of deploying this technology. A secondary objective would be to detect and quantify fugitive CO_2 above the confining zone in the event of a large-scale loss of containment.

Limitations and Difficulties. The success of the technology is affected by array geometry, signal-to-noise levels and accuracies in the data acquisition system, damage due to hostile environments, and electrical current shunting by nearby conductive objects, particularly metallic borehole and pipeline materials.

Cross-well surveys offer high-resolution imaging but are limited to distances of about 3,000 ft between boreholes, and must be performed in non-conductive casing. Cross-well imaging across the entire FutureGen AoR would require a large number of boreholes instrumented with ERT arrays.

Use at Other Sites. This technology has been demonstrated at Nagaoka, Japan; Ketzin, Germany; and the Southeast Regional Carbon Sequestration Partnership (SECARB) site at Cranfield, Mississippi. However for all of these sites, the lateral extent of the CO_2 injection volume was less than a few hundred meters and a small number of borehole-electrode arrays were used. Cross-well ERT monitoring has been demonstrated at Ketzin, where it was supplemented with a surface array to provide surface-to-surface and surface-to-borehole measurements.

Technical Evaluation. Modeling indicates that an ERT surface array augmented with well casings instrumented as long vertical and horizontal electrodes will be unable to image the plume for realistic resistivity changes expected in the injection reservoir during the first several years of injection. An ERT surface array augmented with discrete electrodes emplaced along the horizontal injection wells may be able to image the CO_2 plume but would be difficult to integrate with other aspects of the injection well design.

Finding. *ERT will not be included as part of the FutureGen 2.0 storage site monitoring program.*

6.1.2 Passive Seismic Monitoring

Monitoring Objectives. Elevated pressures in the reservoir caused by injection of CO_2 have the potential to induce seismic events. The objective of the passive seismic monitoring network is to accurately determine the locations, magnitudes, and focal mechanisms of seismic events with the primary goals of 1) addressing public and stakeholder concerns related to induced seismicity, 2) estimating the spatial extent of the pressure front from the distribution of seismic events, and 3) identifying features that may indicate areas of caprock failure and possible leakage.

Limitations and Difficulties. Accurate location of seismic events is affected by the sensor network geometry, assumed velocity structure, and noise attributes of the sensors and field site. Imaging of the CO_2 plume saturations using passive seismic monitoring has similarities to active seismic methods (e.g., reflection seismic, cross-well seismic), but it suffers from the additional contribution of source uncertainty in the inversion process. Passive seismic data collection is highly automated, but the large data sets generated are expensive to manage, store, and analyze.

Use at Other Sites. Passive seismic technology is a proven technology for locating fracture openings and slips along fractures or faults, and determining the type of focal mechanism. Passive seismic monitoring is the most common technology used at CO_2 storage sites to detect the potential for induced seismicity, transfer of stress, and for detecting slip on existing faults. Passive seismic monitoring has produced important input for reservoir management at the Decatur, Illinois site (Will 2012) and at the Midwest Regional Carbon Sequestration Partnership's (MRCSP's) Michigan site, as well as at Weyburn and other sites (Verdon et al. 2013).

Technical Evaluation. A number of scenarios were investigated using various passive seismic network geometries and maximum event distances. Given the various simplifying assumptions, preliminary seismic event location uncertainty results indicate that the array should perform well for most

moderate and larger magnitude (greater than -2 or -1) seismic events that might occur within the CO_2 plume extent as well as smaller magnitude events that occur closer to the borehole arrays.

Finding. *Passive seismic monitoring will be included as part of the FutureGen 2.0 storage site monitoring program.*

6.1.3 Reflection Seismic Monitoring

Monitoring Objectives. Reflection seismic monitoring is an industry-standard technology for imaging the geologic framework and constraining the geologic conceptual model across the study area. Surface-based and vertical seismic profile (VSP) surveys provide similar types of information, with VSP allowing for higher resolution geologic detail in the vicinity of the well. These surveys can be used for site characterization and, under favorable conditions, to 1) track the evolution of the CO_2 plume and/or the pressure front and 2) detect fugitive CO_2. Seismic-based assessments of the geologic framework can also be important for interpreting the geologic cause and implications of induced seismicity.

Limitations and Difficulties. Four-dimensional time-lapse imaging requires exact reoccupation of all seismic source and receiver stations, and identical depth locations of receivers in the well. For VSP surveys, this may be achieved by permanently cementing the sensors in the wellbore. An alternative method is to use semi-permanent vertical receiver arrays that are locked to the casing. Exact repositioning of the array is still a critical parameter for time-lapse applications.

Use at Other Sites. Reflection seismic monitoring provides the framework for reservoir management at most large-scale carbon sequestration sites, including Sleipner (Chadwick et al. 2010), Weyburn (Li 2003), and the nearby Decatur site. 3D surveys at the Decatur site form the framework for geologic interpretation and monitoring, but forward seismic modeling (Coueslan 2012) indicates that the frequency content of surface seismic is too low to allow for detection of CO_2 saturation changes. Seismic modeling of rock properties and variations in CO_2 saturation suggested that seismic amplitude differences at Decatur could be detected out to a distance of 1,000 ft by time-lapse VSP (Coueslan 2012). However, time-lapse 3D VSP acquired in February 2012, after an injected CO_2 volume of 74,000 metric tons failed to detect a CO_2 signal above background noise (Coueslan 2012).

Technical Evaluation. 2D surface seismic and VSP technology was used as a site-screening and characterization tool at the FutureGen 2.0 storage site. Seismic forward modeling using site-specific rock and velocity data suggests that it would be difficult to use time-lapse three-component (3C) 3D seismic or VSP surveys for monitoring CO_2 in the reservoir (Hardage 2014). P-wave attenuating layers in the overburden, fast velocity reservoir rocks (13,000 ft/sec), reservoir porosities of less than 22 percent, and a dominant frequency of less than 75 Hz negatively affect the use of reflection seismic methodologies for monitoring CO_2 within the reservoir.

Finding. *Reflection seismic monitoring will not be included as part of the FutureGen 2.0 storage site monitoring program.*

6.1.4 Cross-Well Seismic Monitoring

Monitoring Objectives. Cross-well seismic monitoring can be used to image CO_2 saturations in heterogeneous or compartmentalized reservoirs, identify fracture zones, and image vuggy porosity zones

in carbonates, such as the Potosi. High-frequency cross-well surveys can produce an image resolution on the order of 10 ft; time-lapse cross-well seismic tomography has the capability, depending on the velocities and porosities of the reservoir rock, to image the CO_2 plume.

Limitations and Difficulties. Cross-well seismic surveys involve placing geophones or seismic sensors in one borehole and a seismic source in another borehole. Wellbores can be vertical or horizontal, but optimally should not be farther apart than 3,000 ft, and in some cases, spacing requirements may be as little as 500 ft. Limitations include cost, required proximity of two wells, and the limited area of investigation.

Use at Other Sites. Cross-well surveys have been demonstrated at Nagaoka, Japan; Frio site near Houston, Texas; Ketzin, Germany; and the SECARB site at Cranfield, Mississippi. However, for all of these sites, the lateral extent of the CO_2 injection volume was less than a few hundred meters

Technical Evaluation. Although this technology has the potential to allow acquisition of a high-resolution image of a discrete portion of the CO_2 plume, a large number of wells would be required at plume scale. Using this methodology to track development of the CO_2 plume would thus be cost-prohibitive.

Finding. *Cross-well seismic monitoring will not be included as part of the FutureGen 2.0 storage site monitoring program.*

6.1.5 Magnetotellurics and Controlled-Source Electromagnetics

Monitoring Objectives. Both magnetotellurics (MT) and controlled-source electromagnetics (CSEM) can, under favorable conditions, measure electrical conductivity, which can be inverted to CO_2 saturation.

Limitations Difficulties. Both MT and CSEM are fairly low-resolution conductivity imaging methods with low sensitivity at the surface. The technology is relatively easy to use.

Use at Other Sites. Numerical studies have demonstrated the possibility of CO_2 injection monitoring using MT/CSEM methods (Gasperikova and Hoverstan 2006; Zhdanov et al. 2013). At the CO_2 site in Ketzin, Germany, a CSEM survey was conducted, but results indicate that using surface-based sources and receivers would be unlikely to map changes caused by injected CO_2.

Technical Evaluation. Forward modeling using site-specific parameters indicates that during 30 years of injection at the FutureGen 2.0 storage site, MT technology shows little sensitivity to increasing saturation change and is not sensitive to the thin injection zone. CSEM using sources at the surface also shows little sensitivity to changes during injection, but does show a slight improvement over MT. Results were improved by using borehole-placed receivers and surface transmitters, but the method is unable to discern lateral saturation variations (Wallin 2012[1]).

Finding. *MT and CSEM will not be included as part of the FutureGen 2.0 storage site monitoring program.*

[1] Unpublished presentation.

6.1.6 Time-Lapse Gravity

Monitoring Objectives. Time-lapse gravity can be used to observe changes in density distribution in the subsurface caused by the migration of fluids, thus providing an independent means of estimating the areal extent of the CO_2 plume.

Limitations and Difficulties. Sensitivity is lost with depth, and there may be site-specific limitations such as noise and infrastructure that limit access. The gravity inverse solution is non-unique and is most useful when combined with other methods such as integrated surface deformation and seismic methodologies. There are few implementation difficulties but permanent station monuments that can be repeatedly accessed throughout the life of the project are required.

Use at Other Sites. This technology has been successfully applied to a variety of subsurface injection studies, including carbon sequestration at Sleipner (Arts et al. 2008), aquifer recharge studies in Utah and elsewhere (Chapman et al. 2008; Davis and Batzle 2008), and to hydrocarbon water flood surveillance in Alaska (Ferguson et al. 2007).

Technical Evaluation. Gravity changes at the surface are expected to be small but analysis of long-term trends may allow for tracking of the CO_2 plume. Costs are the lowest among all methods and combining time-lapse gravity with other surveys can further reduce costs.

Finding. *Time-lapse gravity surveys will be included in the FutureGen 2.0 storage site monitoring program.*

6.1.7 Integrated Deformation Monitoring

Monitoring Objectives. Integrated deformation integrates ground-based data from permanent stations and annual differential global positioning system (DGPS) surveys, along with larger scale differential interferometric synthetic aperture radar (DInSAR) surveys to detect and map temporal ground-surface deformation over large areas. These data reflect the dynamic geomechanical behavior of the subsurface in response to CO_2 injection.

Limitations and Difficulties. DInSAR may be less successful in areas of heavy vegetation or in agricultural areas.

Use at Other Sites. Deformation monitoring has been implemented at a number of CO_2 storage sites, including those at Weyburn and Decatur. The DInSAR technology has been successfully demonstrated at a commercial CO_2 sequestration site at In Salah, Algeria (Morris et al. 2011; Vasco et al. 2010) as a means of characterizing surface uplift and migration of the CO_2 pressure front, and for identifying the location of reservoir compartmentalization and the presence of a previously unmapped fault under non-vegetated desert conditions.

Technical Evaluation. Modeling analysis of elevation changes at the surface indicate deformation of a few to several centimeters is expected as a result of CO_2 injection pressure changes. The expected deformation is well above the measurement thresholds for both global positioning systems (GPS) and DinSAR.

Finding. *Integrated deformation will be included in the FutureGen 2.0 storage site monitoring program.*

6.1.8 Pulsed-Neutron Capture Logging

Monitoring Objectives. PNC logs will be used to quantify CO_2 saturation along one or more boreholes to calibrate reservoir models and identify possible leakage through the sealing layers.

Limitations and Difficulties. PNC logs are only sensitive to a localized region surrounding the borehole (15−30 cm) and are therefore susceptible to interference from features very near the borehole such as changing borehole fluids, poorly installed or degrading cement, or invasion of drilling fluids. PNC measurements are less effective in low porosity (<15%) formations.

Use at Other Sites. PNC logging has been successfully implemented at a number carbon sequestration sites (Sakurai et al. 2005; Butsch et al. 2013; Ivanova et al. 2012).

Technical Evaluation. Reservoir porosities at the FutureGen 2.0 storage site are moderate (15−22%) and should allow for quantitative estimates of CO_2 saturation changes.

Finding. *Pulsed-neutron logging will be included in the FutureGen 2.0 storage site monitoring program.*

6.2 Technical Basis of Geophysical Technologies

This section presents the technical basis of each of the geophysical monitoring technologies considered during the screening and selection process, which is described in Section 6.4.

6.2.1 Electrical Resistivity Tomography

ERT is a potential technique for monitoring the extent of injected $scCO_2$ within a reservoir as well as CO_2 that may leak through caprock and interact with the overlying aquifers. Electrical measurements are well suited for monitoring CO_2 storage because of the contrast in electrical properties between the electrically conductive brine and the resistive $scCO_2$ in a deep reservoir, or by a conductivity increase associated with CO_2 dissolution into freshwater.

Over the last few decades technological advancements in geoelectrical instrumentation and data processing have resulted in numerous ERT monitoring applications (Ramirez et al. 1993; Ramirez and Daily 1996; Slater et al. 2000; Truex et al. 2013). The potential for ERT monitoring of CO_2 injection has also been investigated by several researchers (Newmark et al. 2001; Ramirez et al. 2003; Xue et al. 2009; Kiessling et al. 2010; Bergmann et al. 2012; Carrigan et al. 2013). Successful field-scale ERT monitoring for carbon sequestration has been demonstrated at sites in Nagaoka, Japan; Ketzin, Germany, and more recently Cranfield, Mississippi. At these sites the lateral extent of the CO_2 injection volume was less than of a few hundred meters and a small number of borehole-electrode arrays were used. At the Ketzin site, cross-well ERT monitoring was supplemented with a surface array to provide surface-surface and surface-borehole measurements in addition to the cross-borehole arrangements.

Cross-borehole ERT surveys offer high-resolution imaging but are sensitive to the volume immediately surrounding the boreholes, and have a very limited lateral area of investigation. At the FutureGen 2.0 storage site, an unrealistic number of boreholes would be required for cross-borehole imaging across the entire CO_2 plume; the number of boreholes required can be decreased by incorporating a supplemental surface electrode array. A number of electrode array geometries are possible and must be evaluated in order to optimize the ERT monitoring approach.

In addition to the array geometry, several other factors will have a substantial impact on the performance of the ERT monitoring system, including signal-to-noise levels, accuracies in the data acquisition system, damage due to hostile environments, and electrical current shunting by nearby conductive objects such as highly conductive strata or metallic borehole materials.

6.2.1.1 ERT Monitoring Theory

An individual electrical resistivity measurement is carried out by simultaneously injecting current from electrodes placed in contact with the ground and measuring the resulting potential (voltage) at adjacent locations. Ohm's law states that for a linear material the electrical current density is equal to the product of the conductivity (one over resistivity) and the electric field. In the case of direct current (DC) signals, the electric field is equal to the gradient of the electrical potential. These assumptions combine to produce the governing equation for ERT modeling (Sadiku 2006). For a point current source with magnitude I_0 that is applied at r_s within a material with electrical conductivity $\sigma(r)$, the potential $\varphi(r)$ can be determined from

$$\nabla \cdot (\sigma \nabla \phi) = I_0 \delta(r - r_s) \tag{6.1}$$

One fundamental question is how well a given electrode geometry senses the electrical resistivity structure at specific points in the ground. This can be addressed by determining the sensitivity function. For heterogeneous media calculating the sensitivity function generally must be performed numerically, but for homogeneous media a simple analytical solution can be obtained (Loke and Barber 1995). In 3D, the sensitivity at (x,y,z) for a current source at (0,0,0) and potential electrode at (a,0,0) is given by

$$F_{3D} = \frac{x(x-a) + y^2 + z^2}{\left(x^2 + y^2 + z^2\right)^{\frac{3}{2}} \left((x-a)^2 + y^2 + z^2\right)^{\frac{3}{2}}} \tag{6.2}$$

The total sensitivity is the combined sensitivities for the entire set of electrode measurements used in the ERT survey. This first-order analysis can be used to guide the initial development of the ERT geometry and a preliminary set of measurements. A number of common four-electrode arrays (Wenner, Dipole-Dipole, Schlumberger, Gradient, etc.) have been analyzed using this approach to provide approximate sensitivities for facilitating initial system design (Loke and Barber 1995). The performance of the system can then be modeled using a more realistic resistivity distribution and refinements can be made to the overall strategy.

Given a model of the ground electrical conductivity distribution as well as a set of source locations and magnitudes, Equation (6.1) can be used to generate synthetic data corresponding to the actual measured data acquired with the ERT array. The goal of ERT data processing is to determine the

unknown conductivity model that produces a match to the observed data to within the measurement errors. The results of this optimization, or inversion, process is nearly always non-unique such that many different models are able to fit the data. Errors are an important aspect of inverse methods and can have a major impact on the ability of a geophysical system to detect subsurface features.

The total error of an individual resistivity measurement is the net effect of errors in measuring the electrode positions, as well as the potential, and current. Several researchers have studied the effects of the electrode position errors and found that contribution to the total error can be large for arrangements that have small electrode distances relative to the positional error (Zhou and Dahlin 2003; Oldenborger et al. 2005; Wilkinson et al. 2008). It is expected that geometry errors will be small for FutureGen ERT monitoring because of the large electrode spacing that would be used (>200 m) and the relatively small positional errors (<10 cm).

Two major sources of potential measurement errors are the noise floor of the measuring device and various phenomena that can change the ground potential in addition to the applied current. The most common causes for the latter are by naturally occurring potential differences in the Earth termed self-potentials, and by power lines. These noise sources can often be sufficiently removed using filtering and averaging techniques; however, in some cases this cannot be done and substantial errors occur. Self-potential and power-line noise levels must be evaluated for the intended field site to estimate their effects on the ERT data. The noise floor of a properly designed measuring device can be very small, on the order of microvolts, and it is important to establish that the resulting potential differences are much larger than the system's intrinsic voltage noise floor.

Applied current measurement commonly uses shunt resistors to convert the current to an equivalent voltage that can be measured by the data acquisition system. Precision shunt resistors are used with typical resistance errors of a fraction of a percent. The performance of these resistors, however, is degraded when exposed to mechanical vibration, temperature changes including self-heating, and pulsed electrical signals that are commonly used for ERT current injection.

Reciprocal resistivity measurement can also be used to quantify the data errors. A reciprocal measurement is performed by exchanging the current electrode positions with the potential electrodes. For noise-free data a reciprocal measurement should produce the same data as the normal measurement. The observed difference in the normal and reciprocal measurements can be used to quantify errors that are not accounted for by other preprocessing such as geometry errors.

Error estimates for the various noise sources can be combined to approximate the total data errors required for input into the inversion. One common relationship describes the observed data, d_{obs}, as a linear function of the true data, d_{true}, where the coefficients can be estimated from the noise components:

$$d_{obs} = \alpha\, d_{true} + \beta \tag{6.3}$$

To convert the inverted resistivity distribution within the sequestration reservoir, a relationship between resistivity and $scCO_2$ must be established. Archie's law (Archie 1942) is a simple empirical relationship. In a two-fluid system, brine and $scCO_2$, application of Archie's law results in a relationship between the $scCO_2$ saturation, S_{CO2}, and the resistivity, ρ, given by

$$S_{CO_2} = 1 - \left(\frac{\rho_0}{\rho} \right)^{\frac{1}{n}} \quad (6.4)$$

The numerator on the right-hand side, ρ0, is the resistivity of the fully brine-saturated rock and the exponential is commonly taken to be 0.5 (n = 2) for sandstones. Resistivity analyses on cores from the FutureGen characterization borehole were also performed and values similar to those used for the modeling were observed (see Section 5.4.1.2).

6.2.2 Passive Seismic Monitoring

Passive seismic monitoring has become an important technology for understanding subsurface processes associated with a number of activities, including hydraulic fracturing, geothermal stimulation, mining, and carbon sequestration. Activities that create underground stress changes have the potential to induce very small- to moderate-magnitude seismic events. The injection of CO_2 is expected to generate small-magnitude seismic events and is the focus of the passive seismic monitoring for the FutureGen 2.0 project.

The objectives of passive seismic monitoring systems are to detect a seismic event, accurately determine its location, and measure the source characteristics to understand the failure mechanisms responsible for the event. The monitoring network consists of an array of seismic sensors placed either at the surface and/or within deep boreholes. The accuracy of the network is dependent on both the geometry of the sensor array and the signal-to-noise ratio (SNR) at each of the sensor locations. Sensors need to have a high-sensitivity uniform response over the intended frequency range, and a low intrinsic noise floor. The intrinsic noise floor is the minimum signal that the sensor is capable of measuring if all external sources of noise have been eliminated, and will dictate the minimum magnitude event that can be detected.

External noise sources often occur at the surface as a result of nearby subsurface activities such as drilling. Surface noise attenuates with distance below the surface and it is therefore advantageous to emplace surface sensors within shallow boreholes (~100 m) in order to reduce external noise to an acceptable level. Surface or shallow borehole sensors provide multiple sensing azimuths and offsets, but surface sensors typically suffer from lower SNR. Shallow borehole installations, however, can achieve a noise floor approaching that of sensors located in deep boreholes. Deep borehole monitoring can provide a higher SNR if the passive seismic event occurs close enough to the array, but precise event location can be difficult because of the geometric constraints on most deep borehole networks.

A hybrid approach that combines both a network of near-surface shallow borehole sensors and deep borehole sensor arrays can incorporate the benefits of both types and improve the performance of the passive seismic monitoring system.

6.2.2.1 Seismic Sources and Focal Mechanisms

Seismic waves can be generated by various source mechanisms and produce different wave fields that can be measured by an array of monitoring sensors. Seismic source characteristics are related to the physical processes that release energy into the ground; for example, an explosive force or shear failure on

a fault (Aki and Richards 1980). If the seismic wave field is sufficiently sampled in both space and time, the measurements can be used to determine the characteristics of the source and focal mechanism that generated the wave.

Seismic energy sources can be decomposed into three fundamental types: single forces, force couples, and double couples. A single force, as the name implies, is a single force vector acting in a particular direction and could be used to represent sources such as a vertical vibrator, or some landslides. The amplitude of a seismic wave propagating within a homogeneous elastic medium in the far-field (sufficiently far from the source) decays as one over the distance and is proportional to the source time function (Pujol 2003).

Force couples M_{xy}, consist of two forces with equal magnitude, oppositely acting along direction X but offset from each other along direction Y. A seismic moment tensor is constructed from the nine possible combinations of force couples and provides a means to capture the various possible equivalent body force couple representations for different seismic source geometries. Seismic moment tensors can be decomposed into an isotropic component (M_{iso}) associated with a volume change and a deviatoric component (M_{dev}). The deviatoric component can be further divided into a double-couple (M_{DC}) part associated with shear slip on a plane, and a compensated linear vector dipole (M_{CVLD}), which when combined with M_{iso} can represent a crack opening or closing mechanism.

The displacement wave field caused by a moment tensor source is somewhat more complicated than for a single force, and the far-field displacement is proportional to the time derivative of the source time function. Double-couple mechanisms are traditionally associated with earthquakes; however, non-double-couple mechanisms can be related to a number of seismic events (Julian et al. 1998; Miller et al. 1998). Shear slip and crack opening/closing are typically associated with seismicity induced by fluid injection as a result of increased pore pressure or thermal changes (Sileny 2009). Whereas the isotropic and deviatoric moment tensor components describe the type of source, the seismic moment, M_0, relates to the magnitude of the event.

The seismic moment can be determined from the spectral amplitude function because the frequency tends to zero and from the distance from the event. Information about the duration and rise time of the event can be estimated from the higher frequency portion of the spectrum. This analysis also underscores the need for sensors that have the proper response over the frequency band associated with the desired range of seismic event magnitudes.

6.2.2.2 Passive Seismic Sensors

Sensor types and characteristics play a major role in successful passive seismic monitoring (Warpinski 2009; Eisner et al. 2009; Baig et al. 2012). Sensors must possess high sensitivity, flat frequency response within the desired band, stable performance over time, and have a very low intrinsic noise floor. Sensitivity is a measure of the sensor response to proportional displacements/velocities/ accelerations imparted to it. Seismic signals are often very weak and the sensitivity of the sensors must be chosen to provide optimal output to the data acquisition system. As discussed in the previous section, seismic sources are band-limited and accurate magnitude determination requires proper sensor frequency response. The sensor frequency response can distort the true ground frequency response and must be removed prior to subsequent data processing. Sensors may show adequate performance in the early stages of monitoring but can degrade over time, and it is important to determine the amount of

degradation that can occur within the desired lifetime of the monitoring system. The noise floor determines the minimum detection threshold that the system is capable of and is therefore a critical parameter for system design. Sensor performance is also affected by a number of other factors including the sensor mechanical housing, cables, coupling mechanism, and even the well itself. Each of these factors can degrade sensitivity, alter the frequency response, and introduce additional noise to the system.

Commonly used sensors for seismic applications include moving coil, omni-tilt geophones, and solid-state electronic sensors (Warpinski 2009; Baig et al. 2012). Both sensor types are not affected by the orientation of the sensor and can be configured as velocity sensors or accelerometers. Usable frequency band-width for geophones can be from 5−400 Hz and from 0.5−100 Hz for accelerometers. These devices are built with signal conditioning and digitizer circuitry located on the sensor to improve the electrical performance. The disadvantage of this design is that due to the complexity of the assembly, long-term deployment in a deep borehole environment results in reduced lifetime, on the order of a few years. Permanent borehole emplacement of a standard electronic geophone or accelerometer array would not be expected to last the lifetime of the FutureGen 2.0 project. One option would be to install a semi-permanent array within a borehole casing or attached to tubing string, and periodic sensor replacement could be performed.

In addition to standard geophones or accelerometers, a relatively new type of fiber-optic-based sensor is in the process of becoming an industry standard. A light pulse of a certain frequency traveling within an optical fiber continually scatters light back toward the point where it originated. The frequency of this backscatter is affected by the strain on the fiber and can be used to measure the static or dynamic strain on the fiber. The fiber can be coupled to a device to mechanically amplify the strain on the fiber and produce a sensor with performance that is as good as or better than standard geophones or accelerometers (Paulsson et al. 2013). A key feature of these sensors is that, because they have no electronics located within the borehole, they are extremely robust and have designed lifetimes of and performance stability lasting several decades.

Surface sensors require higher sensitivities and lower noise floors than borehole-based sensors to detect events of similar magnitude that might occur near a borehole array because the distance to the surface is much greater. High-quality broadband seismometers exhibit long working lifetimes, high sensitivity, and extremely low noise floors. These seismometers have an excellent frequency response from 1 m Hz to 200 Hz and can be configured for placement within a shallow borehole (<100 m) to minimize external noise generated at the surface. To minimize signal attenuation and site noise, boreholes will be drilled to at least the uppermost bedrock unit and the casing will be cemented in place and pumped dry prior to sensor emplacement.

An alternative to seismometers would be to install a closely spaced array of geophones within a shallow borehole and stack or average the signals from the individual sensors. If the sensors are spaced properly so that the noise is uncorrelated between the individual sensors, the averaged signal can be used to reduce the noise floor to acceptable levels for detecting microseismic events (Eisner et al. 2011). However, the use of single high-quality seismometers is recommended because of the simplicity of the station design.

6.2.2.3 Seismic Event Location

After sensor selection, the second critical design element of the passive seismic monitoring system is to determine the optimal positioning of the seismic sensor array.

The number and spatial distribution of sensors in a passive seismic monitoring network must be designed to minimize the errors in estimating event locations and origin times. These event parameters can be estimated using a grid search technique whereby a trial seismic event is generated at each point in the parameter domain (both space and time) and the synthetic travel time is calculated to each station and compared to the observed travel times (Fischer et al. 2008; Eisner et al. 2009). The solution is determined from the location and origin time that minimizes the residual errors or absolute values of the differences between synthetic and observed data. Synthetic travel times can be calculated using a number of forward modeling methods such as ray tracing or even full-waveform modeling. In addition to travel times, directional information can be estimated from particle polarizations when using 3C sensors. However, the local nature of polarization measurement can be strongly influenced by local heterogeneities surrounding the borehole. The velocity model has a large influence on the predicted data and must be estimated as accurately as possible to obtain good results. A velocity model can be built using borehole logs and velocity data from VSP or surface seismic surveys.

6.2.2.4 Seismic Moment Tensor and Velocity Inversion

Passive seismic monitoring of fluid/pressure induced seismicity aids in our understanding of the fracture process. Event location can be used to image the spatial distribution of fractures and how they evolve in time in response to the fluid injection (Lumley 2001; Baig and Urbanicic 2010). Seismic waveforms can also be used to compute seismic moment tensors in order to provide additional information about the size, orientation, and type of fracture and can be used to help discriminate potential failure of the reservoir or overlying sealing layers from evolution of the network of smaller fractures and their connectivity (Nolen-Hoeksema and Ruff 2001; Foulger et al. 2004).

A number of aspects of the seismic monitoring network can have a substantive impact on the quality of the derived moment tensor solutions (Varycuk 2007; Sileny 2009; Song and Toksoz 2011). The monitoring network must have a sufficient aperture (distance between farthest stations) and sample a number of azimuths and offsets. Using a single borehole array it is not possible to recover the complete moment tensor (Nolen-Hoeksema and Ruff 2001) so that multiple borehole arrays and/or surface stations must be used. Using the amplitude of both P- and S-waves, the complete moment tensor can be retrieved from data collected in two or more borehole arrays, but the boreholes must be located at different azimuths from the source (Vavrycuk 2007). Using three or more boreholes can further reduce the errors in the moment tensor estimates.

Borehole arrays have traditionally been used for passive seismic monitoring applications (Warpinski 2009). Surface passive seismic arrays are being increasingly used and can recover complete moment tensors (Sileny 2009). Combined surface and deep borehole monitoring arrays can substantially improve results over those obtained using borehole- or surface-based methods alone. Full-waveform-based moment tensor inversion can also be performed and may allow recovery of the complete moment tensor from a single borehole array (Song and Toksoz 2011) or may further improve estimates from multiple borehole and surface arrays. In addition, joint location and velocity model inversion can be performed to

provide better velocity models and a means to monitor velocity changes caused by the fluid injection. However, this type of analysis requires very high-quality data in order to give meaningful results.

6.2.2.5 Operational Protocols

After a seismic event has been identified, a decision must be made about what impacts the event may have on operations and what the proper response to the impacts should be. This decision and response framework should consist of an automated event location and magnitude determination, followed by an alert for a technical review to reduce the likelihood of false positives. The passive seismic monitoring system should incorporate the appropriate alarms and alerting mechanisms.

Identification of events of sufficient magnitude or that are located in a sensitive area (e.g., within the caprock) should be used as input for decisions that guide the adaptive monitoring strategy, implementation of any required reduction in injection rate, or initiation of other mitigating actions. Seismic events that affect the operations of CO_2 injection can be divided into two groups/tiers: 1) events that create felt seismicity at the surface and may lead to public concern or structural damage, and 2) events not in group one, but that might indicate failure or impending failure of the caprock. The operational protocol for responding to events in group one (Tier I) will follow a "traffic light" (Zoback 2012; National Research Council 2012) approach that uses three operational states:

- Green: Continue normal operations unless injection-related seismicity is observed with magnitudes greater than M = 2.
- Yellow: Injection-related seismic events are observed with magnitude $2 < M < 4$. The injection rate will be slowed and the relationship between rate and seismicity will be studied to guide mitigation procedures including reduced operational flow rates.
- Red: Magnitude 4 or greater seismic events are observed that are related to CO_2 injection. Injection operations will stop and an evaluation will be performed to determine if safe operations can continue.

Tier II operational responses to an event or collection of events that indicate possible failure of the sealing rocks above the reservoir may include initiation of supplemental adaptive monitoring activities, injection rate reduction in one or more injection laterals, or pressure reduction using brine extraction wells.

6.2.3 Reflection Seismic Surveys

Reflection seismic methods are an industry-standard technology for imaging the geologic framework. Two acquisition geometries commonly used are surface-based seismic methods and VSP. These surveys can be used for site characterization and if repeated over time, can be used to track the evolution of the CO_2 plume and/or the pressure front, and to detect fugitive CO_2. Surface seismic surveys can provide coverage over large areas for both characterization and monitoring activities. VSP surveys provide the same type of information as surface reflection seismic methodologies, but with higher resolution of geologic detail in the vicinity of the well.

The design basis for both surface-based and VSP reflection seismic monitoring methods are described the following sections.

6.2.3.1 Surface Seismic Methods

Surface-based reflection seismic surveys are an industry-standard methodology for imaging of the subsurface geology between wellbores. Three-dimensional seismic technologies provide the framework for reservoir management and are a means of volumetrically locating the geology associated with reservoir compartmentalization, and areas where passive seismic analysis indicates slip along fractures. In addition, 3C 3D seismic surveys provides volumetric imaging of the overburden, with the capability of detecting upward migration of CO_2 above a depth of 2,500 ft, where CO_2 phase change would occur. Three-component 2D seismic surveys provides a much less expensive option than 3D for imaging the entire subsurface along a line, such as across an area where other monitoring technologies indicate the existence of a previously unknown fault.

Surface seismic (3D/2D) data are acquired from geophones laid out in grids or lines on the Earth's surface and activating seismic source stations along lines between the geophones. The geophones may record only P-waves; more modern 3C geophones record both compressional and shear waves. Seismic sources may emit compressional or shear-wave energy, and P-waves may be converted to shear-wave energy within the Earth. In many areas, shear-wave images may be superior to P-wave images in terms of energy recorded and resolution.

Seismic attributes (amplitude, amplitude versus offset, coherence, instantaneous phase, dip, and frequency) all provide means of mapping structure and seismic properties that are related to physical rock and fluid properties. Surface seismic data are commonly inverted for porosity, gas or oil saturation, pore pressure, or lithology (Chopra and Marfurt 2005)

Although surface seismic technology has been demonstrated to be effective in mapping the pressure front (velocity increase) related to the CO_2 plume in the North Sea, as well as the displacement of brine by CO_2 (velocity decrease) (Verdon et al. 2013), the geologic conditions (e.g., signal-attenuating layers in the overburden, fast velocity reservoir rocks, and low reservoir porosities) have a large impact on the use of surface-based seismic technologies for monitoring the CO_2 plume within the reservoir.

6.2.3.2 Vertical Seismic Profile

Vertical seismic profile surveys are conducted by placing seismic sources at the Earth's surface and recording the seismic signals produced by the surface sources with an array of receivers that are placed in a borehole.

Three-dimensional VSP technology has been used in characterization and monitoring at a number of sequestration sites, including Cranfield (Daley et al. 2013) and Decatur (Coueslan 2012). Daley et al. (2013) acquired and processed a 3D VSP over a monitoring well at the SECARB Phase III Cranfield CO_2 injection site. Although they did not analyze time-lapse data, they concluded that for that site, 3D P-wave VSP data have only slight improvements over conventional 3D surface seismic data in the resolution of high-amplitude, continuous reflectors associated with the injection formation, but that this technology greatly improved imaging of weakly reflective, discontinuous reflectors in a potential monitoring zone above the reservoir.

Placing seismic sensors in the borehole and locating seismic sources on the Earth's surface allows the recording of much higher frequencies than is possible when sensors are only placed on the surface. As a

result of approximately twice the frequency content, the resolution of subsurface features is considerably increased. In addition to recording higher frequency data, borehole seismic data typically have a higher SNR, particularly when the sensors can be strongly coupled to the wellbore (Paulsson et al. 2004).

As previously mentioned, standard modern receivers have three components, and simultaneously measure seismic wave displacements along three orthogonal directions. Ground displacements induced by seismic waves possess orientations relative to the direction the wave propagates. Seismic waves are grouped into two major types, compressional or P-waves and shear or S-waves, each with different velocities and different propagation characteristics.

The basic elements of a VSP survey are an available borehole, either cased or open hole; a seismic energy source; a wireline conveyed downhole receiver array; and a recording truck (Figure 6.1). Receivers in downhole arrays are positioned at regular intervals. The number of receivers in an array used in subsurface characterization has a wide range—up to several hundred is becoming increasingly common. The greater the number of receivers in an array, the fewer times the array must be repositioned for imaging long borehole intervals.

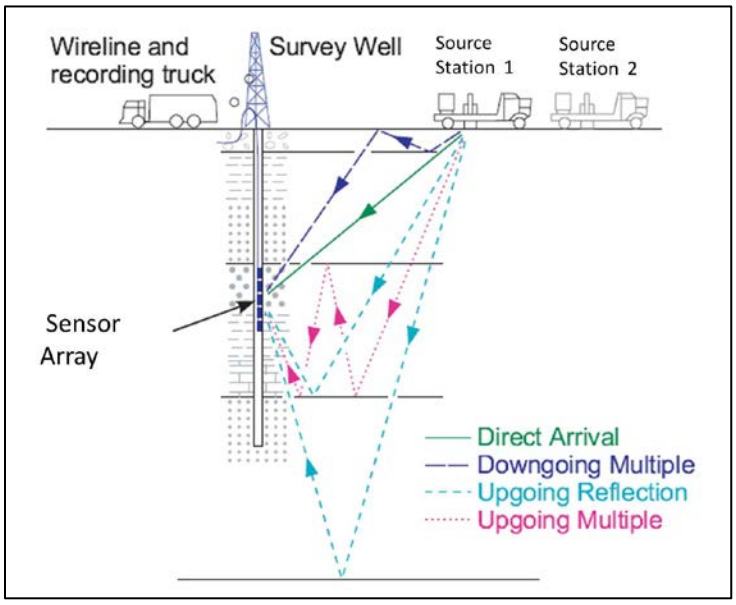

Figure 6.1. Schematic view of a VSP survey and some of the components of the seismic wavefield (after Stewart 2001).

If a single seismic energy source position is used within a few hundred feet of the borehole, the survey is referred to as a zero-offset VSP (ZOVSP); at a longer seismic- source distance the borehole survey is an offset VSP (OVSP) (Figure 6.1). Also, if the source is successively activated at regularly spaced intervals in a line away from the well, the survey is termed a walk-away VSP (WAVSP) (Figure 6.1). Because of the critical angle of reflection, the farthest source in a WAVSP is generally located at a distance approximately equal to the depth of the lowest receiver, and the resulting 2D image will extend about half of that distance away from the borehole. A 360-degree survey consisting of offset VSPs arranged along specified azimuths and radial distances from the borehole is a walk-around survey. Walk-around surveys are especially important for evaluating anisotropy and fracture sets using shear-wave splitting analysis.

Acquisition of a VSP with a full areal pattern of source positions on the Earth's surface constitutes a 3D VSP. To optimize costs, 3D VSP surveys are commonly piggy-backed on 3D surface seismic surveys. The simultaneous acquisition of a 3D VSP and a 3D surface survey produces a full volumetric picture of the subsurface and allows a direct comparison of the data. However the spacing of sources for the VSP survey usually has to be supplemented to provide adequate multiplicity of coverage (seismic "fold").

The typical 3D borehole seismic image volume (Figure 6.2) is somewhat cone-shaped with the top of the cone coincident with the top receiver in the borehole array. The size of the base of the cone is determined by the depth of the image volume and the offset of the sources.

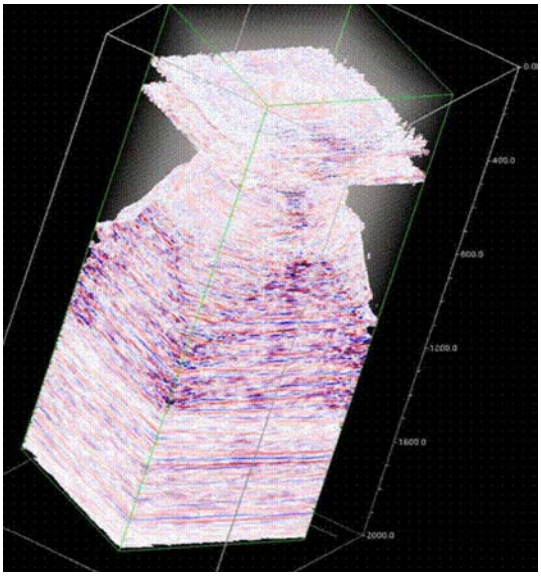

Figure 6.2. Example of a processed, interpretation-ready 3D VSP volume (from Müller et al. 2008).

6.2.4 Cross-Well Seismic Monitoring

Cross-well surveys have been successfully demonstrated for high-resolution imaging of the CO_2 plume at several sites including those at Nagaoka, Japan; Frio site near Houston, Texas; Ketzin, Germany; and the SECARB site in Cranfield, Mississippi.

Cross-well seismic surveying requires a minimum of two wells that extend to at least the base of the injection reservoir. Seismic sources suspended on a cable are lowered down one well and a cable containing a set of receivers is lowered down the other well. This process is illustrated in Figure 6.3. Surveys can be repeated over time to monitor the movement and behavior of the CO_2.

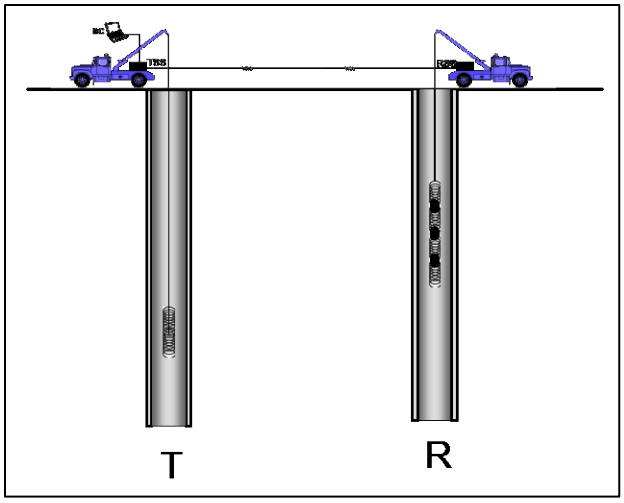

Figure 6.3. Schematic of cross-well seismic survey (Schlumberger).

Information from a single cross-well seismic survey provides data for a 2D cross section between the two wells containing the sources and receivers. A typical well separation for cross-well seismic profiling is on the order of 2,000 ft; well separation greatly depends on site-specific rock properties.

The data from a cross-well seismic survey is initially processed to give a 2D image between the two wells depicting the velocity responses of layers in the subsurface, and heterogeneity of that response between the wells. The resulting data can be processed and interpreted for a variety of attributes that reflect changes in fluid properties and permeability boundaries within the rock. A change in velocity between time-lapse surveys would generally be interpreted as evidence of CO_2 plume migration. Seismic amplitude may change with CO_2 saturation, or with changes in pressure; changes in frequency can also reflect changes in fluid properties.

Cross-well seismic monitoring is generally conducted within the injection zone, and results in much higher frequency and better resolution imaging. The seismic source can emit a signal with frequencies between 100 and 1,200 Hz, compared with the typical surface seismic signal frequency of 8−120 Hz. Depending on the reservoir velocities and dominant seismic frequencies obtained, two successive time-lapse cross-well seismic surveys may be able to detect the presence of the CO_2 plume to within 10 ft. While typically deployed in vertical boreholes, this technology has also been applied to horizontal wells (Guoping and Majer 2002) or between a single horizontal well and the ground surface.

6.2.5 Magnetotellurics and Controlled-Source Electromagnetics

Similar to ERT, MT and CSEM investigations can provide information about the 3D electrical resistivity (inverse of conductivity) of the subsurface. The high salinity and hence high electrical conductivity of the Mount Simon reservoir pore fluid should provide a relatively large contrast with the more resistive CO_2 that may result in a measureable target for the MT and CSEM methods. The granite basement is also expected to have a high resistivity contrast compared to the sandstone reservoir.

While the resolution of layer thickness is low in comparison to 3D seismic techniques, MT combined with CSEM is a relatively inexpensive monitoring method. Prior to data acquisition for characterization and monitoring, forward modeling should be conducted to evaluate the usefulness of the techniques under

site-specific conditions. These simulations will help to more precisely define the resolution limitations and determine the saturation changes that can be resolved.

MT and CSEM methods each measure electromagnetic fields that interact with geologic materials, but the methods differ based on the nature of the sources used. The MT method makes use of the Earth's naturally occurring magnetic fields and their associated induced telluric currents. CSEM, as the name implies, uses artificially generated current sources to produce electromagnetic fields that can then be analyzed to infer subsurface electrical properties.

Several numerical studies have suggested the possibility of monitoring CO_2 injection using MT/CSEM methods (Gasperikova and Hoverstan 2006; Commer and Newman 2009; Zhdanov et al. 2013). Generally, CSEM methods using borehole sources have been shown to provide superior results over MT methods.

6.2.6 Time-Lapse Gravity Monitoring

Four-dimensional (4D or time-lapse) microgravimetry—the temporal change of gravity at the microGal scale (1 μGal = 10−6 m/s^2)—is a cost-effective and relatively rapid means of observing changes in density distribution in the subsurface, particularly those caused by the migration of fluids.

Time-lapse gravity has been used since 1961 (Allis and Hunt 1986), but substantial improvements in gravimeter technology, and the advent of highly precise GPSs, have led to rapid growth in microgravity applications in the last 10 years. This technology has been successfully applied in geothermal fields, volcano monitoring, petroleum production, and reservoir characterization (Biegert et al. 2008), as well as to near-surface groundwater infiltration and migration through sedimentary units (Chapman et al. 2008; Leirião et al. 2009). Several studies in enhanced oil recovery and carbon sequestration have shown the ability to observe subsurface density variations resulting from CO_2 injection (Arts et al. 2008; Chapman et al. 2008; Davis et al. 2008; Ferguson et al. 2007).

Time-lapse gravity monitoring is conducted using repetitive annual surveys at a series of points located at the ground surface (permanent stations). Gravity changes can be linked to replacement of water by CO_2 providing an indirect method of tracing the displacement of the CO_2 plume at depth. Subsurface density changes result from the injection of CO_2 that cause changes in the gravitational acceleration at the surface. A number of other factors also influence the gravity signal and must be corrected for in order to extract useful information related to CO_2 injection.

The Earth is not a static, perfectly homogeneous sphere and as a result, gravitational acceleration is not constant at all points on the Earth's surface. The observed gravitational acceleration is influenced by several factors that must be accounted for in order to isolate the effect of subsurface density variations on the signal. First, both the rotation of the Earth along with its roughly ellipsoidal shape creates latitude-dependent gravity effects. Next, because the gravitational force is proportional to the square of the distance from the center of mass of the Earth, it is necessary to remove changes caused by station elevation, which can be broken down into two types of effects. The first effect is simply the result of elevating the measurement point, whereby air is assumed to be between the measuring device and the vertical reference datum and is removed to give the free-air correction. The second effect is the result of elevating the station and accounting for bulk material between the meter and the datum, and is called the Bouguer correction. In addition, a terrain correction can be used to account for variations in the surface

(hills and valleys) surrounding the station. Also, gravity changes due to movement of the sun and moon and can be accounted for using Earth-tide corrections. Finally, instrument drift occurs and can be removed by repeat measurements at a subset of stations during the gravity survey. After all of the various corrections have been applied to the base gravity measurement, the result is termed the Bouguer anomaly and provides a first-order depiction of lateral variations in the gravitation acceleration.

Gravity data can then be further analyzed through inversion to estimate the 3D subsurface density structure. However the inverse solution is highly non-unique and gives the best results when used as a complement to other methods (e.g., deformation, seismic).

6.2.7 Integrated Deformation Monitoring

Land-surface deformation caused by injection/extraction of subsurface fluids has been a recognized phenomenon since the early to mid-1900s (Jacob 1940; Biot 1941). Recent scientific studies have examined land-surface deformation that is associated with the injection of water for aquifer storage/recovery projects, as well as the injection of CO_2 associated with enhanced oil recovery and carbon sequestration projects (Morris et al. 2011; Vasco et al. 2010).

A simple method of predicting land-surface deformation caused by the formation pressure increases associated with long-term CO_2 injection uses a linear relationship between stress and strain. Using this simplified linear stress-strain conditions deformation can be expressed using the following relationship (Lohman 1961):

$$\Delta m = m\, c_r\, \Delta p \qquad (6.5)$$

where

Δm = change in formation layer thickness, m; (L)
c_r = compressibility of the formation layer; (L2/F)
Δp = change in formation fluid pressure; (F/L2).

Several simplifying assumptions underlie Equation (6.5): 1) the deformation predicted is horizontally constrained, 2) all associated deformation is expressed vertically, 3) vertical deformation occurs instantaneously and concurrently with formation layer pressure change, and 4) vertical deformation at depth for an individual formation layer is expressed equivalently at land surface (i.e., there is no deformation attenuation or amplification attributed to overlying or underlying formation layers). Given these assumptions, deformations calculated using Equation (6.5) are expected to provide maximum value estimates.

In addition to analytical estimates, 3D numerical geomechanical modeling can be used to calculate the expected surface deformation associated with the injection of CO_2. In both cases, compressibility, layer thickness, and the expected fluid pressure changes are required for each geologic layer in order to estimate the injection-induced deformation at the surface.

Using permanent GPS stations, tiltmeters, and annual DGPS surveys, very small surface deformations can be mapped and tracked at discrete points through time. Surface displacements of the ground at a larger scale can also be measured accurately using DInSAR. Each of these methods has been implemented on active storage fields (e.g., water, natural gas, CO_2), and recently the DInSAR technique

was successfully used at a commercial-scale CO_2 sequestration site at In Salah, Algeria, where a significant surface uplift of 5 mm yr^{-1} has been observed after injection of CO_2 and where spatial contours of the deformation helped define the CO_2 plume shape and subsurface discontinuities (Morris et al. 2011; Vasco et al. 2010).

DInSAR provides displacement measurements along the line-of-sight (LOS) between an orbital synthetic aperture radar (SAR) and the ground. Recovery of 3D displacements requires the use of three or more separate InSAR data sets that are acquired using non-coplanar geometries or supplemental information from ground-based GPS surveys. A wide range of surface characteristics and deformation types may be imaged by using different radar frequencies, transmission and reception polarizations, and platform flight headings.

All InSAR deformation measurements are corrupted by spatial and temporal variations in the atmosphere and scattering properties at the Earth's surface. Decorrelation effects are a critical factor affecting the application of InSAR. Noise sources may be mitigated to varying degrees by radar parameter choices tailored to characteristics of the site as well as the timing and frequency of the data acquisitions and by making use of artificial reflectors (ARs). ARs are devices that exhibit a high radar cross section and ideally remain structurally stable over time. In addition, advanced InSAR time-series analyses exploit a subset of pixels in a stack of many SAR images to reduce atmospheric artifacts and decorrelation effects. These pixels exhibit high phase stability through time. The output products from these advanced techniques include a pixel average velocity accurate to 1−2 mm/yr and a pixel time series showing cumulative deformation accurate to 5−10 mm for each of the SAR acquisition times. It should be noted that accuracy improves with time as time series become larger.

6.2.8 Pulsed-Neutron Capture Logging

Pulsed-neutron capture logging is a widely used method for cased-hole saturation monitoring (Youmans et al. 1964). PNC logs can be used to discriminate hydrocarbons, saltwater, and gas-bearing reservoir units. In addition to characterization activities, repeat PNC logs can be used to monitor saturation changes with time (Clavier et al. 1971b; Cowan and Wright 1999).

PNC logs operate by generating a pulse of high-energy neutrons and subsequently measuring the neutron decay over time and across a wide energy spectrum. High-energy neutron pulses are typically generated by creating deuterium or tritium ions and then accelerating them at a deuterium or tritium hydride target. Collisions between deuterium and tritium produce energetic neutrons (~14.1 MeV) that then travel out into the borehole and surrounding formation. The decay rate is affected by the elemental composition of the materials surrounding the PNC tool. For instance, the presence of chlorine in brine, which has a high neutron capture cross section, results in a more rapid neutron decay rate than for hydrocarbons. Neutrons can be detected either directly or by measuring the gamma rays that are emitted as a result of the neutron capture process (Youmans et al. 1964). PNC logs operate in two common modes: thermal capture cross section (sigma) mode and carbon/oxygen ratio (C/O) mode. In sigma mode all elements that capture and slow neutrons contribute to the measurement. In C/O mode only gamma energies associated with carbon (4.1−4.9 MeV) and oxygen (5.8−6.7 MeV) are used.

PNC logs are only sensitive to a localized region surrounding the borehole (15−30 cm) and are therefore susceptible to interference from features very near the borehole such as changing borehole fluids, degraded cement, or invasion of drilling fluids. Borehole effects can be minimized by using the

fact that material near the borehole responds at earlier times than deeper in the formation and by incorporating multiple detectors in the tool. Monte Carlo N-Particle (MCNP) modeling can be done to simulate near borehole interferences and remove their effects from the signal. Modeling is a recommended procedure but requires knowledge of the target formations and fluids. PNC measurements are also less effective in low porosity (<15%) formations, largely because of the smaller volumetric amount of fluids contributing to the measurement.

6.3 Geophysical Technology Screening and Selection

As discussed previously, geophysical monitoring methods considered for the FutureGen 2.0 storage site included electrical resistivity tomography, passive seismic monitoring, 2D and 3D surface seismic surveys, vertical seismic profiling, cross-well seismic imaging, time-lapse gravity, magnetotellurics and controlled-source electromagnetics, integrated deformation monitoring, and PNC logging. Each of the technologies was evaluated, as described in the following sections, with respect to site-specific conditions, subjected to a screening process, and suitable methodologies were selected for deployment as part of the monitoring program. This selection process considered the level of sensitivity, spatial resolution, the costs to install and operate, the potential for interference with other monitoring activities, and the likelihood of landowner acceptance. Technologies that were selected for implementation included passive seismic monitoring, time-lapse gravity, integrated deformation monitoring, and PNC logging.

6.3.1 Electrical Resistivity Tomography

ERT has potential for detecting and quantifying $scCO_2$ saturation within a reservoir and for detecting and quantifying fugitive CO_2 above the primary confining zone in the event of a large-scale loss of containment. Several site-specific aspects of the ERT design were tested under FutureGen 2.0 project site-specific conditions, including 1) laboratory measurements of reservoir core sample resistivity under varying CO_2 saturations and 2) a field-scale evaluation of surface electrode construction, site electrical noise conditions, and the required noise-reduction methods.

6.3.1.1 ERT Core Tests

The first step in the investigation of ERT for monitoring at the FutureGen 2.0 storage site was to measure the change in bulk electrical conductivity of cores as brine is displaced by $scCO_2$. This section is a summary of the methods and results from experiments performed on cores obtained from the initial FutureGen 2.0 stratigraphic borehole.

The relationship between bulk electrical conductivity (EC) and $scCO_2$ saturation was investigated using the following experiments that were conducted using Mount Simon and Eau Claire Formation cores at approximated in situ conditions. This was done using synthetic brine based on O'Conner and Rush (2005) and Mount Simon and Eau Claire (Lombard) cores obtained from depths of 1,202.0 m and 1,156.3 m, respectively. The original, 2.5-cm−diameter cores were cut to lengths of approximately 14 cm and inserted into a core holder as seen in Figure 6.4. These cores were sealed into a core holder with two stainless steel (SS) mesh current electrodes on each end of the cores and two silver/silver chloride coiled wire potential electrodes pressed against the circumference of the cores, which were located 4.5 cm from each end of the core (or approximately 5 cm apart). The inner core holder was contained within a

polyetheretherketone (PEEK) pressure chamber, which was used to contain a 12.1 MPa (1,750 psi) overburden pressure around the core holder using two Teledyne ISCO, Inc. high-pressure pumps. The overburden fluid was deionized water and the valve controlling access to the overburden pressure was closed once the target pressure was reached; this is important for mass balance.

After the PEEK pressure chamber and its contents had thermally equilibrated at ~38°C, experiments that were designed to vary brine/$scCO_2$ saturation and measure bulk EC were performed in two stages. In the first stage, cores were initially saturated with $scCO_2$ and brine was injected into a core to obtain EC values at low brine saturations. In the second stage, cores were initially saturated with brine and $scCO_2$ was injected into the core to obtain EC values at higher brine saturations.

For both stages of the experiment, bulk EC and the mass of the entire pressure chamber were measured after ~0.25, 0.5, 1, 3, 9, and 25 pore volumes were injected into the cores. To measure the mass and collect accurate EC measurements, valves were closed to the core holder and pressure lines were disconnected. The entire pressure chamber was weighed and the $scCO_2$/brine saturation was calculated from the change in mass associated with the difference in specific gravity between $scCO_2$ (density = 0.69 g/mL) and brine (density = 1.05 g/mL) and the porosity and volume of the sample.

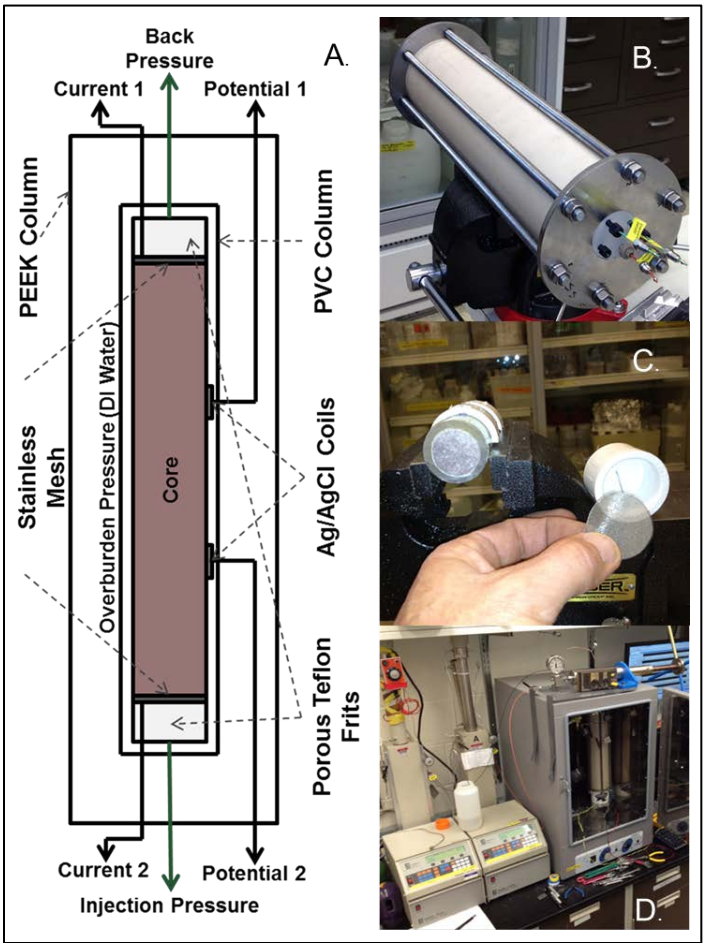

Figure 6.4. (A) The configuration of the core, electrodes, and tubing within the core holder. (B) The PEEK pressure chamber that is used to contain the overburden pressure. (C) Core holder end cap with screen electrode. (D) ISCO pumps and environmental chamber.

The results from these experiments are summarized in Figure 6.5, which shows the bulk conductivity over the brine-saturated bulk conductivity versus the brine saturation. Although the full range from 100% brine content to fully $scCO_2$-saturated shows a very large decline in EC, the brine saturation is not expected to go below 0.4, which at most corresponds to approximately a 5 times reduction in bulk electrical conductivity.

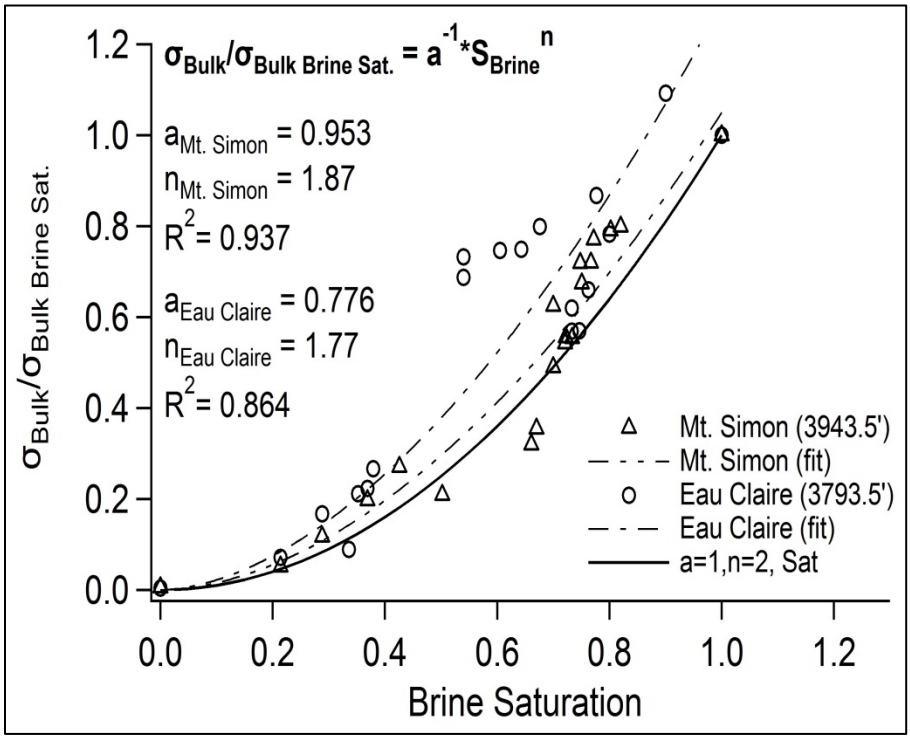

Figure 6.5. Relative bulk conductivity versus brine saturation with calculated Archie's Law parameters for the Mount Simon (triangles) and Eau Claire (circle) cores. The solid line is calculated using typical Archie's law parameters for sandstone.

6.3.1.2 ERT Field Tests

The noise levels present at the field site can have a major impact on the ability of the ERT technology to resolve changes that occur because of injection of CO_2. Signal enhancement and noise reduction can be accomplished by increasing the applied EC and by data averaging and filtering, respectively. Field-scale ERT tests were conducted at the FutureGen 2.0 storage site to investigate the effects of electrical noise and to optimize ERT system components.

Surface-current electrodes capable of efficiently injecting currents up to 20 A would be needed to implement a large-scale ERT array. For a specific electrode, the current injected is proportional to the applied voltage. An efficient current electrode must be able to inject high currents using the lowest possible voltage. This can be done by lowering the contact resistance with the soil by increasing the pore-water salinity, the soil moisture content, or by increasing the surface area of the electrode. Electrodes were tested at the FutureGen 2.0 storage site to determine the optimum required surface area. It was found that the current was roughly proportional to the square root of the plate surface area and that a 4-ft-

square electrode could provide sufficient surface area to deliver 20 A using a 500-V maximum power source, assuming that the resistance of the connecting wiring is less than 10 ohms (Figure 6.6).

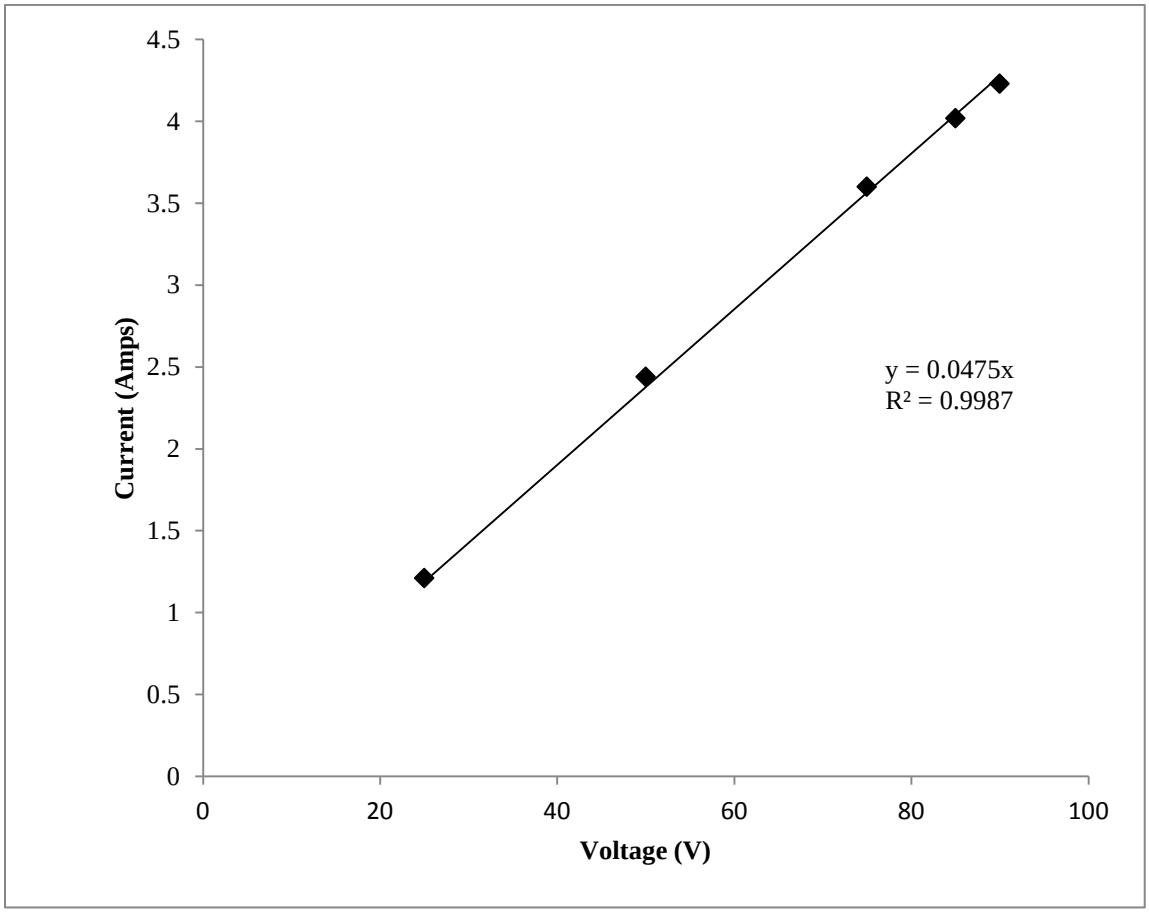

Figure 6.6. Current versus applied voltage relationship for a 4-ft by 4-ft sheet electrode.

The electrical noise characteristics at the FutureGen 2.0 storage site were evaluated using a quasi-2D electrode array (Figure 6.7). The array was just less than 7 km long with an electrode spacing of approximately 400 m. Approximately 40 resistivity measurements were made using multiple array types. The ERT system consisted of a 300 V/4 A Sorenson power supply, a Zonge ZT-30 transmitter, two Zonge ISO-1/B isolation amplifiers, and a 16-bit data acquisition and control unit. For all measurements, the applied current was set at the maximum (4 A) for the power supply. For large arrays, the generated potential signals can be very weak and contaminated with high noise levels. A filtering and averaging scheme similar to Bergmann et al (2012) was used to improve the data quality. An example of the data prior to processing for a 400-m dipole-dipole with 2 km separation is shown in Figure 6.8.

Figure 6.7. Array used to test electrical noise characteristics.

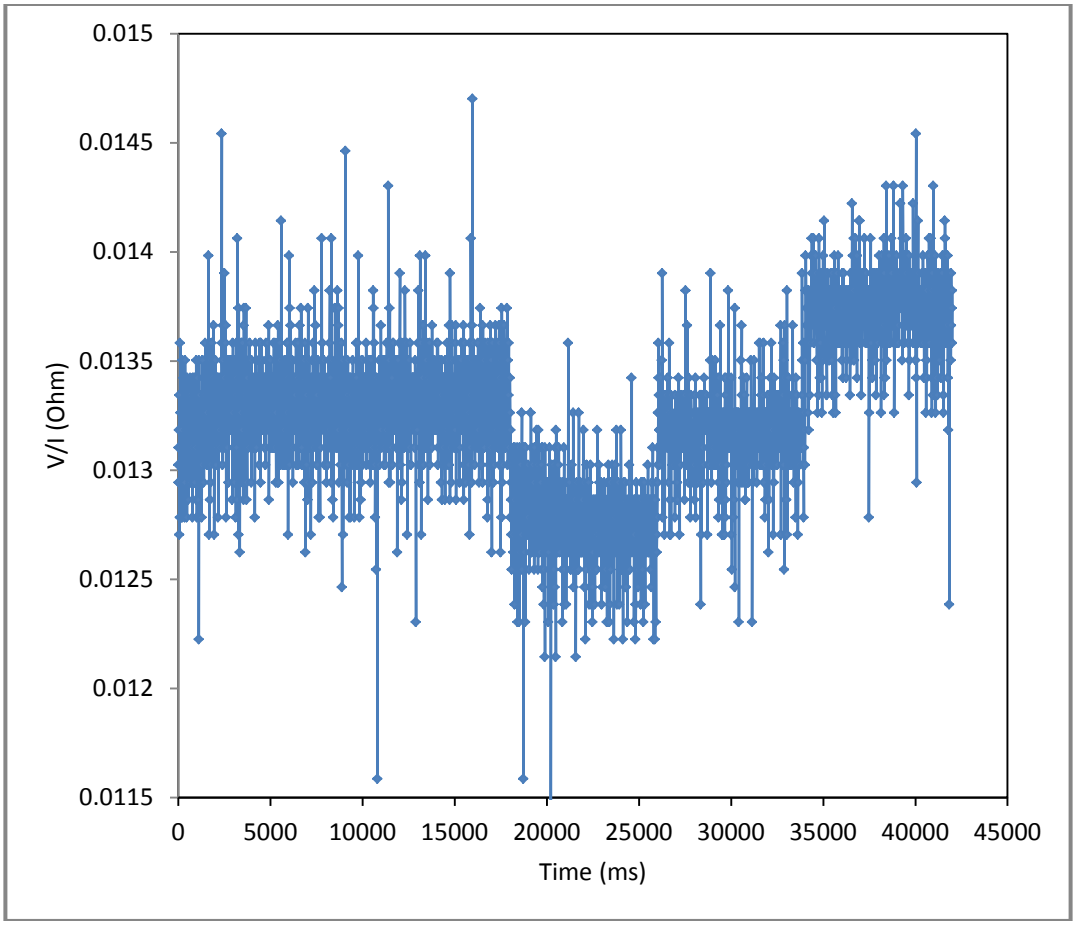

Figure 6.8. Raw resistivity data prior to processing.

It is difficult to distinguish usable information in the raw data; however, an excellent signal is obtained after processing. The results of this evaluation indicated that the data errors were generally quite good in the range of 1−5 percent (Figure 6.9).

Because of the limited number of measurements, a full 2D inversion would not provide useful information from this data set and was not the intended purpose of this evaluation. The data set obtained can be inverted using a starting 1D model to determine how consistent the data are relative to the borehole logs from the characterization well. The inverted data were consistent with the 1D resistivity structure derived from the borehole log (Figure 6.10).

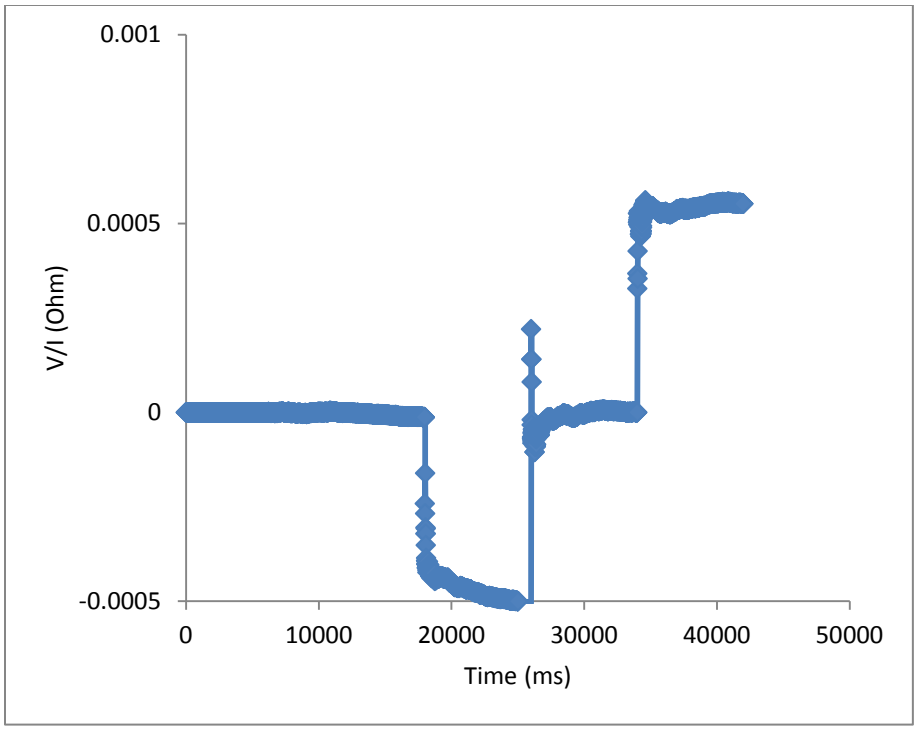

Figure 6.9. Resisitivity data after processing to enhance signal.

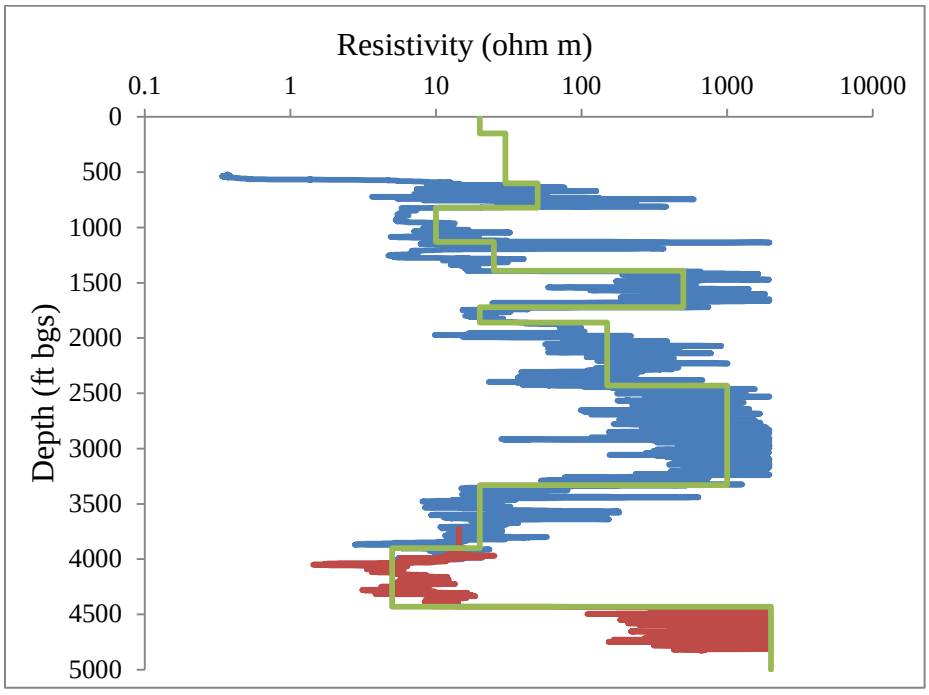

Figure 6.10. Resistivity log from the FutureGen characterization well (red and blue lines). The green line represents the averaged resistivity values used in the modeling.

6.3.1.3 Assessment of ERT

A phased study was completed to determine the feasibility of 4D ERT monitoring at the FutureGen 2.0 storage site. In the first phase, noise assessment surveys described in the previous section were conducted to determine ambient electrical noise levels. As mentioned previously, knowledge of ambient noise is critical for determining through numerical simulation whether changes in subsurface electrical potentials induced by the growing CO_2 plume would likely be detectable. The noise assessment surveys indicated relatively noise-free conditions, allowing for collection of high-quality ERT data and resulting in a decision to proceed with the second phase of the assessment.

The second phase of the assessment included a synthetic modeling study aimed at determining whether the signals produced by the growing CO_2 plume would be adequate for effective time-lapse ERT imaging using ERT arrays that are feasible under site-specific conditions. Feasible ERT arrays comprise electrodes that can be installed at the site without incurring excessive cost or risk. A number of possible ERT arrays were numerically evaluated to quantify their performance and ultimately to determine the feasibility of ERT monitoring for the FutureGen 2.0 project. To do this a parallel, finite element electrical resistivity forward modeling and inversion code was used (Johnson et al. 2010).

Other carbon sequestration projects have used cross-borehole ERT arrays for monitoring. Cross-borehole imaging generally requires that the boreholes are separated by less than two-thirds of the borehole depth (Yilmaz 2001). The volume of the CO_2 injection at the FutureGen 2.0 storage site would require an unrealistic number of boreholes to capture the entire plume extent, or even a significant portion of it. For this reason the initial focus of the evaluation was on the performance of a surface electrode array and several configurations of downhole arrays to augment the surface array. Several options exist for downhole augmentation, including vertically and horizontally discrete borehole electrodes and using the borehole casings themselves as long vertical and horizontal electrodes (Newmark et al. 2001).

The most comprehensive array meeting feasibility requirements consisted of a large array of surface electrodes (500-m spacing) aligned with existing roadways transecting the survey area (Figure 6.11). This array also used all available well casings as long electrodes for electrical potential measurement, including the horizontal injection wells, as shown in Figure 6.12. Figure 6.12 also shows the assumed pre-injected bulk conductivity distribution, which was inferred from wellbore resistivity logging data collected at the site.

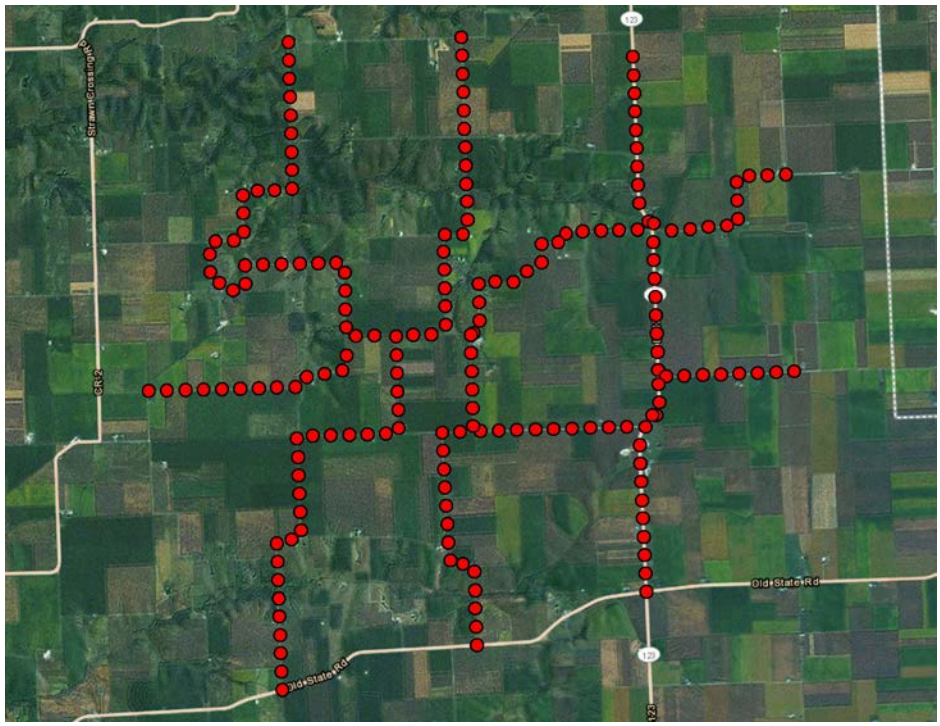

Figure 6.11. Example of ERT coverage, using road-side locations.

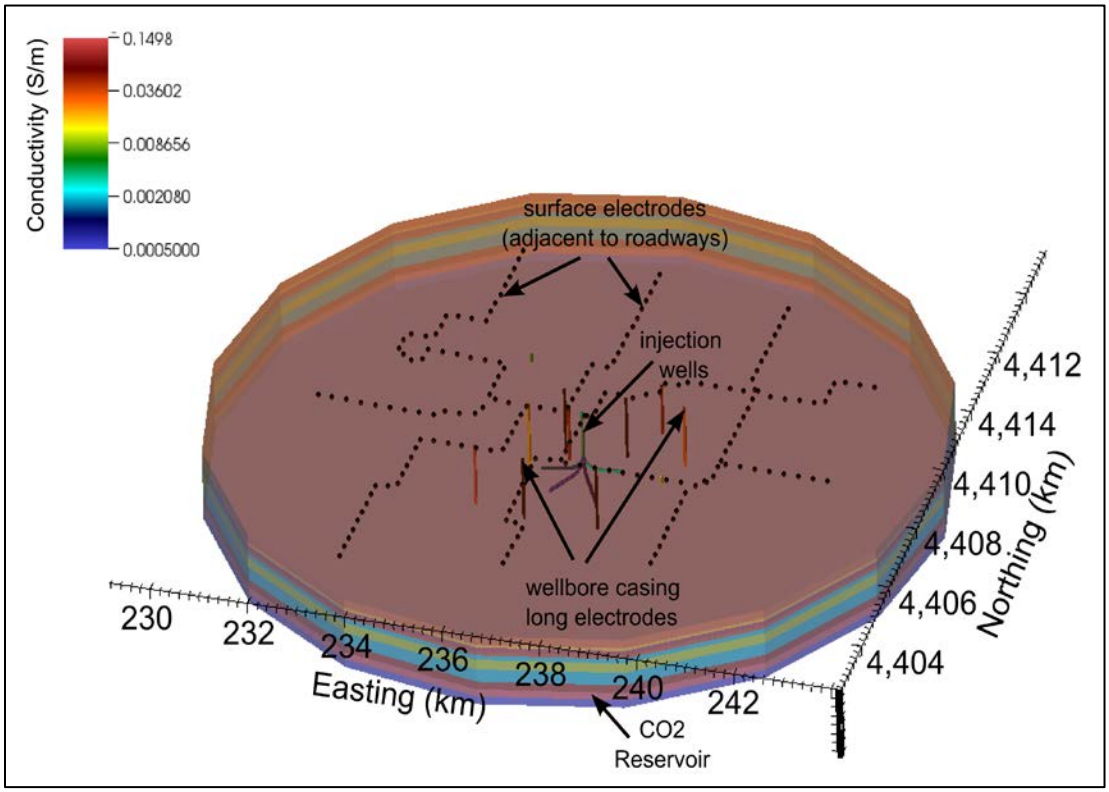

Figure 6.12. Baseline synthetic ERT conductivity model showing locations of surface electrodes, wellbore casings used as long electrodes, and pre-injection bulk conductivity structure derived from wellbore logging (shown in transparent color).

The target CO_2 plume for the synthetic ERT modeling was the simulated 3-year plume generated by the STOMP (Subsurface Transport Over Multiple Phases) model used to support the UIC permit application. To construct the conductivity distribution associated with the 3-year plume, predicted CO_2 saturations were extracted from the model and converted to bulk conductivity with an estimated petrophysical transform (Archie's law), using a reservoir porosity of 0.15, a CO_2 conductivity of 0.0 S/m, and baseline conductivity of 0.15 S/m as extracted from wellbore resistivity logging data. Core-scale lab testing (see Section 6.4.1.1) validated this petrophysical approximation. Next, a comprehensive ERT survey was simulated for both the pre-injection and 3-year conductivity distributions, and data were compared to determine if the difference in simulated responses exceeded noise levels measured during the noise assessment surveys.

These synthetic modeling results revealed that the 3-year plume did not produce a sufficient change in subsurface conductivity to allow effective imaging of the plume using the surface electrodes only. Changes in the simulated data from baseline to 3-year conditions were not sufficient to exceed 5% noise levels and most measurements were found to be less than the noise levels estimated from the field surveys at the site (Figure 6.13. ERT data differences between the baseline and 3-year simulated measurements.). In addition, subsurface potentials generated within the CO_2 plume were largely homogenized by the metallic injection wells, reducing the capability of the ERT system as a whole to detect spatial and temporal potential differences related to plume dimensions.

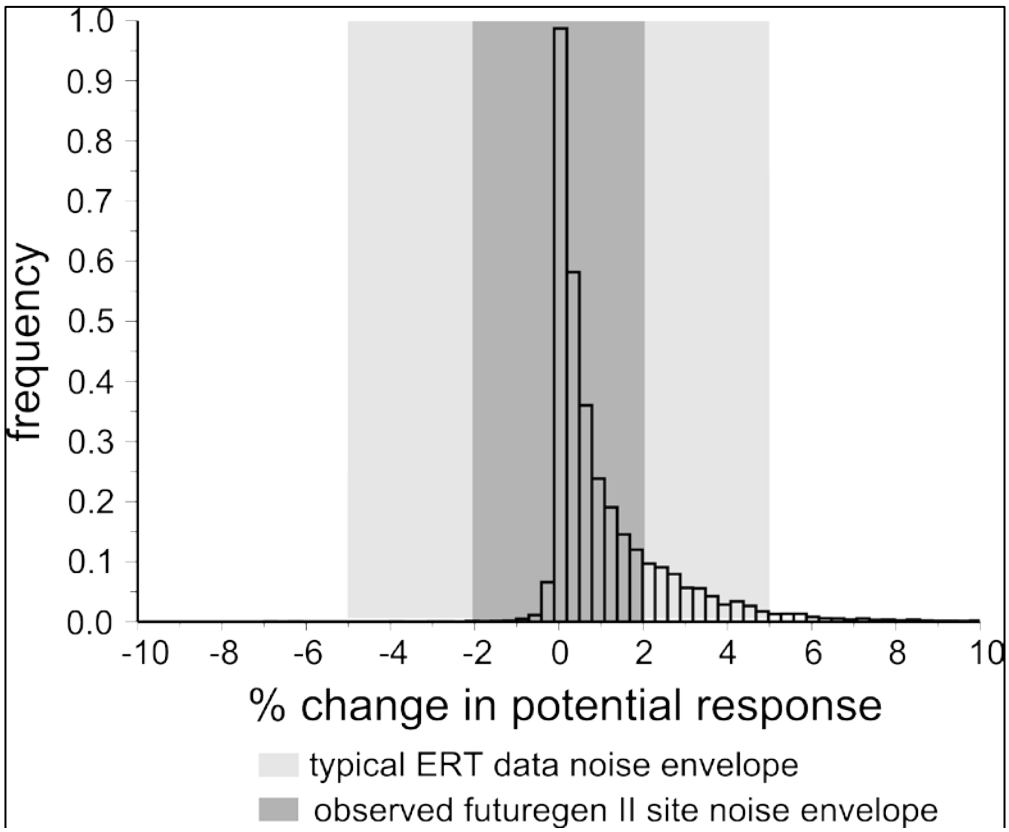

Figure 6.13. ERT data differences between the baseline and 3-year simulated measurements.

ERT data collected using well casings as long electrodes along with surface electrodes produced detectable potential differences between the pre-injection and 3-year plume, particularly those data using

the CO_2 injection wells as potential measurement electrodes. However, given the dimensions of the electrode with respect to the dimensions of the plume, the homogenizing effects of the injection wells and other wellbore casings on the potential distribution, the low number of long electrodes, and several other deleterious factors, the data derived from using wellbore casing as electrodes did not produce enough resolution to effectively image the 20-year plume (Figure 6.14. Inverted image of electrical conductivity changes caused by the 20-year CO2 plume using a surface array and all wells as long electrodes.).

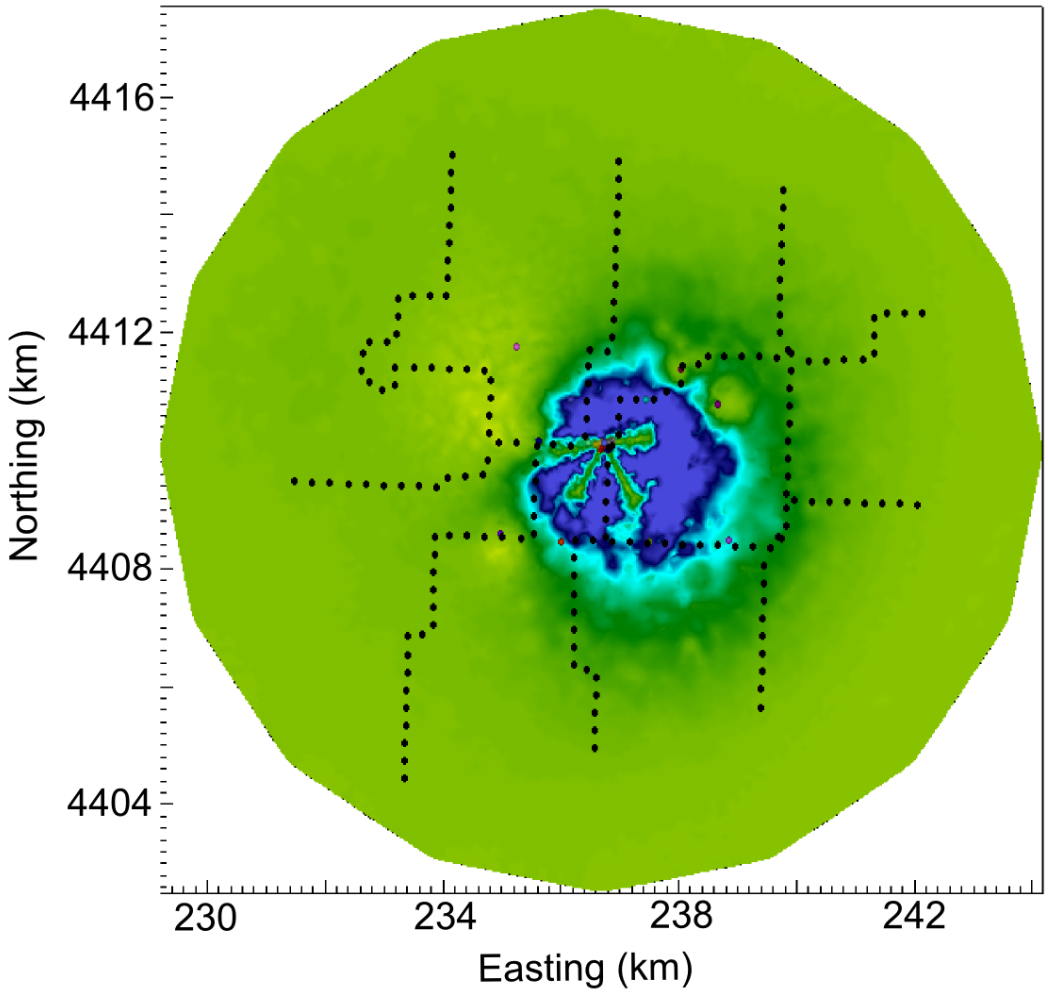

Figure 6.14. Inverted image of electrical conductivity changes caused by the 20-year CO_2 plume using a surface array and all wells as long electrodes.

In all, the factors inhibiting the effective use of ERT monitoring at the FutureGen 2.0 storage site include the following:

- electrically conductive injection and monitoring well casings
- depth of the CO_2 plume from the surface
- relatively low brine displacement (i.e., low CO_2 saturation) away from the injection wells, and consequent small change in-reservoir conductivity
- limited CO_2 plume thickness

- lack of discrete electrodes in the vicinity of the plume.

As a final test, synthetic ERT imaging was conducted assuming discrete electrodes could be placed along electrically isolated well casing (e.g., as in Ketzin, Germany, and Cranfield, Mississippi), particularly the injection wells. Results suggested ERT would effectively image the 3-year plume using this configuration.

The primary objective of implementing an ERT array would be to determine the spatial extent of the injected $scCO_2$ plume within the reservoir to inform both the model calibration and the adaptive monitoring strategy. Modeling and field test results showed that ERT will not be able to quantify the extent of the $scCO_2$ plume over the first several years of injection. Imaging of the plume at later years (~20 years) may be possible but will require that electrical noise remains low. An ERT surface array augmented with discrete electrodes emplaced along the horizontal injection wells may be able to image the CO_2 plume but would be difficult to integrate with other aspects of the injection well design.

Based on the results of this evaluation, ERT monitoring will not be included as part of the FutureGen 2.0 storage site monitoring program.

6.3.2 Passive Seismic Monitoring

Passive seismic monitoring is a useful technology for understanding subsurface processes associated with a number of activities including hydraulic fracturing, geothermal stimulation, mining, and carbon sequestration. Activities that create underground stress changes have the potential to induce very small- to moderate-magnitude seismic events. The injection of CO_2 is expected to generate small-magnitude seismic events and is the focus of the passive seismic monitoring for the FutureGen 2.0 Project.

Two general station types were considered: near-surface stations and deep borehole arrays. Surface stations were designed with a broadband seismometer and geophone emplaced within an approximately 100-m borehole. In addition to these instruments, a strong-motion accelerometer will be installed within a vault at the surface (Figure 6.15). Deep borehole sensors consist of an array of robust 3C sensors cemented on the outside of the final casing with the lowermost sensor beginning at just above the caprock and the uppermost extending to approximately 300 m bgs.

Parameter resolution tests can be performed using a grid search method by generating synthetic "observed" data from calculated travel times to which a specified amount of noise is added (Eisner et al. 2009). The chi-squared statistic can be used to determine whether a given trial solution is within a certain percentile confidence interval of the true value. The chi-squared value can be calculated from the trial, d^{trial}, observed data, d^{obs}, and standard deviation, σ, for each station using the following formula:

$$\chi^2 = \sum \frac{(d_i^{trial} - d_i^{obs})}{\sigma_i} \tag{6.7}$$

If the chi-squared value is less than the cumulative chi-squared statistic for the specified percentile and degree of freedom then the trial solution is included in the set of solutions that lie within the confidence range. If this process is repeated for a large number of trial events the size of the confidence interval for each of the parameters can be estimated.

To examine the performance of a number of possible network geometries that might be used for passive seismic monitoring at the FutureGen 2.0 storage site, an uncertainty analysis based on a grid search was performed. For this test a homogeneous velocity model was used to speed the required calculations. The velocity used was determined from an arithmetic average of the velocity log from the initial stratigraphic borehole and the standard deviation of the travel time errors was set at 1 millisecond.

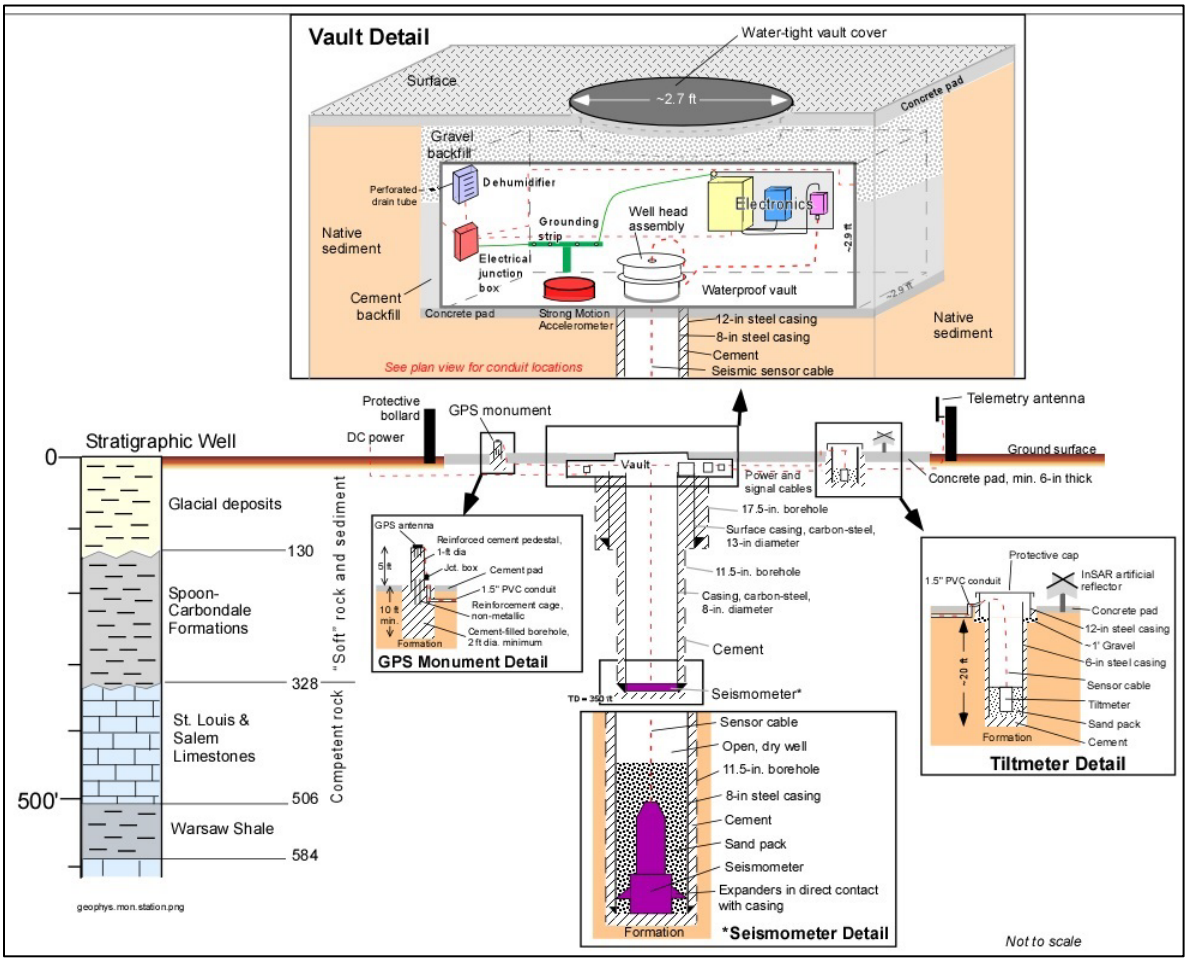

Figure 6.15. Shallow geophysical monitoring station.

Assuming that there are no errors in the velocity model, two primary parameters affect the location errors of a given seismic sensor network: sensor geometry and the maximum observable event distance. A number of cases were investigated using various network geometries and maximum event distances; a subset of cases is discussed in more detail below. For each case, 2D horizontal and vertical location error maps were generated at various depths and along two vertical transects. Location errors can be divided into horizontal (northing and easting) and vertical (depth) errors and various sensor geometries are able to resolve each component differently. A number of simplifying approximations have been used for this analysis; the results are considered a simple scoping tool to assess various passive seismic networks.

The first two cases that were compared used two likely geometries: the first one using a surface array in conjunction with a 20-level borehole array, and another with an identical surface array and an 8-level borehole array with a similar overall aperture. For both cases, the maximum event distance for the

borehole and surface sensors was set at 1,000 m and 3,000 m, respectively. As discussed in Section 6.3.2.3, the recommended surface sensors exhibit much higher sensitivity and lower noise floor than the borehole sensors, and therefore the maximum observable event distance is expected to be larger for the surface sensors. The results showed that the reduction from 20 to 8 geophone levels produced only minor degradation in location uncertainties (Figure 6.16 and Figure 6.17). Next, the effect of limited detection because of event distances was investigated (Figure 6.18 and Figure 6.19). Not surprisingly, for very

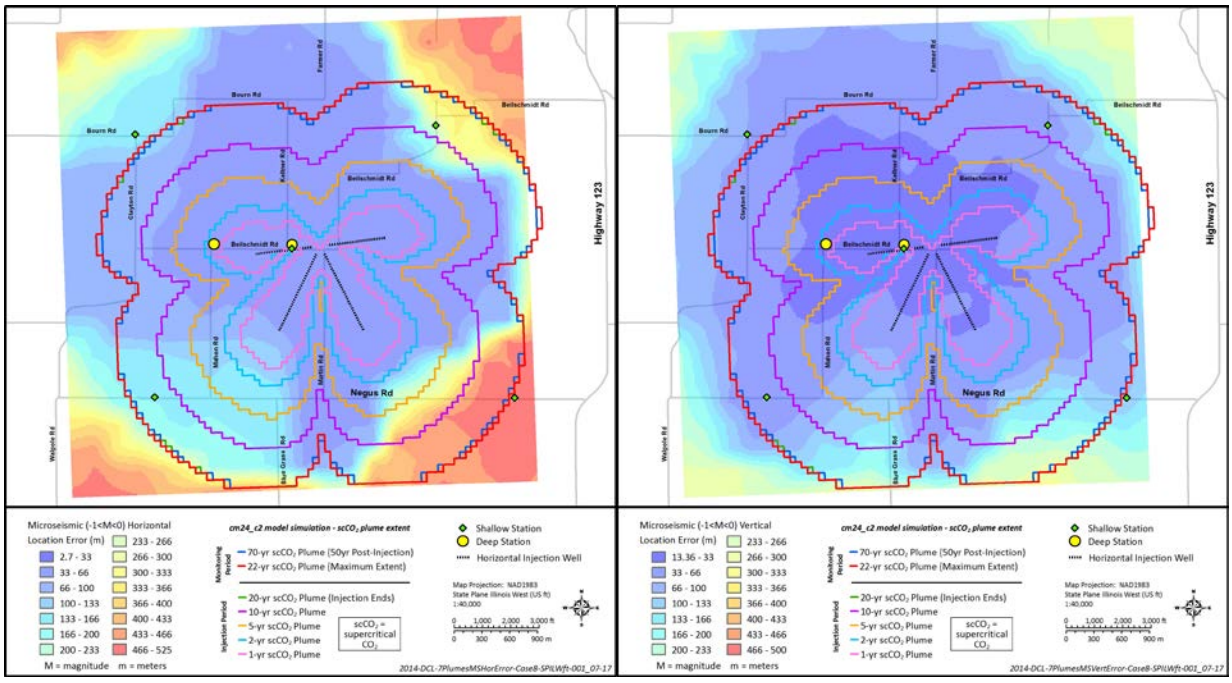

Figure 6.16. Seismic event location uncertainties: five-station surface array and 20-station borehole arrays. Maximum observable event distances: 3,000 m for surface stations and 1,000 m for borehole stations.

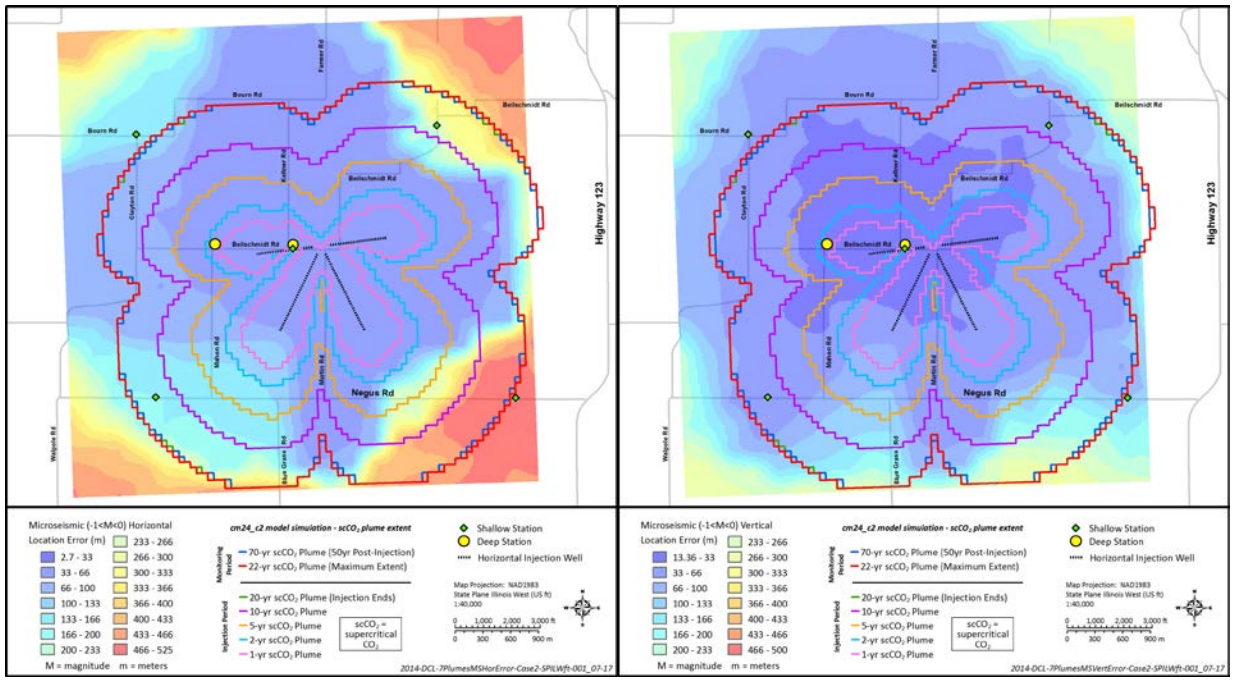

Figure 6.17. Seismic event location uncertainties: five-station surface array and 8-station borehole arrays. Maximum observable event distances: 3,000 m for surface stations and 1,000 m for borehole stations.

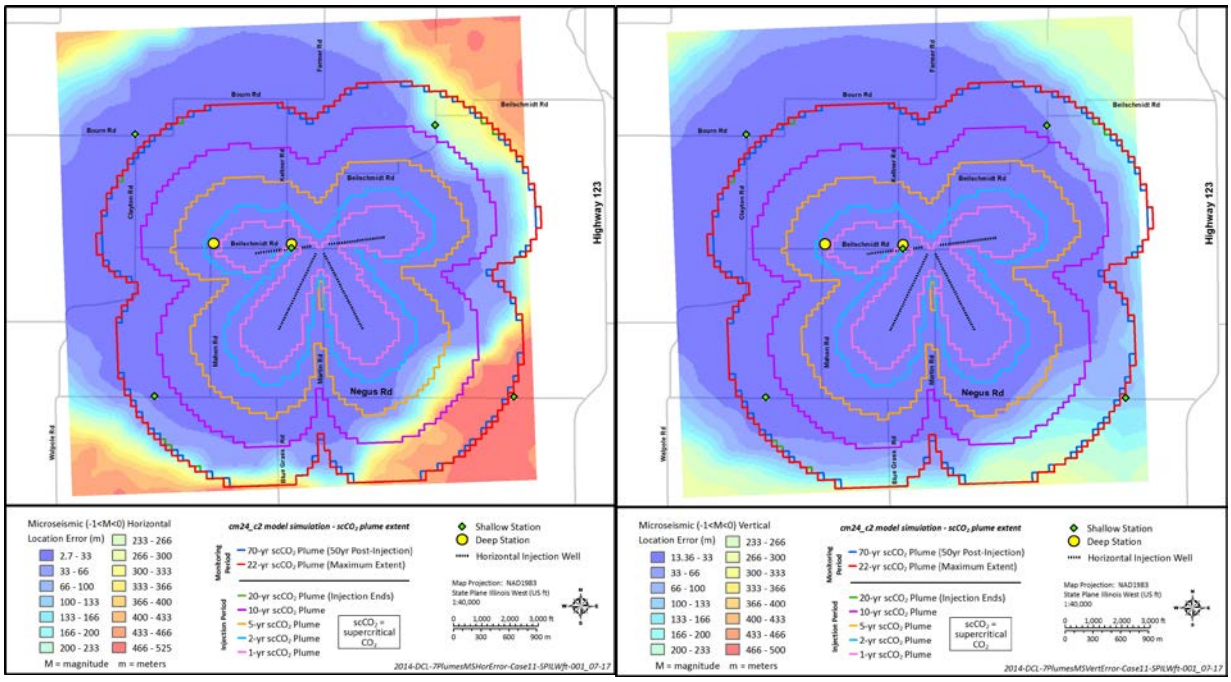

Figure 6.18. Seismic event location uncertainties: five-station surface array and 20-station borehole arrays. Maximum observable event distances: 3,000 m for surface stations and 3,000 m for borehole stations.

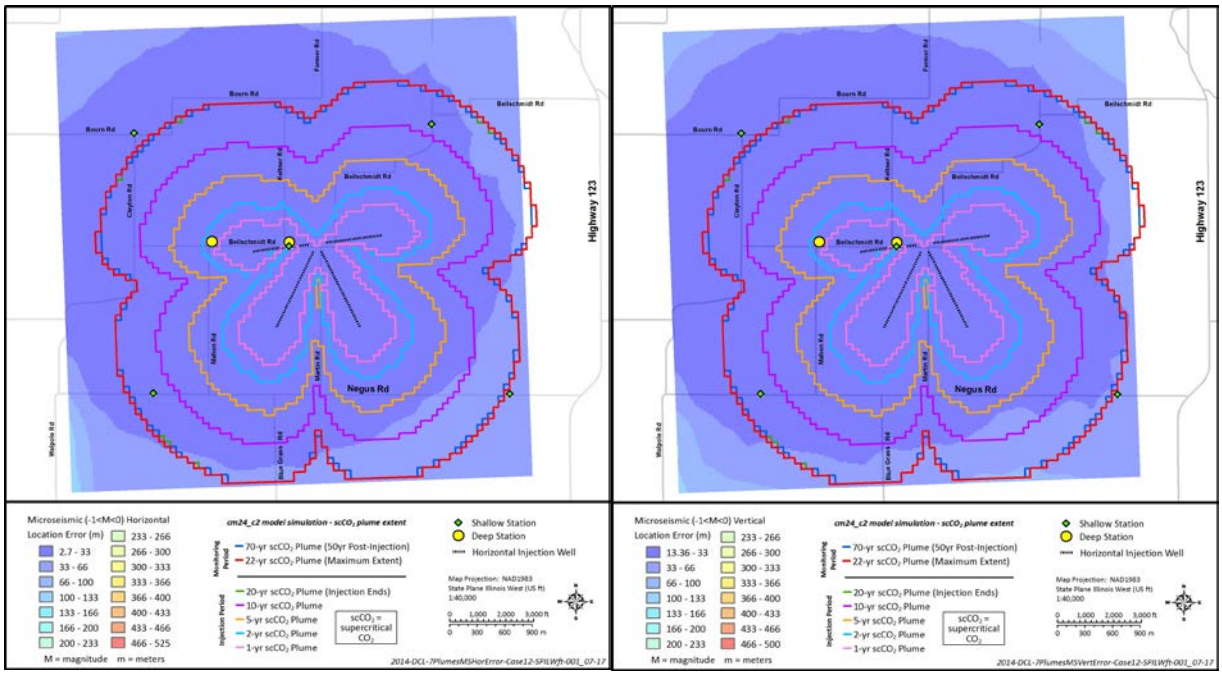

Figure 6.19. Seismic event location uncertainties: five-station surface array and 20-station borehole arrays. Maximum observable event distances: 5,000 m for surface stations and 3,000 m for borehole stations.

small-magnitude events that cannot be seen by stations at the surface, the location errors are very large away from the borehole array. As event magnitude increases the maximum observable event distance also increases; additional stations can then measure the event and the errors are reduced.

Use of a surface array or borehole array alone can also be implemented. A surface array can provide good lateral coverage of the area of interest but is also much more dependent on an accurate velocity model, particularly with regard to determining the depth of an event. As mentioned earlier, this analysis did not investigate the effects of velocity model errors, which can in practice dominate the total error in event location. Alternatively, event location using simple triangulation and an array of borehole sensors that are perfectly vertical will only be able to locate the depth of an event, not an accurate event location. Back projection methods can be used with a borehole array to estimate events both horizontally and vertically, but this approach was not used in this analysis. Back projection methods make use of the polarization of the seismic wave and are therefore very sensitive to velocity errors in the vicinity of the borehole that locally distort the polarization.

In addition to the effects of station network geometry, redundancy and cost must also be considered in choosing the appropriate passive seismic network. While it is clear that increasing the number of borehole sensors from 8 to 20 only minimally improved the ability of the network to locate events, the sensors are required to last several decades. A substantial portion of the equipment used for fiber-optic-based geophones is required regardless of how many sensors are interrogated. As a result, the data acquisition system and initial few sensors make up a majority of the monitoring system cost. Based on the above location uncertainty analysis, the need for sensor redundancy, and the relative partitioning of system component cost, a five-station surface array and two approximately 20-level, 3C deep borehole arrays will be used for the passive seismic monitoring network. The borehole sensor depths of the

proposed seismic network are listed in Table 6.1. Actual noise levels and sensor magnitude detection limits at the stations cannot be determined until after the sensors have been emplaced and monitored for a period of time. The proposed deep borehole and surface sensor arrays are expected to have adequate azimuthal and vertical coverage such that good-quality moment tensor inversions can be performed for events that are detectable at all stations. As part of the overall adaptive monitoring strategy, information obtained from future characterization and monitoring activities may warrant incremental changes to the passive monitoring system.

Given the various simplifying assumptions, preliminary seismic event location uncertainty results for the selected array are shown in Figure 6.16 through Figure 6.19. These results indicate that the array should perform well for most moderate and larger magnitude (greater than -2 or -1) seismic events that might occur within the extent of the 20-year CO_2 plume, as well as smaller magnitude events that occur nearer to the borehole arrays.

Based on the results of this evaluation, passive seismic monitoring will be included as part of the FutureGen 2.0 storage site monitoring program.

Table 6.1. Depths of tested borehole array configurations.

20-Station Borehole Array Station Depths (m)	8-Station Borehole Array Station Depths (m)
300	300
350	600
400	700
450	800

Table 6.1. (contd)

20-Station Borehole Array Station Depths (m)	8-Station Borehole Array Station Depths (m)
500	900
550	940
600	980
650	1,020
700	
750	
800	
850	
900	
920	
940	
960	
980	
1,000	
1,020	
1,040	

6.3.3 Reflection Seismic Surveys

Surface-based reflection seismic technology has been demonstrated at several CO_2 sites including Weyburn, Sleipner, and Decatur. Reflection seismic surveys have been effectively used for mapping the pressure front (velocity increases in response to increased reservoir pressure) and displacement of brine by CO_2 (velocity decreases) during CO_2 injection in the North Sea (Verdon et al. 2013). Fluid substitution modeling suggested that seismic amplitude differences at Decatur could be detected out to a distance of 1,000 ft by time-lapse VSP. However, time-lapse 3D VSP acquired in February 2012, after an injected CO_2 volume of 74,000 metric tons, failed to detect a CO_2 signal above background noise (Coueslan 2012).

The utility of reflection seismic methods for monitoring the injection of CO_2 depends on a number of site-specific properties and should be evaluated on a site-by-site basis. Results from a quantitative assessment of reflection seismic under site-specific conditions are presented below.

6.3.3.1 Seismic Fluid Substitution Modeling

A modeling study was performed to investigate the efficacy of reflection seismic methods for CO_2 monitoring at the FutureGen 2.0 storage site. The model results show that the reflection signal differences between brine-saturated rock and rock having a pore fluid mixture of 20 percent brine and 80 percent CO_2 is small. For the sequestration interval at the FutureGen 2.0 storage site it will likely not be possible to detect sequestered CO_2.

Two different thicknesses were considered for the sequestration interval in this modeling exercise. First, an interval thickness of 54 ft was used extending from 4,036 ft to 4,090 ft bgs. Next, a thinner, 20-ft−thick, high-porosity unit was modeled extending from 4,036 ft to 4,056 ft measured log depth.

The target injection interval logs acquired in the initial stratigraphic borehole are shown in Figure 6.18. A Gassmann fluid substitution model was used to calculate the changes in seismic properties caused by changes in bulk density and compressional-wave velocity. The salinity of the in situ brine was assumed to be 47,500 ppm, resulting in a fluid density of 1.03 gm/cm^3. CO_2 was assumed to be at reservoir pressure and temperature conditions of 1,792 psi and 96.6°F, which produced a supercritical fluid-phase density of 0.74 gm/cm^3. The effects of CO_2 saturation are illustrated in Figure 6.20 for V_P and in Figure 6.21 for bulk density. These fluid substitution results are shown for the highest porosity interval of the potential CO_2 sequestration interval. Several values of CO_2 saturation are assumed in these two illustrations, with the largest CO_2 saturation being 80 percent of available pore space. The largest variations in bulk density and V_P velocity occur in the highest porosity zones of the interval. Even in the highest porosity zones present within the reservoir, the variation in rock properties is only 2 percent for bulk density and 5 percent for V_P at the maximum expected CO_2 saturation of 80 percent. These variations in V_P and bulk density induced by CO_2 injection are quite small compared to the large values for the Mount Simon reservoir sandstone.

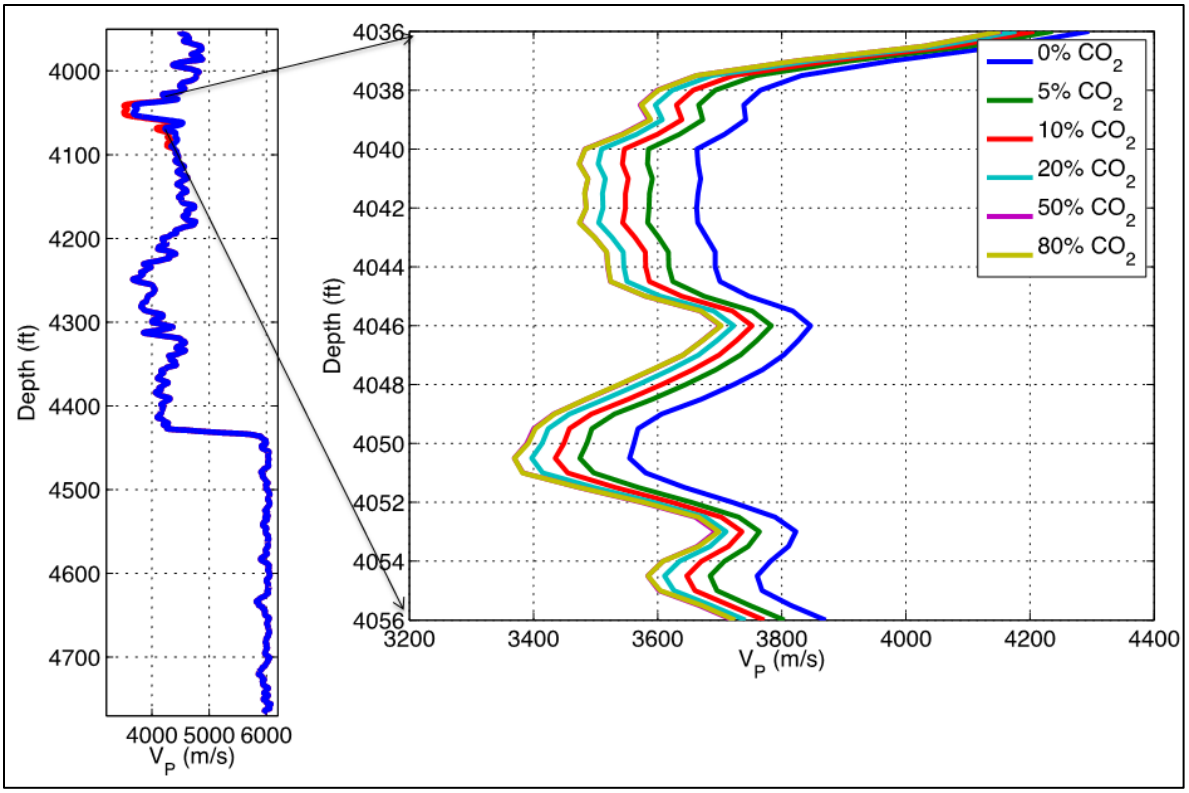

Figure 6.20. Compressional-wave velocity log data from SLR1 and Gassmann fluid substitution predicted velocity changes within the reservoir.

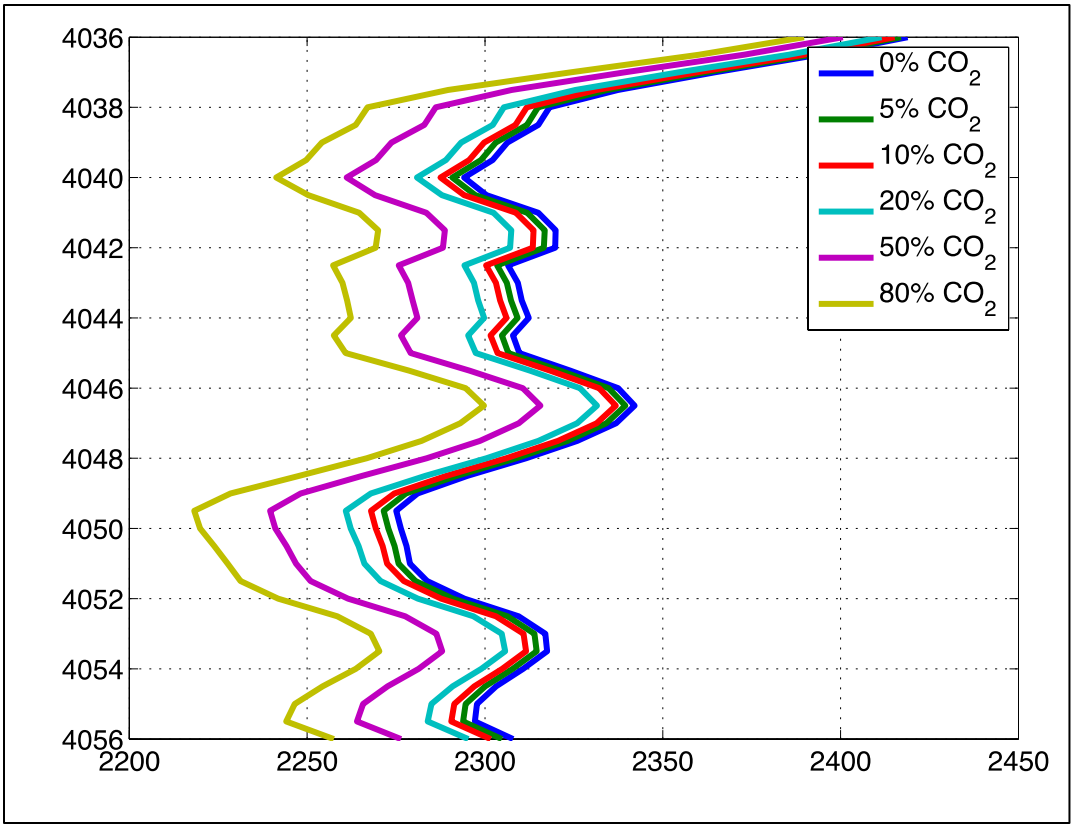

Figure 6.21. Gassmann fluid substitution predicted density changes within the reservoir interval.

Next, compressional-wave (P-P) reflectivity for near normal incidence angles (0−15 degrees) was computed for the extreme cases of 0 percent and 80 percent CO_2 saturation using the predicted changes in seismic properties.

The result of this reflectivity modeling is illustrated by the difference traces shown in Figure 6.22 quantifying the magnitude of the predicted reflectivity change caused by CO_2 injection. While differences are present, these model traces contain no noise and the reflectivity change induced by injected CO_2 is quite small. In reality, seismic data will not be noise-free and when taken into consideration, the expected P-P reflectivity changes are probably too small to be used for monitoring CO_2 saturation changes.

In addition to the analysis described above, amplitude versus angle (AVA) reflectivity and the use of higher frequencies were investigated. The results for both tests, however, indicate that neither AVA nor higher frequency sources will be sufficient to reliably monitor changes due to CO_2 injection.

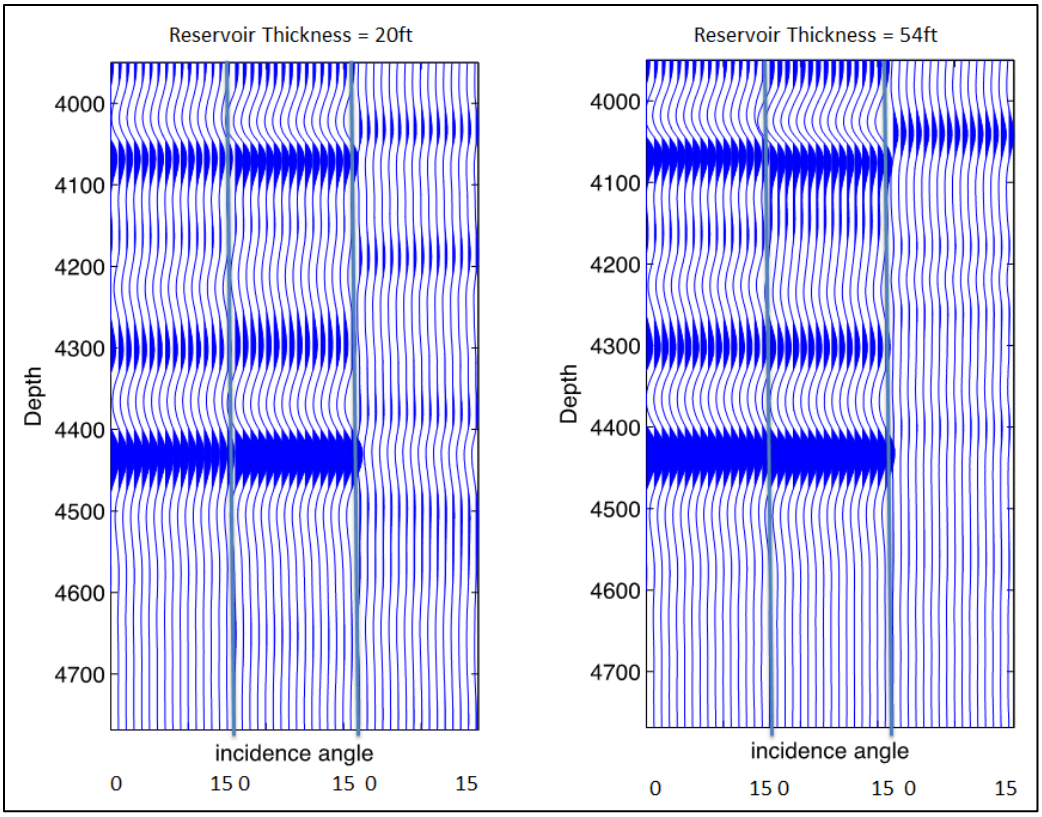

Figure 6.22. P-P reflectivity changes caused by CO_2 injection into a Mount Simon reservoir of variable thickness.

6.3.3.2 2D Surface Seismic Surveys

A 2D seismic-reflection survey was conducted at the FutureGen 2.0 storage site to provide preliminary subsurface characterization and investigate the feasibility of surface-based seismic-reflection methods for CO_2 monitoring and site characterization. Two roughly perpendicular lines were employed using vertical component geophones and vibratory sources (Figure 6.23). The survey provided no clear indication of major tectonic structures or faults. However, the quality of the seismic survey data was insufficient to rule out the presence of small-scale faults/fracture zones. Morgan County is not located in a seismically active part of the state and has no geologic faults or fracture zones shown on the structural geology map published by the Illinois State Geological Survey (ISGS).

An example image is shown in Figure 6.24 for the north-south line L101. A number of reprocessing iterations were performed for this data set using various processing parameters, and all of the images showed several common traits. First, strong and laterally continuous reflectors are present from the surface down to a two-way travel time of approximately 0.3 seconds (roughly just below the Galena Limestone). Between 0.3 and 0.4 seconds, signal attenuation is much more pronounced. Finally, beginning at about 0.55 seconds (near the top of the Eau Claire), a zone of incoherent reflectivity can be seen and continues to about 1.2 seconds. As a result of the poor surface seismic quality at the site combined with the small reflectivity changes anticipated from CO_2 injection described in the previous section, surface seismic methods are not expected to be able to effectively monitor the evolution of the CO_2 plume.

Based on the results of this evaluation, surface seismic monitoring will not be included as part of the FutureGen 2.0 storage site monitoring program.

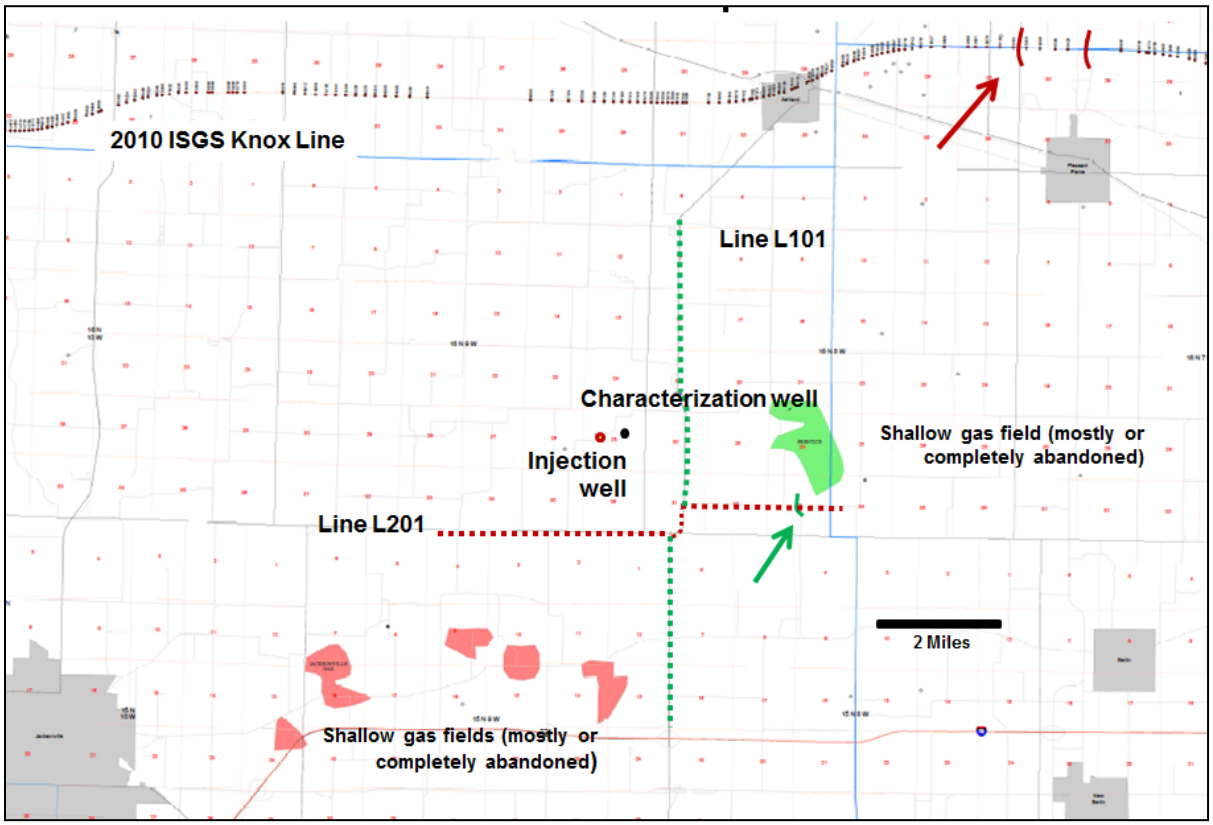

Figure 6.23. Locations of 2D seismic survey lines.

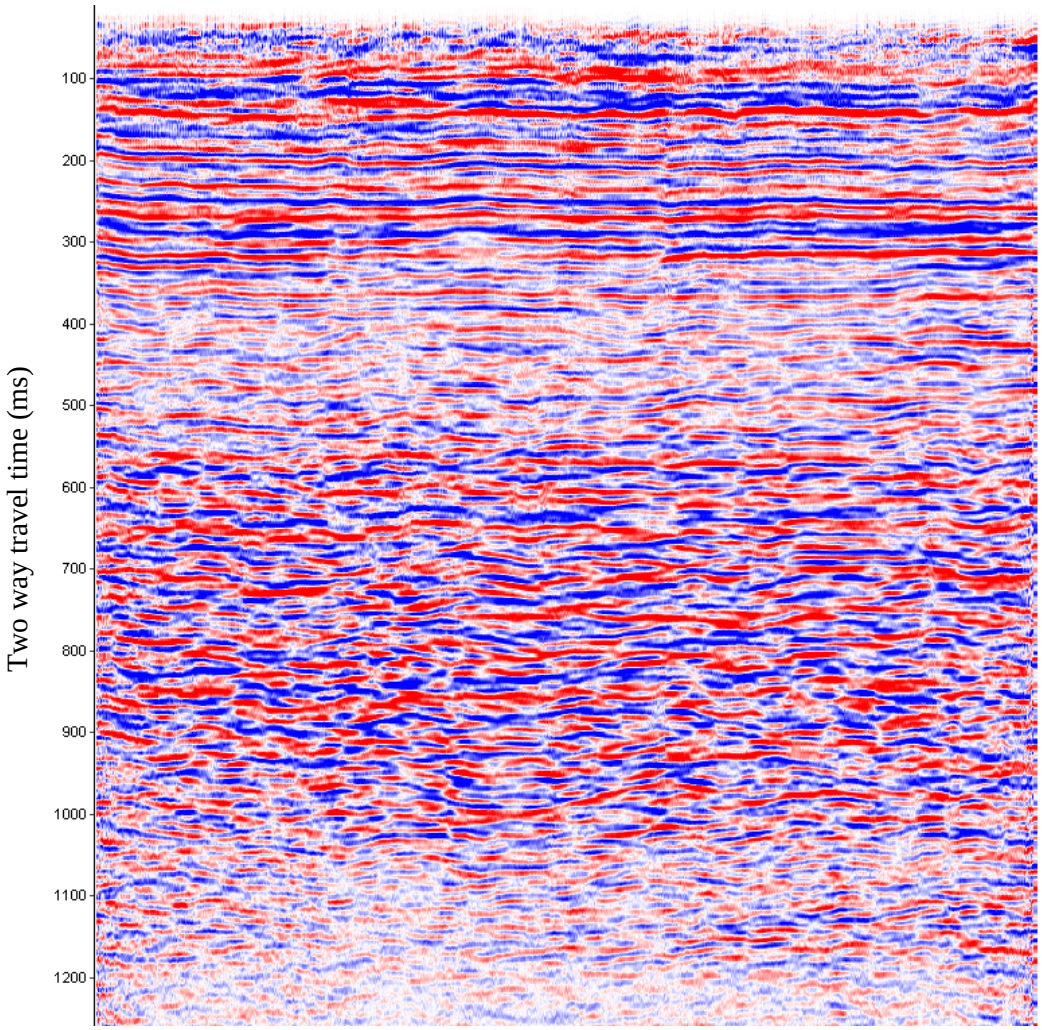

Figure 6.24. Surface seismic line L101 image.

6.3.3.3 Vertical Seismic Profile Survey

A 3C zero-offset plus 15 Offset VSPs were acquired at the initial stratigraphic borehole in March 2013 (Figure 6.25). Compared to 2D surface seismic surveys, resulting imaging was greatly improved at the Eau Claire, Mount Simon, and basement depths. P-wave attenuation was considerable between the Galena and top of the Eau Claire; in contrast, converted wave imaging (P-wave down, S-wave to the receiver) appears to be far superior to P-wave imaging. Results of the 2013 VSP survey included being able to confirm a lack of faulting along all 11 independent cross-section seismic lines that extended out 800 to 1,600 ft from the initial stratigraphic borehole (Figure 6.26).

A 1D velocity model inversion was carried out using both compressional- and shear-wave direct arrival data. Figure 6.27 shows the results of the 1D inversion along with a side-by-side comparison to the sonic velocity logs and corresponding geology from the characterization borehole. The inverted P-wave and S-wave velocities show an excellent match to the borehole logs and several geologic interfaces.

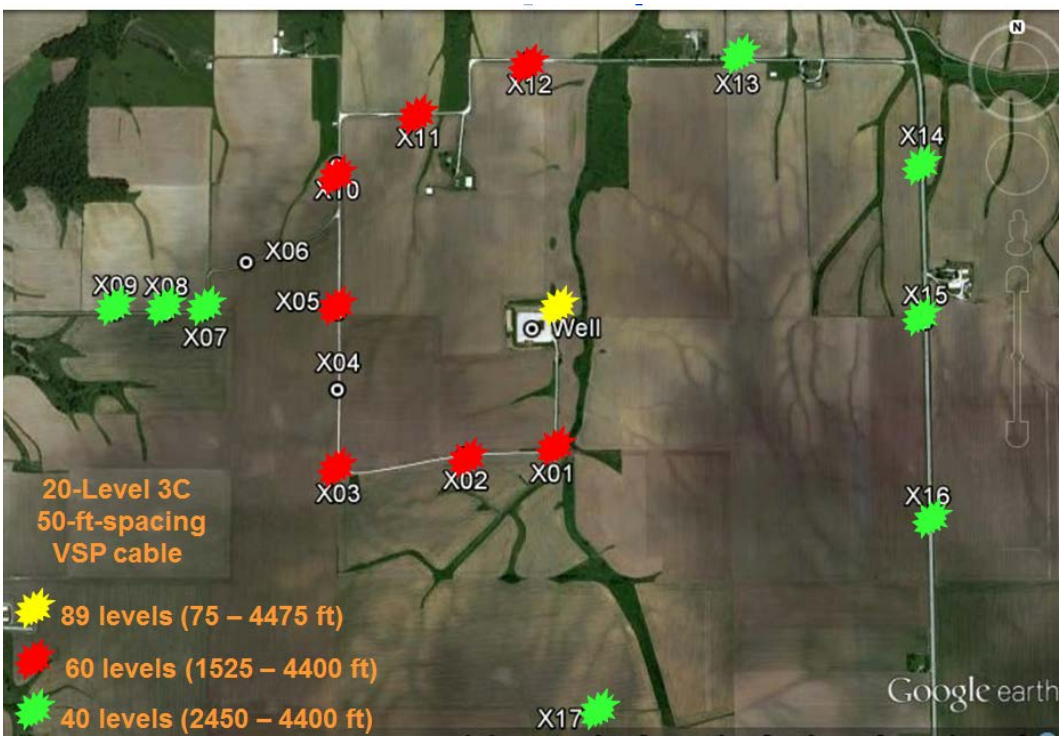

Figure 6.25. Locations of the VSP sources.

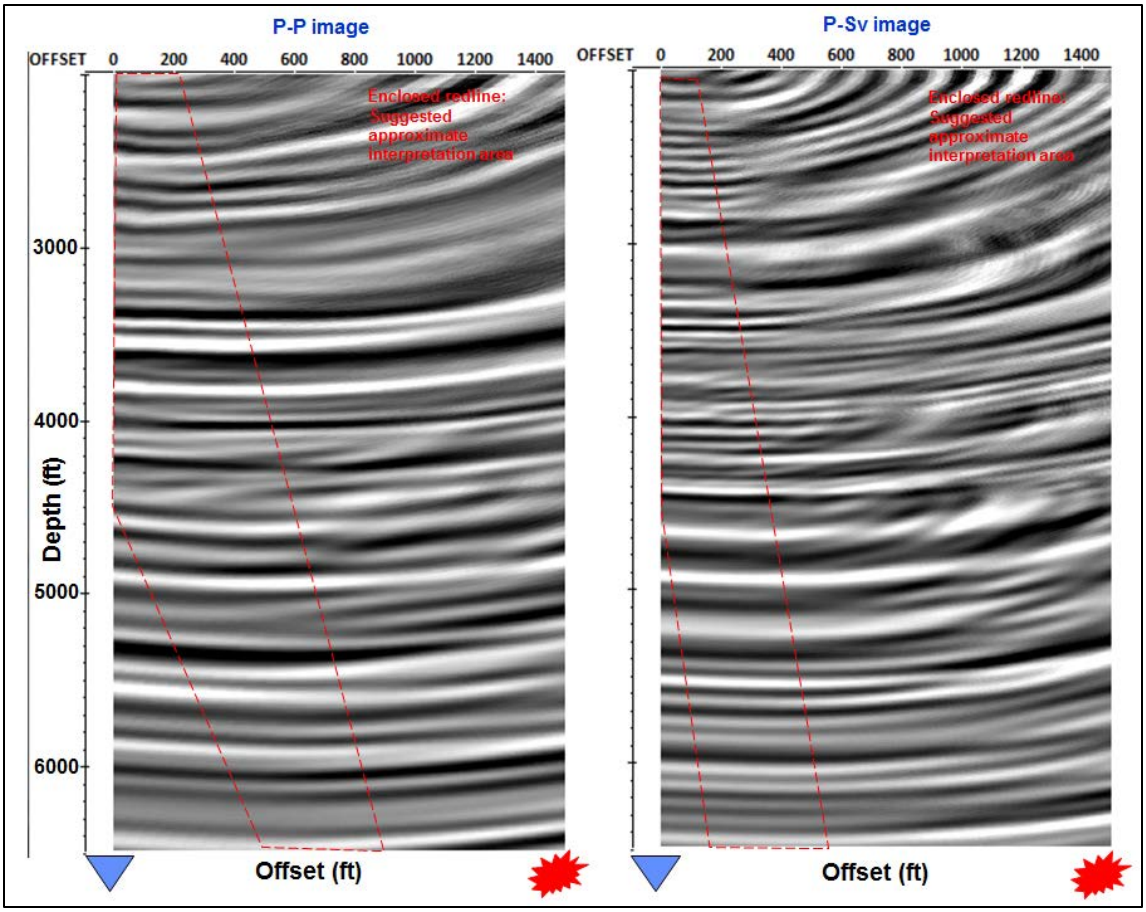

Figure 6.26. 2D VSP migrated images.

Because of the relatively few source locations, 2D/3D velocity inversions are not likely to be well constrained. As an analogue to a full 3D velocity inversion, the travel times predicted using a 1D layered velocity model can be subtracted from the observed travel times. These residual travel times can be calculated for each source-receiver combination and visualized by linearly interpolating and plotting them in 3D. The results of the computed travel-time residuals are plotted in Figure 6.28 and clearly show anomalous behavior to the south of the well. While these data are somewhat sparse they indicate that deviations from a simple flat layered velocity model are likely at the site.

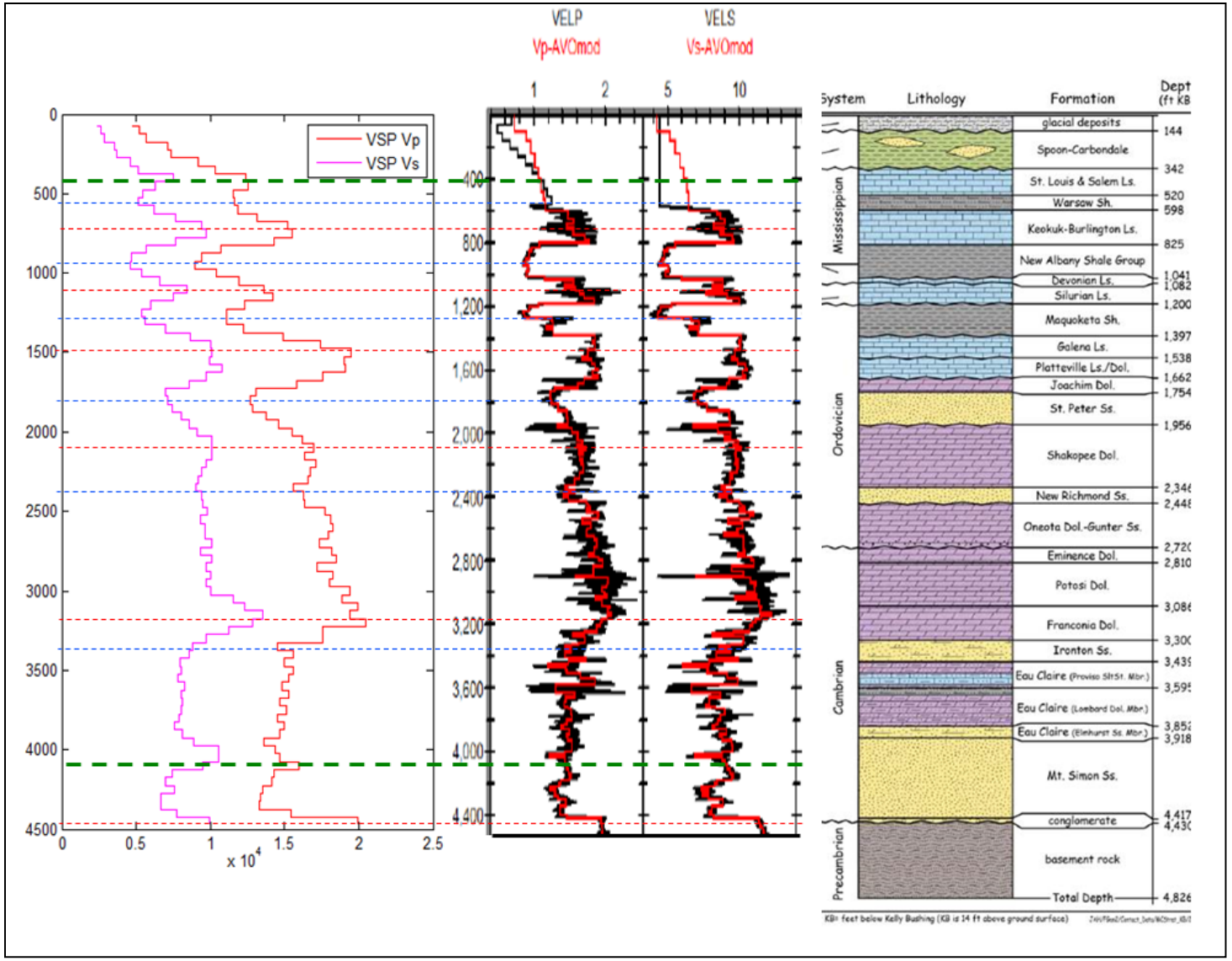

Figure 6.27. 1D VSP inversion results and geology at the characterization log.

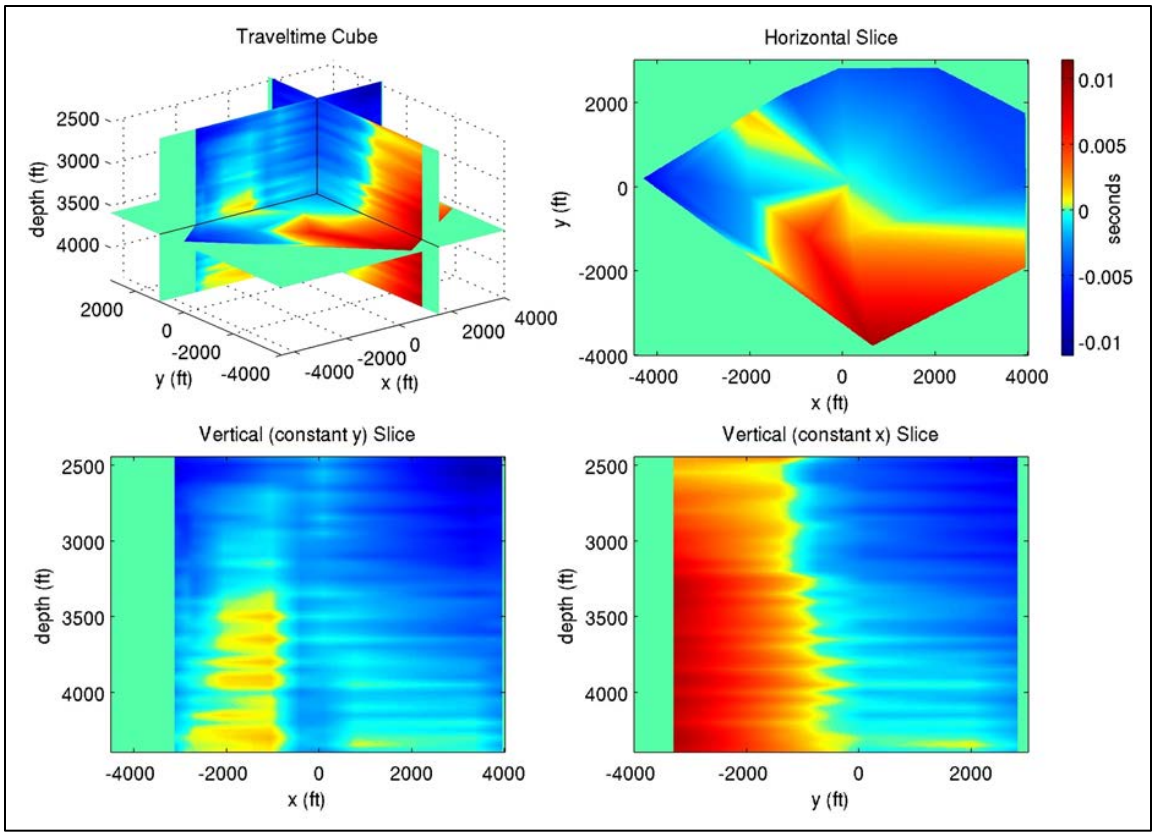

Figure 6.28. VSP residual travel times.

Seismic-reflection changes at the FutureGen 2.0 storage site resulting from injection of CO_2 are expected to be small, as was the case for surface-based reflection seismic methods, and thus it is unlikely that VSP will be able to identify CO_2 saturation changes or be an ineffective technique for tracking evolution of the CO_2 plume. If a need arises for imaging a volumetric area that is within 1,600 ft of an observation well and that may have seismic indications of potential fault slip, or if there is an indication of leakage into the shallower subsurface, this technology could be used to help guide development of an appropriate mitigation strategy.

Based on the results of this evaluation, VSP monitoring will not be included as part of the FutureGen 2.0 storage site monitoring program.

6.3.4 Cross-Well Seismic Monitoring

Cross-well surveys have been demonstrated at a site in Nagaoka, Japan; the Frio site near Houston, Texas; at a site in Ketzin, Germany; and the SECARB site at Cranfield, Mississippi. Cross-well seismic monitoring is conducted within the injection reservoir and thus provides for improved resolution of the rock heterogeneity and CO_2 relative to surface-based methodologies. Depending on reservoir velocities and dominant seismic frequencies obtained, two successive time-lapse cross-well seismic surveys may be able to detect the presence of the CO_2 plume to within 10 ft. This technology has also been applied to horizontal wells, but only to wells that are roughly parallel trajectories (Guoping and Majer 2002).

Cross-well imaging requires borehole separations of less than approximately 1,000 m. Although this technology has the potential to allow for high-resolution images of a discrete portion of the CO_2 plume, using this methodology would require a large number of boreholes to track the development of the 20-year CO_2 plume and would thus be cost-prohibitive.

Because of the limited spatial extent of investigation for this monitoring approach, cross-well seismic monitoring will not be included as part of the FutureGen 2.0 storage site monitoring program.

6.3.5 Magnetotellurics and Controlled-Source Electromagnetics

Previous numerical studies have demonstrated the potential for CO_2 injection monitoring using MT/CSEM methods (Gasperikova and Hoverstan 2006; Commer and Newman 2009; Zhdanov et al. 2013). CSEM is often better suited to resolving the CO_2 plume than using MT data alone.

In time-lapse mode, the CO_2 plume would be expected to appear in the resulting models as a region of increasing resistivity. Resistivity changes are expected to reduce by a factor of 3−5 from the initial values in the reservoir because of CO_2 injection. The question of whether the injection of CO_2 provides measurable electrical resistivity contrast can be answered by forward simulations.

6.3.5.1 Modeling Analysis

To evaluate the feasibility of MT or CSEM methods for monitoring the evolution of the CO_2 plume, a forward modeling and inversion analysis was performed. Flow and transport modeling of the CO_2 injection process shows that CO_2 saturation will vary from near 85 percent near the injection wells, decreasing outward as the plume expands. The saturations within the main volume are expected to be around 50 percent or slightly higher, and at the edge of the plume will be relatively small, with values less than 10 percent. Saturations near the caprock will also be relatively high compared with the overall saturation due to buoyancy effects. A simplified model using CO_2 saturations that were constant with depth and changed only in the lateral extent within the reservoir was used and is shown in Figure 6.29.

Both the background resistivity values and those resulting from changes in saturation of the constituent pore fluids used in the MT/CSEM simulations were similar to those used for the ERT simulations. Resistivity values were calculated using the borehole logs and conversion of CO_2 saturations using Archie's law parameters derived from the core tests.

Resistivity will also decrease as temperature increases. For temperatures between 20 and 150°C and at salinities up to 150 g/L, Arps' empirical law has been found to be a good indicator of the effect of temperature on conductivity (Fleury and Deschamps 2008). However, temperature effects on resistivity are not anticipated to be significant and were therefore not considered in this analysis.

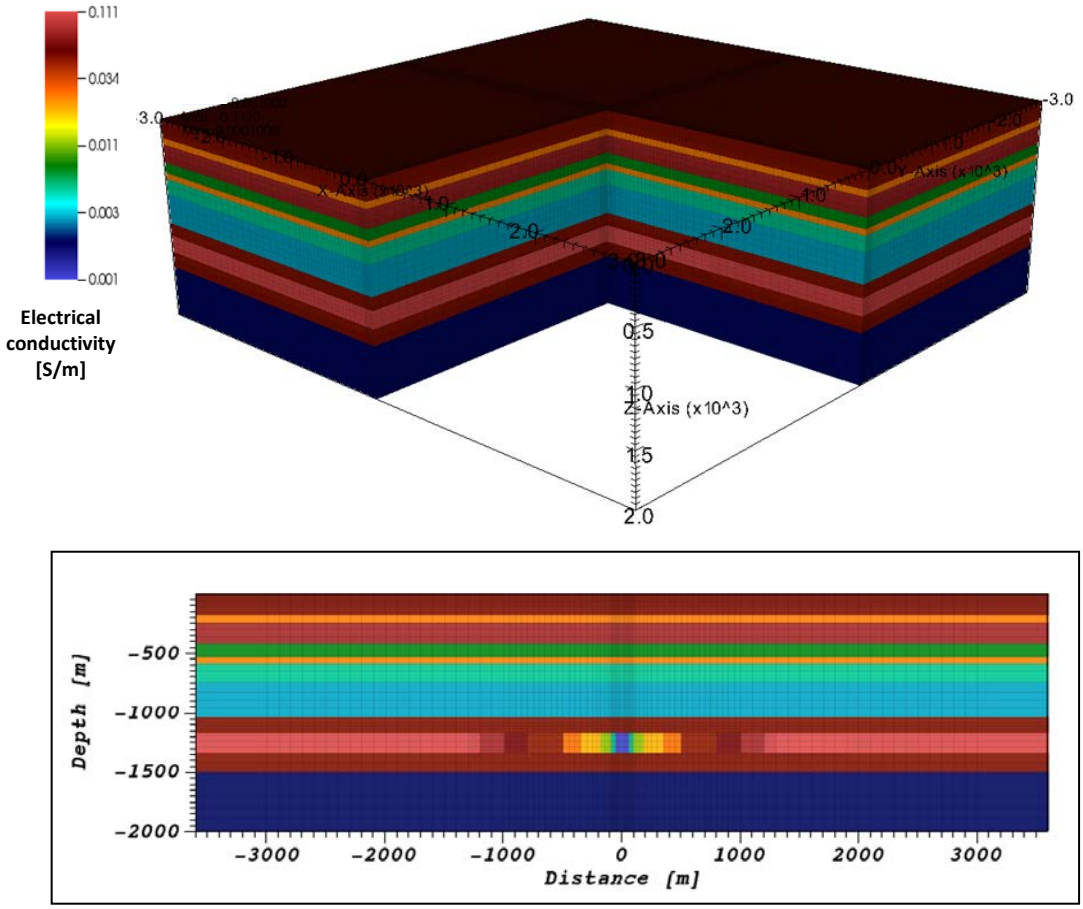

Figure 6.29. Electrical conductivity models for the initial background conditions (upper plot) and for the simulated CO_2 plume (lower plot).

Forward and inverse modeling was performed using EM3D (Commer and Newman 2009). The MT/CSEM stations used in the inverse modeling are shown in Figure 6.30. Inversion of the 30-year MT data is illustrated in Figure 6.31. Instead of the expected increase in resistivity, the simulations showed a slight increase in conductivity resulting from very low sensitivity of the inversion to injection-induced EC changes. The non-uniqueness of the inversion combined with the small changes in injection-related response make it difficult for the inversion to converge at a model where the resistivity has increased.

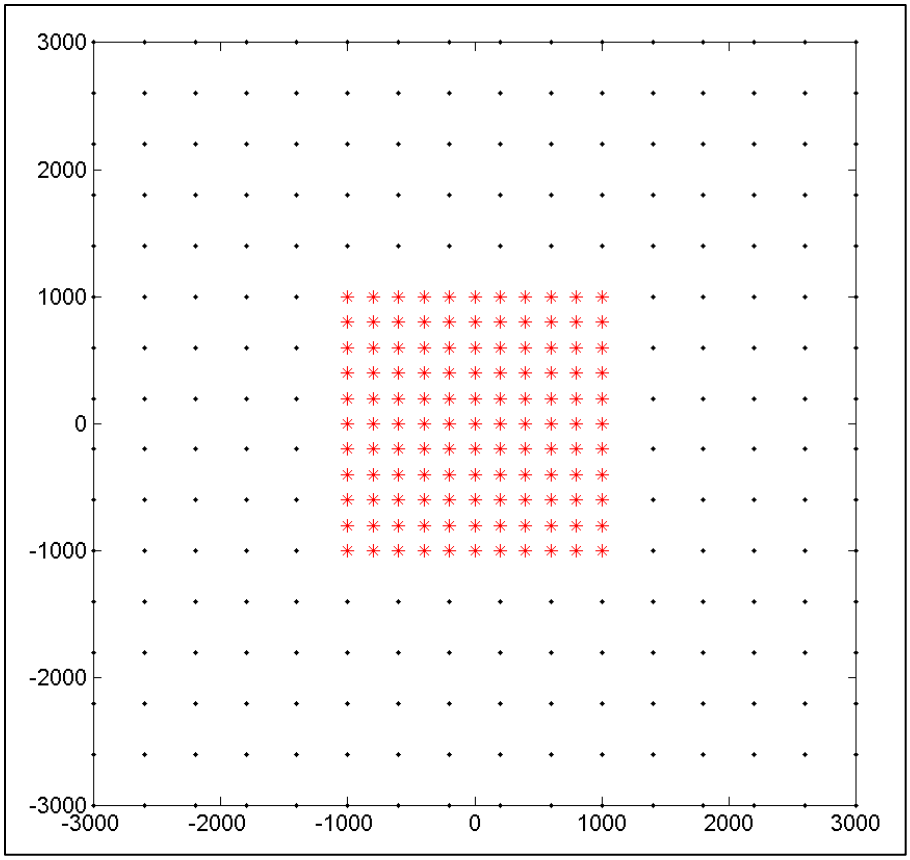

Figure 6.30. MT and CSEM monitoring station locations.

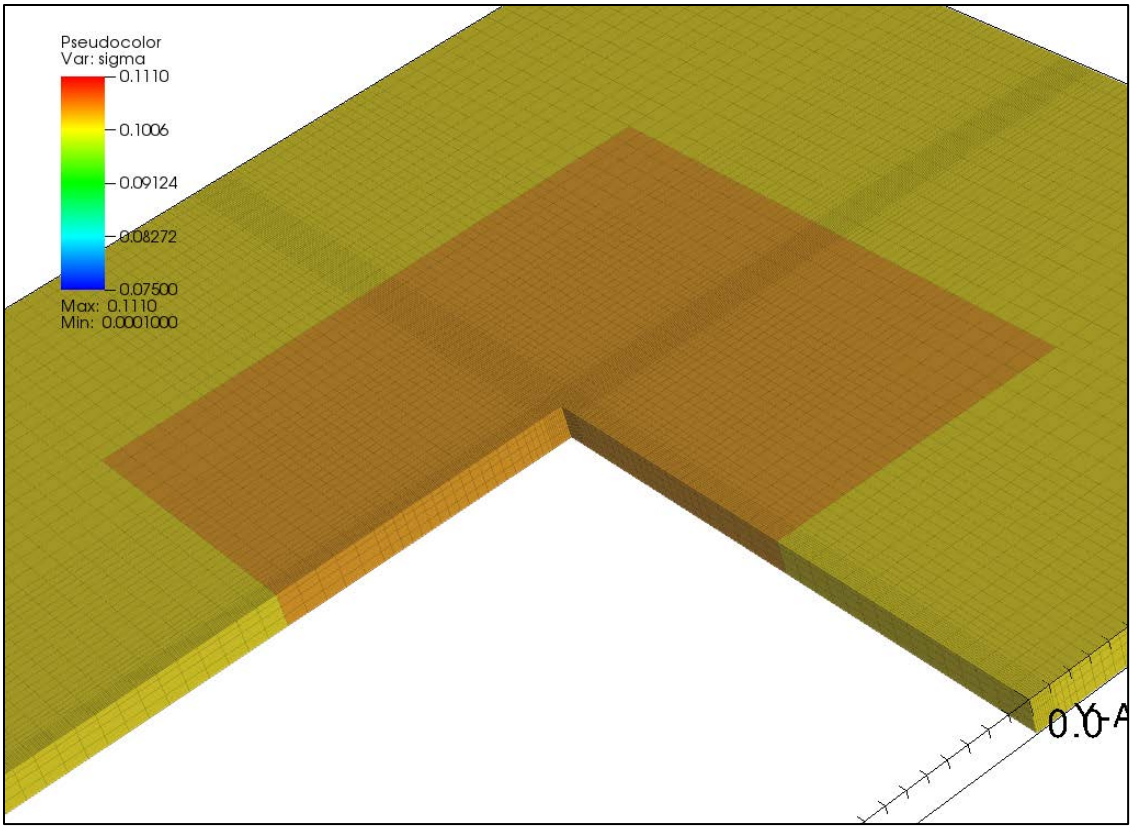

Figure 6.31. Magnetotelluric inversion results, which show negligible sensitivity to the data.

CSEM inversion results using stations at the surface also showed little sensitivity in the inversion. To overcome this problem, the CSEM receivers were placed down the borehole with the transmitter at the surface. In this case, the conductivity of the injection layer was reduced from the background value of 0.111 S/m to 0.052 S/m. The actual mean conductivity of the injection zone is 0.043 S/m (Figure 6.32). The bulk changes within the reservoir were reasonably estimated, but the inversion was unable to identify lateral variations in CO_2 saturation.

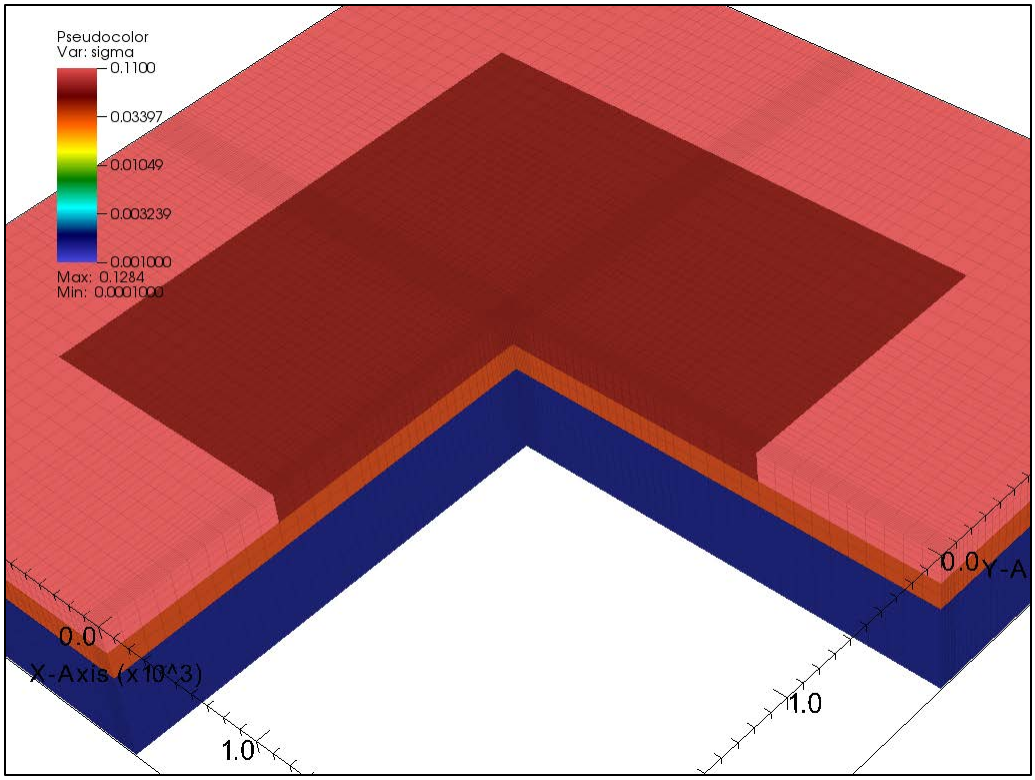

Figure 6.32. CSEM inversion results. Estimated conductivity change is close to bulk value in the reservoir, but the lateral variations were not captured.

Based on the results of this evaluation, MT/CSEM will not be included as part of the FutureGen 2.0 storage site monitoring program

6.3.6 Time-Lapse Gravity Monitoring

The objective of time-lapse gravity monitoring is to provide a means of tracking the spatial extent of the CO_2 plume. Repeat gravity surveys provide a means of measuring changes in the density/mass of the injected CO_2 over time; measurements of density change are not possible with geophysical methods that rely on other indicators of CO_2 presence (i.e., changes in pressure or electrical conductivity).

This technology has been successfully applied to a variety of subsurface injection studies, including carbon sequestration at Sleipner (Arts et al. 2008). As with other geophysical methods, the utility of time-lapse gravity for monitoring the injection of CO_2 depends on a number of site-specific properties and should be evaluated on a site-by-site basis. Results from a quantitative assessment under site-specific conditions are presented below.

6.3.6.1 Baseline Field Survey

A field survey was conducted in November 2011 (Bonneville et al. 2012) to support subsurface characterization at the FutureGen 2.0 storage site and to provide a baseline for future geodetic and gravity monitoring. The gravity survey was designed to obtain 10^{-8} (10 µGal) level accuracy measurements of the Earth's gravitational field that will be used to provide 1) a 3D estimate of density variations in the

subsurface (reservoir and caprock) integrated with reflection seismic data and well log interpretations and 2) a baseline for future surveys that will be conducted after the beginning of the CO_2 injection (time-lapse gravity). The geodetic survey performed for this activity serves mainly to provide a reference for gravity measurements but it will also be used to support interpretation of the surface deformation results. Concurrent geodetic measurements and gravity readings at each survey point are necessary for an accurate and robust gravity processing and interpretation.

The gravity meter used during the survey is a LaCoste & Romberg Model D and real-time kinematic (RTK) method was used for the geodetic measurements. The survey comprised 245 stations with 230 stations regularly spaced on a 2-mi by 2-mi square grid roughly centered on a previously considered injection well location (Figure 6.33). An absolute gravity station located in Hannibal, Missouri, was used to incorporate this local survey into the existing regional data set. Gravity reduction has been performed using the standardized methods proposed by Holom and Oldow (2007). Topographic corrections have not been applied but are expected to be minor in this area and should not appreciably affect the fusion with the existing regional Bouguer anomaly.

The November 2011 survey results have a good correlation with the regional gravity maps of Daniels et al. (2008). The local survey measurements complete the regional survey and allow a better definition of the short wavelength content of the gravity signal at the FutureGen 2.0 storage site. The Bouguer anomaly determined from the local survey that has been integrated with the regional data are shown in Figure 6.34. The results can be used for site characterization, in addition to providing the baseline for subsequent gravity surveys aimed at monitoring the injected CO_2. Because of the large density contrast between the basement rock and the overlying geology the baseline gravity results can be used to infer the thickness/depth of the pre-Cambrian basement rock.

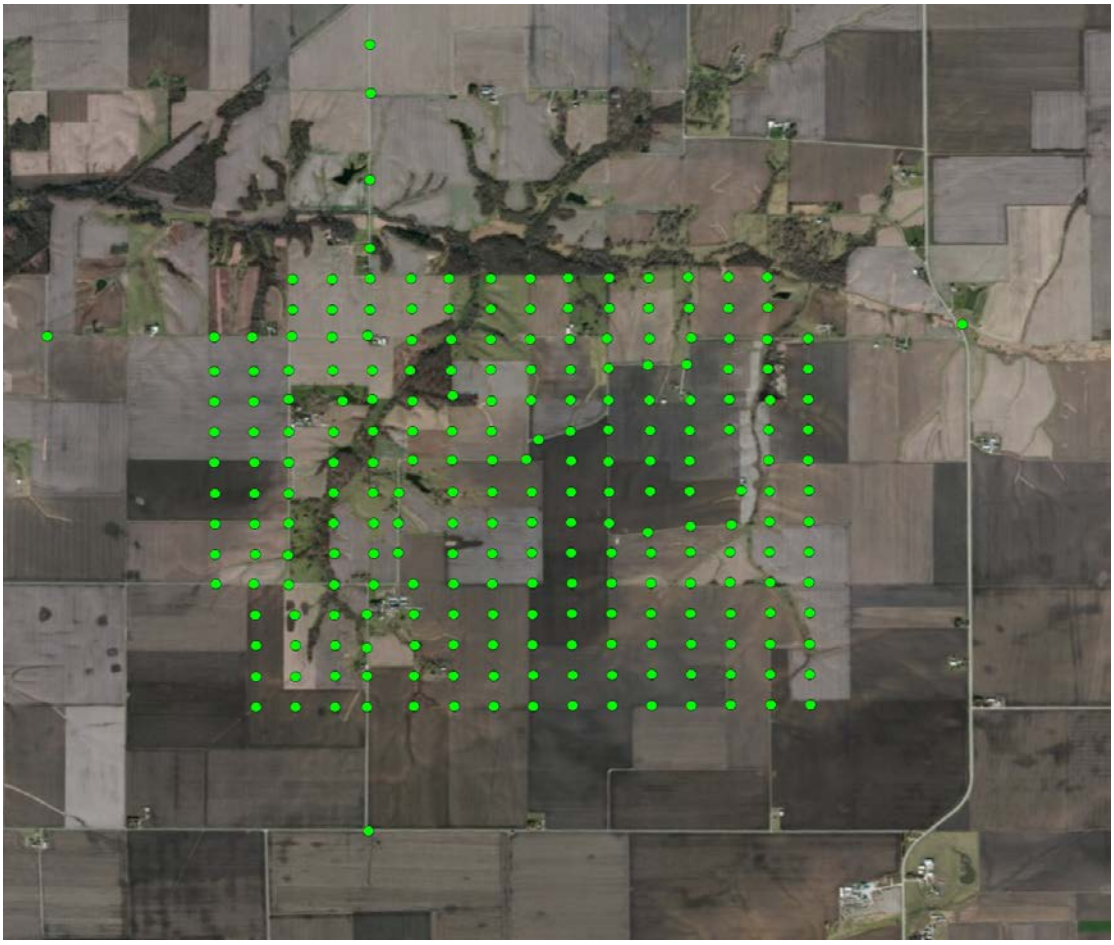

Figure 6.33. Gravity and DGPS stations used in the field survey.

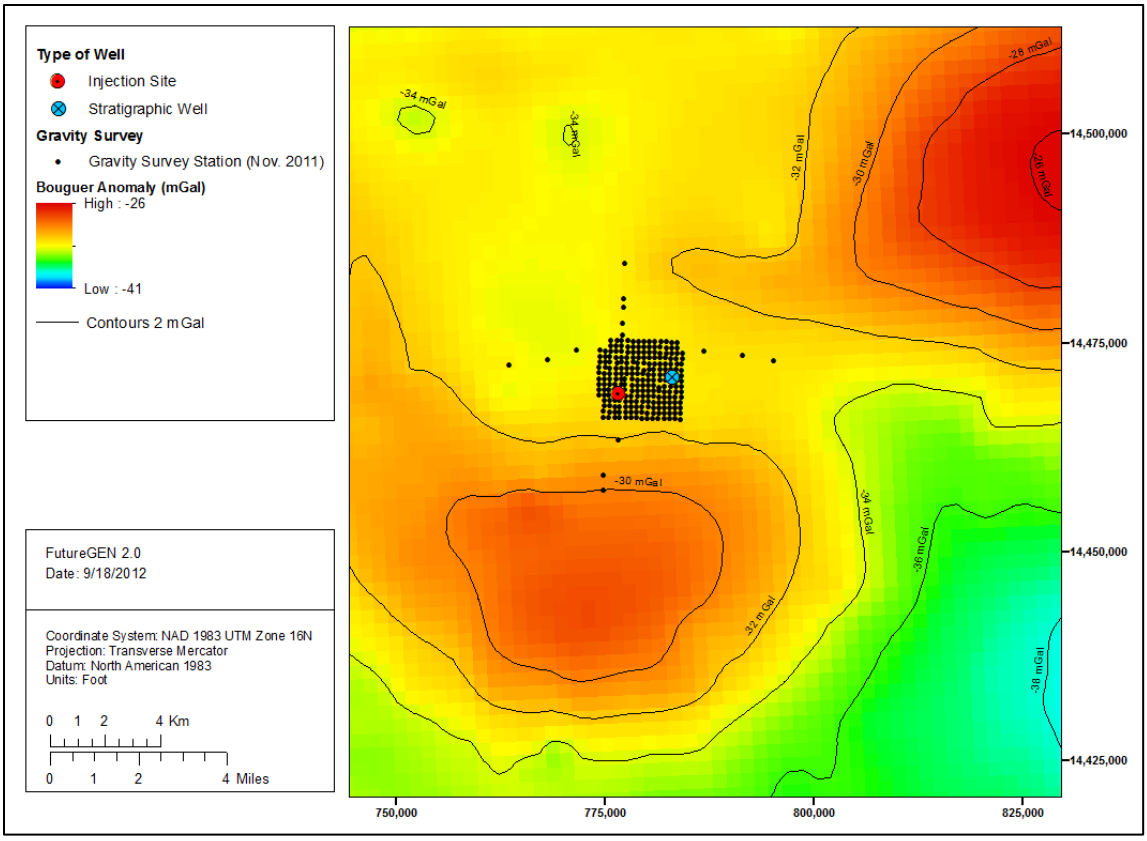

Figure 6.34. Bouguer anomaly showing the lateral gravity variations at the FutureGen 2.0 storage site and surrounding areas.

To investigate the feasibility of monitoring CO_2 saturation changes using time-lapse gravity surveys a modeling analysis was performed using a 3D numerical modeling method (ENcom Model Vision ™ 12.0). A simplified block model representing the reduction in density due to replacement of brine with $scCO_2$ was used as the density anomaly within the reservoir. The brine density was set at 1.09 g/cm^3 and 0.6 g/m^3 for $scCO_2$, and the porosity of rock was set at 0.2. The spatial extent of the density anomaly corresponding to 22 MMT of CO_2 is shown in Figure 6.35 along with the expected gravity signal change for each CO_2 plume scenario. These results indicate gravity signal changes of -50 µGal in response to simulated CO_2 injection.

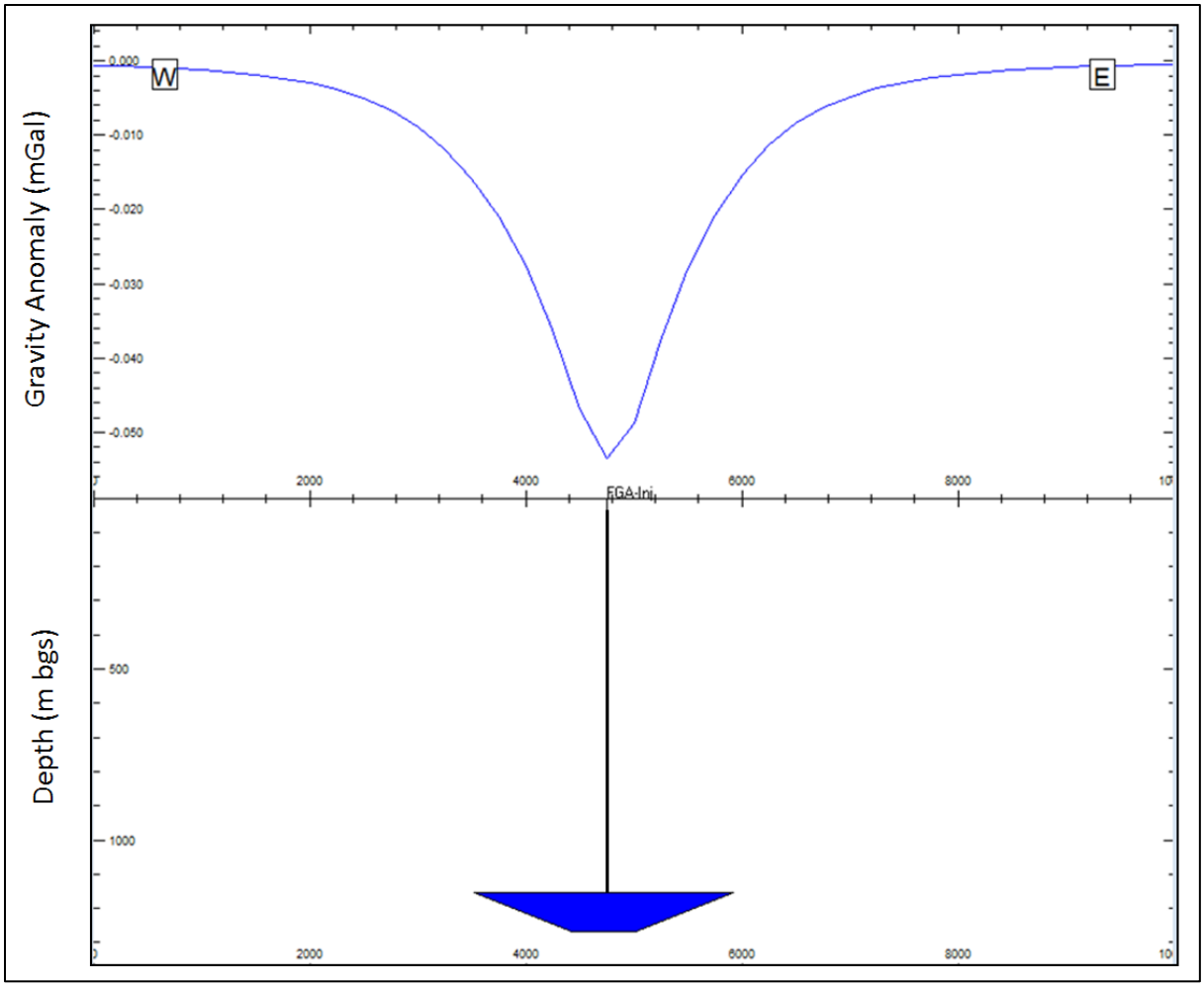

Figure 6.35. Theoretical case of a gravity anomaly that approximates the maximum predicted CO_2 plume extent (blue body).

Gravity changes at the surface are expected to be small and close to the detection limit of 10 µGal; a thorough analysis of the baseline noise levels will be an important component to successful implementation. Site noise is anticipated to be low and can be further reduced through statistical averaging; analysis of long-term trends may then allow for tracking of the CO_2 plume. The cost of implementing this technology is quite low and can be combined with DGPS surveys conducted as part of the integrated surface deformation monitoring to further reduce costs. Time-lapse gravity monitoring is done using repetitive annual surveys at a series of points located at ground surface (permanent stations). Changes in the gravity anomaly with time are determined and used to estimate changes in subsurface densities. These changes provide an indirect method of tracing the displacement of the CO_2 plume at depth. Due to the non-uniqueness of solution, this monitoring method should be used to complement other methods (e.g., surface deformation, seismic methodologies).

Forty-six permanent stations were established in 2011 during a gravity survey for the purpose of future reoccupation surveys. Approximately 35 complementary stations will be established for a total of 81 stations. Based on the analysis of the baseline surveys, additional stations may be included. A map of the gravity stations is provided in Figure 6.36.

Based on the results of this evaluation, time-lapse gravity monitoring will be included as part of the FutureGen 2.0 storage site monitoring program.

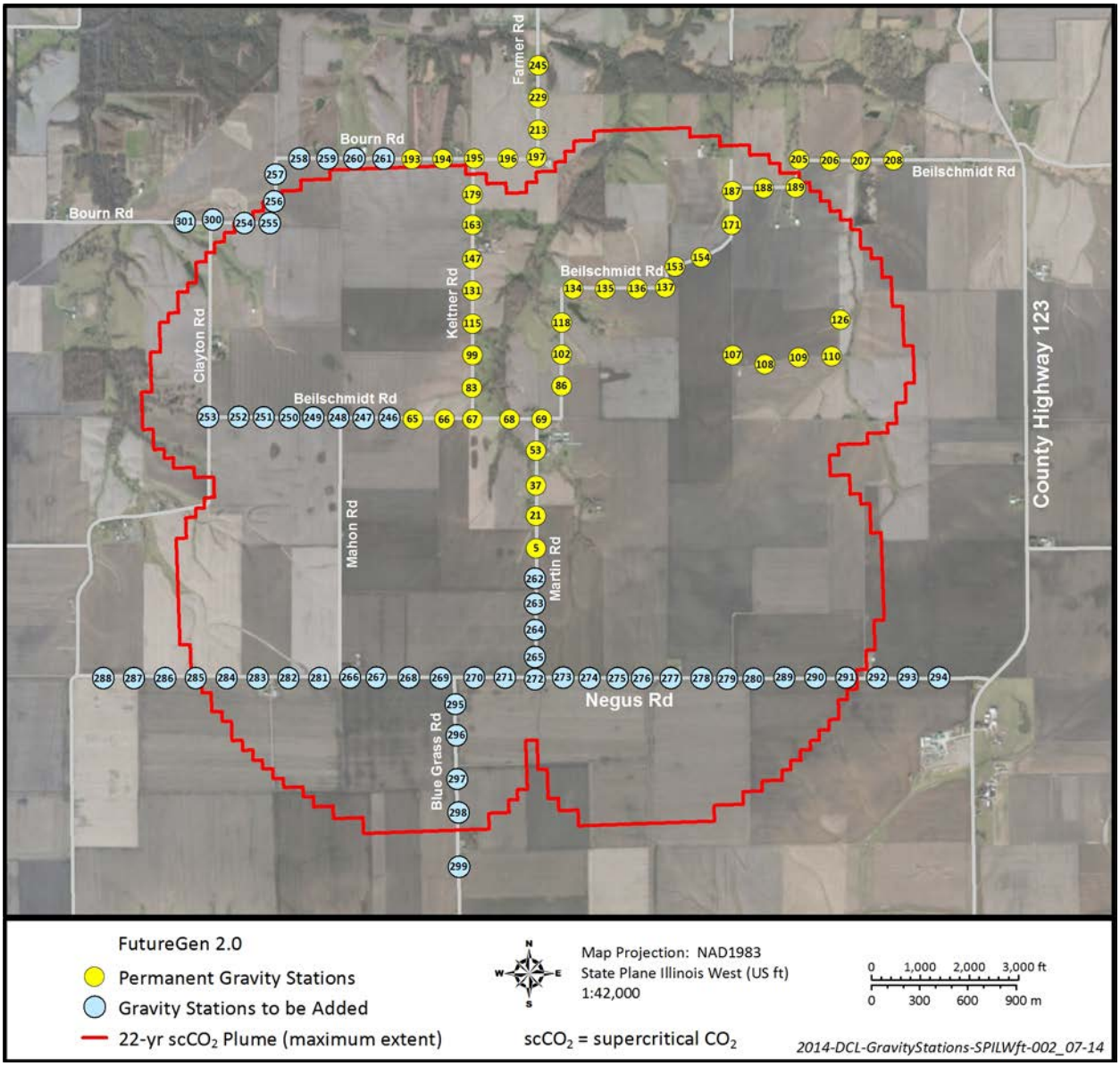

Figure 6.36. Locations of permanent gravity and DGPS stations.

6.3.7 Integrated Deformation Monitoring

A modeling analysis was performed to determine the elevation changes at the surface that would be expected as a result of CO_2 injection pressure changes. Two parallel modeling approaches were used.

First, a simple analytical Biot-based, poro-elastic model was used to translate the expected pore pressure increase in the reservoir into an equivalent vertical displacement at the surface. As indicated in Equation (6.5), if the formation layer thickness and imposed pressure change are known, then the associated formation deformation resulting from an imposed pressure change can be directly predicted.

Rock compressibility for the designated formation layer can be estimated from selected core laboratory geomechanical tests or from elastic parameter moduli as determined from geomechanical wireline geophysical surveys. While core tests provide information for discrete depth intervals, and elastic geomechanical wireline surveys provide essentially continuous depth coverage, both methods are subject to small-scale effects (i.e., inference of large-scale formation characteristics from small-sized samples or small-scale radius-of-investigation), as well as potential alterations imposed by the well-drilling process.

Because of the availability of continuous geomechanical wireline survey coverage of the Mount Simon and Elmhurst reservoir model layers (and lack of complete core coverage for the respective reservoir thickness), wireline survey elastic moduli results from the initial stratigraphic borehole were used in estimating rock compressibility, c_r, for the 24 injection reservoir/model layers. The weighted-average model-layer rock compressibility for the composite Elmhurst–Mount Simon depth section is 2.94×10^{-7} psi^{-1}. This estimated average rock compressibility value is approximately an order of magnitude lower than typical core sample values for consolidated sandstone formations (Newman 1973). It should be noted, however, that both core tests and in situ composite formation rock compressibility, as determined by independent hydrologic characterization tests, also indicated comparably low bulk rock compressibility values within the initial stratigraphic borehole. This suggests that the rock compressibility estimates derived from elastic property/geomechanical wireline logs may be representative of formation/model-layer conditions.

The predicted land-surface deformation was calculated along a ~40,000-ft-long east-west cross section roughly following the two northern injection wells. Deformation estimates were based on simulated pressure changes and formation layer thickness and compressibility for the targeted injection reservoir layers within the Mount Simon and overlying Elmhurst. Model-layer thickness and compressibility values were calculated using the characterization well wireline logs. Pressure changes caused by continuous CO_2 injection after periods of 1, 3, 5, 10, and 20 years were obtained using the CO_2 version of the STOMP computer program, as described by White et al. (2012). The predicted land-surface deformation for these time periods is reflective of a summation of predicted composite deformation for these 24 individual model layers within the Mount Simon and Elmhurst. Results of this analysis are illustrated in Figure 6.37 and show that vertical displacements up to approximately 25 mm can be expected.

The second method used a fully 3D geomechanical modeling analysis to calculate the expected deformation at the surface associated with the injection of CO_2 using the STOMP-CO2/ABAQUS® sequentially coupled simulator (Murray et al. 2014). Material properties for the analyses were derived for the 30-layer model from geophysical well logs generated during drilling of the initial stratigraphic borehole and supplemental data from the literature. The median values of Young's modulus and the Poisson ratio were taken directly from the geophysical logs. STOMP-CO2 was used to model the flow and transport of CO_2 for the 20-year injection period, assuming injection of 1.1 MMT of CO_2 per year. The information from STOMP-CO2 is passed to a -D finite element model (3DS, ABAQUS®) at selected time steps, which calculated the 3D strains (including deformation at the surface) and stresses, and fluid pressure. The resulting surface uplift after 20 years of injection is presented in Figure 6.38. The maximum deformation of 20 mm occurs close to the injection well within the region of maximum pressure increase.

Sub-centimeter accuracies are typical for both InSAR and precision DGPS and are significantly lower than the expected surface deformation resulting from CO_2 injection at the FutureGen 2.0 storage site.

This analysis indicates that these methods will be able to resolve the expected deformation that is related to the injection pressure front out to approximately 5−10 miles from the injection well pad.

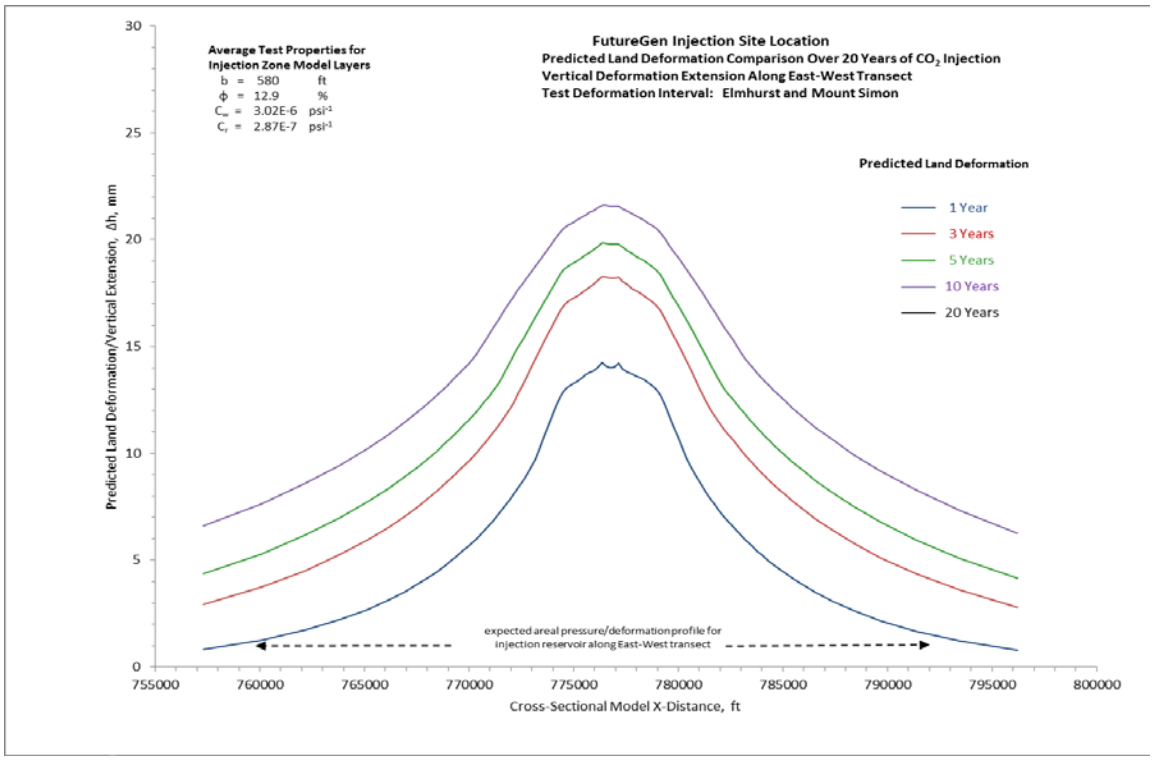

Figure 6.37. Predicted deformation profile across a single transect through the FutureGen 2.0 storage site.

Figure 6.38. Aerial extent for the vertical component of the 3D predicted deformation

An integrated approach for monitoring potential surface deformation at the FutureGen 2.0 storage site will use both orbital InSAR and ground measurements. An assessment of baseline surface deformation prior to fluid injection will be achieved during a 2-year monitoring period prior to CO_2 injection and then measurements to determine injection-related deformation will be collected on a routine basis once injection has started.

The field-scale integrated deformation program will consist of an integrated ground deformation measurement approach combined with a complete geophysical interpretation. The deformation monitoring will include orbital InSAR data (X-band TerraSAR-X, C-band Radarsat-2, X-Band Cosmo-Skymed or any other satellite data that will be available at the time of data collection) and a field survey validation using permanent GPS stations and tiltmeters and annual DGPS surveys. Annual DGPS survey station will be co-located with the gravity stations (Figure 6.36). This approach will also be used to

measure surface deformation during the more dynamic injection phase with the modifications based on the experience gained during the 2-year baseline monitoring period.

Orbital SAR data will be systematically acquired and processed over the sequestration site with at least one scene per month to obtain advanced InSAR time series. These data will be obtained from the available orbital instruments available at the time of collection. It should be noted that the existing TerraSAR-X, Radarsat-2, and Cosmo-Skymed systems provide frequent systematic revisits of 11, 24, and 4 days respectively.

Artificial reflectors will also be deployed onsite to provide isolated coherent pixels that will be exploited to measure deformation over time and different algorithms (e.g., persistent scatters, small baseline subsets, etc.) will be used to determine the best approach for the site. Radar corner cube reflectors will also be used to integrate the orbital InSAR and field deformation measurements. As part of the first field campaign, they will be deployed at five sites within the area of interest and co-located with permanent GPS receiver stations, tiltmeters, and seismic stations (Figure 6.15). The reflectors will be arranged to provide strong radar responses with known properties from the different orbital platform trajectories. The corner cube reflectors will serve as reference pixels in the InSAR time-series analyses. In these advanced InSAR approaches, the pixel deformation measurements are only known relative to a user-defined reference pixel within the SAR image. The deformation at this reference point must be known to obtain the absolute (true) surface deformation at any other radar pixel. The differential GPS measurements acquired at the corner cube reflectors will provide the information needed to determine absolute deformation from the InSAR measurements.

Permanent GPS station and tiltmeters will be used with the annual DGPS surveys to validate and improve InSAR deformation analyses. DInSAR provides displacement measurements along the LOS between orbital SAR and the ground. Recovery of 3D displacements will be aided by using supplemental information from the ground-based GPS and tiltmeter data. To better integrate the various measurements, the annual DGPS and gravity field surveys will be acquired at approximately the same time as the InSAR observations.

An integrated surface deformation monitoring strategy has been evaluated and indicates that the proposed system should be able to resolve induced deformation at the surface for tracking of the injection pressure front out to approximately 5−10 miles from the injection wells. To establish a comprehensive geophysical and geomechanical understanding of the FutureGen 2.0 storage site, InSAR and field deformation measurements will be integrated and processed with other monitoring data collected at the site (e.g., seismicity, gravity, pressure, and temperature). Using this unique and complete geophysical data set it may be possible to constrain the CO_2 plume shape, extension, and migration in the subsurface. *Based on the results of this evaluation, integrated deformation monitoring will be included as part of the FutureGen 2.0 storage site monitoring program.*

6.3.8 Pulsed-Neutron Logging

PNC logging has been successfully implemented at a number carbon sequestration sites and is considered the standard for comparison to other measurements (Sakurai et al. 2005; Butsch et al. 2013; Ivanova et al. 2012). While the PNC method has been demonstrated to be an effective tool for measuring CO_2 saturation, problems associated with CO_2 flooding within the casing and perforation zones have been identified. For this reason non-perforated RATs will be used for PNC logging at the FutureGen 2.0

storage site. PNC logs will be used to quantify CO_2 saturation across the reservoir and caprock at three RAT monitoring locations. These three monitoring installations are located at increasing distances from the injection site to provide measures of CO_2 saturation at the predicted 1-, 2- and 3- to 4-year arrival times, respectively. The three RAT installations are also distributed across three different azimuthal directions, providing CO_2 arrival information for three of the four predicted lobes of the CO_2 plume. These near-field CO_2 saturation measurements will allow for calibration of the numerical model early in the injection phase of the project and verification of whether the CO_2 plume is developing as predicted. The RAT installations will continue to be monitored for the duration of the project to assess the potential for vertical migration of CO_2 into the caprock material.

PNC logs are sensitive to a localized region surrounding the borehole (15−30 cm) and are therefore susceptible to interference from features very near the borehole such as changing borehole fluids, poor cement, or invaded drilling fluids. Borehole effects can be somewhat removed by considering that material near the borehole responds at earlier times than deeper in the formation and by incorporating multiple detectors in the tool. PNC measurements are also less effective in low porosity (<15%) formations largely due to the smaller volumetric amount of fluids contributing to the measurement. Reservoir porosities are expected to be moderate (15−22%) and are expected to allow for quantitative estimates of changes in CO_2.

Based on the results of this evaluation, pulsed-neutron logging will be included as part of the FutureGen 2.0 storage site monitoring program.

7.0 Assessment of ACZ Early-Leak-Detection Capabilities

The objective of the MVA-ULT (MVA Upper Layer Transport) model is to investigate the potential for water-quality impacts associated with any unforeseen loss of $scCO_2$ and/or brine containment resulting from $scCO_2$ storage operations. This evaluation focuses on the first permeable interval (Ironton Sandstone) above the primary confining zone to assess early-leak−detection capabilities. An updated version of the model will eventually be used to assess potential impacts on the lowermost USDW aquifer (St. Peter Sandstone) for a range of theoretical leakage scenarios. A discussion of geochemical monitoring considerations, including an evaluation of the relative benefits of intrinsic indicators versus co-injected tracers for early-leak detection, is provided in Section 5.0. This preliminary modeling evaluation will consider both pressure response and geochemical signals in the overlying Ironton Sandstone. Results from this study, along with results from an updated MVA-ULT model that incorporates additional site-specific characterization data, will be used to guide any required refinement of the ACZ monitoring well designs.

The sections below describe the MVA-ULT model, leakage scenarios to which it was applied, and provide a summary of the investigative results.

7.1 MVA-ULT Model Description

Currently, site-specific characterization data are very limited for the units represented in the MVA-ULT model because the focus of the initial stratigraphic borehole was characterization of the reservoir (Mount Simon Sandstone and Elmhurst member of the Eau Clair Formation) and caprock (Proviso and Lombard members of the Eau Claire Formation). The few deep wells that exist in the area have limited characterization data available for theIronton Sandstone and overlying units. Planned characterization activities during installation of the FutureGen 2.0 storage site injection and monitoring well network will provide a comprehensive data set of material properties for the formations of interest. This preliminary MVA-ULT model will be updated once these data become available. The MVA-ULT model is independent of the FutureGen 2.0 reservoir model in that it does not simulate caprock discontinuities, faults, or failure scenarios. Instead this modeling effort looks at theoretical leakage scenarios that are based on volumetric rates of leakage. The MVA-ULT model is implemented using the STOMP-CO2 simulator (White et al. 2012).

7.1.1 Hydrostratigraphy and Grid

The bottom of the MVA-ULT model domain starts at the bottom of the Ironton Sandstone, which is the first permeable unit above the Eau Claire caprock (see Figure 2.2). The top of the model domain is within the Platteville Limestone, which is one of the carbonate units above the St. Peter Sandstone. The hydrostratigraphy for the model domain (see Figure 7.1) was derived from a PETREL solid Earth model of the FutureGen 2.0 storage site (Alliance 2013). The solid Earth model is based on characterization data collected from the initial stratigraphic borehole and numerous other wells in the Illinois Basin.

The MVA-ULT STOMP model grid is shown in Figure 7.2. The non-uniform grid is refined in the X and Y directions around a hypothetical leak location and applies 1/2 symmetry with a Y-direction mirror plane roughly parallel to the dip direction; the 1/2 symmetry is used to reduce the number of nodes

required. The overall domain size is 5,000 ft in the X direction, 2,500 ft in the Y direction, and 1,820 ft in the Z direction. The horizontal (X and Y) grid spacing is 1 ft near the leak location and gets progressively larger (roughly doubling at each change) to a final 100-ft spacing for much of the domain. The vertical grid spacing is 5 ft at the bottom within the Ironton Sandstone, Davis Dolomite, and most of the Franconia Dolomite and then is increased, stepwise, to 30-ft spacing for the remainder of the domain. The decreased Z grid spacing at the bottom was implemented to support the preliminary simulations focused on leakage into the Ironton Sandstone. The grid has 62 X-direction nodes, 31 Y-direction nodes, and 120 Z-direction nodes, yielding 230,640 nodes overall. The grid has 5,266 inactive nodes along the bottom due to the dip.

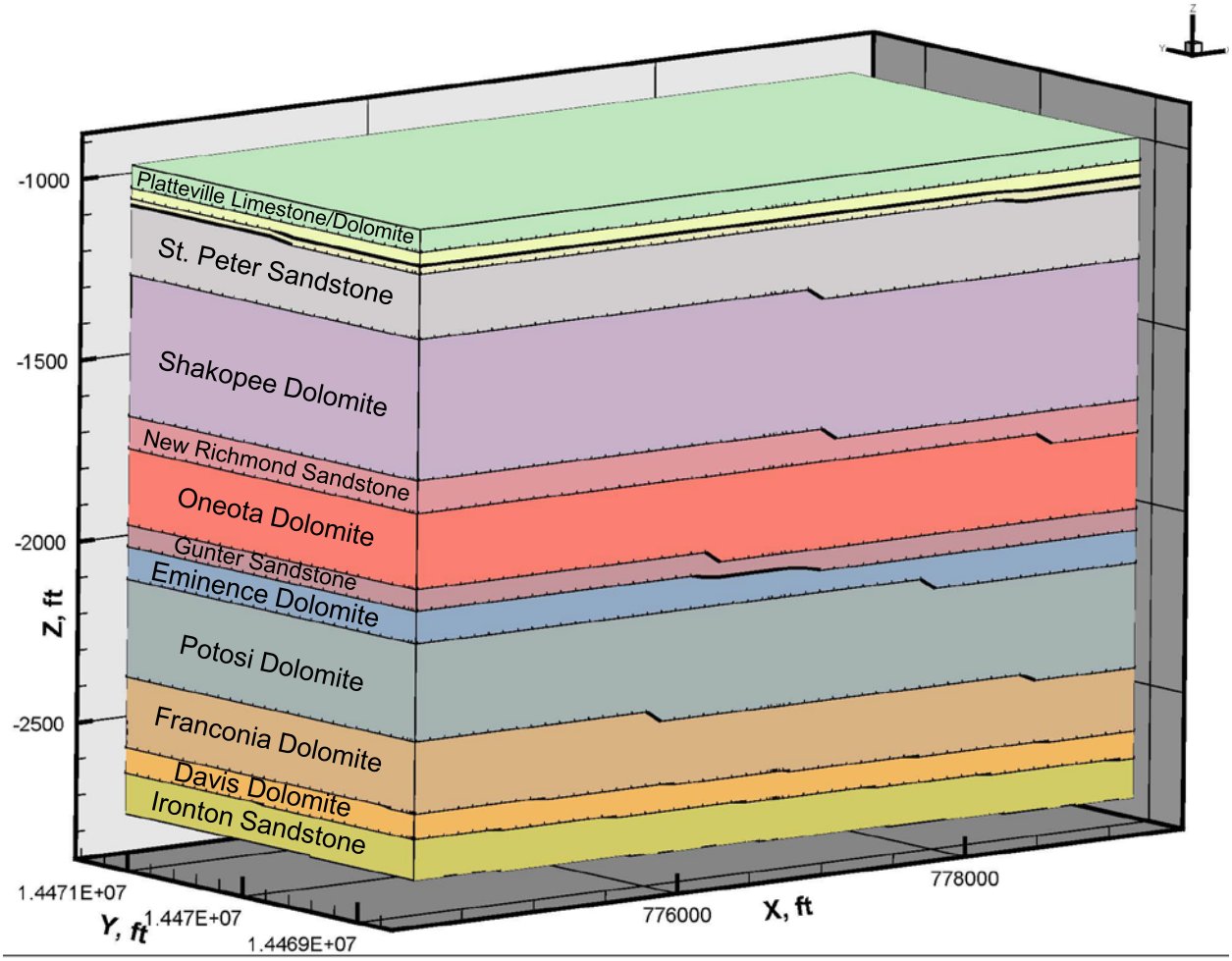

Figure 7.1. Model domain and hydrostratigraphic units for the preliminary MVA-ULT model.

Initial simulations were conducted on the preliminary MVA-ULT model to assess the impact of node spacing and domain size on the simulation results. Two different types of tests were conducted: 1) a simulation with 1/4 symmetry and a higher esolution X-Y grid, with the maximum spacing of 50 ft (instead of 100 ft), and 2) a simulation that extended the domain by 1,000 ft in the Y direction and 2,000 ft in the X direction (i.e., 1,000 ft extra on both the east and west sides). The results of these simulations are reported in Appendix A. In summary, the results of these tests were similar to the base case, but there was less numerical dispersion apparent at the more distant locations, which affected aqueous solute arrivals for the higher resolution grid (i.e., sharper arrivals of aqueous CO_2). Some of the slight

differences seen in the higher resolution 1/4 symmetry case can be attributed to the different overall hydrostratigraphic structure from the 1/4 symmetry assumption (i.e., no down-dip section on the east side). The extended boundary case had a slightly lower pressure increase for the 20-year $scCO_2$ leakage case. Pressure changes in the Ironton Sandstone were slightly less than the 20-year base case (see Figure 7.15 in Section 7.2.2) for all lateral distances and depths, except for the top of the Ironton at the 80-ft distance. CO_2 saturations and aqueous CO_2 concentrations for the 100-year extended domain case were nearly identical to the 100-year base case (see Figure 7.13 in Section 7.2.2).

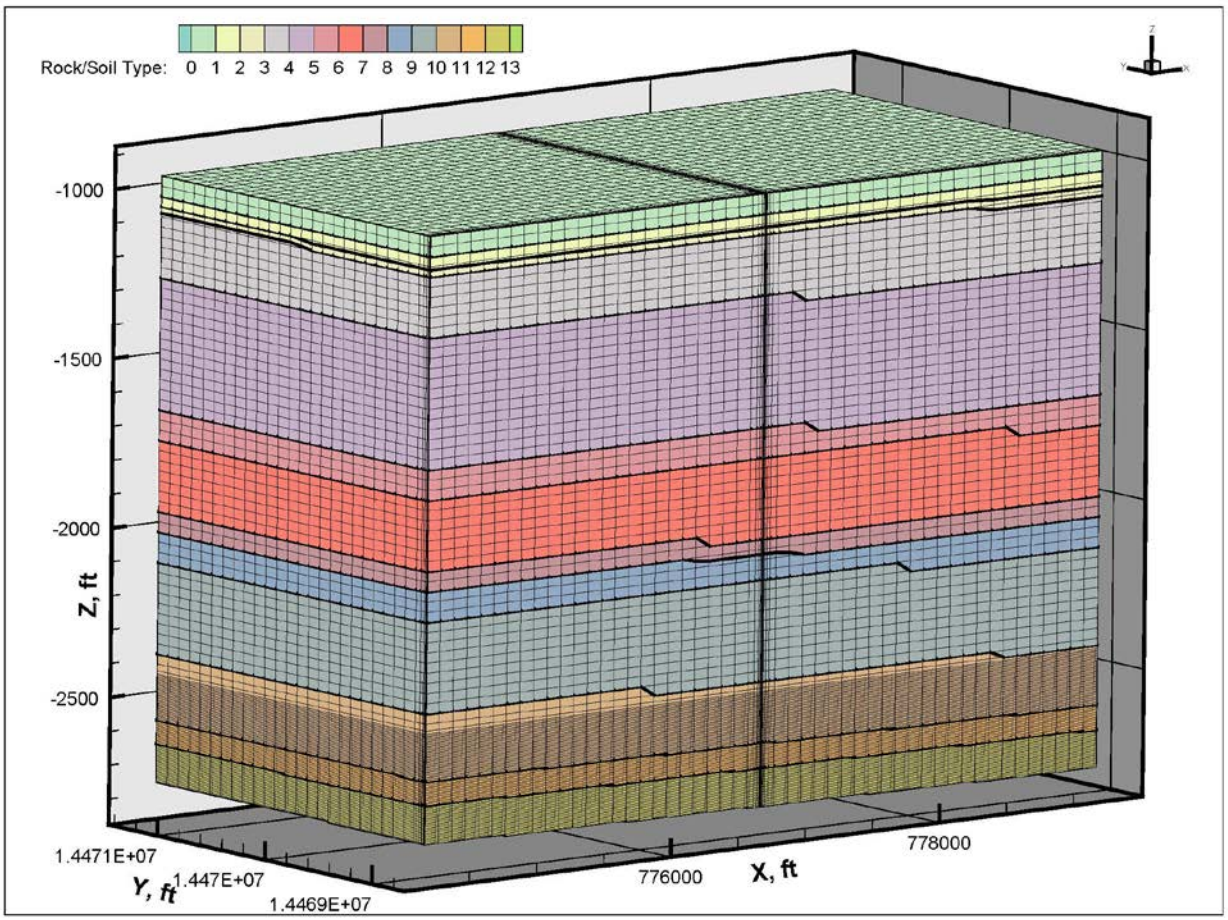

Figure 7.2. Model domain, hydrostratigraphic units, and STOMP-CO2 grid for the preliminary MVA-ULT model.

7.1.1.1 Material Properties

As discussed previously, limited site-specific characterization data are available for this preliminary, scoping-level, MVA-ULT model. Sidewall core samples were collected from all of the major units and laboratory analyses of these samples is one source of the property estimates used in this preliminary model. Regional studies of the units were used to fill in the gaps in material property values. For this modeling effort, each stratigraphic unit was assigned a uniform set of material properties (i.e., there were no material property variations within stratigraphic units). The properties that were used are shown in Table 7.1, along with the source of the property estimates.

Table 7.1. Preliminary properties assigned for the initial Upper Layer Transport Model. Corelabs Sample IDs are listed in the Unit column where representative samples were available. Unshaded rows are permeable units.

Unit	Porosity (fraction)	Permeability (mD)	Specific Storage[a] (m^{-1})	Kv/Kh or Kv Value	Brooks/Corey Saturation Properties[j] (Corelabs Sample ID)
Platteville Limestone Corelabs ID: 70	0.0189	1.96E-4	1.0E-6	0.1	46m[e]
Joachim Dolomite Corelabs ID: 69	0.0168	7.25E-5	1.0E-6	0.1	34m[e]
Glenwood Dolomite Corelabs ID: 68	0.047	1.94E-3	1.0E-6	0.1	45m[e]
St. Peter Sandstone	0.18[c]	1,220[d]	1.0E-6	0.5[b]	9m[e]
Shakopee Dolomite Corelabs ID: 62m	0.075	8.05E-3	1.0E-6	2.12E-4 mD[f]	62m
New Richmond Sandstone	0.132[f]	333[f]	1.0E-6	0.5[b]	11Vm[e]
Oneota Dolomite Corelabs ID: Sidewall 58 and 59	0.0766 (mean)	3E-7 (NA – value from Eminence)	1.0E-6	0.1	43m[e]
Gunter Dolomite/ Sandstone Corelabs ID: Sidewall 56	0.0255	3E-7 (NA – values from Eminence)	1.0E-6	0.1	27Hm[e]
Eminence Dolomite Corelabs ID: 54m	0.003	3E-7	1.0E-6	0.1	54m
Potosi Dolomite	0.038 (mean of 6 sidewall core samples)	9,000[g]	1.0E-6	0.1	9m[e]
Franconia Dolomite Corelabs ID: 46m	0.029	2.7E-4	1.0E-6	2.46E-6 mD[f] (value from Davis)	46m
Davis Dolomite Corelabs ID: 45m	0.039	1.72E-3	1.0E-6	2.46E-6 mD[f]	45m
Ironton Sandstone Sample ID: 40m and 43m	0.118[h]	41.6[h]	1.0E-6	0.5[i]	40m

(a) Specific storage for units use a default value calculated based on a mid-range of compressibility for sound rock (Table 2.5 of Freeze and Cherry [1979]).
(b) No specific data available; Gupta and Bair (1997) Ironton Formation is used.
(c) Representative porosity not available for unit, picked from similar unit, ID in table.
(d) Buschbach and Bond (1967, 1973)
(e) Saturation properties not available for this unit. Properties were taken from another sample with similar permeability and porosity.
(f) Corelabs (1966): Special Core Analysis Tests, Waverly Field. Porosity is the mean of samples, horizontal permeability (air) is the mean of samples, vertical permeability (water) is the harmonic mean of samples.
(g) Value reported for Potosi at Cabot Waste Injection Well in Tuscola, Illinois
(h) Mean of two samples (Mercury injection K_{sw} and porosity)
(i) Reported anisotropy of Kerbel-Galesville-Ironton in Gupta and Bair (1997)
(j) Brooks-Corey Parameters derived from Corelabs Mercury Injection data from stratigraphic borehole (see Rockhold et al. 2014)

7.1.2 Initial Conditions

Initial conditions specified for the model are aqueous pressure, temperature, and salinity. Pressures were based on interpolation of measurements from the initial stratigraphic borehole (Alliance 2012, 2013). The temperature profile is similar to the profile reported in the borehole completion and characterization report (Alliance 2012), but was slightly modified based on additional measurements collected during the geomechanical testing program, conducted in the fall of 2013. This modification to the temperature profile was made to account for drilling-related temperature variations that were apparent in the original profile. Initial salinities were specified as the mean salinity calculated for each hydrostratigraphic unit, based on salinity logs from the initial stratigraphic borehole (Alliance 2012, 2013). Aqueous sample results from fluid samples collected during drilling and hydrologic testing of the initial stratigraphic borehole were compared. The mean salinity based on the geophysical logs for the St. Peter Sandstone was higher than the limited number of aqueous samples collected from the St. Peter Sandstone but was similar to both depth discrete and composite aqueous samples collected from the Mount Simon Sandstone.

7.1.3 Boundary Conditions

On the side and back boundaries of the 3D model (north, east, and west), a Dirichlet boundary condition is specified based on the initial conditions for pressure, salinity, and temperature. A no-flow boundary is imposed on the front (south) of the domain due to the 1/2 symmetry scheme used. For the top boundary (applied to the top of the Platteville, above the lowermost USDW [St Peter Sandstone] to minimize boundary effects), Dirichlet boundary conditions for pressure, temperature, and salinity were specified based on initial condition values. A no-flow boundary was also specified for the bottom boundary.

Regional flux through the Ironton Sandstone was not considered in this preliminary modeling effort. Based on estimates from regional models (Young 1992; Mandel and Kontis 1992), groundwater flux through the Ironton is likely negligible over the time scales of these leakage simulations.

7.2 Leakage Scenarios

The leakage source is applied through a single node at the bottom of the Ironton Sandstone in the center of the X-direction model domain in the 1-ft X-Y refined grid area. This source is intended to approximate a leak from an artificial penetration or some other localized source of leakage. The initial scoping-level leakage scenarios assume 1% of the total planned $scCO_2$ injection mass (22 MMT) has leaked (0.22 MMT) over three different time periods as follows:

- 1% of total injected mass is leaked over 20 years (0.011 MMT/yr)
- 1% of total injected mass is leaked over 100 years (0.0022 MMT/yr)
- 1% of total injected mass is leaked over 500 years (0.00044 MMT/yr).

In addition, a 20-year brine leakage case was simulated with the brine volume equivalent to the 1% $scCO_2$ volume. These cases are described in the following sections along with a discussion of preliminary results.

7.2.1 20-Year $scCO_2$ Leakage Case

Figure 7.3 shows simulated $scCO_2$ saturations from the 20-year leakage case at node locations within the Ironton Sandstone. This line plot shows the simulated values at three lateral distances from the point-source leakage location (80, 455, and 955 ft toward the west) and three vertical positions within the Ironton Sandstone (top, middle, and bottom). Initial $scCO_2$ arrivals occur rapidly (i.e., <1 year) at the 80-ft lateral distance for all three depth intervals. Conversely, an observed arrival response at the 455- and 955-ft distance only occurs in the top portion of the Ironton, with initial arrivals occurring at approximately 2.5 and 8 years, respectively. The vertical distribution of $scCO_2$ in the simulation is a result of buoyancy-driving forces because of the lower fluid density of $scCO_2$ relative to brine. Figure 7.4 shows a contour plot of the $scCO_2$ at the end of the 20-year leakage simulation. The $scCO_2$ plume is very narrow above the leakage location and spreads out at the contact with the Davis Dolomite, which has a much greater entry pressure than the Ironton Sandstone and a much lower intrinsic permeability (see Table 7.1). No $scCO_2$ enters the Davis Dolomite in the simulation. Figure 7.5 shows the same 20-year $scCO_2$ saturations in a 3D view to depict the plume spread and the 1/2 symmetry used in the model. The preferential lateral spreading of the $scCO_2$ to the west (left of figure) is associated with the dip in the Ironton/Davis contact and the buoyancy of the $scCO_2$. Figure 7.6 shows the growth of the $scCO_2$ plume during earlier time periods in the simulation (i.e., 2 and 7 years).

Simulated aqueous pressures are shown in Figure 7.7 for the same nodal locations where $scCO_2$ saturation was reported. These trend plots show that the near-leak pressures quickly rise but then decrease even though the $scCO_2$ leakage flux is constant. This behavior is due to the increase in $scCO_2$ saturations as the plume grows, which causes a corresponding increase in the $scCO_2$ relative permeability and a decrease in pressure gradients required to support the leakage flux. Aqueous pressures at the intermediate distance (i.e., 455 ft) show a similar behavior but take longer to develop and the magnitudes of the pressures are attenuated. Figure 7.8 shows a contour plot of the aqueous pressure near the beginning of the simulation when the near-leak pressures are at or near the peak values. Note that the higher formation pressures on the down-dip side of the leak are due to the greater depth because these plots are showing total pressure, not buildup from initial pressures. Figure 7.9 shows a contour plot of the much lower aqueous pressures at the end of the 20-year $scCO_2$ leak simulation.

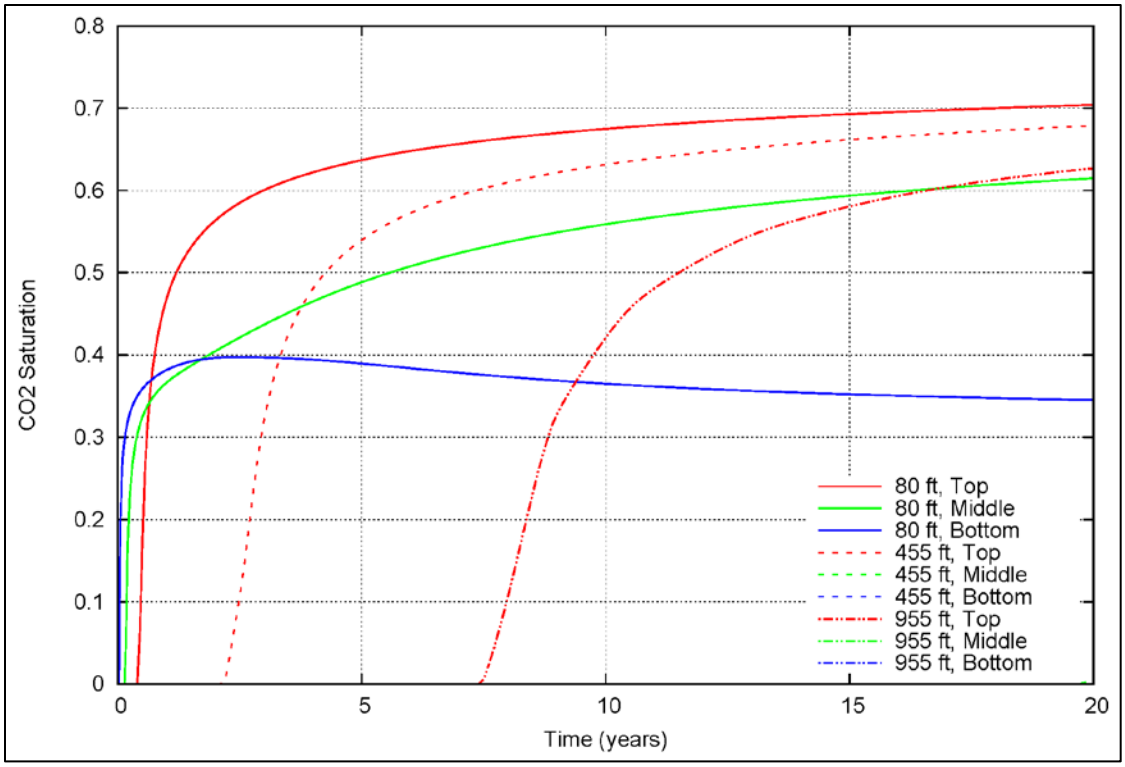

Figure 7.3. Simulated $scCO_2$ saturation values at nodes within the Ironton Sandstone for the 20-year $scCO_2$ leakage case. Distances are at nodes west of the leak and at the top, middle, and bottom of the Ironton Sandstone.

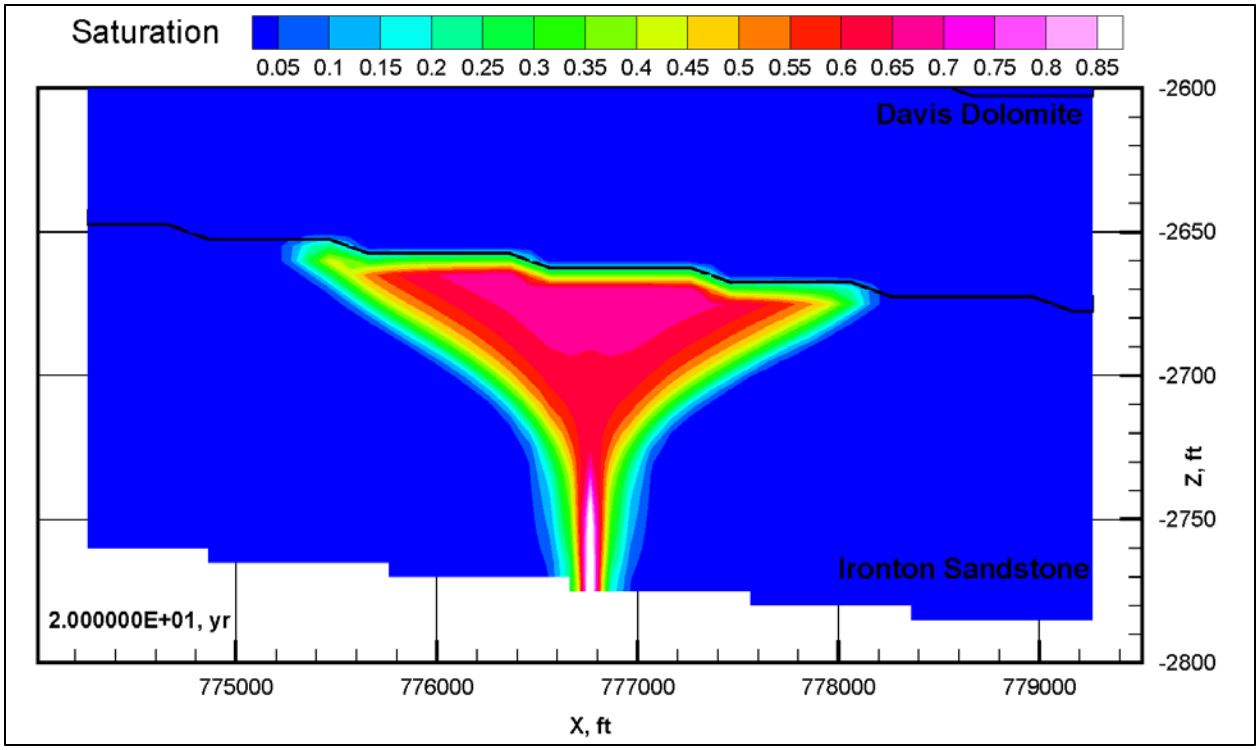

Figure 7.4. Simulated $scCO_2$ saturations at 20 years for the 20-year $scCO_2$ leakage case. Note that west is toward the left of the diagram.

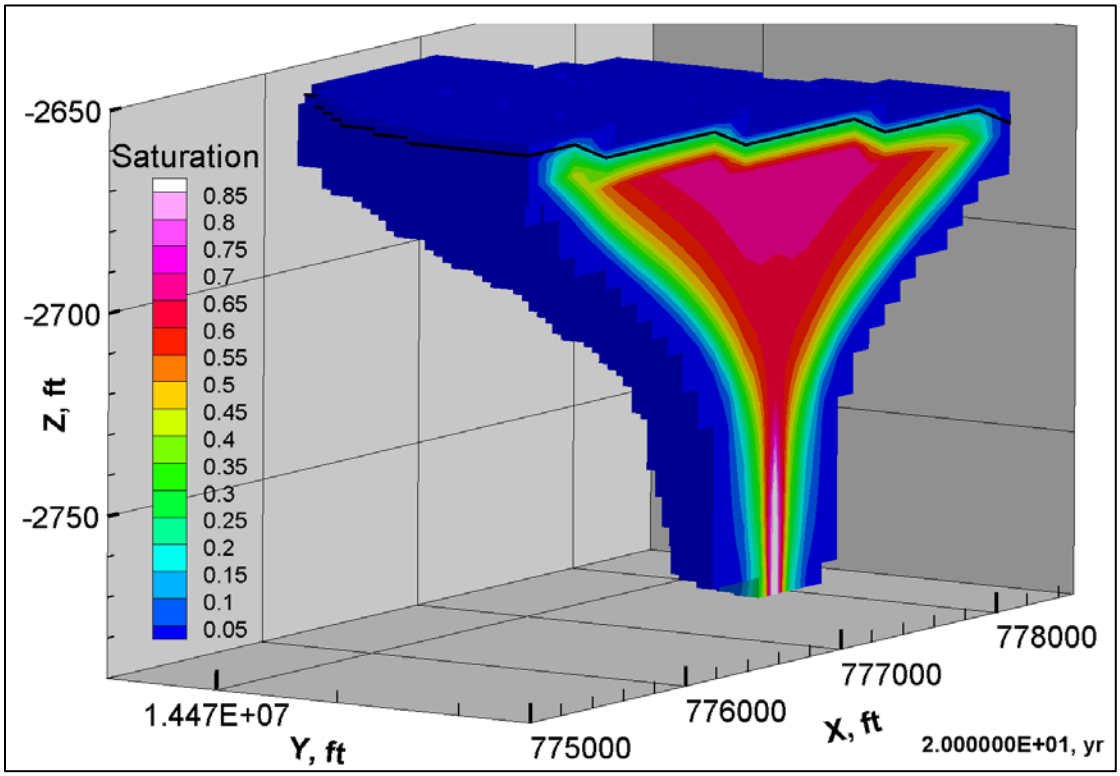

Figure 7.5. Three-dimensional view of simulated $scCO_2$ saturations at 20 years for the 20-year $scCO_2$ leakage case.

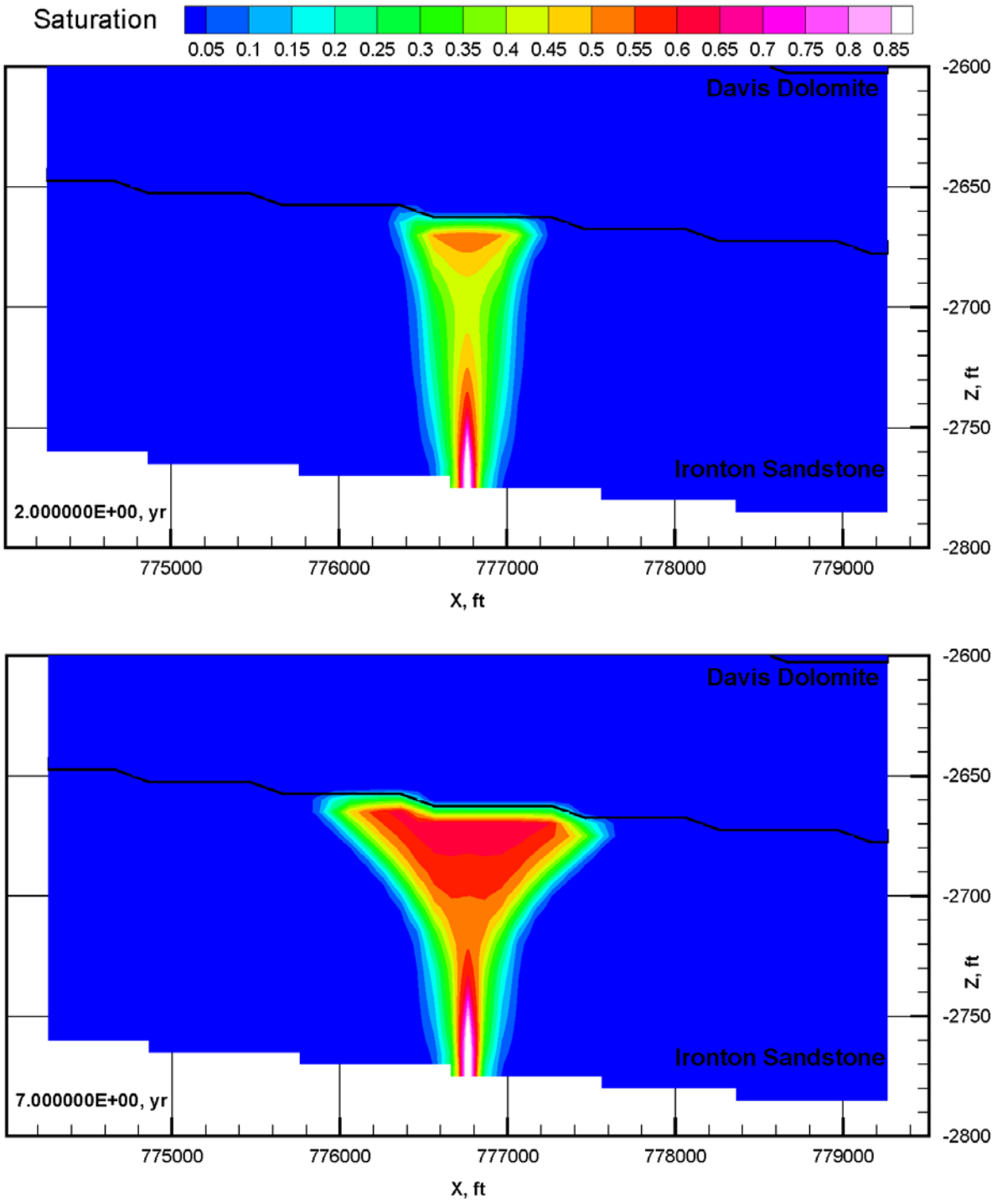

Figure 7.6. Simulated $scCO_2$ saturations at 2 years (top) and 7 years (bottom) for the 20-year $scCO_2$ leakage case.

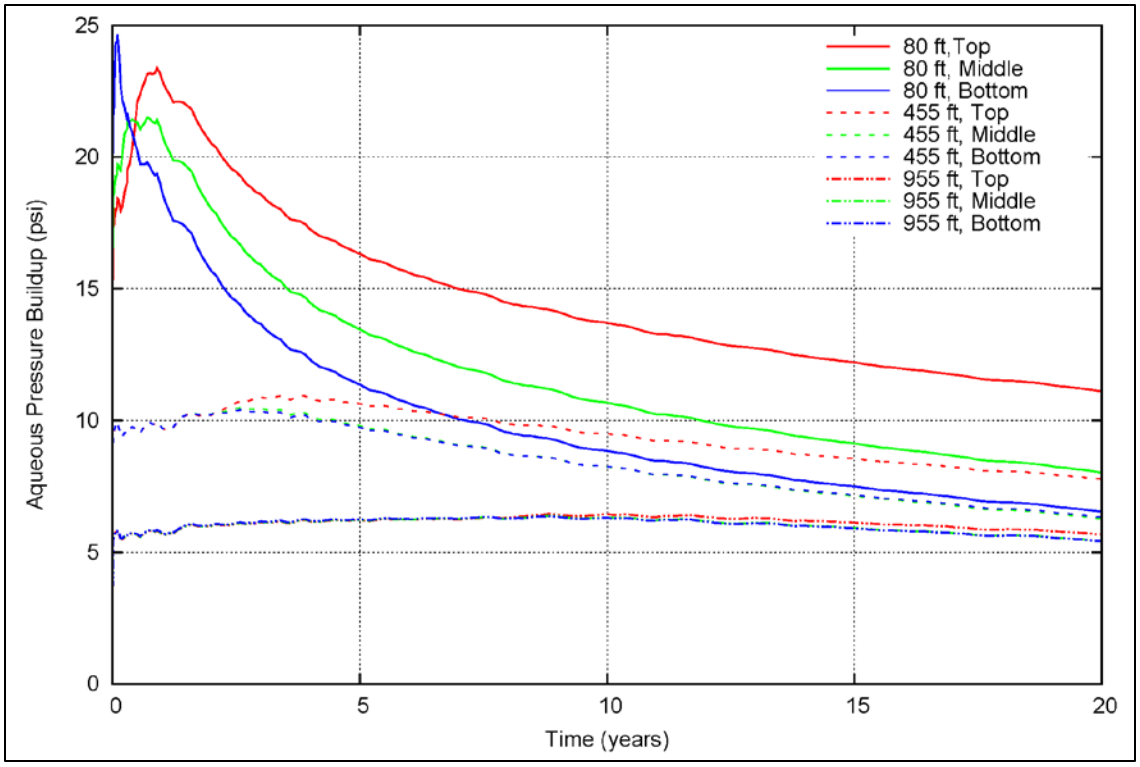

Figure 7.7. Simulated aqueous pressures at nodes within the Ironton Sandstone for the 20-year $scCO_2$ leakage case. Distances are at nodes west of the leak and at the top, middle, and bottom of the Ironton Sandstone.

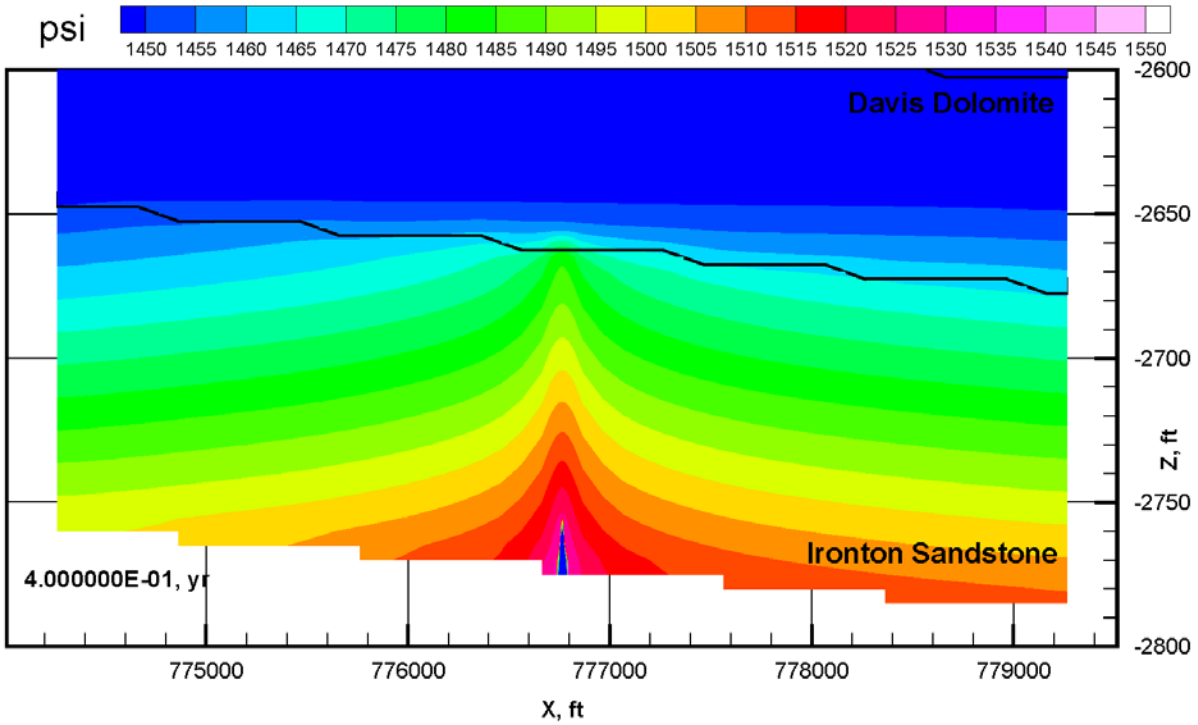

Figure 7.8. Simulated aqueous pressures at 0.4 years for the 20-year $scCO_2$ leakage case. Note that the higher formation pressures on the down-dip side of the leak (right) are due to the greater depth because this plot is showing total pressures, not buildup from initial pressures.

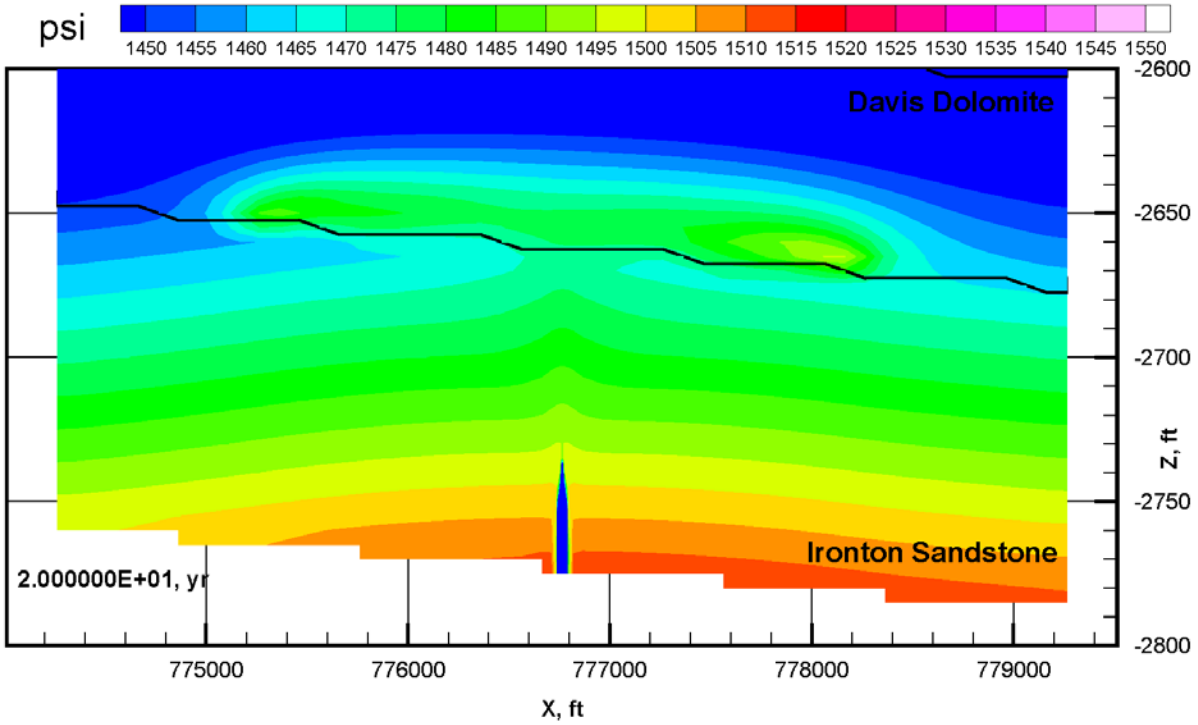

Figure 7.9. Simulated aqueous pressures at 20 years for the 20-year $scCO_2$ leakage case.

Figure 7.10 shows the trend plots at the selected node locations (80, 455, and 955 ft west of the leak) for aqueous CO_2 concentrations. The aqueous CO_2 plume is larger than the $scCO_2$ plume because it is formed within and at the margins of the growing $scCO_2$ plume. The aqueous CO_2 is also influenced by the brine flow patterns within the Ironton Sandstone. Contour plots of the aqueous CO_2 are shown in Figure 7.11 at the end of the simulation period and in Figure 7.12 for time periods 0.7 and 7 years to illustrate the plume growth.

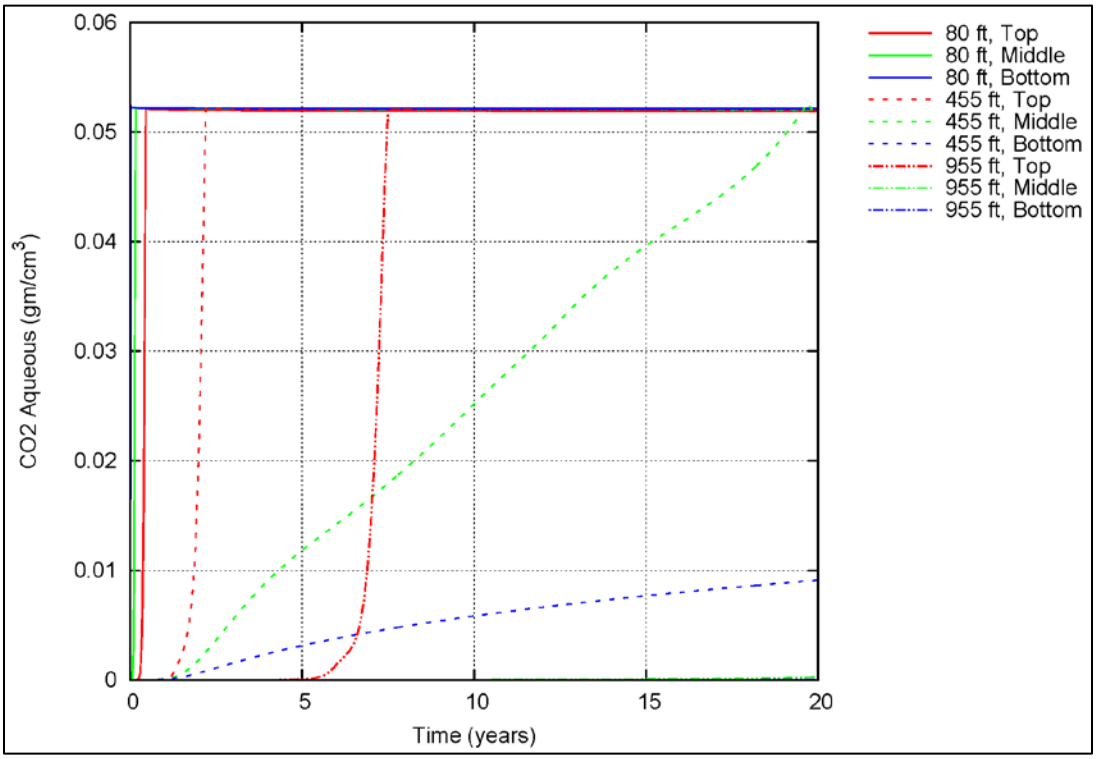

Figure 7.10. Simulated aqueous CO_2 concentrations at nodes within the Ironton Sandstone for the 20-year $scCO_2$ leakage case. Distances are at nodes west of the leak and at the top, middle, and bottom of the Ironton Sandstone.

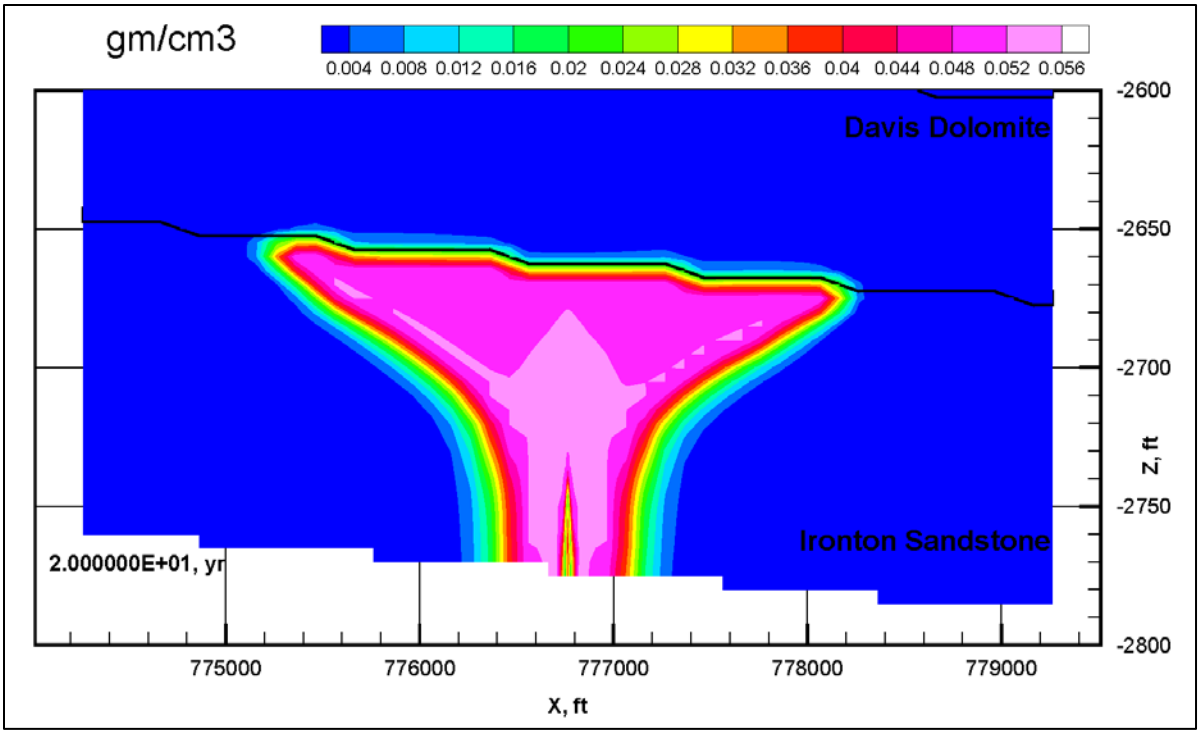

Figure 7.11. Simulated aqueous CO_2 concentrations at 20 years for the 20-year $scCO_2$ leakage case.

7.2.2 100-Year $scCO_2$ Leakage Case

The same sequence of simulation results described above for the 20-year $scCO_2$ leakage case is presented here for the 100-year $scCO_2$ leakage case. Figure 7.13 and Figure 7.14 show the simulated $scCO_2$ saturations, Figure 7.15 and Figure 7.16 show the simulated aqueous pressure results, and Figure 7.17 and Figure 7.18 show the simulated aqueous CO_2 results. With the lower $scCO_2$ leakage rate in this case, but longer simulation time (i.e., the same mass but spread out over 100 years instead of 20), the resulting $scCO_2$ plume extends farther laterally in the upper portion of the Ironton Formation than was simulated for the 20-year case. The 100-year $scCO_2$ case also results in less lateral spreading of the plume over the bottom and middle portions of the Ironton than for the 20-year case. Overall the magnitude of the increase in aqueous pressure is lower for the 100-year case, which is expected given the lower $scCO_2$ flux. However the pressure trends (i.e., a sharp increase followed by a decline) are similar. Simulated aqueous CO_2 concentrations also spread farther laterally in the 100-year case compared to the 20-year case.

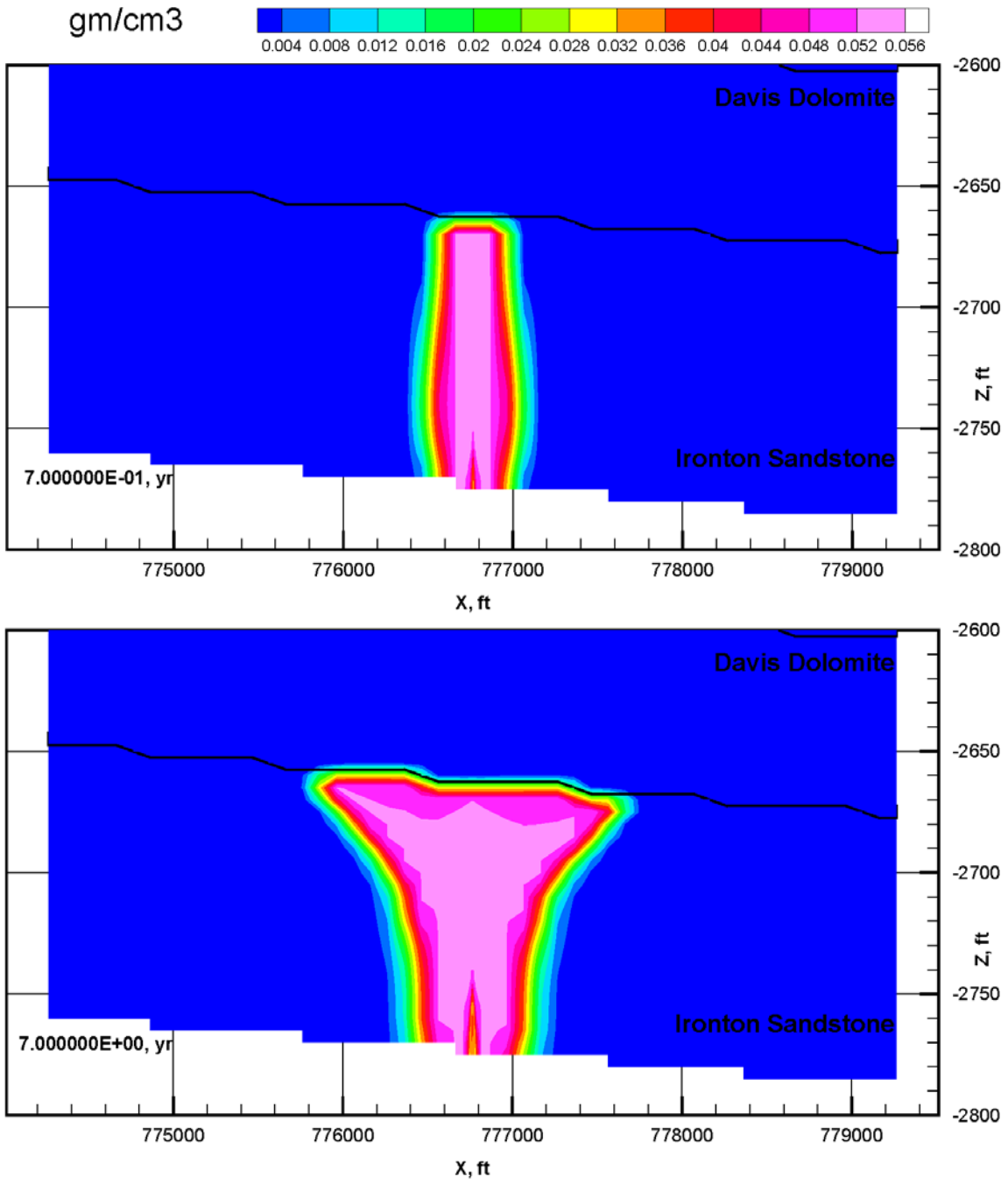

Figure 7.12. Simulated aqueous CO_2 concentrations at 0.7 years (top) and 7 years (bottom) for the 20-year $scCO_2$ leakage case.

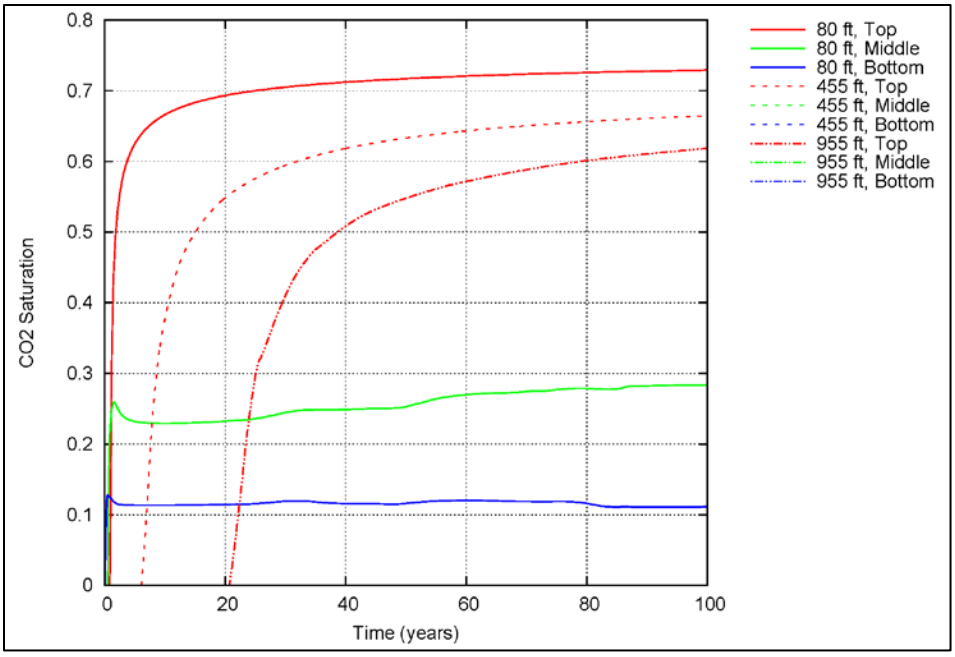

Figure 7.13. Simulated $scCO_2$ saturation values at nodes within the Ironton Sandstone for the 100-year $scCO_2$ Leakage Case. Distances are at nodes west of the leak and at the top, middle, and bottom of the Ironton Sandstone.

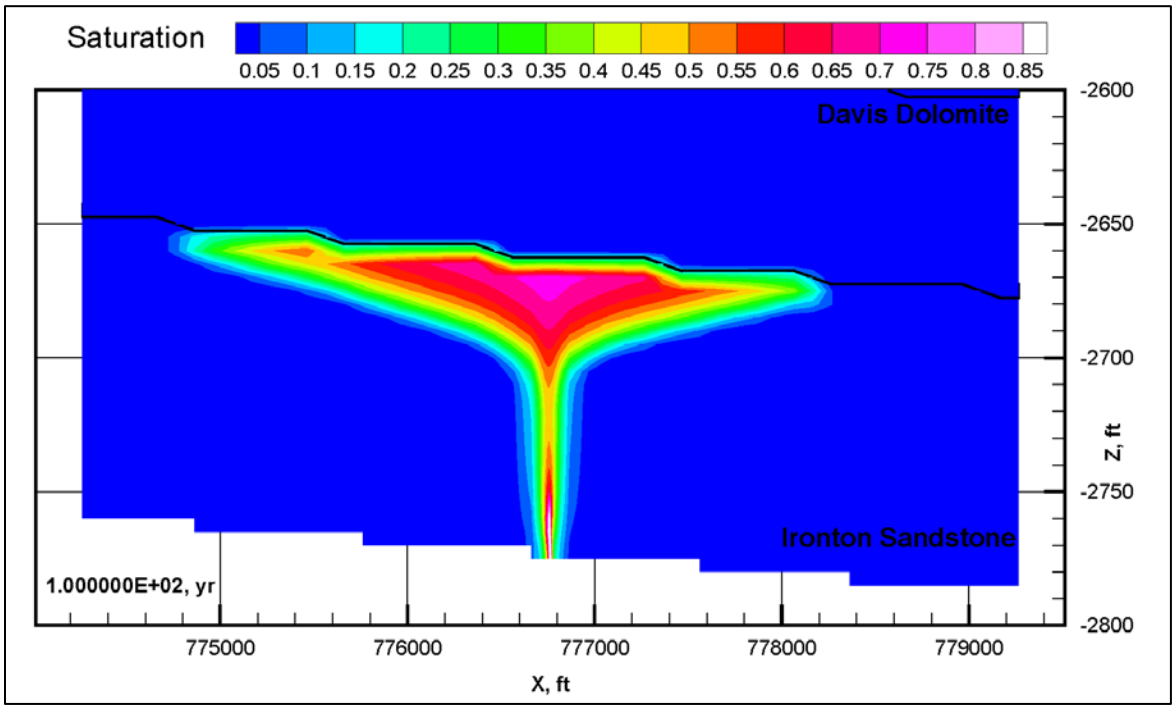

Figure 7.14. Simulated $scCO_2$ saturations at 100 years for the 100-year $scCO_2$ leakage case.

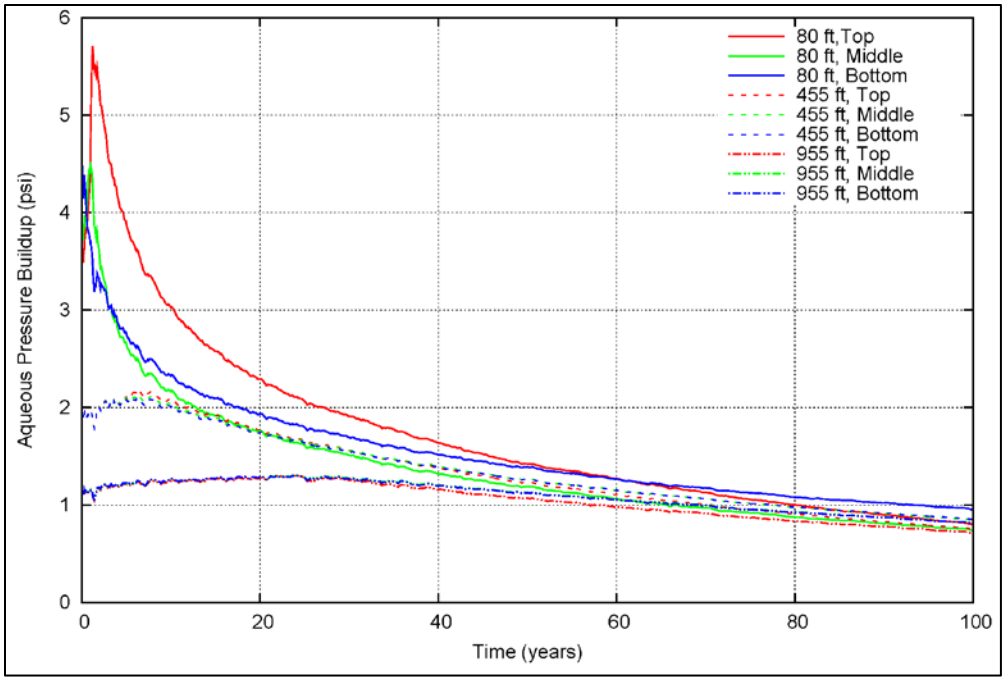

Figure 7.15. Simulated aqueous pressures at nodes within the Ironton Sandstone for the 100-year $scCO_2$ leakage case. Distances are at nodes west of the leak and at the top, middle, and bottom of the Ironton Sandstone.

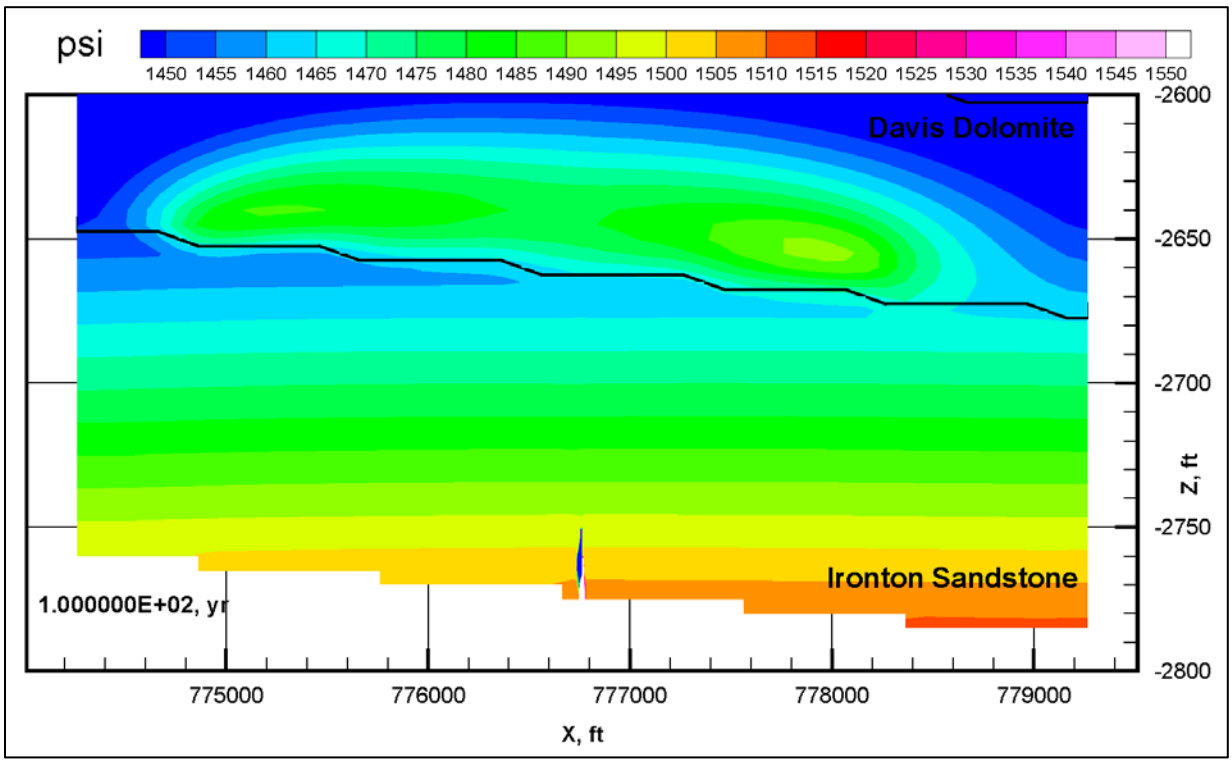

Figure 7.16. Simulated aqueous pressures at 100 years for the 100-year $scCO_2$ leakage case**.**

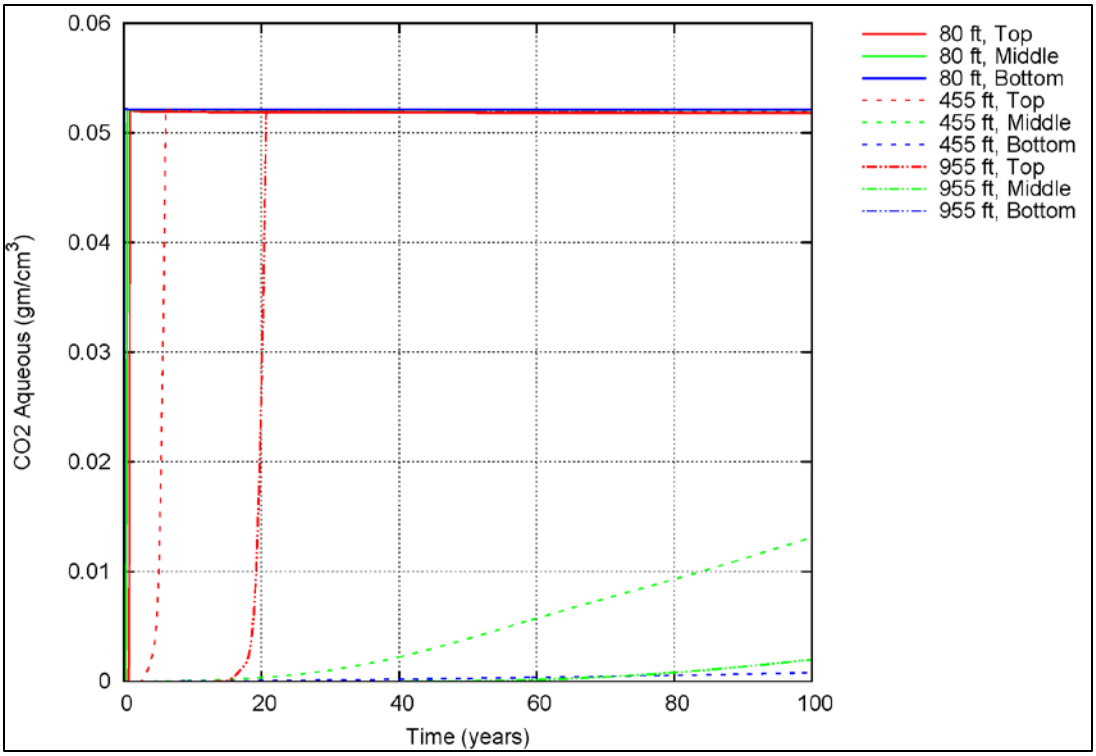

Figure 7.17. Simulated aqueous CO_2 concentrations at nodes within the Ironton Sandstone for the 100-year $scCO_2$ leakage case. Distances are at nodes west of the leak and at the top, middle, and bottom of the Ironton Sandstone.

7.2.3 500-Year $scCO_2$ Leakage Case

The same sequence of simulation results described for the leakage cases above is presented here for the 500-year $scCO_2$ leakage case. Figure 7.19 through Figure 7.21 show the simulated $scCO_2$ saturations, Figure 7.22 and Figure 7.23 show the simulated aqueous pressure results, and Figure 7.24 and Figure 7.25 show the simulated aqueous CO_2 results for the 500-year leakage case. At this leakage rate and simulation duration, which was the lowest rate and longest duration evaluated, the resulting $scCO_2$ plume extends farther laterally in the upper portion of the Ironton Formation than the shorter duration leakage cases (but all have the same total $scCO_2$ leakage mass). The 500-year $scCO_2$ case also results in a thinner plume over the bottom and middle portions of the Ironton relative to shorter duration leakage cases (i.e., higher leakage rates). As shown in Figure 7.20, the $scCO_2$ plume extends so far laterally that it flows out of the western boundary of the model domain during the latter part of the simulation. Figure 7.21 shows the $scCO_2$ saturations at 300 years, where the $scCO_2$ is still contained within the model domain. As expected, the magnitude of the aqueous pressure increase is lower for the 500-year $scCO_2$ leakage case because of the lower leakage rate (Figure 7.22 and Figure 7.23). However the pressure trends (i.e., an initial increase followed by a decline) are similar. Simulated aqueous CO_2 concentrations (see Figure 7.24 for arrival curves) also spread farther laterally in the 500-year case compared to the other cases. As with the $scCO_2$ saturations, the aqueous CO_2 plume was flowing out the western boundary during the latter part of the simulation, but to a much larger extent. The simulated aqueous CO_2 plume results (see Figure 7.25) also show some signs of density effects in the flow field in the latter half of the simulated period (e.g., convection and sinking), but the veracity of these results needs to be confirmed in simulations with extended boundaries to eliminate the potential for boundary-induced artifacts.

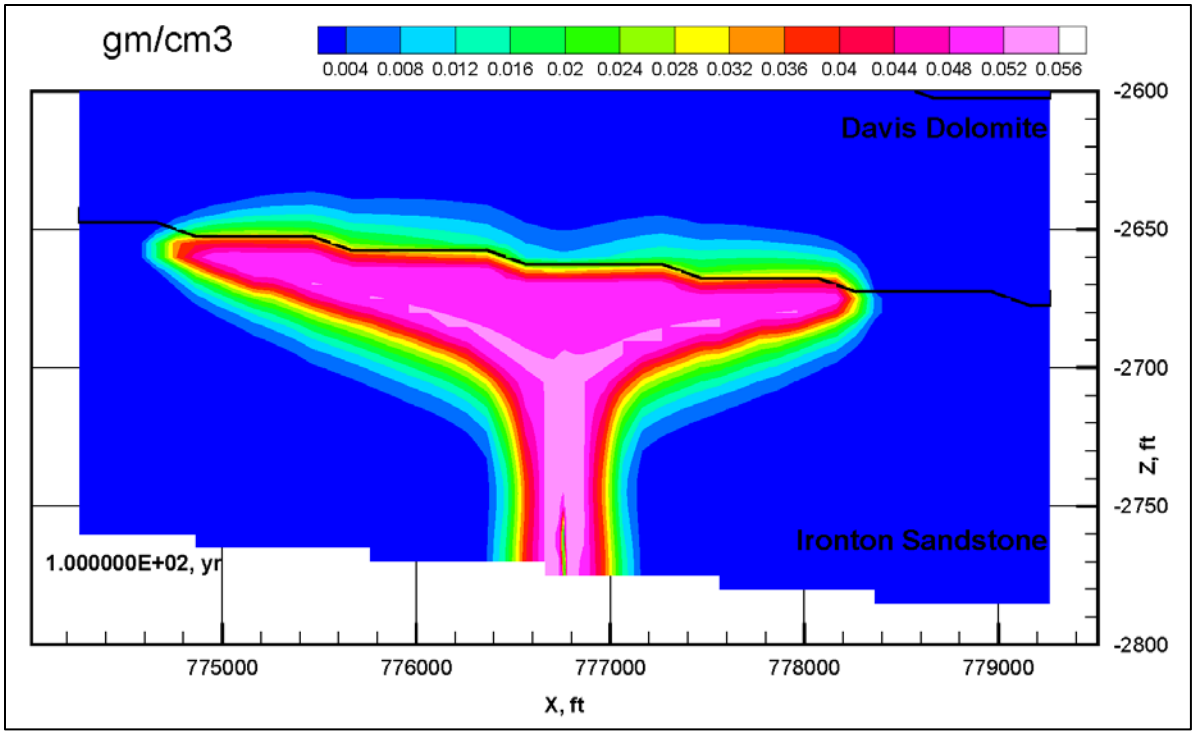

Figure 7.18. Simulated aqueous concentrations at 100 years for the 100-year $scCO_2$ leakage case.

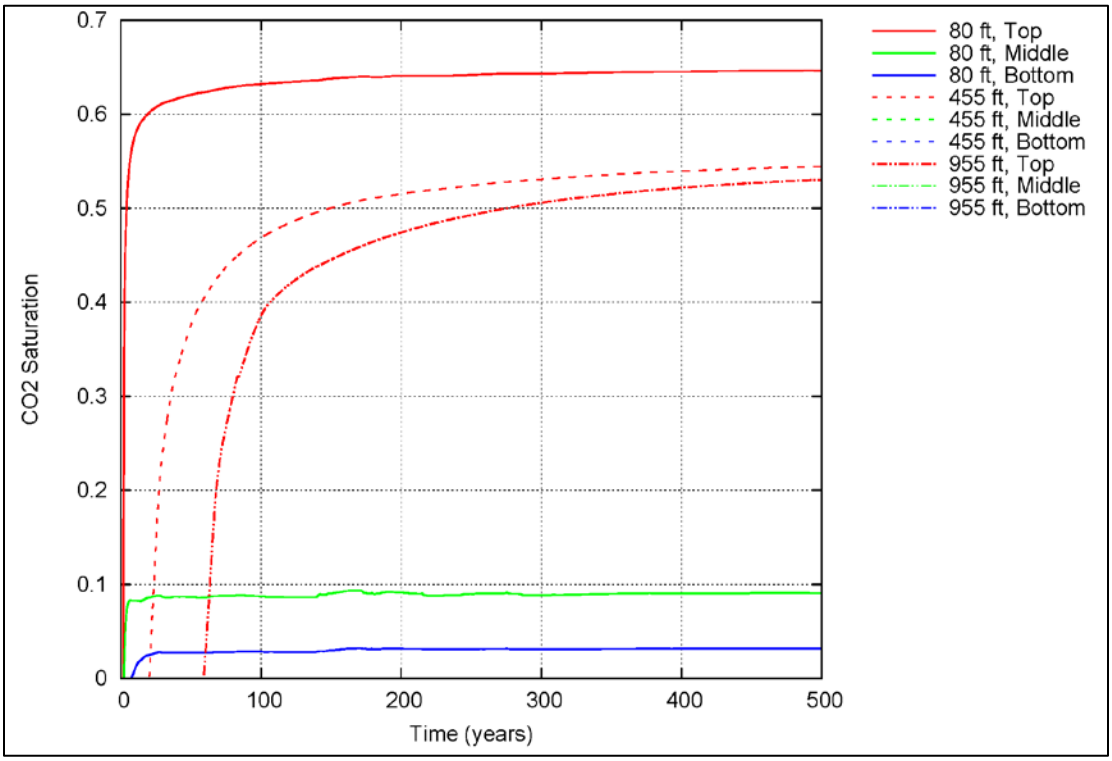

Figure 7.19. Simulated $scCO_2$ saturation values at nodes within the Ironton Sandstone for the 500-year $scCO_2$ leakage case. Distances are at nodes west of the leak and at the top, middle, and bottom of the Ironton Sandstone.

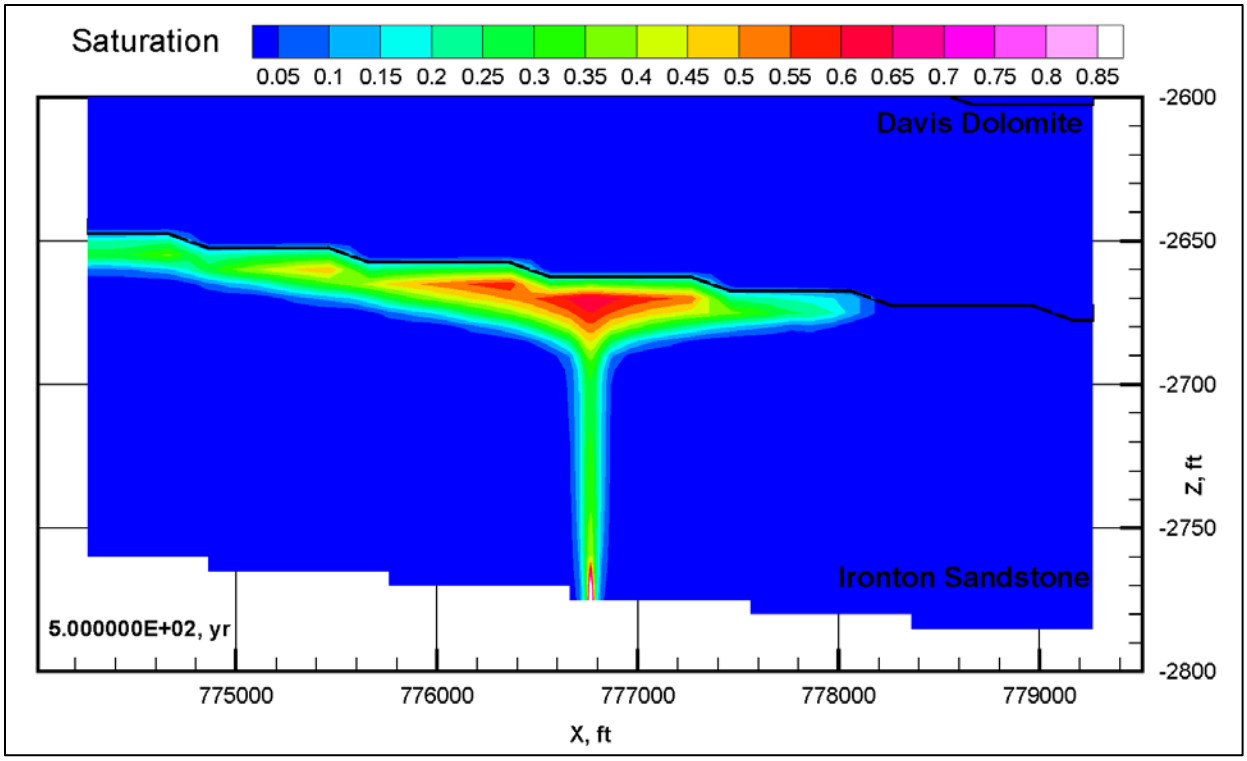

Figure 7.20. Simulated $scCO_2$ saturations at 500 years for the 500-year $scCO_2$ leakage case.

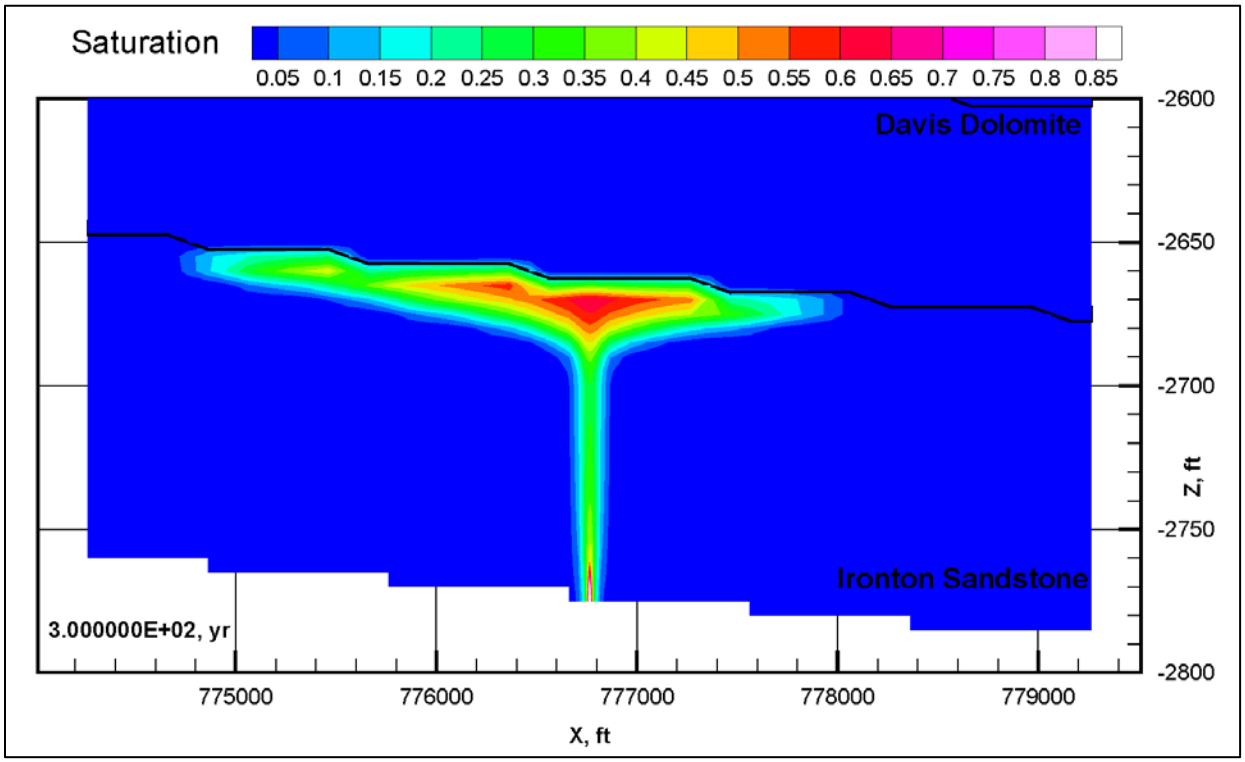

Figure 7.21. Simulated $scCO_2$ saturations at 300 years for the 500-year $scCO_2$ leakage case.

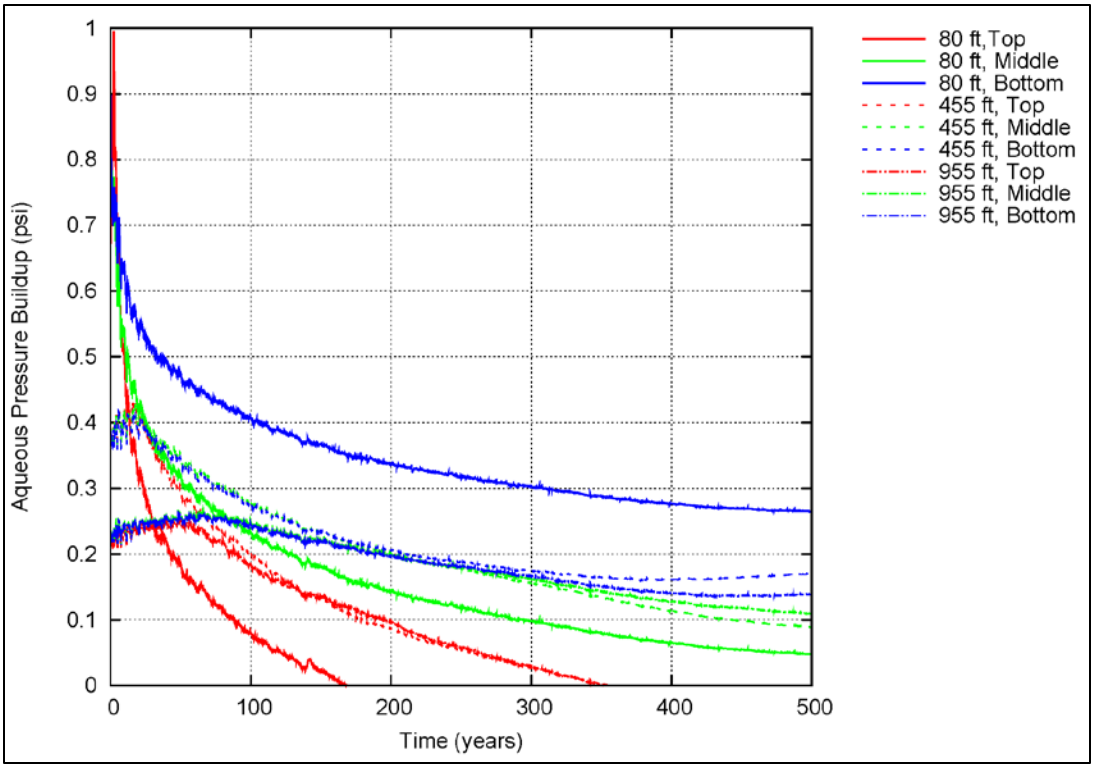

Figure 7.22. Simulated aqueous pressures at nodes within the Ironton Sandstone for the 500-year scCO$_2$ leakage case. Distances are at nodes west of the leak and at the top, middle, and bottom of the Ironton Sandstone.

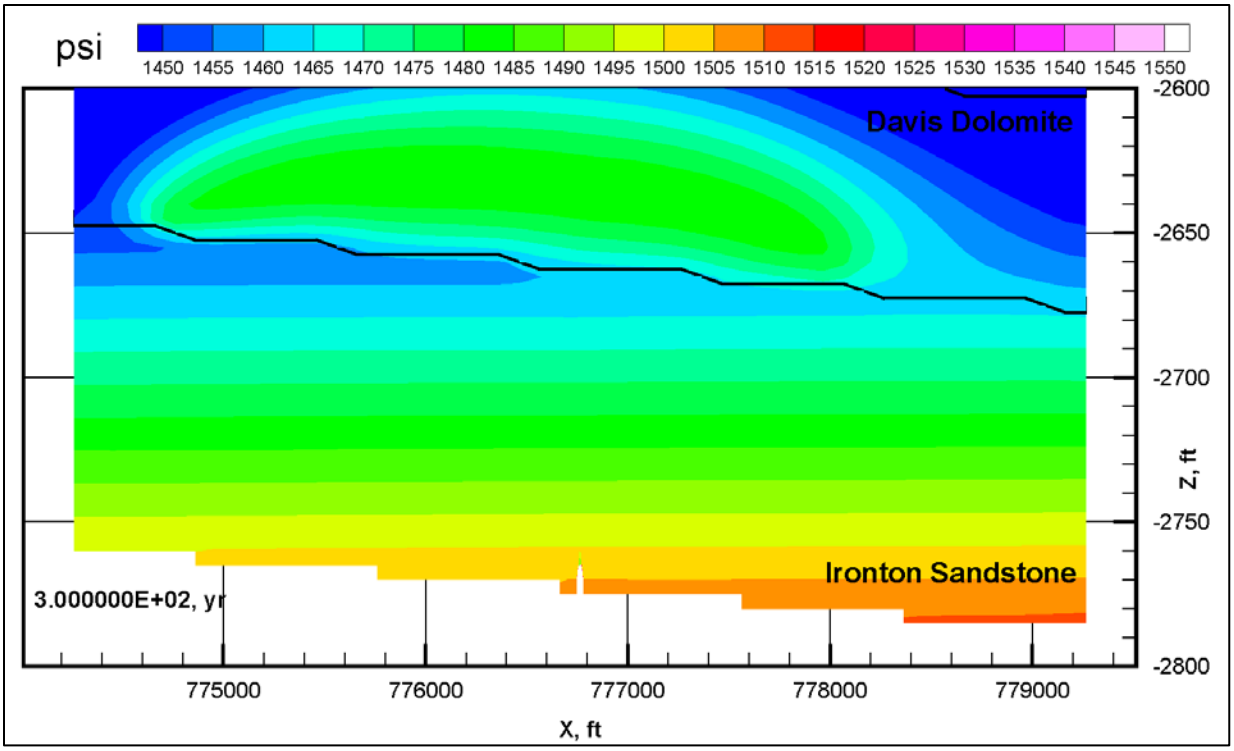

Figure 7.23. Simulated aqueous pressures at 300 years for the 500-year scCO$_2$ leakage case.

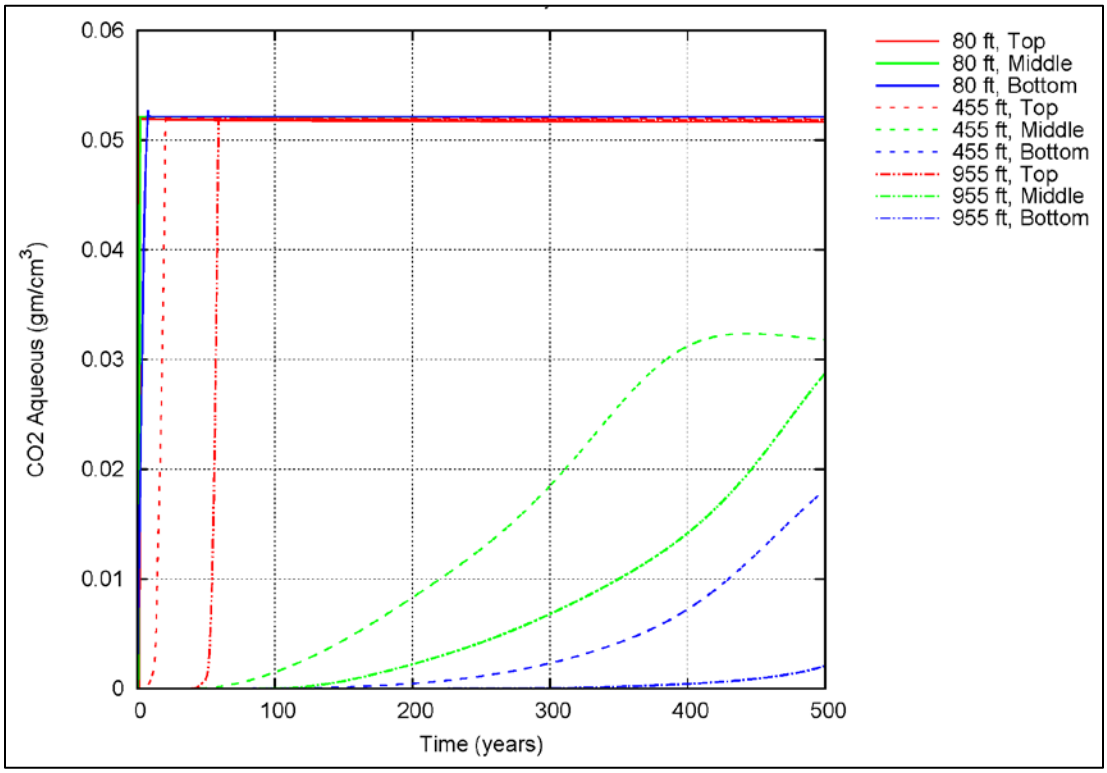

Figure 7.24. Simulated aqueous CO_2 concentrations at nodes within the Ironton Sandstone for the 500-year scCO$_2$ leakage case. Distances are at nodes west of the leak and at the top, middle, and bottom of the Ironton Sandstone.

7.2.4 Brine Leakage Case – 20 Year

A brine leakage simulation was conducted to evaluate the pressure and geochemical responses for leakage that occurs through preferential pathways in the caprock, as a result of increased reservoir pressure outside of the $scCO_2$ plume. To compare equivalent leakage rates for $scCO_2$ and brine, the 20-year $scCO_2$ leakage rate (Section 7.2.1) was converted to an equivalent volumetric brine leakage rate. With a $scCO_2$ density of 738.1 kg/m^3 (at 1,500 psi and 93°F), the 0.011 MMT/yr $scCO_2$ leakage rate equates to a volumetric rate of 1.49×10^7 L/yr. Using a density of 1,032.51 kg/m^3 (Alliance 2013) for the Mount Simon brine yields a brine mass leakage rate of 1.54×10^7 kg/yr. In addition to measuring aqueous pressures, a conservative tracer was added to the brine simulation to track brine leakage movement. As was the case for $scCO_2$, results are reported for three lateral distances from the point-source leakage location (80, 455, and 955 ft toward the west) and three vertical positions within the Ironton Sandstone (top, middle, and bottom).

For tracer results (Figure 7.26 through Figure 7.28), the highest relative concentrations of tracer occur closest to the leakage source and at the bottom of the Ironton Sandstone (Figure 7.26). Unlike $scCO_2$ (where buoyancy effects result in preferential vertical migration and higher concentrations at the top of the Ironton), the brine tracer is driven upward from the leakage point and diffuses outward in a columnar shape, with the highest concentrations occurring at the bottom of the Ironton (Figure 7.27 and Figure 7.28). Such results are also seen at intermediate lateral distances from the leakage source, where tracer concentrations break through at the formation bottom first, followed by the middle, and top portions of the Ironton. No breakthrough of tracer occurs at the farthest lateral distance during the 20-year simulation.

Formation aqueous pressures, unlike $scCO_2$ results, remain relatively constant after an initial buildup (Figure 7.29 and Figure 7.30). This is because brine does not induce the same changes in relative permeability as the $scCO_2$. That is, single-phase leakage does not change existing saturation phases in the formation, so the relative permeability remains constant. The highest pressure buildups are consistent with the location of highest tracer concentrations (i.e., closest to the leakage source at the bottom of the Ironton). At farther lateral distances, these maximum pressure buildups at the bottom of the formation are smaller.

Increases in the aqueous salt mass fraction and fluid density in the Ironton Formation can indicate the breakthrough of leaking brine because the leaking Mount Simon reservoir brine has a higher salinity and density than the Ironton Formation brine. The mean salinity in the Ironton Sandstone, based on the wireline log from the stratigraphic well, was 15 g/kg; Mount Simon Sandstone salinity measurements, from aqueous samples collected during hydraulic testing on February 8, 2012, were from 46 to 58 g/kg (Alliance 2012). As Figure 7.31 (salt mass fraction) and Figure 7.33 (aqueous density) demonstrate, simulated brine leakage migration occurs relatively quickly at the closest lateral distances, particularly for the bottom of the Ironton. At farther lateral distances, salt mass fraction concentration changes are delayed and attenuated. The migration of salt mass fraction increases as shown in Figure 7.32 and directly mimics tracer concentration in terms of both shape and extent. At 955 ft, the virtual lack of salt mass fraction increases or density increases suggests that brine migration has not reached this point.

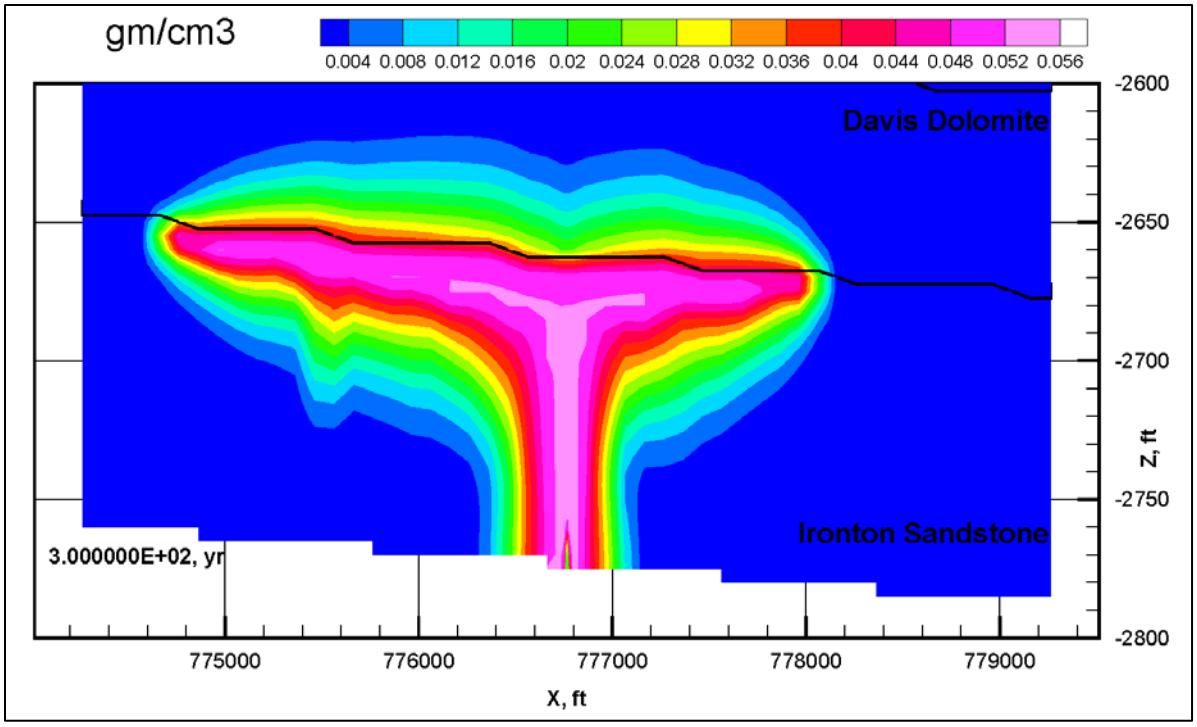

Figure 7.25. Simulated aqueous concentrations at 300 years for the 500-year scCO$_2$ leakage case.

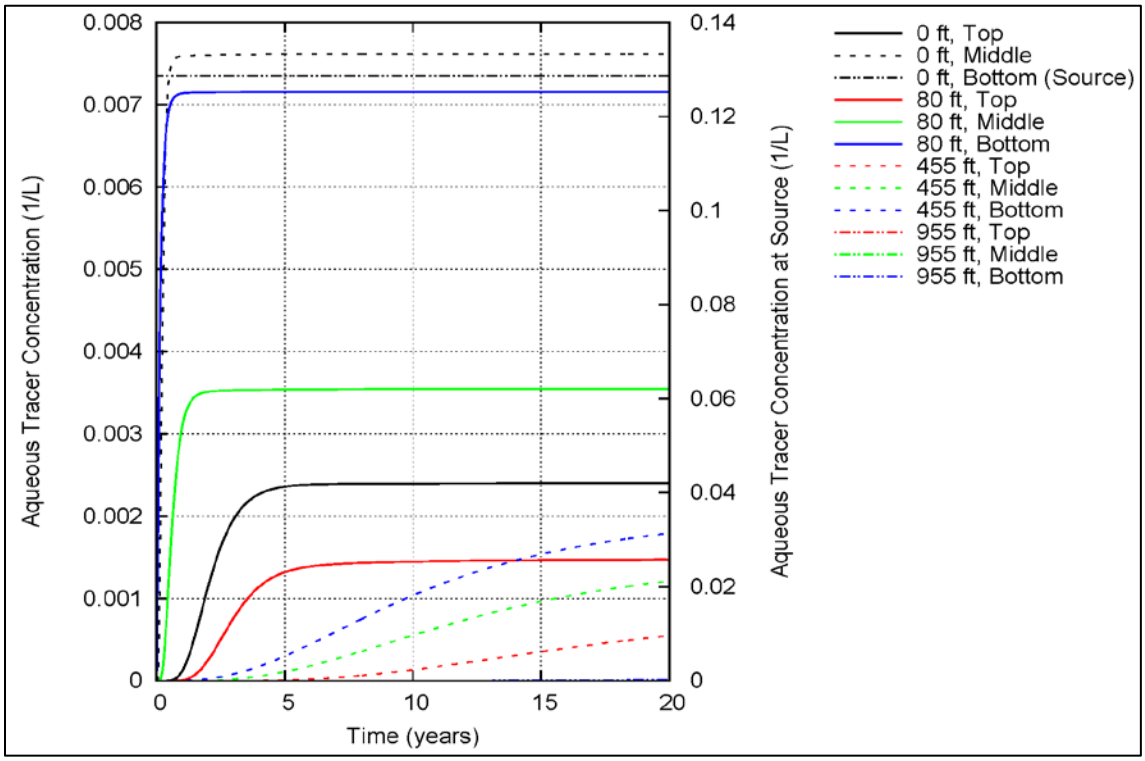

Figure 7.26. Simulated tracer concentrations at nodes within the Ironton Sandstone for the 20-year brine leakage case. Distances are at nodes west of the leak and at the top, middle, and bottom of the Ironton Sandstone.

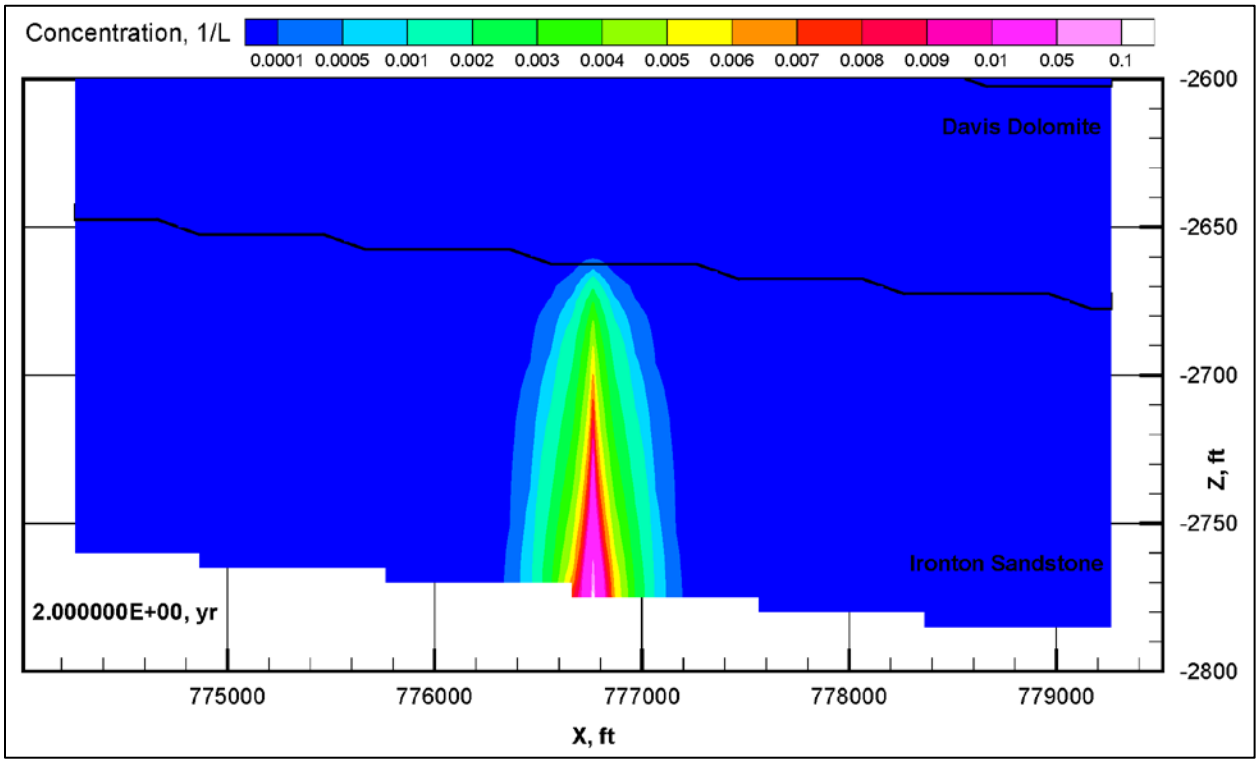

Figure 7.27. Simulated tracer concentrations at 2 years for the 20-year brine leakage case.

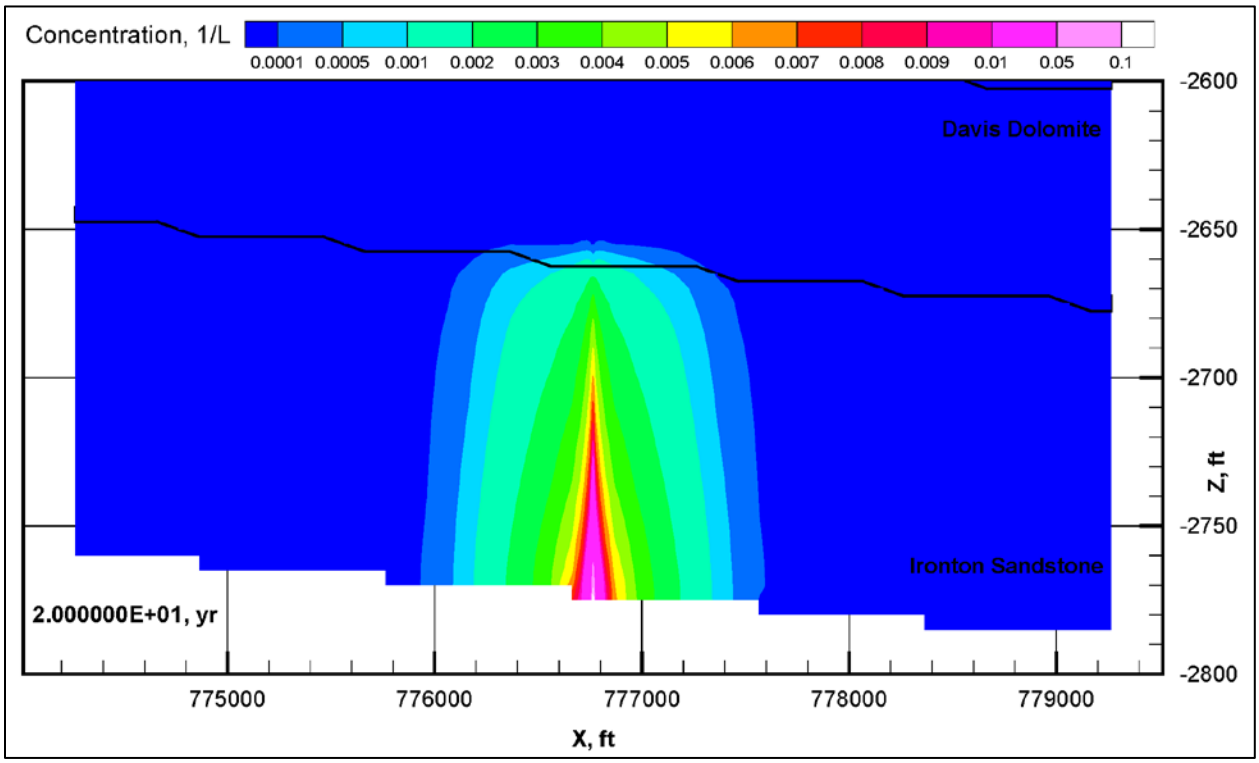

Figure 7.28. Simulated tracer concentrations at 20 years for the 20-year brine leakage case.

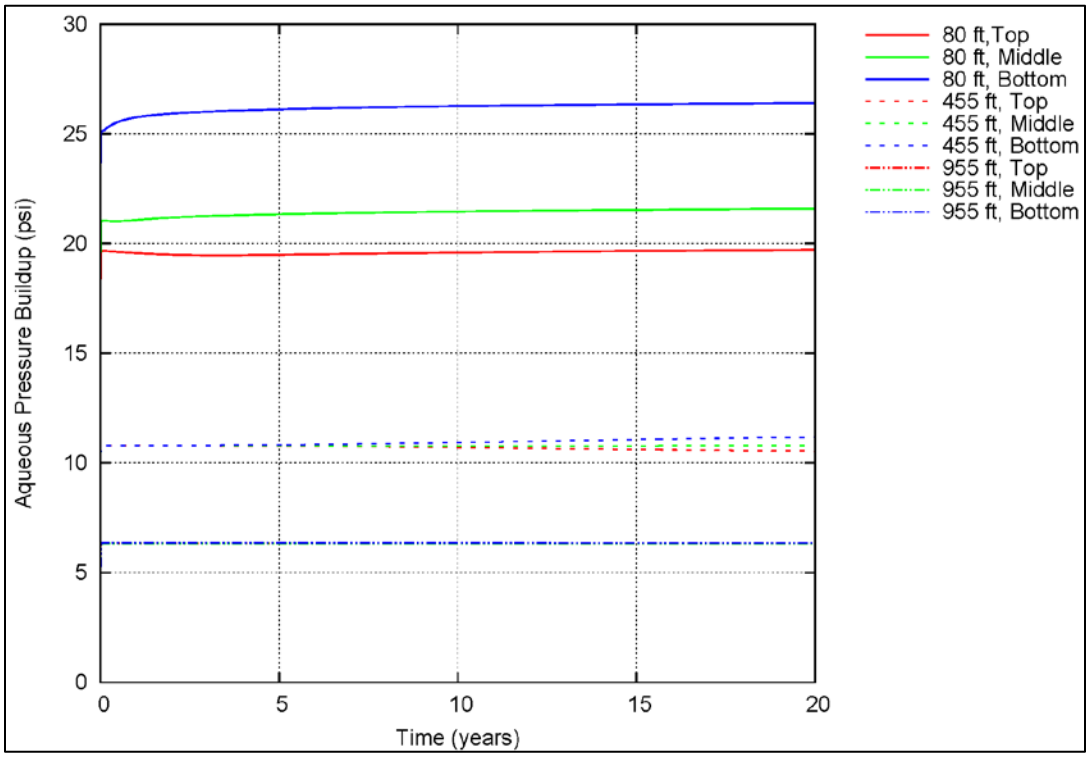

Figure 7.29. Simulated aqueous pressures at nodes within the Ironton Sandstone for the 20-year brine leakage case. Distances are at nodes west of the leak and at the top, middle, and bottom of the Ironton Sandstone.

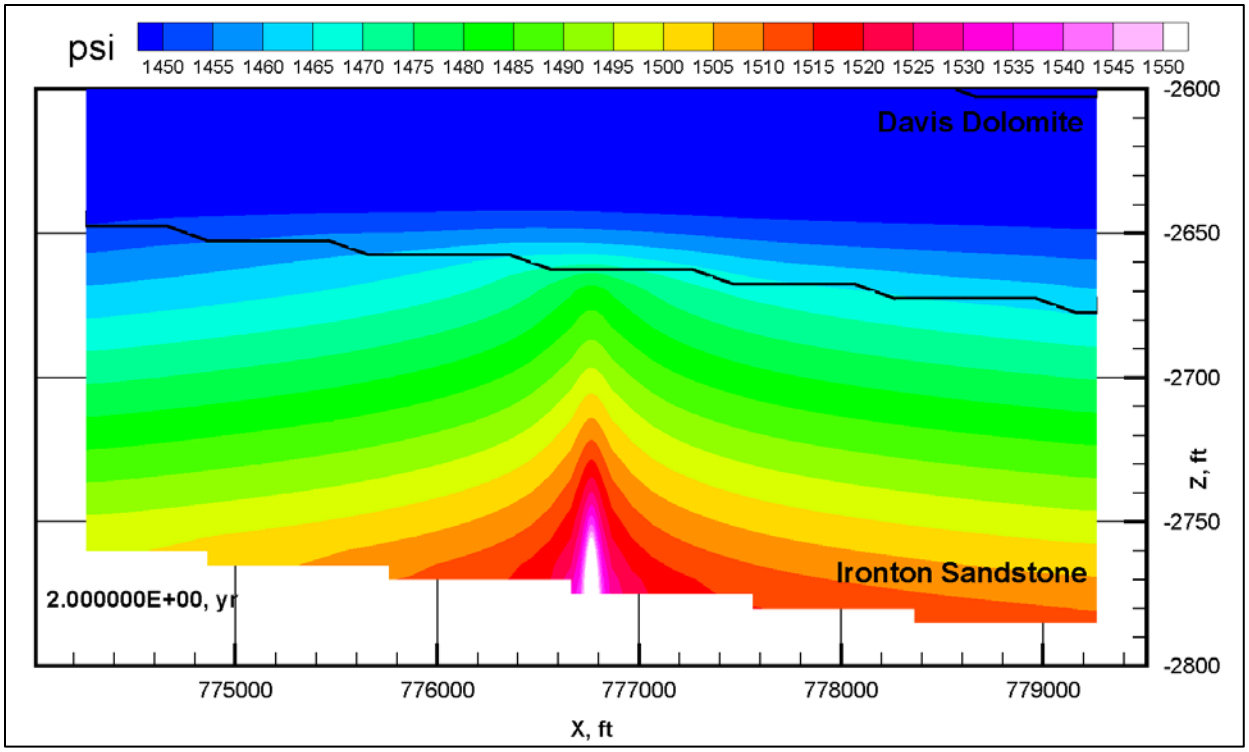

Figure 7.30. Simulated aqueous pressures at 2 years for the 20-year brine leakage case.

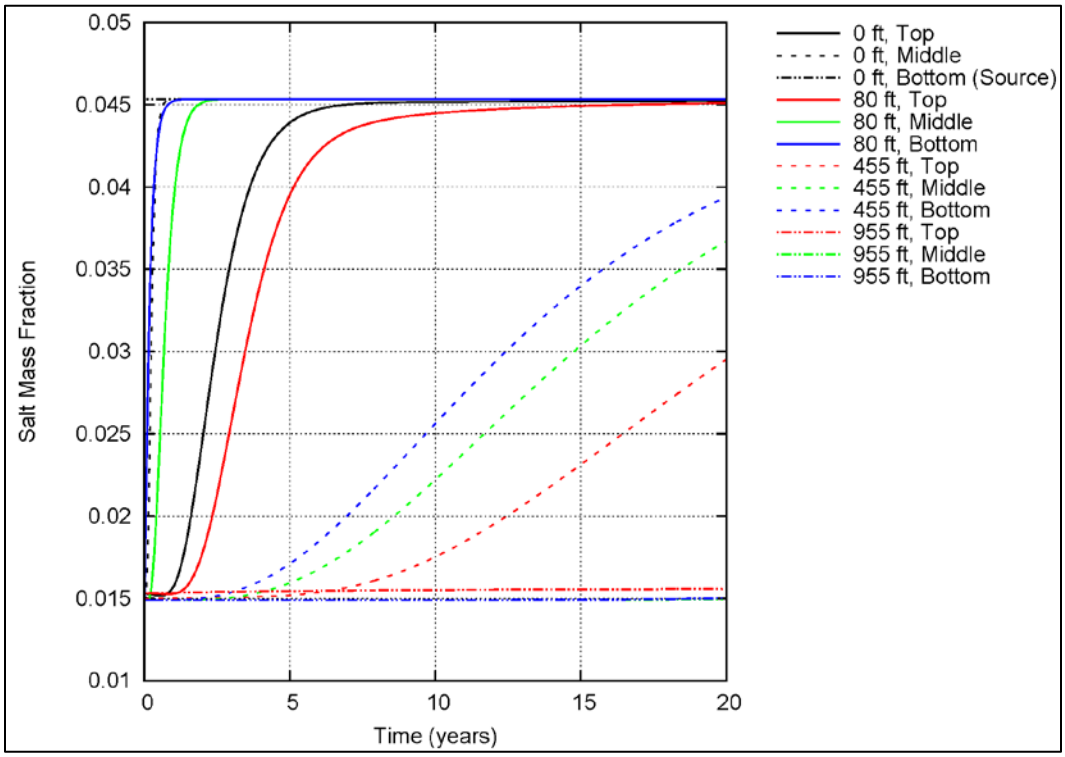

Figure 7.31. Simulated salt mass fraction at nodes within the Ironton Sandstone for the 20-year brine leakage case. Distances are at nodes west of the leak and at the top, middle, and bottom of the Ironton Sandstone.

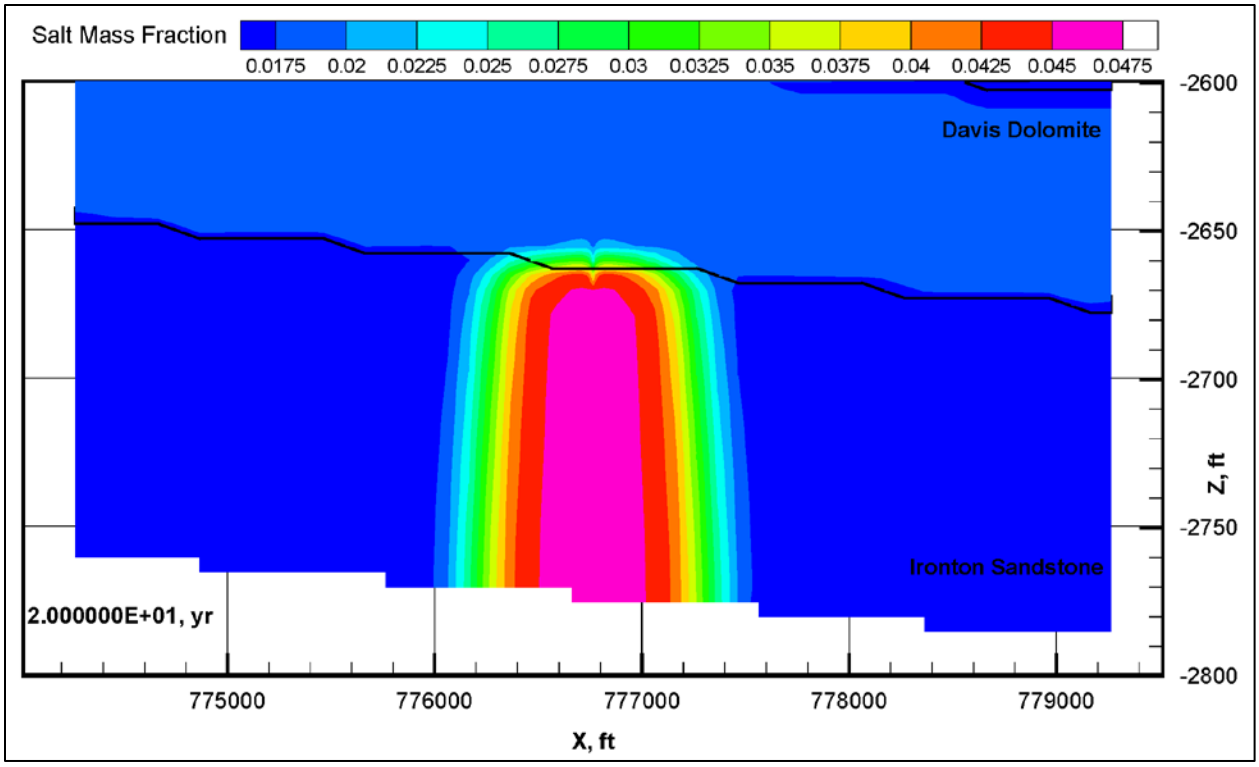

Figure 7.32. Simulated salt mass fraction at 20 years, brine leakage case.

7.3 Summary of Leakage Scenario Results

Appendix B contains summary tables for pressures and concentration arrivals for a range of threshold values, meant to represent a range of instrument detection values, that were calculated from the simulated leak-detection scenarios described in Section 7.2. Graphical representations of threshold arrival times for aqueous pressure are provided in Figure 7.34 and aqueous CO_2/tracers (for the brine leakage case) are provided in Figure 7.35. These multi-category bar charts illustrate the sensitivity of early leak-detection signals (presented as time to first detection) at the multiple lateral distances and depth intervals investigated. The data presented (which include both aqueous pressure and aqueous concentrations) are expected to be the first indicators of any unforeseen loss of CO_2 and/or brine containment.

Based on the results presented in Section 7.2 for several leakage scenarios and different monitoring locations, leak-detection sensitivity can be distinguished between the different leak-detection signals. A joint evaluation of both the $scCO_2$ and brine simulations shows that pressure is likely to be the earliest indicator of leakage, given the rapid pressure responses seen for 20-, 100-, and 500-year scenarios (Figure 7.34). Accounting for the accuracy and resolution of the sensors that will be used to monitor pressure at the FutureGen 2.0 storage site (2 and 0.05 psi, respectively), it is expected that a pressure response would be detected within a week for all of the 20- and 100-year leakage scenarios, at all of the distances from the leak and depths within the permeable unit above the leak (i.e., Ironstone Sandstone) that were evaluated. For the 500-year leakage scenario, higher resolution equipment may be necessary for pressure detection, given that the only pressure value thresholds crossed were 0.2 psi at all selected distances and depths. Pressure responses above the lowest threshold value (0.2 psi) within ~450 ft from the leak location generally respond quickly, from essentially instantaneously to within 24 hours of the start of

leakage. Higher threshold pressures and more distal locations take longer for detection and in some cases may not be detected at all, as shown in Figure 7.34.

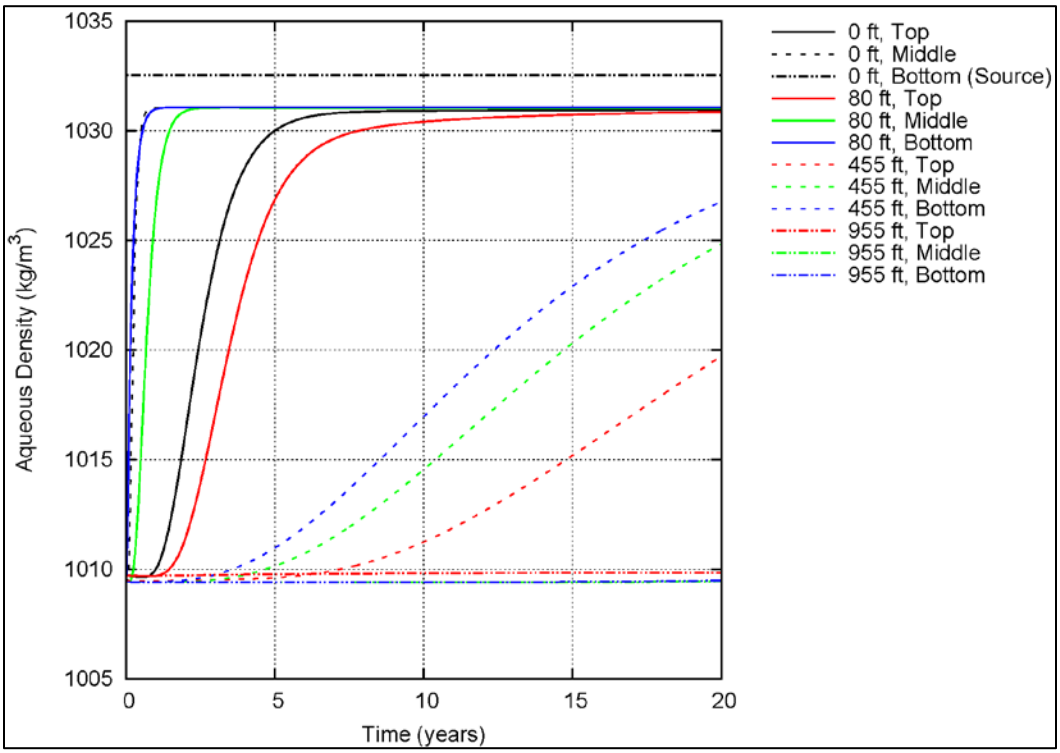

Figure 7.33. Simulated aqueous fluid density at nodes within the Ironton Sandstone for the 20-year brine leakage case. Distances are at nodes west of the leak and at the top, middle, and bottom of the Ironton Sandstone.

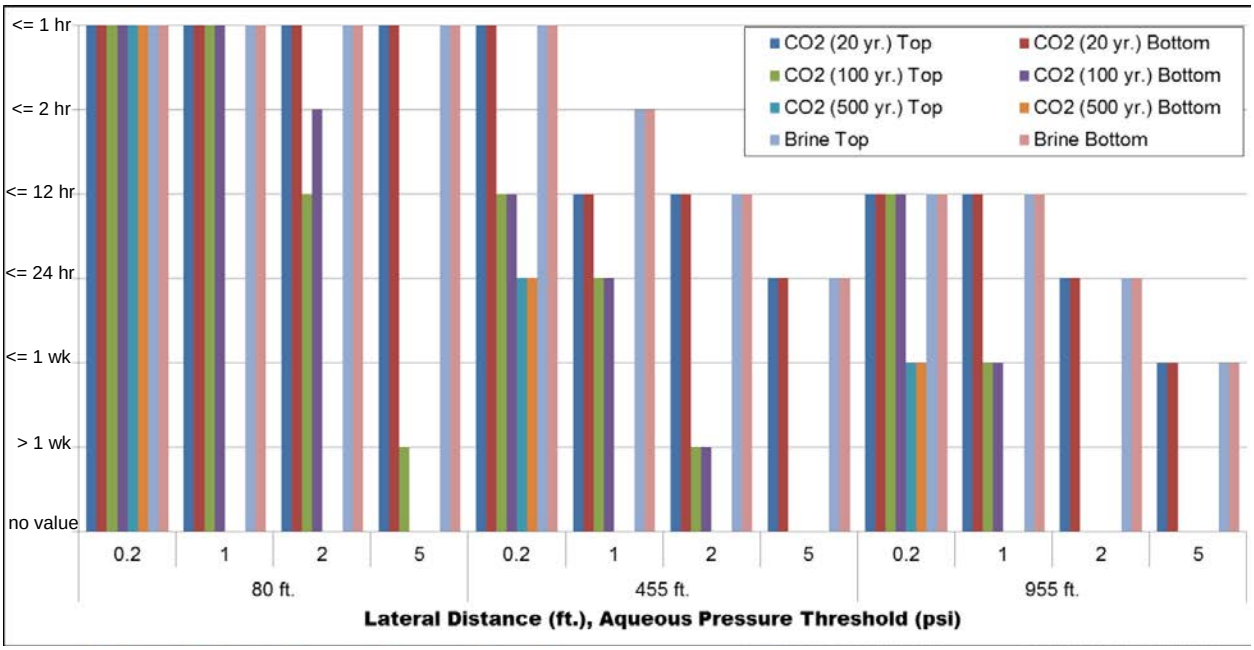

Figure 7.34. Time to first detection of pressure responses exceeding specified threshold values (0.2, 1, 2, and 5 psi) calculated from the simulated leak cases in the top and bottom of the Ironton Sandstone at three distances from the leak.

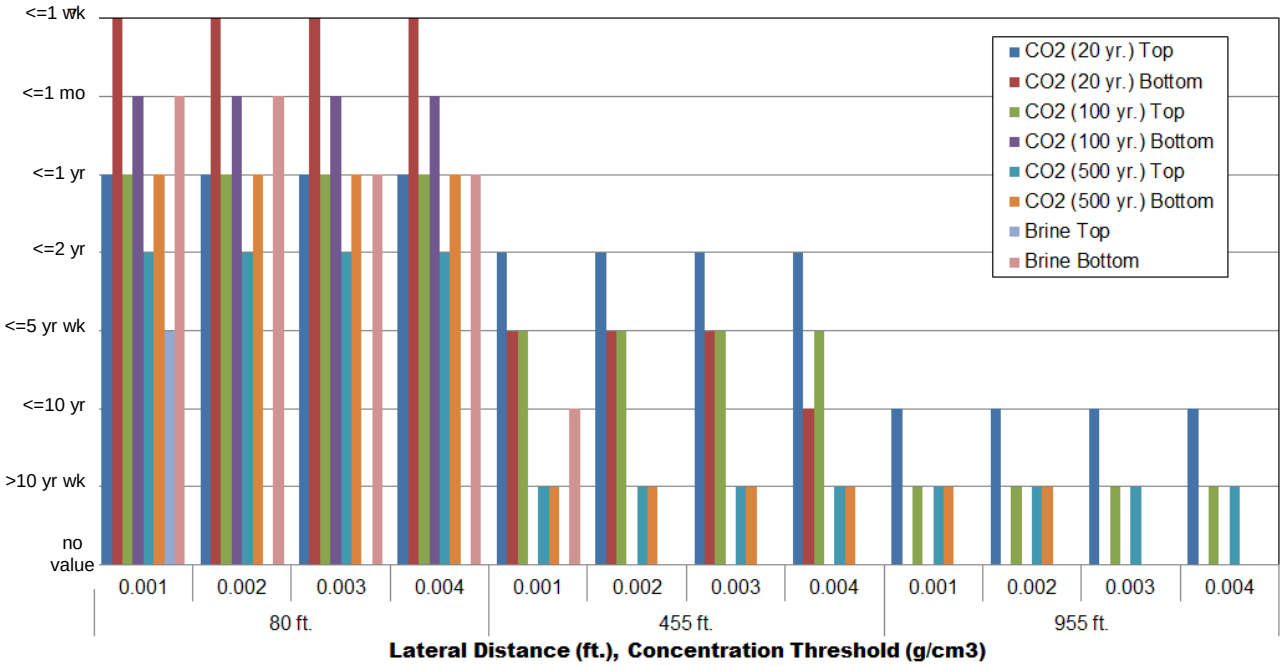

Figure 7.35. Time to first detection of aqueous CO_2 concentrations and tracers (for the brine leakage case) exceeding specified threshold values calculated from the simulated leak cases in the top and bottom of the Ironton Sandstone at three distances from the leak.

Figure 7.35 compares the arrival times of aqueous CO_2 (for $scCO_2$ simulations) and tracer (for brine simulations) above specified concentration thresholds. As expected, these geochemical signals are much more localized and take much longer to develop than the pressure responses. In addition, because of the

buoyancy effect associated with $scCO_2$ injection, early-leak-detection monitoring for these leakage scenarios is best achieved through upper zone monitoring, particularly as monitoring distances from the leakage source increase. It should be noted that the aqueous CO_2 arrival time results assume that no aqueous CO_2 is present prior to the $scCO_2$ leak (i.e., does not account for baseline aqueous CO_2 concentrations). However, these results, along with tracer arrival time results for the brine leakage case, are presented as a proxy for intrinsic $scCO_2$ injection-related and co-injected tracer-related signals that might be present at the leading edge of the $scCO_2$ plume. Future modeling efforts will explicitly evaluate 1) the predicted increase in aqueous CO_2 concentration over background levels and 2) the predicted magnitude of signal provided by both intrinsic and potential co-injected tracers.

No geochemical signals for either the $scCO_2$ or brine simulations occurred in less than a day, and arrivals generally occurred on timescales ranging from months to years. At the closest lateral monitoring location (~80 ft), a geochemical arrival response is predicted to occur within a year or two for all of the $scCO_2$ leakage cases considered. Tracer arrival in the brine leakage case is predicted to occur within a month at the bottom of the Ironton and within 5 years at the top (i.e., the opposite response from that observed for the $scCO_2$ leakage cases, which are affected by $scCO_2$ buoyancy). The geochemical arrival response was less pronounced at more distal locations. For the largest $scCO_2$ leakage rate case (20-year leakage), the aqueous CO_2 arrival in the upper zone is predicted to occur within 2 years at the ~450-ft lateral distance and within 10 years at the ~ 950-ft lateral distance

Results from this preliminary modeling effort are expected to be highly sensitive to layering and heterogeneities within the Ironton Sandstone. Low-permeability layers within the Ironton Sandstone would inhibit the upward buoyant migration of $scCO_2$ and would also influence the aqueous pressure responses. For this study, the Ironton Sandstone formation was assigned uniform properties for the entire unit.

Additional work planned for assessment of leak-detection capabilities includes updating the hydrostratigraphy and material properties of the MVA-ULT model as more site-specific characterization data become available, especially for the layers above the primary confining zone. Lateral boundary conditions will be extended based on observed pressure differences in the extended boundary test for the 20-year leakage cases and the aqueous CO_2 and $scCO_2$ leakage out of the western boundary for the 500-year case. In addition, sensitivity cases will be run on material properties and heterogeneities in Ironton Sandstone. Other uses of the model will include leaky well scenarios and similar focused leakage cases extending into the upper layers, which will be used to assess impacts on the lowermost USDW.

8.0 Conclusion

An evaluation that considered pertinent hydrologic, geochemical, and geophysical processes has been performed as a part of testing and monitoring program development for the FutureGen 2.0 project. This evaluation informed the technology screening process and, in conjunction with project- and regulation-driven monitoring objectives, was the basis for monitoring technology selection. The proceeding sections of this report provide a detailed description of this evaluation. A summary of the overall monitoring approach adopted by the FutureGen 2.0 project, and a detailed description of the testing and monitoring activities that the FutureGen Industrial Alliance, Inc. will undertake at the FutureGen 2.0 storage site near Jacksonville, Illinois, are documented in a project-maintained testing and monitoring plan. All testing and monitoring activities will be performed in accordance with 40 CFR Sections 146.89, 146.90, and 146.91 to verify that the storage site is operating as permitted and is not endangering any USDWs.

9.0 References

40 CFR 146. Code of Federal Regulations, Title 40, *Protection of the Environment*, Part 146 − "Underground Injection Control Program: Criteria and Standards." U.S. Environmental Protection Agency, Washington, D.C.

75 FR 77230. 2010. "Federal Requirements Under the Underground Injection Control (UIC) Program for Carbon Dioxide (CO_2)." *Federal Register*. U.S. Environmental Protection Agency.

Ahmadlouydarab M, Z Liu, and J Feng. 2012. Relative permeability for two-phase flow through corrugated tubes as model porous media. *International Journal of Multiphase Flow* 47:85−93.

Aki K and PG Richards. 2002. *Quantitative Seismology: Theory and Methods*. University Science Books.

Alliance (FutureGen Industrial Alliance, Inc.). 2012. *Borehole Completion and Characterization Summary Report for the Stratigraphic Well, Morgan County, Illinois*. FG-RPT-015 Rev 1, Washington, D.C.

Alliance (FutureGen Industrial Alliance, Inc.). 2013. *Underground Injection Control Permit Applications for FutureGen 2.0 Morgan County Class VI UIC Wells 1, 2, 3, and 4 – SUPPORTING DOCUMENTATION*. FG-RPT-017-Revision 1. Jacksonville, Illinois.

Allis RG and TM Hunt. 1986. Analysis of exploitation-induced gravity changes at Wairakei Geothermal Field. *Geophysics* 51(8):1647−1660.

Amonette JE, JL Barr, LM Dobeck, K Gullickson, and SJ Walsh. 2010. Spatiotemporal changes in CO_2 emissions during the second ZERT injection, August-September 2008. *Environmental Earth Sciences* 60:263−272.

Amonette JE, JL Barr, RL Erikson, LM Dobeck, JL Barr, and JA Shaw. 2013. Measurement of advective soil gas flux: results of field and laboratory experiments with CO_2. *Environmental Earth Sciences* 70:1717−1726.

Archie GE. 1942. The electric resistivity log as an aid in determining some reservoir characteristics. *Transactions of the American Institute of Mineralogy* 146:54–62.

Arts R, A Chadwick, O Eiken, S Thibeau, and S Nooner. 2008. Ten years' experience of monitoring CO_2 injection in the Utsira sand at Sleipner (offshore Norway). *First Break* 26:65−72.

Bachelor PP, JI McIntyre, JE Amonette, JC Hayes, BD Milbrath, and P Saripalli. 2008. Potential method for measurement of CO_2 leakage from underground sequestration fields using radioactive tracers. *Journal of Radioanalytical and Nuclear Chemistry* 277(1):85−89.

Baig A and T Urbancic. 2010. Magnitude Determination, Event Detectability, and Assessing the Effectiveness of Microseismic Monitoring Programs in Petroleum Applications. *CSEG Recorder* 35:22–26.

Baig A, T Urbancic, G Viegas, and S Karimi. 2012. Can small events (M < 0) observed during hydraulic fracture stimulations initiate large events (M > 0)? *The Leading Edge* 31:1470−1474.

Bailey J and DF Ollis. 1986. *Biochemical Engineering Fundamentals*. Second Edition, McGraw Hill Chemical Engineering Series, New York.

Bennion D. 2008. Drainage and imbibition relative permeability relationships for supercritical CO2/brine and H2S/brine systems in intergranular sandstone, carbonate, shale, and anhydrite rocks. SPE Reservoir Evaluation and Engineering 11(3), 487−496.

Berglund M and ME Wieser. 2011. Isotopic compositions of the elements 2009 (IUPAC Technical Report). *Pure and Applied Chemistry* 83:397−410.

Bergmann P, C Schmidt-Hattenberger, D Kiessling, C Rücker, T Labitzke, J Henninges, G Baumann, and H Schütt. 2012. Surface-Downhole electrical resistivity tomography applied to monitoring of the CO_2 storage Ketzin (Germany). *Geophysics* 77(6):B253−B267.

Biegert E, J Ferguson, and X Li. 2008. 4D gravity monitoring – Introduction. *Geophysics* 73(6):WA1−WA2.

Biot MA. 1941. General Theory of Three-Dimensional Consolidation. *Journal of Applied Physics* 12:155−164.

Bonneville A, C Strickland, J Dermond, and M Sweeney. 2012. *Gravity Survey of the FutureGen 2.0 Morgan County Site, 5−22 November 2011*. PNNL internal report, Pacific Northwest National Laboratory, Richland, Washington.

Buschbach TC and DC Bond. 1967. Underground Storage of Natural Gas in Illinois − 1967. Illinois Petroleum 86. Illinois State Geological Survey, Champaign, Illinois.

Buschbach TC and DC Bond. 1974. Underground Storage of Natural Gas in Illinois – 1973 (updated). Illinois Petroleum 101. Illinois State Geological Survey, Champaign, Illinois.

Butsch R, AL Brown, B Bryans, C Kolb, and S Horvorka. 2013. Integration of well-based monitoring technologies: Lessons learned at SECARB study, Cranfield, MS. *International Journal of Greenhouse Gas Control* 18:409−420.

Cameron DA and LJ Durlofsky. 2012. Optimization of well placement, CO_2 injection rates, and brine cycling for geological carbon sequestration. *International Journal of Greenhouse Gas Control* 10:100−112. doi: 10.1016/j.ijggc.2012.06.003.

Carrigan CR, X Yang, DJ LaBrecque, D Larsen, D Freeman, AL Ramirez, W Daily, R Aines, R Newmark, J Friedmann, S Hovorka. 2013. Electrical resistance tomographic monitoring of CO_2 movement in deep geologic reservoirs. *International Journal of Greenhouse Gas Control*18:401.

Chadwick RA, D Noy, R Arts, and O Eiken. 2010. Latest time-lapse seismic data from Sleipner yield new insights into CO_2 plume development. *Energy Procedia* 1(2009):2103−2110

Chandra S and SC Joshi. 2002. Diurnal and seasonal variation in CO_2 levels in the surface air of Garhwal Himalaya. *Indian Journal of Forestry* 25:205−208.

Chapman DS, E Sahm, and P Gettings. 2008. Monitoring aquifer recharge using repeated high-precision gravity measurements: A pilot study in South Weber, Utah. *Geophysics* 73(6):WA83−WA93.

Chopra S and KJ Marfurt. 2005. Seismic attributes − A historical perspective. *Geophysics* 70**:**3SO−28SO.

Clavier C, W Hoyle, and D Meunier. 1971b. Quantitative interpretation of thermal neutron decay time logs. Part II. Interpretation example, interpretation accuracy, and time-lapse technique. *Journal of Petroleum Technology* 23:756–763.

Commer M and GA Newman. 2009. Three-dimensional controlled-source electromagnetic and magnetotelluric joint inversion. *Geophysical Journal International* 178:1305–1316.

Computer Modeling Group. 2009. User's Guide − CMG. Calgary, Alberta.

Core Laboratories. 1966. Borehole Criswell No. 1-6 at the Waverly field: Core Laboratories, Inc. October 31, 1966, memo to Panhandle Eastern Pipeline Company, Liberal, Kansas (Waverly Field, Criswell 1-16), File #: SCAL-65269. Houston, Texas.

Coueslan M. 2012. Monitoring with time-lapse 3D VSP's at the Illinois Basin Decatur Project. Available at: http://sequestration.org/resources/PAGSept2012Presentations/10-Marcia_PAG2012.pdf.

Cowan P and GA Wright. 1999. Investigations into improved methods of saturation determination using pulsed neutron capture tools. 40th Annual Logging Symposium, Society of Petrophysicists and Well Log Analysts.

Crawford H, G Neill, B Bucy, and P Crawford. 1963. Carbon Dioxide: a multipurpose additive for effective well stimulation. *Journal of Petroleum Technology* 237.

Cunningham A and W Characklis. 1991. Influence of biofilm accumulation on porous media hydrodynamics. *Environmental Science and Technology* 24:1305−1311.

Daley TM, EC Sullivan, S Tan, L Huang, and W Harbert. 2013. *An Analysis of Field VSP Data: Cranfield 3D VSP Project, NRAP Milestone Repor*t. PNNL-22386, Pacific Northwest National Laboratory, Richland, Washington.

Daniels DL, RP Kucks, and PL Hill. 2008. Illinois, Indiana, and Ohio Magnetic and Gravity Maps and Data: A Website for Distribution of Data. U.S. Geological Survey Data Series 321. Available at: http://pubs.usgs.gov/ds/321/.

Davis K, Y Li, and M Batzle. 2008. Time-lapse gravity monitoring: A systematic 4D approach with application to aquifer storage and recovery. *Geophysics* 73(6):WA61−WA69.

Dean JA. 1992. Lange's Handbook of Chemistry. McGraw Hill, Inc., New York.

Dietz RN. 1986. *Regional and Long-range Transport of Air Pollution*. BNL-38847, Brookhaven National Laboratory, Upton, New York.

Dutta P and MD Zoback. 2012. CO_2 sequestration into the Wyodak coal seam of Powder River Basin-Preliminary reservoir characterization and simulation. *International Journal of Greenhouse Gas Control* 9:103-116. DOI: 10.1016/j.ijggc.2012.03.004.

Eisner L, A De La Pena, S Wessels, W Barker, and W Heigl. 2011. Why Surface monitoring of Microseismic Events Works. Third Passive Seismic Workshop – Actively Passive! 27-30 March 2011, Athens, Greece. European Association of Geoscientists & Engineers, Houten, The Netherlands.

Eisner L, W Heigl, P Duncan, and W Keller. 2009. Uncertainties in passive seismic monitoring. *The Leading Edge* 28:648– 655.

Ferguson JF, T Chen, J Brady, CLV Aiken, and J Seibert. 2007. The 4D microgravity method for waterflood surveillance II − Gravity measurements for the Prudhoe Bay reservoir, Alaska. *Geophysics* 72(2):I33−I43.

Fischer T, S Hainzl, L Eisner, SA Shapiro, and J Le Calvez. 2008. Microseismic signatures of hydraulic fracture growth in tight sandstone-shale formation: Observation and modeling. *Journal of Geophysical Research* 113, B02307.

Fleury M and H Deschamps. 2008. Electrical Conductivity and Viscosity of Aqueous NaCl Solutions with Dissolved CO_2. *Journal of Chemical and Engineering Data* 53:2505−2509.

Flury M and NN Wai. 2003. Dyes as tracers for vadose zone hydrology. *Reviews of Geophysics* 41:1002.

Forster P, V Ramaswamy, P Artaxo, T Berntsen, R Betts, DW Fahey, J Haywood, J Lean, DC Lowe, G Myhre, J Nganga, R Prinn, G Raga, M Schulz, and R Van Dorland. 2007. "Changes in Atmospheric Constituents and in Radiative Forcing." In: *Climate Change 2007: The Physical Science Basis. Contribution of Working Group I to the Fourth Assessment Report of the Intergovernmental Panel on Climate Chang.* Solomon S, D Qin, M Manning, Z Chen, M Marquis, KB Averyt, MTignor, and HL Miller (eds.), Cambridge University Press, Cambridge, United Kingdom and New York.

Foulger GR, BR Julian, DP Hill, AM Pitt, PE Malin, and E Shalev. 2004. Non-double-couple microearthquakes at Long Valley caldera, California, provide evidence for hydraulic fracturing. *Journal of Volcanology and Geothermal Research* 132:45−71.

Freeze RA and JA Cherry. 1979. *Groundwater*. Prentice-Hall, Inc., Englewood Cliffs, New Jersey.

Galli I, S Bartalini, S Borri, P Cancio, D Mazzotti, P De Natale, and G Giusfredi. 2011. Molecular Gas Sensing Below Parts Per Trillion: Radiocarbon-Dioxide Optical Detection. *Physical Review Letters* 107(270802).

Garrels R and C Christ. 1965. *Solutions, Minerals, and Equilibria*. Freeman, Cooper and Company, San Francisco, California.

Gasperikova E and GM Hoversten. 2006. A feasibility study of non-seismic geophysical methods for monitoring geologic CO_2 sequestration. *The Leading Edge* 25(10)1282−1288

Gaus I, P Audigane, A Laurent, J Lions, N Jacquemet, P Durst, I Czernichowski-Lauriol, and M Azaroual. 2008. Geochemical and solute transport modeling for CO_2 storage, what to expect from it? *International Journal of Greenhouse Gas Control* 2:605−625.

Geller LS, JW Elkins, JM Lobert, AD Clarke, DF Hurst, JH Butler, and RC Myers. 1997. Tropospheric SF6: Observed latitudinal distribution and trends, derived emissions and interhemispheric exchange time. *Geophysical Research Letters* 24(6):675−678.

Gislason SR and EH Oelkers. 2014. Carbon storage in basalt. *Science* 344:373−374.

Green C and K Scow. 1999. Analysis of phospholipid fatty acids (PLFA) to characterize microbial communities in aquifers. *Hydrogeology Journal* 8:126−141.

Guoping L and E Majer. 2002. High resolution crosswell seismic imaging between horizontal wells *Canadian SEG Recorder* November 2002, 18−22.

Gupta N and ES Bair. 1997. Variable-density flow in the midcontinent basins and arches region of the United States. *Water Resources Research* 33(8):1785-1802. doi: 10.1029/97wr01199.

Hardage B. 2014. Seismic detection of sequestered CO_2 at the FutureGen site -A modeling study based on rock physics principles. Unpublished report to Battelle, University of Texas, Austin, Texas.

Holom DI and JSOldow. 2007. Gravity reduction spreadsheet to calculate the Bouguer anomaly using standardized methods and constants. *Geosphere* 3(2) 89−90.

Inagaki F, T Nunoura, S Nakagawa, and A Teske. 2006. Biogeographical distribution and diversity of microbes in methane hydrate-bearing deep marine sediments on the Pacific Ocean Margin. *PNAS* 103(8):2815−2820.

Ingle S. 1975. Solubility of calcite in the ocean. *Marine Chemistry* 3:301−319.

Ivanova A, A Kashubin, N Juhojuntti, J Kummerow, J Henninges, C Juhlin, S Luth, and M Ivandic. 2012. Monitoring and volumetric estimation of injected CO_2 using 4D seismic, petrophysical data, core measurements and well logging: a case study at Ketzin, Germany. *Geophysical Prospecting* 60:957–973.

Jacob CE. 1940. On the Flow of Water in an Elastic Artesian Aquifer. *Transactions*, American Geophysical Union, Part 2:574−586.

Jadhawar PS and HK Sarma. 2012. Effect of well pattern and injection well type on the CO_2-assisted gravity drainage enhanced oil recovery. *Journal of Petroleum Science and Engineering* 98-99:83-94. DOI: 10.1016/j.petrol.2012.09.004.

Jarrell P, C Fox, H Stein, and S Webb. 2002. Practical aspects of CO_2 flooding. *SPE Monograph* 22.

Johnson TC, RJ Versteeg, A Ward, FD Day-Lewis, and A Revil. 2010. Improved hydrogeophysical characterization and monitoring through parallel modeling and inversion of time-domain resistivity and induced polarization data. *Geophysics* 75(4):WA27–WA41.

Johnson JW and BJ Rostron. 2012. "Geochemical Monitoring". In B. Hitchon (editor). *Best Practices for Validating CO_2 Geological Storage: Observations and Guidance from the IEAGHG Weyburn-Midale CO_2 Monitoring Project*, p. 119-154. Geoscience Publishing.

Juanes R, E Spiteri, F Orr Jr, and M Blunt. 2006. Impact of relative permeability hysteresis on geological CO_2 storage. *Water Resources Research* 42:1−13.

Julian BR, AD Miller, and GR Foulger. 1998. Non-double-couple earthquakes. 1. Theory. *Review of Geophysics* 36:525–549.

Kavanaugh MC and RR Trussell. 1980. Design of aeration towers to strip volatile contaminants from drinking water. *Journal of the American Water Works Association* 72:684−692.

Kiessling D, C Schmidt-Hattenberger, H Schütt, F Schilling, K Krüger, B Schöbel, E Danckwardt, and J Kummerow, and the CO2SINK Group. 2010. Geoelectrical methods for monitoring geological CO_2 storage: First results from cross-hole and surface-downhole measurements from the CO2SINK test site at Ketzin (Germany). *International Journal of Greenhouse Gas Control* 4:816–826.

Klusman RW. 2011. Comparison of surface and near-surface geochemical methods for detection of gas microseepage from carbon dioxide sequestration. *International Journal of Greenhouse Gas Control* 5:1369−1392.

Lackner KS and S Brennan. 2009. Envisioning carbon capture and storage: expanded possibilities due to air capture, leakage insurance, and C-14 Monitoring. *Climatic Change* 96:357−378.

Lasa J, P Mochalski, and E Lokas. 2002. Determination of Argon in Air and Water. *Chem. Anal.* (Warsaw) 47:839.

Leirião S, X He, L Christiansen, OB Andersen, and P Bauer-Gottwein. 2009. Calculation of the temporal gravity variation from spatially variable water storage change in soils and aquifers. *Journal of Hydrology* 365(3–4):302−309.

Li G. 2003. 4D seismic monitoring of CO_2 flood in a thin fractured carbonate reservoir. *The Leading Edge* 22:690−695.

Lide DR and HPR Frederikse. 1995. *CRC Handbook of Chemistry and Physics*. 76th edition. CRC Press, Inc., Boca Raton, Florida.

Liu F, K Ellett, Y Xiao, and JA Rupp. 2013. Assessing the feasibility of CO_2 storage in the New Albany Shale (Devonian-Mississippian) with potential enhanced gas recovery using reservoir simulation. *International Journal of Greenhouse Gas Control* 17:111−126. DOI: 10.1016/j.ijggc.2013.04.018.

Lohman SW. 1961. Compression of Elastic Artesian Aquifers. U.S. Geological Survey *Professional Paper* 424-B:47−49.

Loke MH and RD Barker. 1995. Least-squares deconvolution of apparent resistivity pseudosections. *Geophysics* 60:1682−1690.

Lumley DE. 2001. The next wave in reservoir monitoring: The instrumented oil field. *The Leading Edge* 20:640–648.

Mandel RJ and AL Kontis. 1992. Simulation of Regional Ground-water Flow in the Cambrian-Ordovician Aquifer System in the Northern Midwest, United States. U.S. Geological Survey Professional Paper 1405–C.

Marino BDV, M Bright, and G Gronniger. 2011. Design and package of a 14CO2 field analyzer: The Global Monitor Platform. *SPIE* 8156:81560E-1−81560E-15.

Massen F, A Kies, and N Harpes. 2007. Seasonal and diurnal CO_2 patterns at Diekirch LU, 2003-2005. http://meteo.lcd.lu/papers/co2_patterns/co2_patterns.html, accessed 25 July 2014.

Matter JM, WS Broecker, SR Gislason, E Gunnlaugsson, EH Oelkers, M Stute, H Sigurdardottir, A Stefansson, HA Alfredsson, ES Aradottir, G Axelsson, B Sigfusson, and D Wolff-Boenisch. 2011. The CarbFix pilot project—storing carbon dioxide in basalt. *Energy Procedia* 4:5579−5585.

Maxfield BT, DM Ginosar, RD McMurtrey, HW Rollins, and GM Shook. 2005. The effect of moisture content on retention of fluorocarbon tracers on sand. *Geothermics* 34:47–60.

McAlexander I, GH Rau, J Liem, T Owano, R Fellers, D Baer, and M Gupta. 2011. Deployment of a carbon isotope ratiometer for the monitoring of CO_2 sequestration leakage. *Analytical Chemistry* 83:6223−6229.

Meij R and H Winkel. 2004. The emissions and environmental impact of PM_{10} and trace elements from a modern coal-fired power plant equipped with ESP and wet FGD. *Fuel Processing Technology* 85:641−656.

Miller AD, GR Foulger, and BR Julian. 1998. Non-double-couple earthquakes. 2. Observations. *Review of Geophysics* 36:551–568.

Mitiku AB and S Bauer. 2013. Optimal use of a dome-shaped anticline structure for CO_2 storage: a case study in the North German sedimentary basin. *Environmental Earth Sciences* 70(8):3661−3673. DOI: 10.1007/s12665-013-2580-z.

Monson PR Jr. 1982. *Krypton Retention on Solid Adsorbents*. DP-1615, Savannah River Laboratory, Aiken, South Carolina.

Morris JP, Y Hao, W Foxall, W McNab. 2011. A study of injection-induced mechanical deformation at the In Salah CO_2 storage project. *International Journal of Greenhouse Gas Control* 5(2):270–280.

Morrison TJ and NB Johnstone. 1954. Solubilities of the inert gases in water. *Journal of the Chemical Society* 1954:3441−3446.

Mortazavi, B, BJ Wilson, F Dong, M Gupta, and D Baer. 2013. Validation and application of cavity-enhanced, near-infrared tunable diode laser absorption spectrometry for measurements of methane carbon isotopes at ambient concentrations. *Environmental Science and Technology* 47:11676−11684.

Müller K, M Al-Baloushi, O Al-Jeelani, W Soroka, S Marmash, B Paulsson, D Dushman, and M Karrenbach. 2008. 3-DVSPs Provide High-Resolution Seismic Images for Improved Reservoir Monitoring and Characterization. GEO2008, Middle East Conference and Exhibition.

Manama B, DE Murnick, O Dogru, and E Ilkmen. 2008. Intracavity Optogalvanic Spectroscopy: An Analytical Technique for 14C Analysis with Subattomole Sensitivity. *Analytical Chemistry* 80:4820−4824.

Murnick Dl, O Dogru, and E Ilkmen. 2010. 14C analysis via intracavity optogalvanic spectroscopy. *Nuclear Instruments and Methods in Physics Research* 268(B):708−711.

Murray CJ, BN Nguyen, Z Hou, ZF Zhang, and SK White. 2014. *Mechanical Evaluation of the Thermal Impact of CO_2 Injection for a Range of Potential Injection Temperatures*. FG-02-RPT-0008, prepared for the FutureGen 2.0 Project, by Battelle−Pacific Northwest Division, Richland, Washington.

Myers M, L Stalker, B Pejcic, and A Ross. 2013. Tracers − Past, present, and future applications in CO_2 geosequestration. *Applied Geochemistry* 30:125−135.

National Research Council. 2012. *Induced Seismicity Potential in Energy Technologies*. National Academy of Sciences, Washington, D.C.

Nazzari M, A Sciarra, and F Quattrocchi. 2013. A simple and sensitive gas chromatography-electron capture detection method for analyzing perfluorocarbon tracers in soil gas samples for storage of carbon dioxide. *International Journal of Greenhouse Gas Control* 14:60−64.

Newman GH. 1973. Pore-Volume Compressibility of Consolidated, Friable, and Unconsolidated Reservoir Rocks Under Hydrostatic Loading. *Journal of Petroleum Technology* 25(2):129−134.

Newmark RL, AL Ramirez, and WD Daily. 2001. Monitoring carbon dioxide sequestration using electrical resistance tomography (ERT): Sensitivity studies. UCRL-JC-140527, Lawrence Livermore National Laboratory, Berkeley, California.

Nolen-Hoeksema RC and LJ Ruff. 2001. Moment tensor inversion of microseisms from the B-sand propped hydrofracture, M-site, Colorado. *Tectonophysics* 336:163−181.

O'Connor WK and GE Rush. 2005. CO_2 flood tests on whole core samples of the Mt. Simon Sandstone, Illinois Basin. Report DOE/ARC-2005-013, Albany Research Center, U.S Department of Energy, Albany, Oregon.

Ogram A, W Sun, F Brockman, and J Fredrickson. 1995. Isolation and characterization of RNA from low-biomass deep-subsurface sediments. *Applied and Environmental Microbiology* 61(2):763−768.

Okwen R, M Stewart, and J Cunningham. 2011. Effect of Well Orientation (Vertical vs. Horizontal) and Well Length on the Injection of CO_2 in Deep Saline Aquifers. *Transport in Porous Media* 90(1):219−232. DOI: 10.1007/s11242-010-9686-5.

Oldenborger GA, PS Routh, and MD Knoll. 2005. Sensitivity of electrical resistivity tomography data to electrode position errors. *Geophysical Journal International* 163:1−9.

Paulsson B, M Karrenbach, P Milligan, A Goertz, A Hardin, J O'Brien, D McGuire. 2004. High resolution 3D seismic imaging using 3C data from large downhole seismic arrays. *First Break* 23:73−85.

Paulsson BNP, JL Toko, JA Thornburg, F Slopko, R He, and C-H Zhang. 2013. A High Performance Fiber Optic Seismic Sensor System. *Proceedings of the Thirty-Eighth Workshop on Geothermal Reservoir Engineering*, Stanford University, Stanford, California, February 11-13, 2013, SGP-TR-198.

Perrin J, M Krause, C Kuo, L Miljkovic, and S Benson. 2008. Relative permeability properties of CO_2 and brine in reservoir rocks. American Geophysical Union, Annual Fall Meeting 2008, abstract H12C-05.

Persson A, G Eilers, L Ryderfors, E Mukhtar, G Possnert, and M Salehpour. 2013. Evaluation of Intracavity Optogalvanic Spectroscopy for Radiocarbon Measurements. *Analytical Chemistry* 85:6790−6798.

Pham VTH, F Riis, IT Gjeldvik, EK Halland, IM Tappel, and P Aagaard. 2013. Assessment of CO_2 injection into the south Utsira-Skade aquifer, the North Sea, Norway. *Energy* 55:529−540. doi: 10.1016/j.energy.2013.03.026.

Pruess K. 2005. ECO2N: A TOUGH2 Fluid Property Module for Mixtures of Water, NaCl, and CO_2. LBNL-57952, Lawrence Berkeley National Laboratory, Berkeley, California.

Pruess K, C Oldenburg, and G Moridis. 1999. TOUGH2 user's guide. Version 2.0. LBL-43134, Lawrence Berkeley Laboratory, Berkeley, California

Preuss K and J Garcia. 2002. Multiphase flow dynamics during CO_2 disposal into saline aquifers. *Environmental Geology* 42:282−295.

Pruess K, T Xu, J Apps, and J Garcia. 2003. Numerical modeling of aquifer disposal of CO_2. *Society of Petroleum Engineers Journal* 8(1):49−60.

Pujol J. 2003. Elastic wave propagation and generation in seismology. Cambridge University Press, Cambridge, Massachusetts.

Ramirez A, W Daily, D LaBrecque, E Owen, and D Chesnut. 1993. Monitoring an underground steam injection process using electrical-resistance tomography. *Water Resources Research* 29:73–87.

Ramirez A and W Daily. 1996. *Detection of Leaks in Underground Storage Tanks Using Electrical Resistance Methods: 1996 Results*. UCRL-ID-125918, Lawrence Livermore National Laboratory, Livermore, California

Ramirez AL, RL Newmark, and WD Daily. 2003. Monitoring carbon dioxide floods using electrical resistance tomography (ERT): Sensitivity studies. *Journal of Environmental and Engineering Geophysics* 8(3):187–208.

Ringelberg D, S Sutton, and D White. 1997. Biomass, bioactivity and biodiversity: microbial ecology of the deep subsurface: analysis of ester-linked phospholipid fatty acids. *FEMS Microbiology Review* 20:371−377.

Rizeq R, D Hansell, and W Seeker. 1994. Predictions of metals emissions and partitioning on coal-fired combustion systems. *Fuel Processing Technology* 39:219−236.

Rockhold ML, ZF Zhang, SK White, A Bonneville, and TJ Gilmore. 2014. Estimation of Rock Mechanical, Hydraulic, and Thermal Properties using Wire-line Log and Core Data from the FutureGen 2.0 Site, Well No. 1, Morgan County, Illinois. PNWD-SA-10424, presented by Mark Rockhold (Invited Speaker) at Society of Exploration Geophysicists (SEG), Denver, Colorado, on October 27, 2014.

Romanak KD, PC Bennett, C-B Yang, and SD Hovorka. 2012. Process-based approach to CO_2 leakage detection by vadose zone gas monitoring at geologic CO_2 storage sites. *Geophysical Research Letters* 39:L15405. DOI: 10.1029/2012GL052426.

Rose PE, WR Benoit, PM Kilbourn. 2001. The application of the polyaromatic sulfonates as tracers in geothermal reservoirs. *Geothermics* 30:617−640.

Rutqvist J and C-F Tsang. 2003. TOUGH-FLAC: A Numerical Simulator for Analysis of Coupled Thermal-Hydrologic-Mechanical Processes in Fractured and Porous Geological Media Under Multi-Phase Flow Conditions. TOUGH Symposium, Berkeley, California, May 12−14.

Rutqvist J, DW Vasco, and L Myer. 2010. Coupled reservoir-geomechanical analysis of CO_2 injection and ground deformations at In Salah, Algeria. *International Journal of Greenhouse Gas Control* 4(2):225−230. DOI: 10.1016/j.ijggc.2009.10.017.

Sadiku MNO. 2006. *Elements of Electromagnetics*. 4th edition, Oxford University Press, New York.

Sakurai S, TS Ramakrishnan, A Boyd, N Mueller, and S Hovorka. 2005. Monitoring saturation changes for CO_2 sequestration: petrophysical support of the Frio brine pilot experiment. 46th Annual Logging Symposium Transactions, Society of Petrophysicists and Well Log Analysts, New Orleans, Louisiana.

Sander R. 1999. Compilation of Henry's Law Constants for Inorganic and Organic Species of Potential Importance in Environmental Chemistry (Version 3). Available at: http://www.henrys-law.org; accessed 29 July 2014.

Scheele RD, CF Wend, WC Buchmiller, AE Kozelisky, and RL Sell. 2002. *Preliminary Evaluation of Spent Silver Mordenite Disposal Forms Resulting from Gaseous Radioiodine Control at Hanford's Waste Treatment Plant*. PNWD-3225, Battelle−Pacific Northwest Division, Richland, Washington.

Schlumberger. 2010. *ECLIPSE User Manual*. In "Technical Description." Sugar Land, Texas.

Senum GI, TW D'Ottavio, WM Loss, RW Goodrich, DJ Spandau, and RN Dietz. 1997. *HPFF Cable Leak Location Using Perfluorocarbon Tracers*. TR-109086, 7905-01, Electric Power Research Institute, Palo Alto, California.

Šílený J. 2009. Resolution of non-double-couple-mechanisms: simulation of hypocenter mislocation and velocity structure mismodeling. *Bulletin of the Seismological Society of America* 99.

Slater L, AM Binley, W Daily, and R Johnson. 2000. Crosshole electrical imaging of a controlled saline tracer injection. *Journal of Applied Geophysics* 44(2–3):85–102.

Sobers LE, MJ Blunt, and TC LaForce. 2013. Design of Simultaneous Enhanced Oil Recovery and Carbon Dioxide Storage With Potential Application to Offshore Trinidad. *SPE Journal* 18(2):345−354.

Song F and MN Toksoz. 2011. Full-waveform based complete moment tensor inversion and source parameter estimation from downhole microseismic data for hydrofracture monitoring. *Geophysics* 76, 6 WC103.

Stewart RR. 2001. SP: An in-depth seismic understanding. *SEG Recorder* 79−83.

Stetzenbach KJ, SL Jensen, and GM Thompson. 1982. Trace enrichment of fluorinated organic acids used as groundwater tracers by liquid chromatography. *Environmental Science and Technology* 16:250−254.

Suekane T, S Soukawa, S Iwatani, S Tsushima, and S Hirai. 2005. Behavior of supercritical CO_2 injected into porous media containing water. *Energy* 30:2370−2382.

Szecsody J, M Rockhold, M Oostrom, R Moore, C Burns, M Williams, L Zhong, J Fruchter, J McKinley, V Vermeul, M Covert, T Wietsma, A Breshears, and B Garcia. 2009. *Sequestration of Sr-90 Subsurface Contamination in the Hanford 100-N Area by Surface Infiltration of a Ca-Citrate-Phosphate Solution.* PNNL-18303, Pacific Northwest National Laboratory, Richland, Washington.

Taylor SW and PR Jaffe. 1990. Biofilm growth and the related changes in the physical properties of a porous medium. *Water Resources Research* 26:2153−2159.

Truex MJ, TC Johnson, CE Strickland, JE Peterson, and SS Hubbard. 2013. Monitoring vadose zone desiccation with geophysical methods. *Vadose Zone Journal* 12(2).

Turnbull JC, SJ Lehman, S Morgan, and C Wolak. 2010. A new automated extraction system for 14C measurement for atmospheric CO_2. *Radiocarbon* 52:1261−1269.

Uhl R, J Franzke, and U Haas. 2001. Detection of argon and krypton traces in noble gases by diode laser adsorption spectrometry. *Applied Physics* B 73:71−74.

Vasco DW, A Rucci, A Ferretti, F Novali, RC Bissell, PS Ringrose, AS Mathieson, and IW Wright. 2010. Satellite-based measurements of surface deformation reveal fluid flow associated with the geological storage of carbon dioxide. *Geophysical Research Letters* 37:L03303. DOI: 10.1029/2009GL041544, 2010.

Vavrycuk V. 2007. On the retrieval of moment tensors from borehole data. *Geophysical Prospecting* 55:381−391.

Verdon JP, J-M Kendall, AL Stork, RA Chadwick, DJ White, and RC Bissell. 2013. Comparison of geomechanical deformation induced by meagatonne-scale CO_2 storage at Sleipner, Weyburn and In Salah. In *Proceedings of the National Academy of Sciences of the United States of America* 110(30):E2762-E2771.

Vermeul VR, ME Kelley, RD Mackley, CE Strickland, JE Szecsody, PD Thorne, and MD Williams. 2014. *FutureGen 2.0 – CO_2 Pipeline and Storage Project Testing and Monitoring Plan*. FG-02-PLN-TAMP, PNWD-4428, prepared for the FutureGen Industrial Alliance, Inc., Washington, D.C., by Battelle−Pacific Northwest Division, Richland, Washington.

Vilarrasa V, D Bolster, M Dentz, S Olivella, and J Carrera. 2010. Effects of CO_2 Compressibility on CO_2 Storage in Deep Saline Aquifers. *Transport in Porous Media* 85 (2):619−639. DOI: 10.1007/s11242-010-9582-z.

Vilarrasa V, D Bolster, S Olivella, and J Carrera. 2010. Coupled hydromechanical modeling of CO_2 sequestration in deep saline aquifers. *International Journal of Greenhouse Gas Control* 4 (6):910−919. DOI: 10.1016/j.ijggc.2010.06.006.

Vilarrasa V, S Olivella, J Carrera, and J Rutqvist. 2014. Long-term impacts of cold CO_2 injection on the caprock integrity. *International Journal of Greenhouse Gas Control* 24:1−13. DOI: 10.1016/j.ijggc.2014.02.016.

Wallin E. 2012. MT and CESM Monitoring of CO_2 Sequestration. Pacific Northwest National Laboratory, Richland, Washington. (Unpublished presentation)

Warpinski NR. 2009. Microseismic monitoring: inside and out. *Journal of Petroleum Technology* 61:80−85.

Watson TB, and T Sullivan. 2012. Feasibility of a Perfluorocarbon tracer based network to support Monitoring, Verification, and Accounting of Sequestered CO_2. *Environmental Science and Technology* 46:1692−1699.

Watson TB, R Wilke, RN Dietz, J Heiser, and P Kalb. 2007. The Atmospheric Background of Perfluorocarbon Compounds Used as Tracers. *Environmental Science and Technology* 41(20):6909−6913.

Weast RC, MJ Astle, and WH Beyer (eds). 1983. *CRC Handbook of Chemistry and Physics*, CRC Press, Boca Raton, Florida.

Wells AW, JR Diehl, G Bromhal, BR Strazisar, TH Wilson, and CM White. 2007. The use of tracers to assess leakage from the sequestration of CO_2 in a depleted oil reservoir, New Mexico, USA. *Applied Geochemistry* 22:996−1016.

Wells AW, JR Diehl, BR Strazisar, TH Wilson, and DC Stanko. 2013. Atmospheric and soil-gas monitoring for surface leakage at the San Juan Basin CO_2 pilot test site at Pump Canyon New Mexico,

using perfluorocarbon tracers, CO_2 soil-gas flux and soil-gas hydrocarbons. *International Journal of Greenhouse Gas Control* 14:227−238.

Wells A, B Strazisar, JR Diehl, and G Veloski. 2010. Atmospheric tracer monitoring and surface plume development at the ZERT pilot test in Bozeman, Montana, USA. *Environmental Earth Sciences* 60:299−305.

White SP. 1995. Multiphase non-isothermal transport of systems of reacting chemicals. *Water Resource Research* 31(7).

White S, R Allis, J Moore, T Chidsey, C Morgan, W Gwynn, and M Adams. 2005. Simulation of reactive transport of injected CO_2 on the Colorado Plateau, Utah, USA. *Chemical Geology* 217:387−405.

White MD, DH Bacon, BP McGrail, DJ Watson, SK White, and ZF Zhang. 2012. *STOMP Subsurface Transport Over Multiple Phases: STOMP-CO2 and STOMP-CO2e Guide, Version 1.0*. PNNL-21268, Pacific Northwest National Laboratory, Richland, Washington.

Whiticar MJ. 1996. Stable Isotope geochemistry of coals, humic kerogens, and related natural gases. *International Journal of Coal Geology* 32:191−215.

Wilhelm E, R Battino, and RJ Wilcock. 1977. Low-pressure solubility of gases in liquid water. *Chemical Reviews* 77:219−262.

Wilkinson PB, JE Chambers, M Lelliot, CP Wealthall, and RD Ogilvy. 2008. Extreme sensitivity of crosshole electrical resistivity tomography measurements to geometric errors. *Geophysics Journal International* 173:49–62.

Will B. 2012. *Micoseismic Monitoring at IBDP: Systems Review and Current Status*. Midwest Geological Sequestration Consortium, Champaign, Illinois.

Xu T, E Sonnenthal, N Spycher, and L. Zheng. 2014. *TOUGHREACT V3.0-OMP Reference Manual: A Parallel Simulation Program for Non-Isothermal Multiphase Geochemical Reactive Transport*. Lawrence Berkeley National Laboratory, Berkeley, California.

Xue Z, J Kim, S Mito, K Kitamura, and T Matsuoka. 2009. Detecting and monitoring CO_2 with P-wave velocity and resistivity from both laboratory and field scales. SPE 126885, Society of Petroleum Engineers International Conference on CO_2 Capture, Storage and Utilization.

Yaws CI and HC Yang. 1992. Henry's law constant for compound in water. Pp. 181−206 in CI Yaws (ed.), *Thermodynamic and Physical Property Data*, Gulf Publishing Company, Houston, Texas.

Yilmaz O. 2001. *Seismic Data Analysis: Processing, inversion and interpretation of seismic data, Volumes 1 and 2*. Society of Exploration Geophysicists, Tulsa, Oklahoma.

Young HL. 1992. Hydrogeology of the Cambrian-Ordovician Aquifer System in the Northern Midwest, United States. U.S. Geological Survey Professional Paper 1405–B.

Youmans AH, EC Hopkinson, RA Bergan, and HF Oshry. 1964. Neutron Lifetime, new nuclear log. *Journal of Petroleum Technology* 16:319−328.

Zhang G, C Taberner, L Cartwright, and T Xu. 2011. Injection of Supercritical CO_2 Into Deep Saline Carbonate Formations: Predictions from Geochemical Modeling. *SPE Journal* 16 (4):959−967.

Zhdanov MS, M Endo, N Black, L Spangler, S Fairweather, A Hibbs, GA Eiskamp, and R Will. 2013. Electromagnetic monitoring of CO_2 sequestration in deep reservoirs. *First Break* 31:71−78.

Zhou B and T Dahlin. 2003. Properties and effects of measurement errors on 2D resistivity imaging surveying. *Near Surface Geophysics* 1, 105–117.

Zhong L, JE Amonette, AV Mitroshkov, and KB Olsen. 2014. Transport of perfluorocarbon tracers and carbon dioxide in sediment columns – Evaluating the application of PFC tracers for CO_2 leakage detection. *Applied Geochemistry* 45:25−32.

Zink K, K Mangelsdorf, L Granina, and B Horsfield. 2008. Estimation of bacterial biomass in subsurface sediments by quantifying intact membrane phospholipids. *Analytical and Bioanalytical Chemistry* 390:885−896.

Zoback MD. 2012. Managing the seismic risk posed by waste water disposal. *Earth Magazine* 57:38−43.

Appendix A

Grid Spacing Tests for Ironton Leakage Simulations

Appendix A

Grid Spacing Tests for Ironton Leakage Simulations

This Appendix describes the grid spacing and domain size simulations that were run for developing the preliminary model used in the Assessment of ACZ Early-Leak-Detection Capabilities (Section 7).

A.1 Refined Grid Spacing Case

The first comparison case used a refined domain with 1/4 symmetry (Figure A.1), with a grid domain size of 2,510 ft in the X direction, 2,000 ft in the Y direction, and 1,820 ft in the Z direction. The grid has 45 X-direction nodes, 45 Y-direction nodes, and 120 Z-direction nodes, yielding 202,500 nodes overall. The domain features higher X-Y grid resolutions of (50-ft instead of the 100-ft spacing used in the base case), but Z grid resolutions identical to the base case (5-ft spacing at the base of the model within the Ironton Sandstone and the Davis Dolomite and increasing stepwise to 30-ft spacing for the upper part of the domain).

Supercritical CO_2 saturations at the end of the 20-year simulation period, as well as changes in saturation over time, are shown in Figures A.1 and A.2, respectively. The $scCO_2$ saturations of the grid refinement scenario and the base case were similar (Figure 7.3); slight decreases occurred in the maximum $scCO_2$ saturation in the Ironton at 80 ft from the leakage source, as well as delays in breakthrough of $scCO_2$ at the top of the Ironton at 455 and 955 ft away from the leakage source. For aqueous pressure, slight attenuations for all lateral and vertical measurement locations were observed for the refined 1/4 symmetry grid when compared to the base case (Figures A.3 and 7.7). Based on a comparison of aqueous CO_2 concentrations for the refined and base case simulations (Figures A.4 and 7.10), delays in breakthrough time were observed at the top of the Ironton at 455 and 955 ft for the refined grid case. In addition, drops in maximum CO_2 aqueous concentrations were observed at 455 ft from the leakage source in the middle and bottom of the Ironton Formation, with decreases from 0.052 to 0.028 and from 0.0091 to 0.00073, respectively.

Some of the slight differences between the higher resolution case and the base case can be attributed to the different overall hydrostratigraphic structure from the 1/4 symmetry assumption (i.e., no down-dip section on the east side). These small differences, along with the faster run times, make the base case adequate for this preliminary analyses.

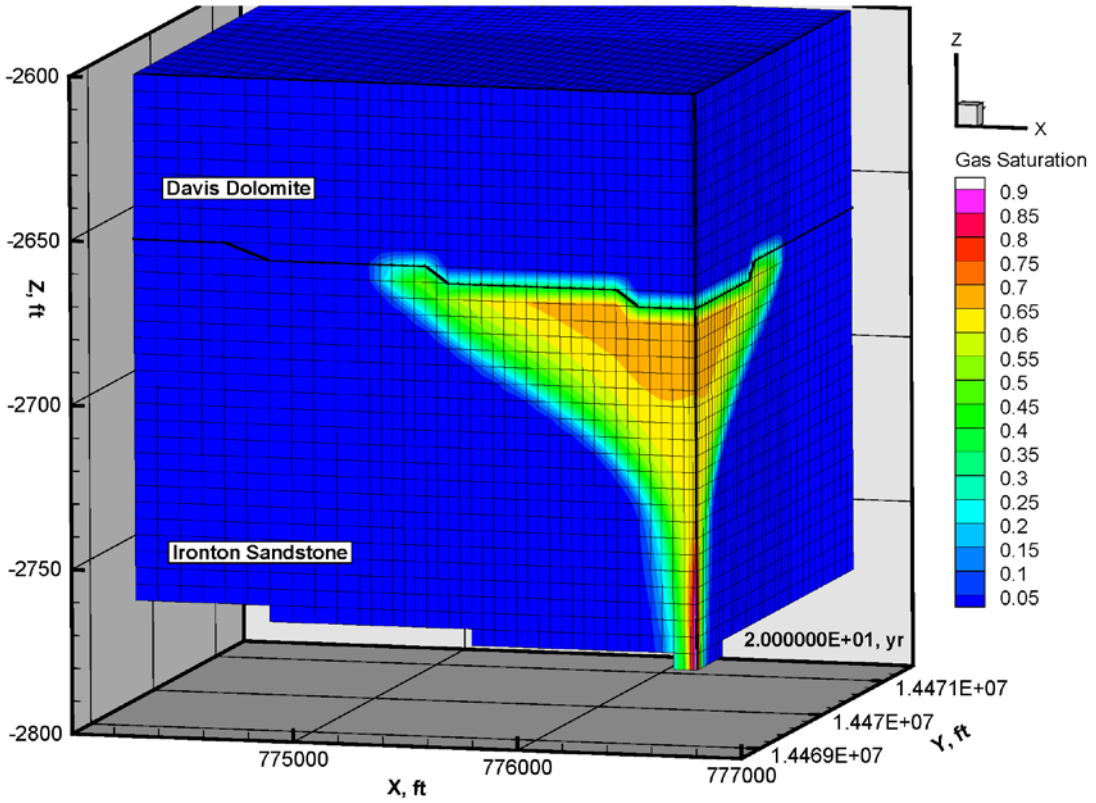

Figure A.1. Refined grid and 1/4 symmetry showing $scCO_2$ saturations at 20 years for the 20-year $scCO_2$ leakage case.

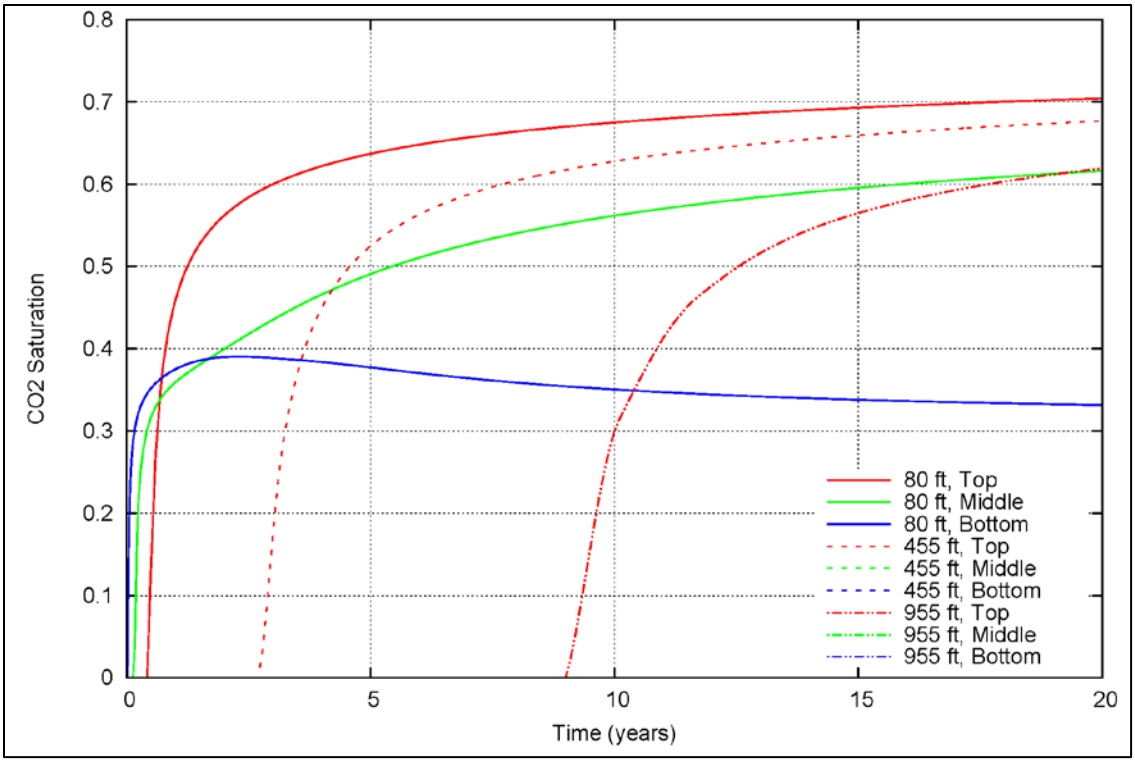

Figure A.2. $scCO_2$ breakthrough curves (compare to Figure 7.3)

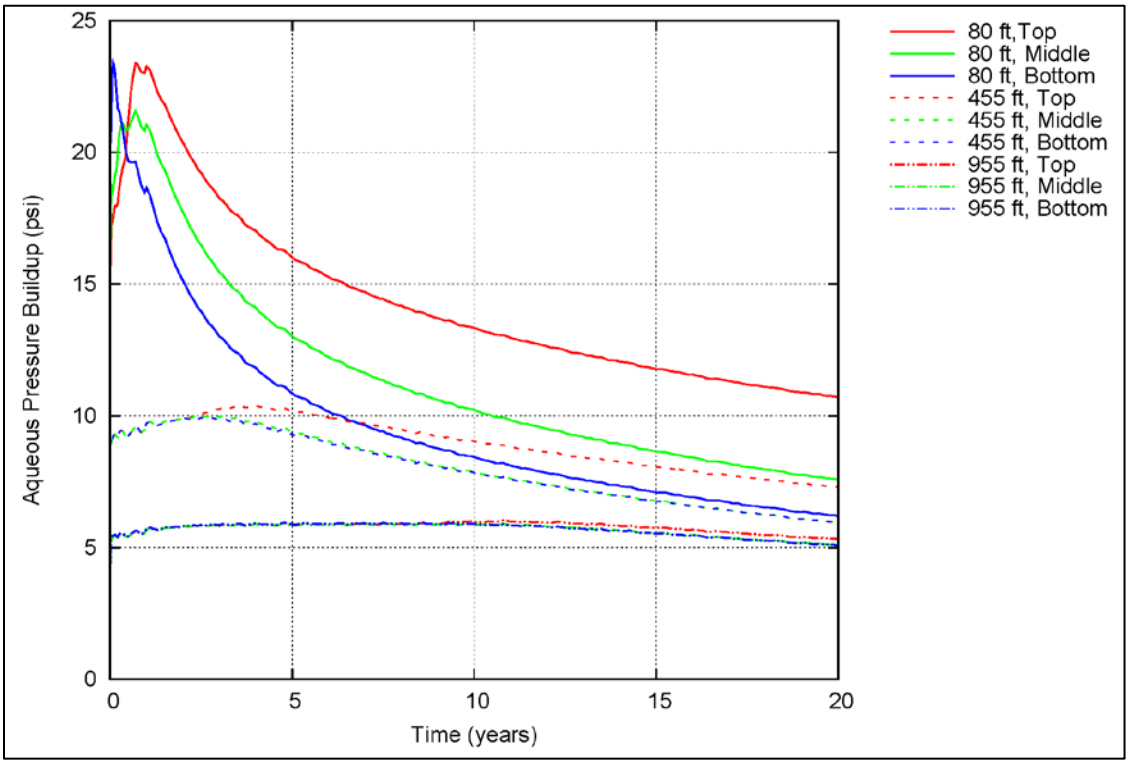

Figure A.3. Aqueous Pressures (compare to Figure 7.7)

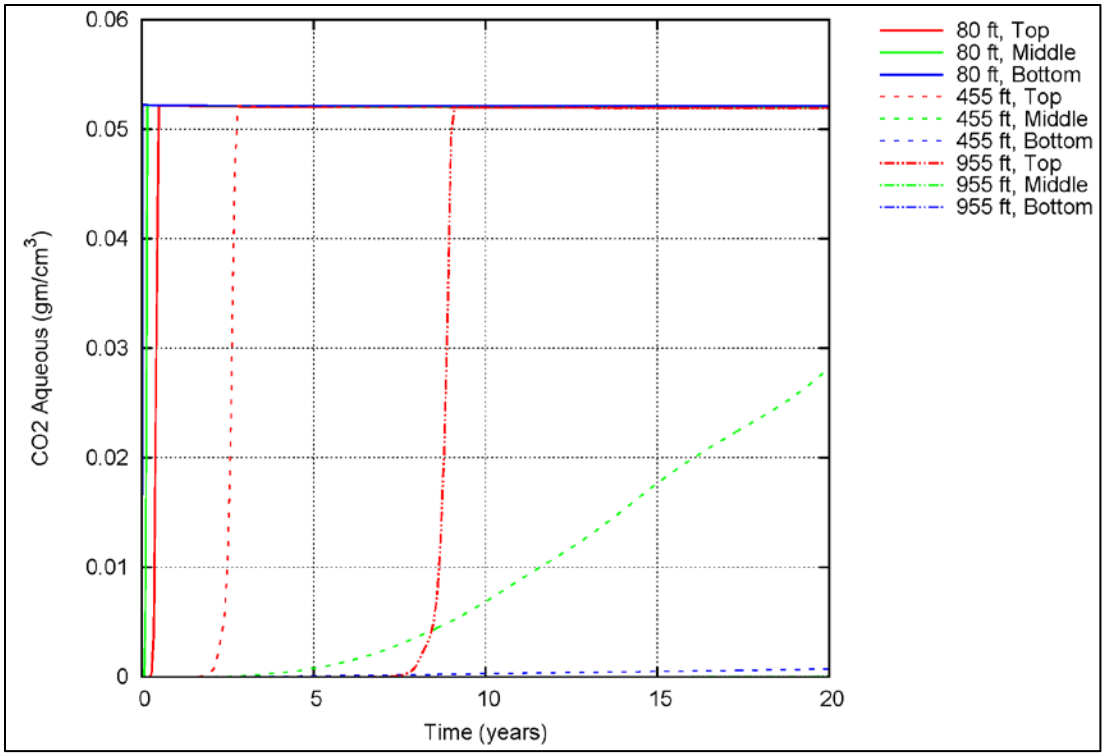

Figure A.4. Aqueous CO_2 breakthrough curves (compare to Figure 7.10)

A.2 Extended Boundary – 20-Year $scCO_2$ Leakage Case

The geometry of the second comparison case adds 2,000 ft in the X direction and 1,000 ft in the Y direction, resulting in a total domain length of 5,800 ft for the X direction, 2,000 ft for the Y direction, and 1,820 ft for the Z direction (i.e., vertical resolution was not changed). The grid has 62 X-direction nodes, 31 Y-direction nodes, and 120 Z-direction nodes, yielding 230,640 nodes overall.

Comparing $scCO_2$ saturations between the base case and extended boundaries case, $scCO_2$ saturation values are almost identical for all lateral distances and vertical depths (Figures A.5 and 7.3). For aqueous pressure, the extended boundary simulation showed slight increases in the maximum aqueous pressure buildup when compared to the base case for all distances and depth profiles (Figures A.6 and 7.7). Simulated aqueous CO_2 concentrations for the extended case were nearly identical to the base case (Figures A.7 and 7.10). Based on this comparison, the grid used for the Section 7 simulations was determined to be sufficient for this preliminary modeling effort and development of a leakage-detection modeling framework. However, future simulations that incorporate updated site characterization data will have an extended domain to account for the observed pressure differences and the leakage of aqueous CO_2 at the model boundaries during longer duration simulations, as discussed in Section A.3.

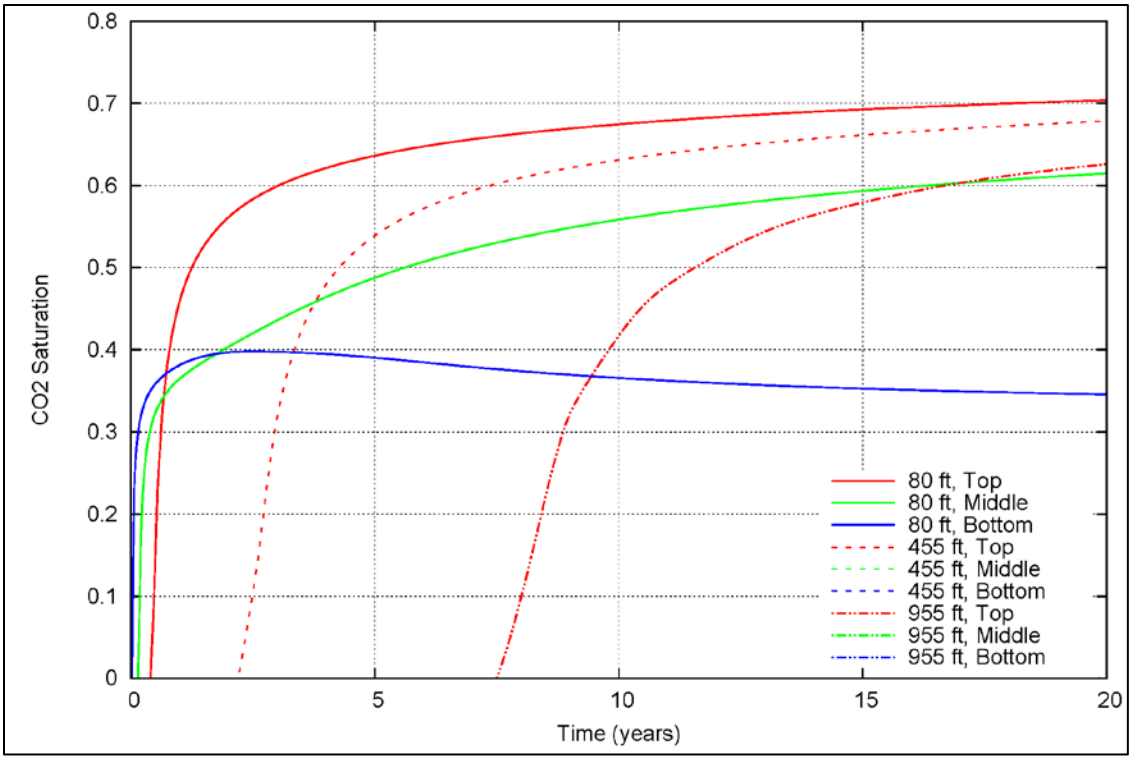

Figure A.5. $scCO_2$ breakthrough curves (compare to Figure 7.3)

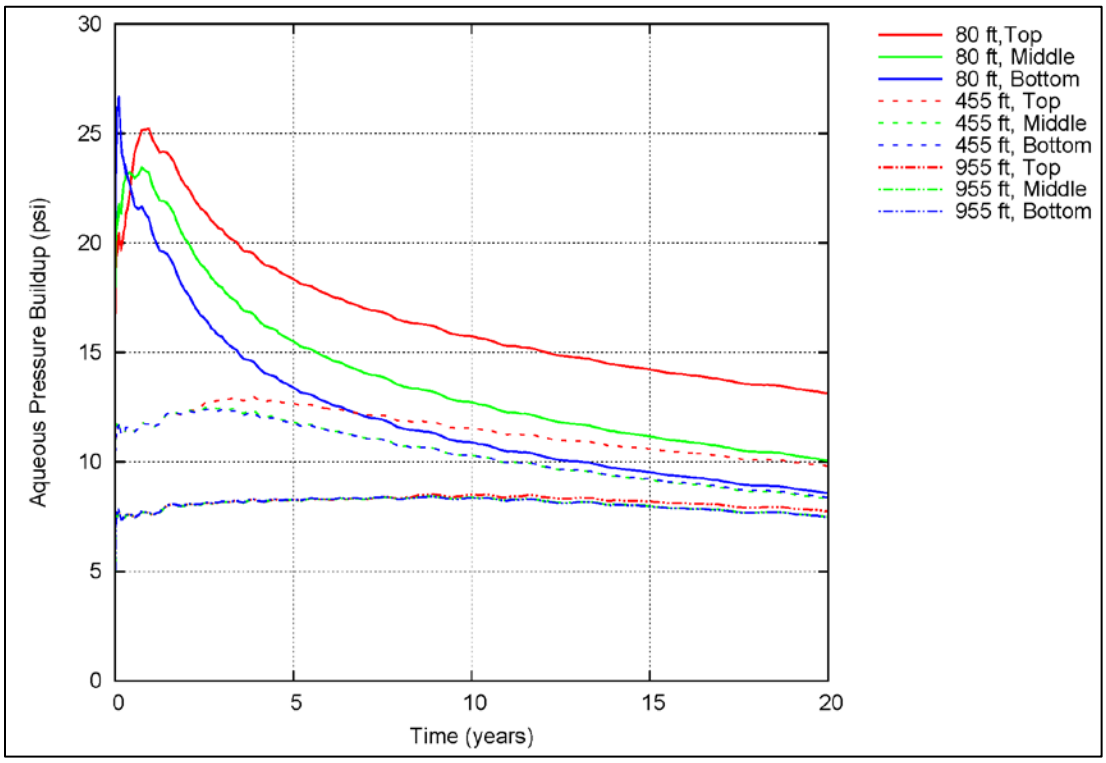

Figure A.6. Aqueous pressure line plot (compare to Figure 7.7)

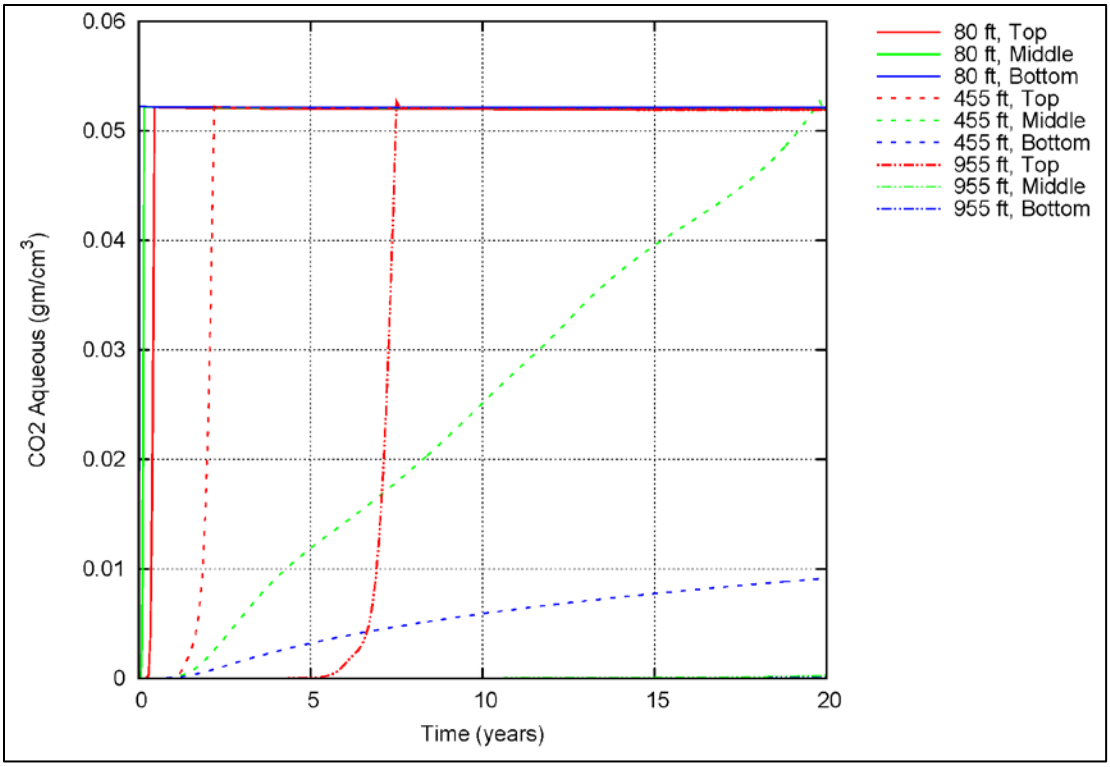

Figure A.7. Aqueous CO_2 breakthrough curves (compare to Figure 7.10)

A.3 Extended Boundary – 100-Year $scCO_2$ Leakage Case

The geometry of the third comparison case is identical to that presented in Section A.2, but with an extended simulation period of 100 years (i.e., at the 100-year leakage rate, as discussed in Section 7.2).

Comparison of $scCO_2$ saturations between the 100-year base case model (Section 7.2.2) and the extended boundary case indicates that $scCO_2$ saturation values are noticeably attenuated for the extended boundary conditions case (Figures A.8 and 7.13). While $scCO_2$ saturations at 80 ft for all depth profiles in the Ironton show only slight decreases in maximum values when compared to the base case, more significant decreases are seen at the top of the Ironton at 455 and 955 ft from the leakage source. Aqueous pressure trends were similar between the cases, with only slight increases for all lateral distances and vertical profiles within the Ironton for the extended case simulation (Figures A.9 and 7.15). In addition, aqueous pressures decreases in the extended boundary case did not return to levels seen in the base case after 100 years but remained slightly higher. Simulated aqueous CO_2 concentrations were very similar between the 100-year extended boundary and base cases (Figures A.10 and 7.17). Based on this comparison, the grid used for the Section 7 simulations was sufficient for this preliminary modeling effort and development of a leakage-detection modeling framework. However, future simulations that incorporate updated site characterization data will use the extended model domain.

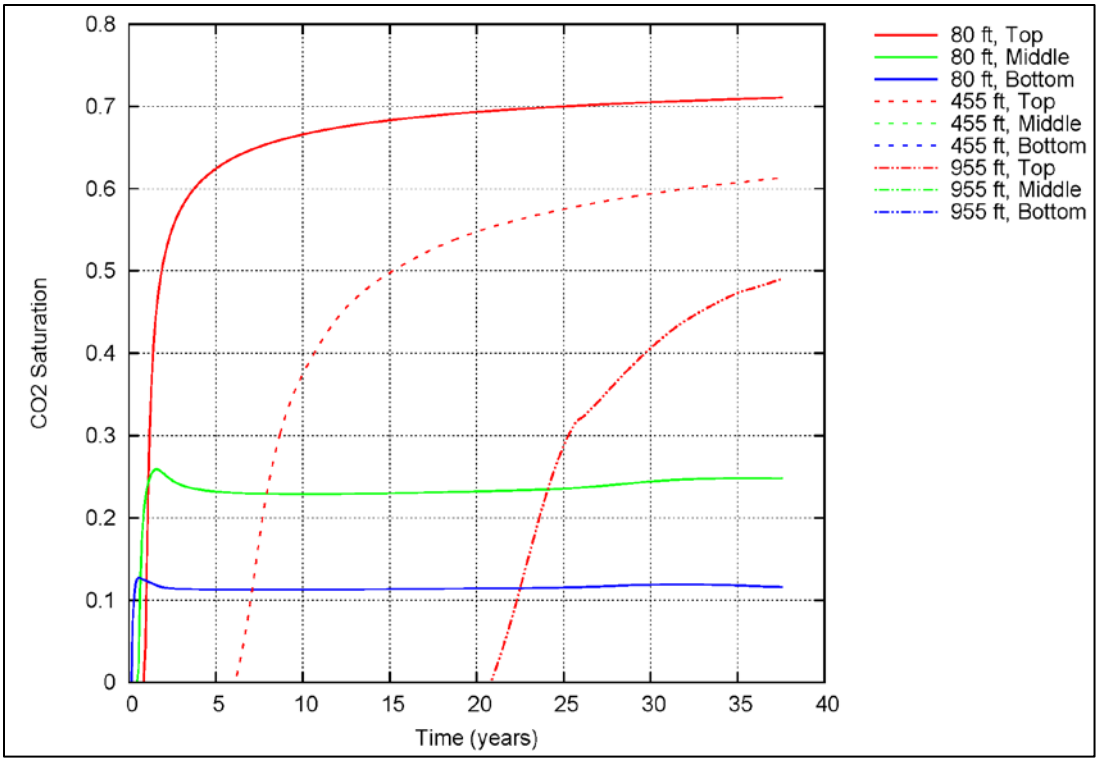

Figure A.8. $scCO_2$ breakthrough curves (compare to Figure 7.13).

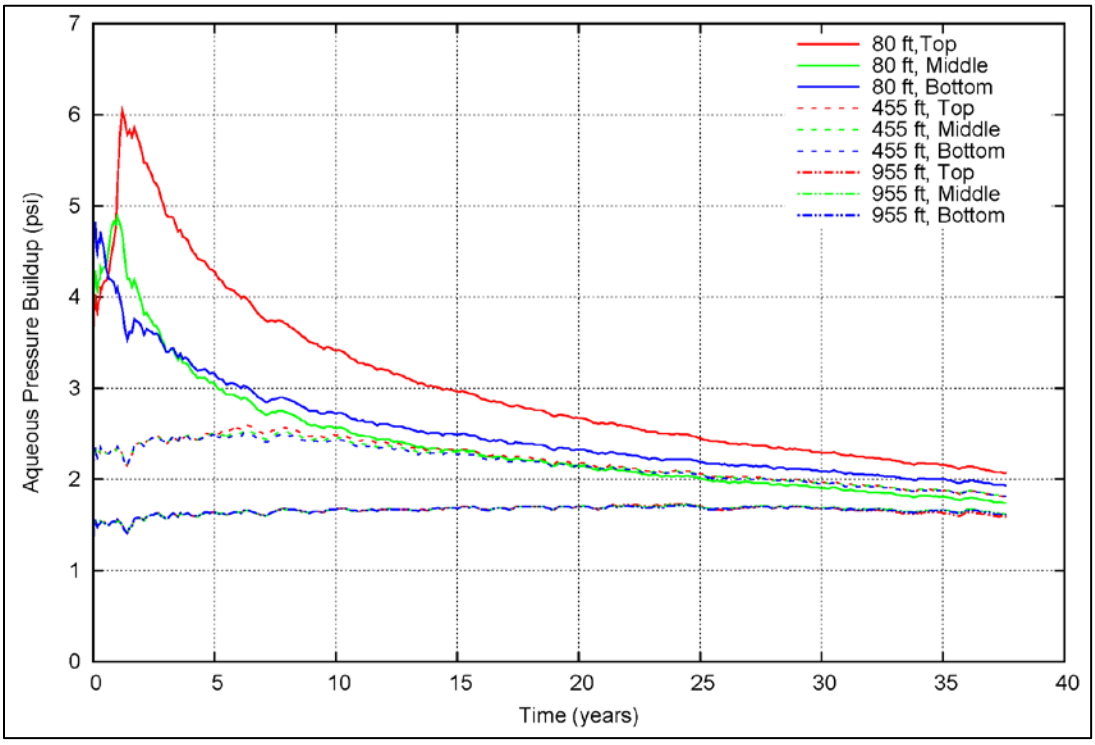

Figure A.9. Aqueous pressure line plot (compare to Figure 7.15).

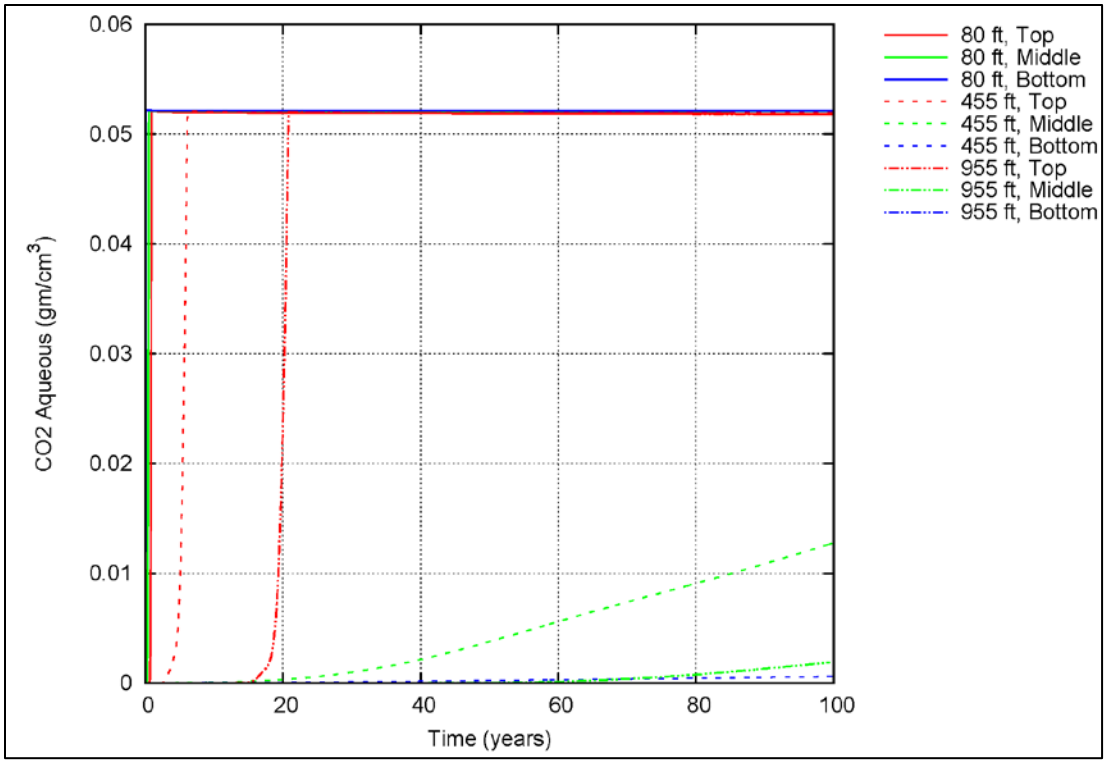

Figure A.10. Aqueous CO_2 breakthrough curves (compare to Figure 7.17)**.**

Appendix B

MVA-ULT Model Simulation Summary Tables

Appendix B

MVA-ULT Model Simulation Summary Tables

B.1 $scCO_2$ Simulation Data Results

Table B.1. Aqueous pressure and arrival times for multiple detection levels, top zone of the Ironton Formation.

Distance from Leak	Detection Level	20-Year Case		100-Year Case		500-Year Case	
		Time	Value	Time	Value	Time	Value
(ft)	(psi)	(year)	(psi)	(year)	(psi)	(year)	(psi)
80	0.2	1.08E-05	2.00E-01	2.19E-05	2.80E-01	5.47E-05	2.03E-01
	1	2.19E-05	1.38E+00	1.08E-04	1.08E+00		
	2	3.47E-05	2.38E+00	6.45E-04	2.01E+00		
	5	1.08E-04	5.09E+00	1.10E+00	5.39E+00		
	Peak Value	9.29E-01	2.34E+01	1.20E+00	5.69E+00	2.20E+00	9.86E-01
	10% Peak Value	3.47E-05	2.38E+00	4.36E-05	6.40E-01	2.76E-05	1.11E-01
	50% Peak Value	1.26E-03	1.18E+01	3.85E-03	2.95E+00	1.26E-03	5.16E-01
	90% Peak Value	4.60E-01	2.12E+01	1.10E+00	5.39E+00	2.00E+00	8.95E-01
455	0.2	8.59E-05	2.40E-01	2.11E-04	2.40E-01	1.26E-03	2.12E-01
	1	2.64E-04	1.21E+00	1.97E-03	1.10E+00		
	2	5.16E-04	2.31E+00	1.70E+00	2.00E+00		
	5	1.97E-03	5.31E+00				
	Peak Value	3.80E+00	1.09E+01	6.20E+00	2.19E+00	1.62E+01	4.36E-01
	10% Peak Value	2.64E-04	1.21E+00	2.11E-04	2.40E-01	4.36E-05	4.53E-02
	50% Peak Value	2.46E-03	5.88E+00	1.97E-03	1.10E+00	1.58E-03	2.28E-01
	90% Peak Value	1.00E-01	9.87E+00	3.00E-01	1.98E+00	2.20E+00	3.94E-01
955	0.2	4.13E-04	2.60E-01	1.01E-03	2.30E-01	9.40E-03	2.01E-01
	1	1.01E-03	1.02E+00	1.18E-02	1.05E+00		
	2	1.97E-03	2.07E+00				
	5	1.18E-02	5.24E+00				
	Peak Value	8.80E+00	6.45E+00	2.36E+01	1.31E+00	4.97E+01	2.53E-01
	10% Peak Value	8.07E-04	7.70E-01	6.45E-04	1.40E-01	2.76E-05	2.87E-02
	50% Peak Value	3.85E-03	3.37E+00	3.85E-03	6.80E-01	3.08E-03	1.33E-01
	90% Peak Value	1.33E+00	5.86E+00	2.20E+00	1.18E+00	2.70E+00	2.28E-01

Note: Cells without a time value indicate that no breakthrough was observed for that scenario.

Table B.2. Aqueous pressure and arrival times for multiple detection levels, bottom zone of the Ironton Formation.

Distance from Leak	Detection Level	20-Year Case		100-Year Case		500-Year Case	
		Time	Value	Time	Value	Time	Value
(ft.)	(psi)	(year)	(psi)	(year)	(psi)	(year)	(psi)
80	0.2	0.00E+00	1.39E+00	0.00E+00	1.39E+00	0.00E+00	1.39E+00
	1	0.00E+00	1.39E+00	0.00E+00	1.39E+00	0.00E+00	1.39E+00
	2	3.97E-06	2.10E+00	1.08E-04	2.01E+00		
	5	1.74E-05	5.18E+00				
	Peak Value	1.00E-01	2.47E+01	4.48E-02	4.48E+00	0.00E+00	1.39E+00
	10% Peak Value	5.16E-06	2.51E+00	0.00E+00	1.39E+00	0.00E+00	1.39E+00
	50% Peak Value	3.30E-04	1.30E+01	1.69E-04	2.29E+00	0.00E+00	1.39E+00
	90% Peak Value	3.59E-02	2.26E+01	6.02E-03	4.20E+00	0.00E+00	1.39E+00
455	0.2	0.00E+00	1.44E+00	0.00E+00	1.44E+00	0.00E+00	1.44E+00
	1	0.00E+00	1.44E+00	0.00E+00	1.44E+00	0.00E+00	1.44E+00
	2	5.16E-04	2.32E+00	1.70E+00	2.00E+00		
	5	1.97E-03	5.32E+00				
	Peak Value	2.60E+00	1.04E+01	6.20E+00	2.11E+00	0.00E+00	1.44E+00
	10% Peak Value	0.00E+00	1.44E+00	0.00E+00	1.44E+00	0.00E+00	1.44E+00
	50% Peak Value	1.97E-03	5.32E+00	0.00E+00	1.44E+00	0.00E+00	1.44E+00
	90% Peak Value	1.47E-02	9.44E+00	2.87E-02	1.91E+00	0.00E+00	1.44E+00
955	0.2	0.00E+00	1.37E+00	0.00E+00	1.37E+00	0.00E+00	1.37E+00
	1	0.00E+00	1.37E+00	0.00E+00	1.37E+00	0.00E+00	1.37E+00
	2	1.97E-03	2.08E+00				
	5	9.40E-03	5.00E+00				
	Peak Value	8.80E+00	6.36E+00	0.00E+00	1.37E+00	0.00E+00	1.37E+00
	10% Peak Value	0.00E+00	1.37E+00	0.00E+00	1.37E+00	0.00E+00	1.37E+00
	50% Peak Value	3.85E-03	3.38E+00	0.00E+00	1.37E+00	0.00E+00	1.37E+00
	90% Peak Value	5.61E-02	5.74E+00	0.00E+00	1.37E+00	0.00E+00	1.37E+00

Note: Cells without a time value indicate that no breakthrough was observed for that scenario.

Table B.3. $scCO_2$ saturation values and arrival times for multiple detection levels, top zone of the Ironton Formation.

Distance from Leak	Detection Level	20-Year Case		100-Year Case		500-Year Case	
		Time	Value	Time	Value	Time	Value
(ft.)	CO_2 sat.	(year)	CO_2 sat.	(year)	CO_2 sat.	(year)	CO_2 sat.
80	0.1	5.35E-01	2.18E-01	1.00E+00	1.02E-01	1.90E+00	1.14E-01
	0.2	5.35E-01	2.18E-01	1.10E+00	2.22E-01	2.10E+00	2.40E-01
	0.3	6.29E-01	3.17E-01	1.20E+00	3.08E-01	2.30E+00	3.20E-01
	0.4	8.29E-01	4.16E-01	1.40E+00	4.04E-01	2.80E+00	4.13E-01
	Peak Value	2.00E+01	7.04E-01	1.00E+02	7.29E-01	4.93E+02	6.46E-01
	10% Peak Value	5.35E-01	2.18E-01	1.00E+00	1.02E-01	1.90E+00	1.14E-01
	50% Peak Value	7.29E-01	3.77E-01	1.30E+00	3.65E-01	2.40E+00	3.47E-01
	90% Peak Value	4.80E+00	6.34E-01	8.30E+00	6.57E-01	1.13E+01	5.82E-01
455	0.1	2.50E+00	1.05E-01	7.00E+00	1.03E-01	2.37E+01	1.03E-01
	0.2	2.80E+00	2.44E-01	7.70E+00	2.05E-01	2.74E+01	2.01E-01
	0.3	3.00E+00	3.21E-01	8.70E+00	3.05E-01	3.59E+01	3.01E-01
	0.4	3.40E+00	4.10E-01	1.07E+01	4.03E-01	5.77E+01	4.00E-01
	Peak Value	2.00E+01	6.79E-01	1.00E+02	6.65E-01	5.00E+02	5.44E-01
	10% Peak Value	2.40E+00	6.99E-02	6.80E+00	7.56E-02	2.22E+01	5.58E-02
	50% Peak Value	3.10E+00	3.49E-01	9.20E+00	3.38E-01	3.29E+01	2.73E-01
	90% Peak Value	8.10E+00	6.11E-01	3.13E+01	5.98E-01	1.30E+02	4.90E-01
955	0.1	8.00E+00	1.06E-01	2.22E+01	1.01E-01	6.36E+01	1.01E-01
	0.2	8.40E+00	2.05E-01	2.35E+01	2.02E-01	6.82E+01	2.01E-01
	0.3	8.90E+00	3.14E-01	2.52E+01	3.03E-01	8.00E+01	3.01E-01
	0.4	9.80E+00	4.04E-01	2.95E+01	4.00E-01	1.07E+02	4.00E-01
	Peak Value	2.00E+01	6.27E-01	1.00E+02	6.19E-01	5.00E+02	5.30E-01
	10% Peak Value	7.90E+00	8.29E-02	2.17E+01	6.36E-02	6.17E+01	5.45E-02
	50% Peak Value	8.90E+00	3.14E-01	2.54E+01	3.11E-01	7.48E+01	2.65E-01
	90% Peak Value	1.40E+01	5.65E-01	5.33E+01	5.57E-01	2.07E+02	4.77E-01

Table B.4. $scCO_2$ saturation values and arrival times for multiple detection levels, bottom zone of the Ironton Formation.

Distance from Leak	Detection Level	20-Year Case		100-Year Case		500-Year Case	
		Time	Value	Time	Value	Time	Value
(ft.)	CO_2 sat.	(year)	CO_2 sat.	(year)	CO_2 sat.	(year)	CO_2 sat.
80	0.1	4.48E-02	1.52E-01	2.93E-01	1.00E-01		
	0.2	7.01E-02	2.31E-01				
	0.3	1.67E-01	3.08E-01				
	0.4		0.00E+00				
	Peak Value	2.50E+00	3.98E-01	5.35E-01	1.27E-01	1.69E+02	3.21E-02
	10% Peak Value	2.87E-02	4.28E-02	1.67E-01	2.51E-02	8.50E+00	3.39E-03
	50% Peak Value	7.01E-02	2.31E-01	2.42E-01	7.88E-02	1.22E+01	1.62E-02
	90% Peak Value	5.35E-01	3.61E-01	3.52E-01	1.15E-01	1.41E+02	2.89E-02
455	0.1		0.00E+00				
	0.2		0.00E+00				
	0.3		0.00E+00				
	0.4		0.00E+00				
	Peak Value	0.00E+00	0.00E+00	0.00E+00	0.00E+00	0.00E+00	0.00E+00
	10% Peak Value	0.00E+00	0.00E+00	0.00E+00	0.00E+00	0.00E+00	0.00E+00
	50% Peak Value	0.00E+00	0.00E+00	0.00E+00	0.00E+00	0.00E+00	0.00E+00
	90% Peak Value	0.00E+00	0.00E+00	0.00E+00	0.00E+00	0.00E+00	0.00E+00
955	0.1						
	0.2						
	0.3						
	0.4						
	Peak Value	0.00E+00	0.00E+00	0.00E+00	0.00E+00	0.00E+00	0.00E+00
	10% Peak Value	0.00E+00	0.00E+00	0.00E+00	0.00E+00	0.00E+00	0.00E+00
	50% Peak Value	0.00E+00	0.00E+00	0.00E+00	0.00E+00	0.00E+00	0.00E+00
	90% Peak Value	0.00E+00	0.00E+00	0.00E+00	0.00E+00	0.00E+00	0.00E+00

Note: Cells without a time value indicate that no breakthrough was observed for that scenario.

Table B.5. Aqueous CO_2 concentrations and arrival times for multiple detection levels, top zone of the Ironton Formation.

Distance from Leak	Detection Level	20-Year Case		100-Year Case		500-Year Case	
		Time	Value	Time	Value	Time	Value
(ft)	(g/cm^3)	(year)	(g/cm^3)	(year)	(g/cm^3)	(year)	(g/cm^3)
80	0.001	3.52E-01	4.56E-03	7.29E-01	1.80E-03	1.50E+00	2.10E-03
	0.002	3.52E-01	4.56E-03	8.29E-01	1.29E-02	1.50E+00	2.10E-03
	0.003	3.52E-01	4.56E-03	8.29E-01	1.29E-02	1.60E+00	1.07E-02
	0.004	3.52E-01	4.56E-03	8.29E-01	1.29E-02	1.60E+00	1.07E-02
	Peak Value	4.60E-01	5.22E-02	9.29E-01	5.21E-02	1.80E+00	5.21E-02
	10% Peak Value	4.00E-01	1.68E-02	8.29E-01	1.29E-02	1.60E+00	1.07E-02
	50% Peak Value	4.60E-01	5.22E-02	9.29E-01	5.21E-02	1.70E+00	3.67E-02
	90% Peak Value	4.60E-01	5.22E-02	9.29E-01	5.21E-02	1.80E+00	5.21E-02
455	0.001	1.33E+00	1.25E-03	3.50E+00	1.10E-03	1.03E+01	1.00E-03
	0.002	1.53E+00	2.63E-03	4.10E+00	2.22E-03	1.23E+01	2.05E-03
	0.003	1.63E+00	3.73E-03	4.40E+00	3.10E-03	1.30E+01	3.16E-03
	0.004	1.73E+00	5.42E-03	4.60E+00	4.02E-03	1.34E+01	4.23E-03
	Peak Value	2.20E+00	5.22E-02	6.10E+00	5.23E-02	2.04E+01	5.21E-02
	10% Peak Value	1.73E+00	5.42E-03	4.80E+00	5.59E-03	1.37E+01	5.33E-03
	50% Peak Value	2.10E+00	3.47E-02	5.60E+00	2.66E-02	1.76E+01	2.62E-02
	90% Peak Value	2.20E+00	5.22E-02	6.10E+00	5.23E-02	2.01E+01	4.73E-02
955	0.001	5.90E+00	1.04E-03	1.69E+01	1.01E-03	5.02E+01	1.01E-03
	0.002	6.20E+00	2.07E-03	1.80E+01	2.04E-03	5.17E+01	2.07E-03
	0.003	6.50E+00	3.26E-03	1.84E+01	3.16E-03	5.24E+01	3.19E-03
	0.004	6.60E+00	4.04E-03	1.86E+01	4.12E-03	5.28E+01	4.08E-03
	Peak Value	7.50E+00	5.21E-02	2.08E+01	5.20E-02	5.92E+01	5.20E-02
	10% Peak Value	6.70E+00	5.29E-03	1.88E+01	5.46E-03	5.33E+01	5.49E-03
	50% Peak Value	7.20E+00	2.66E-02	2.00E+01	2.66E-02	5.68E+01	2.66E-02
	90% Peak Value	7.50E+00	5.21E-02	2.06E+01	4.78E-02	5.88E+01	4.80E-02

Table B.6. Aqueous CO_2 concentrations and arrival times for multiple detection levels, bottom zone of the Ironton Formation.

Distance from Leak	Detection Level	20-Year Case		100-Year Case		500-Year Case	
		Time	Value	Time	Value	Time	Value
(ft.)	(g/cm^3)	(year)	(g/cm^3)	(year)	(g/cm^3)	(year)	(g/cm^3)
80	0.001	7.52E-03	1.42E-03	3.59E-02	1.12E-03	1.50E+00	2.10E-03
	0.002	9.40E-03	3.27E-03	4.48E-02	2.24E-03	1.50E+00	2.10E-03
	0.003	9.40E-03	3.27E-03	5.61E-02	5.00E-03	1.60E+00	1.07E-02
	0.004	1.18E-02	7.74E-03	5.61E-02	5.00E-03	1.60E+00	1.07E-02
	Peak Value	2.30E-02	5.25E-02	1.67E-01	5.22E-02	1.80E+00	5.21E-02
	10% Peak Value	1.18E-02	7.74E-03	7.01E-02	1.04E-02	1.60E+00	1.07E-02
	50% Peak Value	1.84E-02	3.09E-02	1.00E-01	2.65E-02	1.70E+00	3.67E-02
	90% Peak Value	2.30E-02	5.25E-02	1.39E-01	5.21E-02	1.80E+00	5.21E-02
455	0.001	2.40E+00	1.03E-03			1.03E+01	1.00E-03
	0.002	3.50E+00	2.05E-03			1.23E+01	2.05E-03
	0.003	4.70E+00	3.00E-03			1.30E+01	3.16E-03
	0.004	6.20E+00	4.00E-03			1.34E+01	4.23E-03
	Peak Value	2.00E+01	9.23E-03	1.00E+02	7.99E-04	2.04E+01	5.21E-02
	10% Peak Value	2.30E+00	9.40E-04	1.97E+01	8.00E-05	1.37E+01	5.33E-03
	50% Peak Value	7.30E+00	4.63E-03	6.41E+01	4.00E-04	1.76E+01	2.62E-02
	90% Peak Value	1.67E+01	8.32E-03	9.39E+01	7.19E-04	2.01E+01	4.73E-02
955	0.001					5.02E+01	1.01E-03
	0.002					5.17E+01	2.07E-03
	0.003					5.24E+01	3.19E-03
	0.004					5.28E+01	4.08E-03
	Peak Value	2.00E+01	8.93E-06	1.00E+02	1.28E-07	5.92E+01	5.20E-02
	10% Peak Value	8.90E+00	9.04E-07	6.51E+01	1.28E-08	5.33E+01	5.49E-03
	50% Peak Value	1.48E+01	4.49E-06	9.26E+01	6.44E-08	5.68E+01	2.66E-02
	90% Peak Value	1.91E+01	8.10E-06	9.89E+01	1.16E-07	5.88E+01	4.80E-02

Note: Cells without a time value indicate that no breakthrough was observed for that scenario.

B.2 Brine Simulation Data Results

Table B.7. Aqueous tracer concentrations and arrival times for multiple detection levels, top and bottom zones of the Ironton Formation.

Distance from Leak	Detection Level	20-Year Case		100-Year Case	
		Time	Value	Time	Value
(ft)	(g/cm^3)	(year)	(g/cm^3)	(year)	(g/cm^3)
80	0.001	3.60E+00	1.01E-03	4.48E-02	1.32E-03
	0.002			7.01E-02	2.37E-03
	0.003			8.76E-02	3.01E-03
	0.004			1.39E-01	4.47E-03
	Peak Value	2.00E+01	1.47E-03	1.99E+01	7.16E-03
	10% Peak Value	1.83E+00	1.81E-04	3.59E-02	9.34E-04
	50% Peak Value	3.00E+00	7.58E-04	1.18E-01	3.94E-03
	90% Peak Value	5.10E+00	1.33E-03	3.52E-01	6.61E-03
455	0.001			9.80E+00	1.01E-03
	0.002				
	0.003				
	0.004				
	Peak Value	2.00E+01	5.47E-04	2.00E+01	1.79E-03
	10% Peak Value	7.70E+00	5.47E-05	4.10E+00	1.86E-04
	50% Peak Value	1.33E+01	2.76E-04	9.00E+00	8.98E-04
	90% Peak Value	1.85E+01	4.95E-04	1.62E+01	1.62E-03
955	0.001				
	0.002				
	0.003				
	0.004				
	Peak Value	2.00E+01	6.09E-07	2.00E+01	1.12E-05
	10% Peak Value	1.50E+01	6.42E-08	1.35E+01	1.12E-06
	50% Peak Value	1.83E+01	3.15E-07	1.77E+01	5.67E-06
	90% Peak Value	1.98E+01	5.66E-07	1.97E+01	1.03E-05

Note: Cells without a time value indicate that no breakthrough was observed for that scenario.

Table B.8. Aqueous pressure and arrival times for multiple detection levels, top and bottom zones of the Ironton Formation.

Distance from Leak	Detection Level	20-Year Case (Ironton Top)		20-Year Case (Ironton Bottom)	
		Time	Value	Time	Value
(ft.)	(psi)	(year)	(psi)	(year)	(psi)
80	0.2	1.08E-05	2.90E-01	0.00E+00	1.39E+00
	1	1.74E-05	1.14E+00	0.00E+00	1.39E+00
	2	2.76E-05	2.23E+00	3.97E-06	2.40E+00
	5	8.59E-05	5.35E+00	1.38E-05	5.51E+00
	Peak Value	1.93E+01	1.97E+01	1.97E+01	2.64E+01
	10% Peak Value	2.76E-05	2.23E+00	5.16E-06	2.92E+00
	50% Peak Value	4.13E-04	9.94E+00	2.11E-04	1.34E+01
	90% Peak Value	6.02E-03	1.78E+01	7.52E-03	2.38E+01
455	0.2	8.59E-05	2.80E-01	0.00E+00	1.44E+00
	1	2.11E-04	1.08E+00	0.00E+00	1.44E+00
	2	4.13E-04	2.19E+00	4.13E-04	2.20E+00
	5	1.58E-03	5.40E+00	1.58E-03	5.40E+00
	Peak Value	4.48E-02	1.08E+01	1.99E+01	1.12E+01
	10% Peak Value	2.11E-04	1.08E+00	0.00E+00	1.44E+00
	50% Peak Value	1.58E-03	5.40E+00	1.97E-03	6.01E+00
	90% Peak Value	9.40E-03	9.93E+00	1.18E-02	1.03E+01
955	0.2	3.30E-04	2.00E-01	0.00E+00	1.37E+00
	1	1.01E-03	1.17E+00	0.00E+00	1.37E+00
	2	1.97E-03	2.35E+00	1.97E-03	2.36E+00
	5	7.52E-03	5.22E+00	7.52E-03	5.24E+00
	Peak Value	4.48E-02	6.32E+00	4.48E-02	6.34E+00
	10% Peak Value	8.07E-04	8.80E-01	0.00E+00	1.37E+00
	50% Peak Value	3.08E-03	3.31E+00	3.08E-03	3.32E+00
	90% Peak Value	1.18E-02	5.86E+00	1.18E-02	5.88E+00

Table B.9. Salt mass fraction and arrival times for multiple detection levels, top and bottom zones of the Ironton Formation.

Distance from Leak	Detection Level	20-Year Case (Ironton Top)		20-Year Case (Ironton Bottom)	
		Time	Value	Time	Value
(ft.)	Fraction	(year)	Fraction	(year)	Fraction
80	0.01	0.00E+00	1.49E-02	0.00E+00	1.49E-02
	0.02	2.40E+00	2.05E-02	7.01E-02	2.12E-02
	0.03	3.50E+00	3.03E-02	1.67E-01	3.16E-02
	0.04	5.20E+00	4.02E-02	3.52E-01	4.06E-02
	Peak Value	2.00E+01	4.51E-02	3.10E+00	4.53E-02
	10% Peak Value	0.00E+00	1.49E-02	0.00E+00	1.49E-02
	50% Peak Value	2.70E+00	2.31E-02	8.76E-02	2.34E-02
	90% Peak Value	5.40E+00	4.08E-02	4.00E-01	4.18E-02
455	0.01	0.00E+00	1.49E-02	0.00E+00	1.49E-02
	0.02	1.25E+01	2.00E-02	7.00E+00	2.01E-02
	0.03			1.25E+01	3.01E-02
	0.04				
	Peak Value	2.00E+01	2.95E-02	2.00E+01	3.94E-02
	10% Peak Value	0.00E+00	1.49E-02	0.00E+00	1.49E-02
	50% Peak Value	0.00E+00	1.49E-02	6.80E+00	1.97E-02
	90% Peak Value	1.77E+01	2.66E-02	1.62E+01	3.56E-02
955	0.01	0.00E+00	1.49E-02	0.00E+00	1.49E-02
	0.02				
	0.03				
	0.04				
	Peak Value	2.00E+01	1.55E-02	2.00E+01	1.50E-02
	10% Peak Value	0.00E+00	1.49E-02	0.00E+00	1.49E-02
	50% Peak Value	0.00E+00	1.49E-02	0.00E+00	1.49E-02
	90% Peak Value	0.00E+00	1.49E-02	0.00E+00	1.49E-02

Note: Cells without a time value indicate that no breakthrough was observed for that scenario.

Pacific Northwest
NATIONAL LABORATORY

Proudly Operated by Battelle *Since 1965*

U.S. DEPARTMENT OF
ENERGY

902 Battelle Boulevard
P.O. Box 999
Richland, WA 99352
1-888-375-PNNL (7665)
www.pnnl.gov